

ALMA MATER STUDIORUM · UNIVERSITÀ DI BOLOGNA

DOTTORATO DI RICERCA IN
FISICA
Ciclo XXVII

Settore Concorsuale di afferenza: 02/B1

Settore Scientifico disciplinare: FIS/03

Transport Properties and Novel Sensing Applications of Organic Semiconducting Crystals

Presentata da: Andrea Ciavatti

Coordinatore Dottorato:
Prof. Fabio Ortolani

Relatore:
Prof. Beatrice Fabroni

Esame finale anno 2013/2014

Dedicated to my family

Contents

Introduction	ix
1 Organic Electronics	3
1.1 Development of Organic Electronics	3
1.2 Organic Semiconducting Single Crystals	6
1.2.1 OSSCs growth techniques	7
1.2.2 Structural Characteristics	11
1.3 Charge Transport in Organic Crystals	13
1.3.1 Band-like transport in Organic Single Crystals	17
1.4 Single Crystal Field-Effect Transistors	21
2 Overview on Organic X-ray Detectors	25
2.1 General concept of X-ray detectors	25
2.1.1 Sources of Electromagnetic Radiation	26
2.1.2 Radiation Interaction with Matter	29
2.1.3 Radiation Quantities Glossary	30
2.2 X-ray Detectors	35
2.2.1 Scintillators	36
2.2.2 Semiconductor Detectors	37
2.3 Organic Indirect Radiation Detectors	43
2.3.1 Organic Scintillators	43
2.3.2 Organic Photodiode	46
2.4 Organic Direct Detectors	48

3	Materials and Methods	57
3.1	Electrical Characterization	57
3.1.1	Space Charge Limited Current	58
3.1.2	Organic Thin Film Transistors	65
3.2	Photocurrent Spectroscopy	66
3.3	Detectors Characterization	70
3.3.1	X-ray Mo Tube	70
3.3.2	SYRMEP Beamline - ELETTRA	71
3.3.3	Gamma Sources	72
3.4	Materials	73
3.4.1	4-hydroxycyanobenzene (4HCB)	74
3.4.2	5,6,11,12-Tetraphenyltetracene (Rubrene)	79
3.4.3	TIPS-pentacene	83
3.4.4	DNN	84
3.4.5	NTI	85
4	OSSCs as X-ray Detectors	89
4.1	4HCB Single crystal direct detectors	90
4.1.1	X-ray Direct Detectors	91
4.1.2	Substrate and Electrodes contribution to X-ray induced signal	93
4.1.3	All Organic Detectors	97
4.1.4	Detector Characterization and Performances	97
4.1.5	Electrodes Geometric effects	105
4.2	Flexible devices	109
4.2.1	Space Charge Transport analyses	111
4.2.2	Bendability Properties	113
4.3	Other molecules	115
4.4	High Energy Detection	124
5	OTFTs as X-ray Sensors	127
5.1	Thin film planar structure	128

5.1.1	X-ray Direct Detectors	129
5.1.2	High Energy Detection	132
5.2	OTFT structure	133
6	OSSCs as Alpha particle Sensors	137
6.1	Overview on Organic alpha particle detectors	138
6.2	Experimental Setup	139
6.3	Results and Discussion	141
7	OSSCs as Chemical Sensors	149
7.1	Experimental Setup	151
7.2	Chemiresistor effects	152
7.3	Intrinsic effects	154
7.4	Modeling	156
8	High Mobility Crystalline Organic TFTs	159
8.1	Rubrene Thin Film Structure and Morphology	160
8.2	Electrical Characterization	162
8.3	Opto-electronic Characterization	165
8.4	Rubrene OTFTs	168
8.4.1	OTFTs with SiO ₂ dielectric	169
8.4.2	OTFTs with Cytop [®] dielectric	171
	Conclusions	179
	Bibliography	207
	Acknowledgements	209

Introduction

The light weight, simple processability, and mechanical flexibility of π -conjugated organic small molecules and polymers has recently led to remarkable research efforts towards the realization of new opto-electronic devices. Moreover, organic materials can be deposited and grown by means of easy, low temperature and low cost technologies as inkjet printing, with the possibility of covering large areas onto flexible substrates. In recent years, opto-electronic devices based on single crystals of conjugated organic molecules have gained the attention of the research community because of their potentiality in combining the high performances of molecular single crystals with the advantages of organic electronics. Thanks to their high chemical purity and the low density of defects (e.g. grain boundaries, typical of polycrystalline semiconductor thin films), organic single crystals can be indeed considered as the most performing organic materials in terms of charge mobility, exciton diffusion length and stability against degradation [1].

The present thesis is focused on the study of Organic Semiconducting Single Crystals (OSSCs) and crystalline thin films. In particular solution-grown OSSC, e.g. 4-hydroxycyanobenzene (4HCB) and crystalline films have been characterized in view of their applications as novel sensors of X-rays, gamma and alpha radiations, and as sensors to polar volatile molecules.

The study has been carried out at the Department of Physics and Astronomy of the University of Bologna, Italy, in close cooperation with the Synchrotron Laboratory ELETTRA, Trieste, Italy.

In the first chapter a general introduction to the field of Organic Elec-

tronics is given, with particular focus on the performance and interesting properties of organic single crystals properties.

In the field of ionizing radiation detection, organic semiconductors have been proposed so far mainly as indirect detectors, i.e. as scintillators or as photodiodes active materials [2]. Although direct detection of the ionizing radiation, i.e. its direct conversion into an electrical signal, allows to reduce the signal-to-noise ratio and the response time of the device, only few examples of organic-based direct detectors have been reported in the literature, all employing thin films of organic semiconducting or conductive materials [3, 4, 5]. The state of the art of this kind of organic X-ray detectors, as well as an overview on the commonly used radiation sources and on the general characteristic of X-ray detectors, are discussed in chapter two.

The materials and experimental tools used for the devices under study are described in chapter three.

I have focused my research activity, in chapter four, on the study of the performance of 4HCB single crystals as direct X-ray detector, and the results indicate that they can effectively operate at room temperature and in atmosphere, showing a stable and linear response with increasing dose rate. In addition, a dedicated study of the collecting electrodes geometry, contacts materials, crystal thickness and interaction volume allowed us to maximize the charge collection efficiency and to take advantage of the transport and charge collection anisotropy of the crystals. In order to improve our knowledge about the processes involved in the observed X-ray induced photocurrent signal, a comparative study is presented on OSSCs based on several small molecules, namely 1,5-dinitronaphthalene (DNN), 1,8-naphthaleneimide (NTI), with different molecular structures and polarizability, which crystallize with different geometries and molecular packing. Furthermore, with the aim to investigate how the polarity of the molecule affects the response of the detector, we characterized Rubrene OSSCs-based devices and TIPS-pentacene thin films: which have well known electrical performances and are considered the benchmarks in organic electronics.

Chapter five is dedicated to the investigation of TIPS-pentacene thin film as direct X-ray detectors.

Regarding others ionizing radiations, the proof of principle of alpha particles has been assessed for 4HCB single crystals in chapter six.

The electrical transport properties of organic materials are greatly affected by environmental conditions [6], thus in chapter seven I have carried out a thorough investigation of the electrical characterization of single crystals when exposed to vapour of volatile molecules, both polar (ethanol and heptane) and non-polar (isopropanol), to assess their potential as chemical sensing devices.

The last chapter of this thesis (chapter eight) deals with rubrene, one of the most promising molecular crystals for electronic and optoelectronic applications, since it shows the highest intrinsic charge-carrier mobility (up to $20 \text{ cm}^2/\text{Vs}$ at room temperature) [7] and the longest reported exciton diffusion length ($2\text{-}8 \mu\text{m}$), [8] Indeed, the integration of crystalline rubrene thin films, having the same performances as single crystals, in flexible electronic devices, would represent a crucial technological improvement. We present an investigation on high quality, millimeter-sized, crystalline and fully oriented rubrene thin films of different thicknesses (varying in the range between 10 nm and 100 nm) realized by exploiting organic molecular beam epitaxy on water-soluble substrates. To investigate the electrical and opto-electronic transport properties of the thin films, Space Charge Limited Current (SCLC) analyses and Wavelength-resolved photocurrent spectroscopy measurements have been carried out, on samples with different thicknesses. Moreover, a field-effect thin transistor (OTFT) employing rubrene thin film have been fabricated and fully characterized.

In order to accomplish the research activity presented in this PhD thesis, I have carried out two visiting research periods: one at Department of Physics, University of Surrey, UK, under the supervision of Prof. P.J. Sellin and the second one at the Optical Material Engineering Laboratory (OMEL), ETH, Zurich, under the supervision of Prof. D. Norris and Dr. D. Braga.

Chapter 1

Organic Electronics

1.1 Development of Organic Electronics

The first studies on organic materials date back to the beginning of the 20th century. In 1950s an intensive investigation on the photoconductivity of organic semiconducting crystals began and later in the 1960s followed the discovery of their electroluminescence. Since the 1970s, the successful synthesis and controlled doping of conjugated polymers established the second important class of organic conductors, and in the 1980s the demonstration of an efficient photovoltaic cell with an organic p-n heterojunction and the fabrication of the first thin film transistor based on conjugated polymers were reported. In the last 20 years, under the thrust of the Nobel Prize in Chemistry in the 2000, with a growing interest of private industries, the technological development of organic electronics arises. The great appeal of organic electronics is the low fabrication costs, low temperature processes that not require big and expensive equipments, and the possibility to cover large areas, almost on every substrate, also on extremely stretchable ones, resulting in the easy fabrication of transparent and flexible devices. The application of organic electronics, spans from transparent solar cells, OLED displays and flexible screens to RFID tags and sensors, taking advantage of their extremely sensitivity to environmental conditions like temperature,

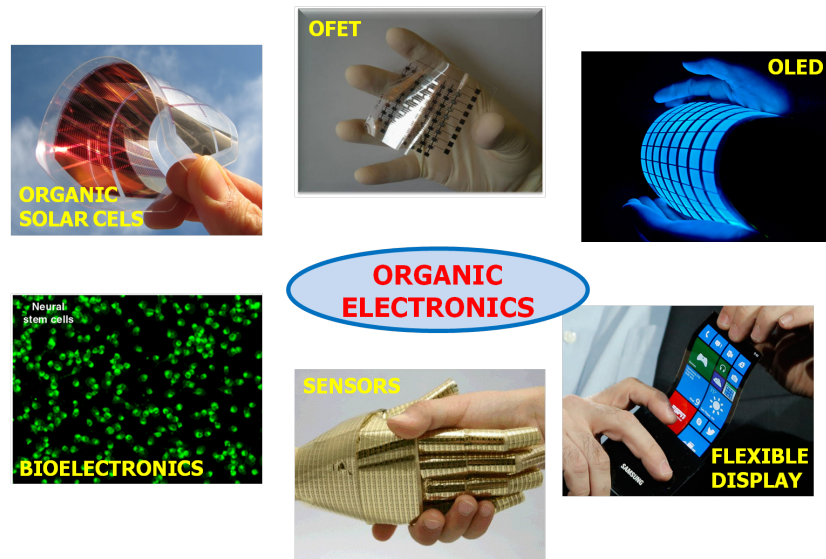


Figure 1.1: Some of the most promising organic electronics applications.

gas, pressure and humidity (figure 1.1). Furthermore, because of their light atomic weight and chemical composition organic semiconductors are tissue-equivalent and bio-compatible materials, and this feature opens new ways to their applications in bio-medical sensor field as smart tissues and bio-medical patches able to inject a medicine in case of necessity. These new possibilities are the engine that makes the challenge of this research so intriguing.

The key points to implement all these promises are the research efforts to fabricate working devices able to accomplish the industrial challenges. Organic materials properties are extremely encouraging for Organic Photovoltaic (OPV) to accomplish the third generation photovoltaic requests; indeed very recently a new record for OPV has been established, reaching 40% of transparency and 12% of efficiency, overcoming the efficiency limit of merchantability of 10% [9, 10]. Organic Light-Emitting Diodes (OLEDs) are the most advanced technology among organic electronics, thanks to the discovery of high-performance electroluminescent diodes, and the progress in charge collection performances of blended films of conjugated polymers. Nowadays low power consumption OLEDs are commercially available and many of the new smartphones generation mount OLED display [11]; more-

over many world leading electronics industries are assessing the commerciality of OLED-based flexible screens [12]. Organic Field-Effect Transistors (OFETs) are the most important devices for the development of organic electronics, being the fundamental building-blocks of any complex electronic system, e.g logic circuits. Very recently organic thin films have reached the mobility value of amorphous silicon, open the way to real application like in AMOLED (active matrix organic light emitting diode) that allow the realization of a full organic and flexible displays [13]. Concerning the application of OFETs as mechanical sensors, extraordinary performances have been assessed in the realization of artificial robotic skins based on OFETs-based pressure sensors matrices fabricated onto extremely flexible and light substrates [14]. Moreover, a new class of organic transistor devices are rising in the last years, i.e. Organic Electro-Chemical Transistors (OECTs), particularly suitable for bioelectronic applications since they employ ions as charge carriers in the same way of biochemical processes, being thus the connection between electronic and biological system [15]. Nowadays organic electronic devices are already a commercial reality, however, the next step to improve their availability on the market is to face the challenge of exiting from the laboratories, targeting low cost, reliable and high credit standing technology. For example TetraPak, world leader in packaging, estimates that the cost for an organic RFID devices cannot exceed about 0.2 Eurocents per package. In addition two more steps are necessary to accomplish the commercially low cost, the proper choice of the substrate and the integration of the same active material for several devices; in fact, currently, for each type of organic device (OLEDs, logic OFETs, sensor OFETs) a different organic molecule have been optimized, in such a way more than 50 fabrication steps would be necessary for the realization of a full organic system. One of the most interesting fabrication technique, developed also in order to overcome this issue, is inkjet printing of organic materials for the realization of organic devices [16], it allows very low fabrication costs and a extremely controlled pattern design, even for the deposition of several layers. Furthermore the

possibility to print organic devices directly on paper, cheap and massive produced, has been already demonstrated through this method, and employing PEDOT:PSS as organic active material, an OECT, a display with logic gates and a pressure sensor on the same paper have been realised [17].

1.2 Organic Semiconducting Single Crystals

Many organic solids and polymers are perfect insulators and are used to considerable extent technically as such. However, there is also a large number of organic semiconductors employed, as already mentioned in the previous paragraph, in the development of new flexible and disposable electronic devices, such as organic solar cells, OLEDs, smart tags and sensors. The appealing market for these new applications requires a combination of performance, low cost, light weight and easy processability. Under the lead of industrial applications, the devices development is more focused on the technological improvement, which often goes beyond the poor knowledge of the underlying physics, with the drawback that the understanding of the fundamental properties of this important class of semiconductor is limited still today. This discrepancy is also strongly due to the structural disorder of polycrystalline and amorphous organic thin films, which are extremely complex systems, that suffer of lack of reproducibility and are challenging to theoretically model with a good agreement with experimental results.

Organic Semiconducting Single-Crystals (OSSCs) offer a suited environment for fundamental research: high structural order (i.e. long range order and the absence of grain boundaries), high chemical purity (i.e the absence of unwilling chemical impurities within the crystalline structure), and the availability of several efficient methods for fabrication of high quality defect-free single crystals. In some extremely high purity crystals the first demonstration of band-like transport in organic materials was observed [18] and thanks to the success in the development of organic-dielectric interfaces with very low defects, high performance OFETs based on single crystals, have shown

very high performances in terms of charge carriers mobility at room temperature, exceeding the value of $1 \text{ cm}^2/\text{Vs}$, typical of amorphous silicon and usually the reference value for most of the commercial electronic applications [19]. Specifically, the most studied and purified crystals are p-type polycyclic aromatic materials such as 5,6,11,12-tetraphenyltetracene (commonly called “rubrene”, $\mu_{RUB} \sim 5 - 40 \text{ cm}^2/\text{Vs}$), tetracene ($\mu_{TET} \sim 2.4 \text{ cm}^2/\text{Vs}$) and pentacene ($\mu_{PEN} \sim 5 - 40 \text{ cm}^2/\text{Vs}$); for n-type materials we can mention N,N'-bis(n-alkyl)-(1,7 and 1,6)-dicyanoperylene-3,4:9,10-bis(dicarboximide) (PDIF-CN₂) ($\mu_{PDIF-CN_2} \sim 1 - 6 \text{ cm}^2/\text{Vs}$) [20] and 5,7,12,14-tetrachloro-6,13-diazapentacene (TCDAP) ($\mu_{TCDAP} \sim 3.36 \text{ cm}^2/\text{Vs}$) [21]. In addition, the intrinsic order and the low density of traps in OSSCs allow a series of fundamental studies upon the intrinsic polaronic transport, the correlation between crystalline structure and material properties (like the anisotropy of mobility), the investigation of Hall effect and the observation of very long excitons lifetime ($100 \mu\text{s}$) and diffusion length ($\sim 10 \mu\text{m}$) [8]. Furthermore the crystals structure is easier to model and can be used in computational simulations and calculation.

1.2.1 OSSCs growth techniques

A crucial stage for an high performance OSSC-based device is the purity and the high quality of the single crystal, on account of this, several growth methods have been developed [22]. As organic crystals show a good solubility in numerous organic solvents and have low melting temperatures and high vapour pressures, physical vapour transport methods, melt growth methods and solution growth methods are exploited.

Physical vapour transport methods (PVT) are used to grow crystals and to purify the material at the same time. The property of organic semiconductors of subliming without decomposition makes PVT suitable for their growth. Organic powder material or pristine impure crystals are heated in a tube under a flow of inert gas (hydrogen, argon or nitrogen gas); the evaporating molecules are transported by the gas flow through a tempera-

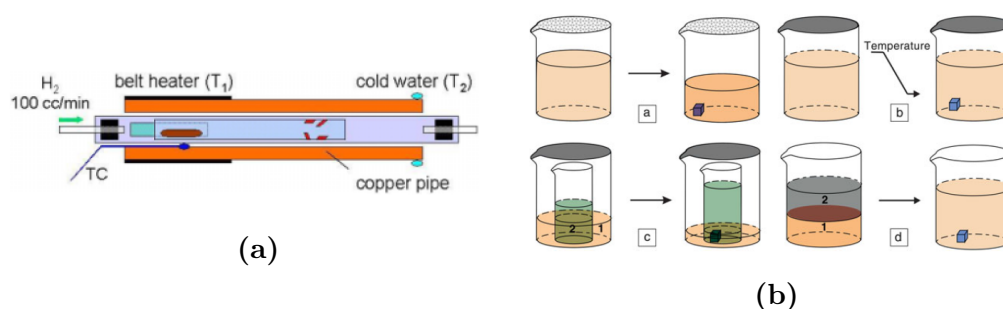


Figure 1.2: a) Sketch of a typical PVT tube. Reported from [23]. b) Some solution-based growth methods. From upper left: solvent evaporation, slow cooling, vapour diffusion and liquid-liquid diffusion [22].

ture gradient since they reach a critical temperature and crystallization takes place. Since impurities have melting temperatures different from those of the specific molecules, they are thrown away by the gas (figure 1.2a). The gas flow and temperature control is very important to tune the speed of sublimation, deposition and crystal growth. Most of high quality organic crystals, like rubrene, anthracene, pyrene, naphthalene and fullerene, are grown by PVT.

Melt growth methods like Bridgman, zone melting and Czochralski growth methods, are the most used for growing large inorganic semiconductor crystals. They are very efficient for inorganic materials but owing to the high vapor pressure and chemical instability of large organic materials around melting temperature, only few and available in large quantities organic molecules have been tested on this methods. For few of them large high quality single-crystalline ingots were obtained.

Solution growth methods are used for various organic molecules, especially for those having good solubility in common organic solvents. Such methods are easy, very low cost and capable of producing a large amount of crystals in one step. The growth procedure is very simple and can be summarized as follow: the small molecule is dissolved in a solution, and as the mixture cools and solvent evaporates, the organic material crystallizes into a vial or directly onto the substrates. The rate and size of the crystals may be

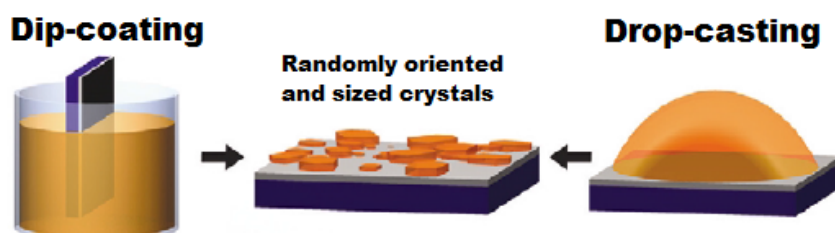


Figure 1.3: Dip-coating procedure (left): dip substrate in supersaturated semiconductor solution, remove and allow solvent to evaporate. Drop-casting procedure (right): Apply a drop of semiconductor solution onto the substrate surface, and allow solvent to evaporate. Adapted from [24].

controlled by tuning the cooling and the evaporation rates, along with solvent type and solution concentration. The simplest and most efficient is the “Solvent evaporation method” (figure 1.2a), where the molecule is dissolved in an organic solvent like chloroform, toluene or benzene and a saturated solution is placed in a closed beaker not hermetically sealed; the solvent can slowly evaporate forming supersaturated solution and large crystals start to grow from nuclei seeds. A large number of crystals can be grown by this method, among them several polar crystals such as 4-hydroxycyanobenzene (3.4.1) and other crystals discussed in this thesis. Other solution growth methods (slow cooling, vapour diffusion, liquid-liquid diffusion, organic flux solid solvent, supercritical solvent) are reported in [22] and some of them are show in figure 1.2b. It is mandatory to mention two solution-phase growth methods which are technologically relevant, for the ease of covering large substrate with solution grown single crystals aggregate in thin films: drop-casting and dip-coating (figure 1.3). The first simply refers to a drop of supersaturated solution of a soluble semiconductor deposited onto a substrate and let dry; in the second the substrate is soaked into the solution, then removed and let dry. The main issue of these two coating techniques is that the crystals have random orientations and sizes; moreover only few soluble small molecules are able of forming single crystals by the employment of these techniques [25].

Printing techniques have recently rise the attention as simply way of

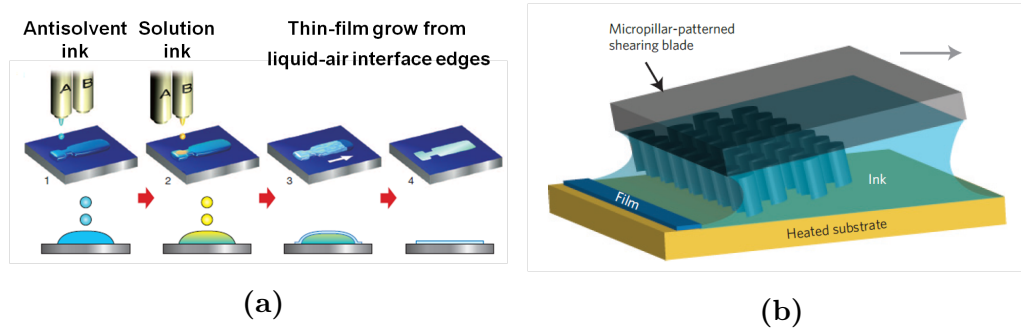


Figure 1.4: Schematic of the processes of a) inkjet printing of organic single-crystal thin films[26]. b) solution shearing using a micropillar-patterned blade. The arrow indicates the shearing direction [27].

producing organic electronic devices. “Printed electronics” is being explored for the development of large-area and flexible electronic devices by the patterned application of organic semiconductor-based functional inks [28]. Noteworthy, solution growth methods can be developed to realize printed organic single crystals. Recently, antisolvent crystallization has been exploited to achieve a controlled solidification. An antisolvent ink (a liquid in which a substance is insoluble) is first patterned, and then a second ink with the material is added. The particular patterning choice promote the ordered crystallization (figure 1.4a). High performances OSSCs-based devices have been realized my means of this inkjet printing technique [26]. In addition, high performing large area (several mm^2) organic crystals have been made by means of shear-deposition (figure 1.4b) by properly patterning the blade and the substrate [27].

Organic molecular beam epitaxy (OMBE) is an ultra high vacuum technique that is commonly used for thin film deposition. It’s not usually employed for single crystals growth, in fact some organic semiconductors cannot crystallize in high vacuum, for example Rubrene forms quasi-amorphous disordered films. Nonetheless the crystallization can be enhanced by means of a proper conditioning. In this thesis an highly crystalline thin film of rubrene is discussed; it was grown with OMBE onto a particular substrate

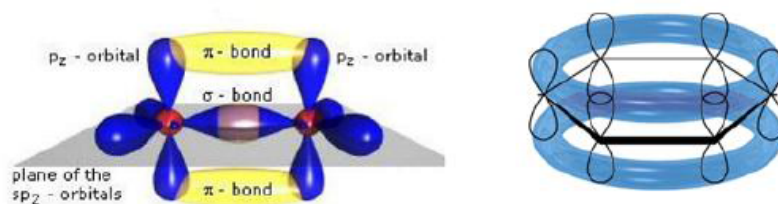


Figure 1.5: Schematic view of σ and π bonds and delocalization of π orbitals in aromatic ring.

(an amino acid called β -alanina), resulting in a highly ordered rubrene film thanks to the exceptionally good match between the crystallographic axes of such substrate and the rubrene crystal itself (see chapter 8).

1.2.2 Structural Characteristics

In an aromatic molecule the hybridized atom orbitals of carbon atoms are bounded by σ - or π - bonds: the first are strong connection parallel to the molecular plane, the second are delocalized bonds that form molecular orbitals (figure 1.5), in particular two important molecular orbitals are called Highest Occupied Molecular Orbital (HOMO) and Lowest Unoccupied Molecular Orbital (LUMO), respectively the outer orbital occupied by electrons and the first unoccupied energy level. It has been proved that in conjugated molecules, an increase of aromatic rings (a longer chain) correspond to a smaller energy gap between HOMO-LUMO and a larger bandwidth. In a molecular non-ordered solid the interactions are dominated by weak Van der Waals forces that only slightly perturb the energy levels of isolated molecule; their morphology is usually undetermined or amorphous. Instead, in molecular crystals long range order takes place, therefore a greater energetic shift arises. From the morphological point of view the crystal structure is determined by intramolecular forces and weak interactions, i.e. dipolar, hydrogen bonds or $\pi - \pi$ interactions; they are really hard to predict and knowing exactly the structure adopted by a specific compound it's almost impossible. Also in single crystals, several polymorphs with comparable cohesion energies

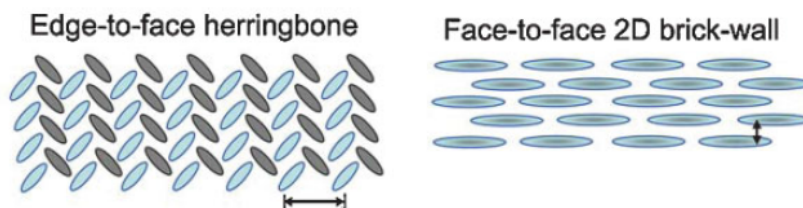


Figure 1.6: Schematic view of two molecular arrangements; herringbone (left) and brick-wall (right) [29].

are generally obtained employing the common growing techniques described in the previous paragraph and such variability strongly depends on the slight differences in growth conditions. Most of the properties are set by molecular packing, starting from the high packing differences between axes, that give rise to strong anisotropy properties. Usually, non-polar aromatic single crystals have a 2D layered structure, in which the highest intermolecular orbital overlap is found along the crystal plane; in the same way, molecules having only one axis with a strong overlap grow in needle-like shape. However, depending on molecular size and intermolecular forces, some different molecular arrangements can be found, as a result of a competitive process between strong $\pi - \pi$ overlap and the minimization of lattice energy due to packing density. The most common arrangement is the herringbone motif that combine high packing density, short-range interaction and low repulsive forces that give stability to the structure (figure 1.6). The $\pi - \pi$ stacking does not affect only the morphological structure of organic crystals, but has dramatically effects on their electrical properties; in fact strong $\pi - \pi$ overlap results also in a better charge transport. In general the weak interactions involved in molecular crystals yield narrow bandwidth, in the order of 0.1-0.5 eV for rubrene single crystals [30], which marks the main difference with inorganic materials that are tied by strong covalent bonding with large bandwidth ($W \approx 10$ eV) and a strong delocalization of electrons. Many charge transport peculiarities arise for that reason in organic materials, they will be treated in more details in the next section.

1.3 Charge Transport in Organic Crystals

The earliest studies on the electrical conduction, dark current and photoconductivity of organic materials were published in the first decades of the 20th century, but only from the second half of the century the scientists began to sequentially investigate organic solids [31, 32]. Many organic solids and polymer are perfect insulators. There is, however, also a large number of organic semiconductors, organic solids with high dark conductivity or quasi-metallic conductivity. Organic crystals with conjugate π -electron systems are highly resistive, semi-insulating materials (e.g. 4-hydroxycyanobenzene, see par. 3.4.1) or semiconductor like rubrene (see par. 3.4.2) and TIPS-pentacene (see par. 3.4.3). They have very small intrinsic charge carriers density but can change their electrical properties by injections or extraction of charge carriers generated by external stimuli.

In this section we briefly define the parameters used to describe conduction in solid, with particular attention to organic molecular crystals. The electrical conductivity σ is defined by the relation between current density \mathbf{j} and the electric field \mathbf{E} :

$$\mathbf{j} = \sigma \mathbf{E} \quad (1.1)$$

In general, organic single crystals are highly anisotropic and the conductivity σ is a tensor. The charge carriers move in the crystal with a mean drift velocity \mathbf{v}_D and its proportionality with electric field is called mobility μ :

$$\mathbf{v}_D = \mu \mathbf{E} \quad (1.2)$$

From the microscopic definition of current density $\mathbf{j} = qn\mathbf{v}_D$ results the following relation 1.3:

$$\sigma_{ij} = qn\mu_{ij} \quad (1.3)$$

The conductivity is therefore the product of two independent quantities: the carrier density n , and the mobility μ ; thus from a simple measurement of current I at a given voltage V , μ and n cannot be determined separately. However n and μ are specific parameters of materials and often depend on

the experimental conditions, such as applied electric field or temperature, and their behaviour can be theoretically modelled, hence these two parameters provide a powerful experimental tool for the investigation of charge transport in solids. Some factors affecting charge carrier mobility are: molecular packing, structural disorder, environmental conditions like temperature and pressure, electric field applied, impurities of the material, charge-carrier density, size/molecular weight [33]. Because of the amount of variables a lot of care in the control of experimental conditions is needed and also it could make very complicated the interpretation of experimental output. However, several experimental techniques allow to extract charge carrier mobility [18], among them the most used are: Time-of-flight (TOF) [34, 35], Space Charge Limited Current (SCLC) [36] method, Hall measurements [37], and Field-Effect Transistors method (OFET) [38, 39]. In this thesis the SCLC (3.1.1) and OFET (3.1.2) methods will be discussed and used.

From the electrical point of view, a narrow bandwidth means more localized charges, thus charge carriers spend more time in every single molecular state with a typical mean transfer time $\tau \approx 10^{-16}$ s, lower than the electronic polarization relaxation time of $\approx 10^{-15}$ s [40]. By means of this effect for each excess charge carrier (i.e electron) in the LUMO level, the charged molecule polarizes the closest molecules. Thus the polarization follow the charges along the lattice, and the resulting effect is that the charge carriers are not electrons or holes, but charged polarization clouds that move through the lattice: the so called *polaron*. The lattice relaxation due to polarons formation leads to a shift of the energy levels which become different respect of that of the isolated molecule, as displayed in figure 1.7. In the limit of an ideal crystal with a perfect periodic lattice the energy levels can be considered discrete. Any kind of deviation from ideal lattice perturbs the periodicity, resulting in a shift of energetic levels E_h and E_e and the formation of shallow levels in the energy-gap (figure 1.7c). On the other hand, impurities or defects in the crystal give rise to deep levels, with energies E_t deeper in the gap, enough that trapped carriers cannot be released by means of thermal

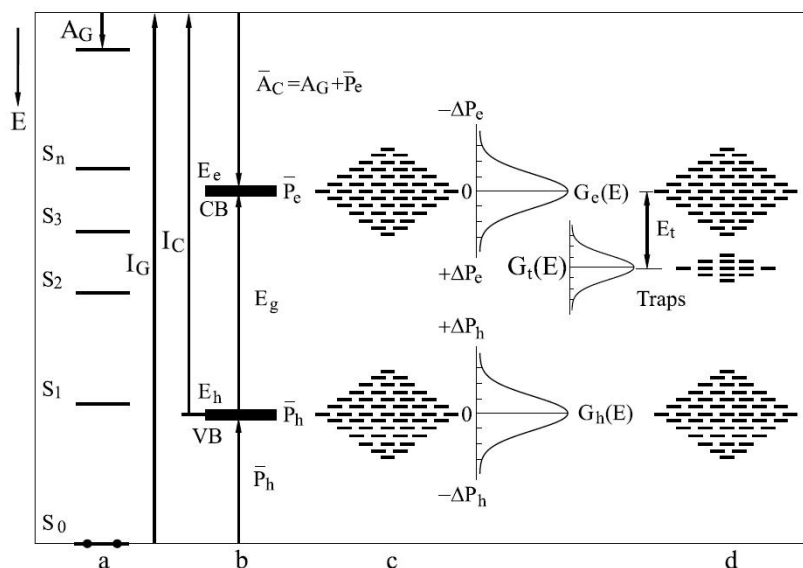


Figure 1.7: The energy diagram of an organic semiconductor. a) The energy levels of the neutral isolated molecules. I_G is the molecular ionization energy, A_G the electron affinity of the isolated molecule. b) The energy bands of the ionized states of the ideal crystal. E_h , E_e are the energies of holes and electrons respectively, P_h and P_e are the mean polarization energies of the holes and the electrons. I_C and A_C are the ionization energy and electron affinity of the crystal. c) The energy levels of the ionized crystal states with a statistical distribution of polarization energies. d) The energy levels of traps within the energy gap.

fluctuations (figure 1.7d). In both cases the levels in an organic material have a continuous statistical distribution, typically gaussian-like:

$$G_t(E) = \frac{N_t}{\sqrt{2\pi}\sigma_t} \cdot e^{-\frac{(E-E_t)^2}{2\sigma_t^2}} \quad (1.4)$$

where E_t is the mean shallow energy level inside the gap, N_t is number of shallow sites and σ_t is the energy spread of the level.

Narrow bandwidth combined with large energy gap leads to low mobility values and very small intrinsic carrier density n_0 , i.e. small conductivity. As a result the most important process in an organic device is the charge injection and extraction at the metal/semiconductor contact (in a resistor or in a field-effect transistor) or induction at the dielectric/semiconductor

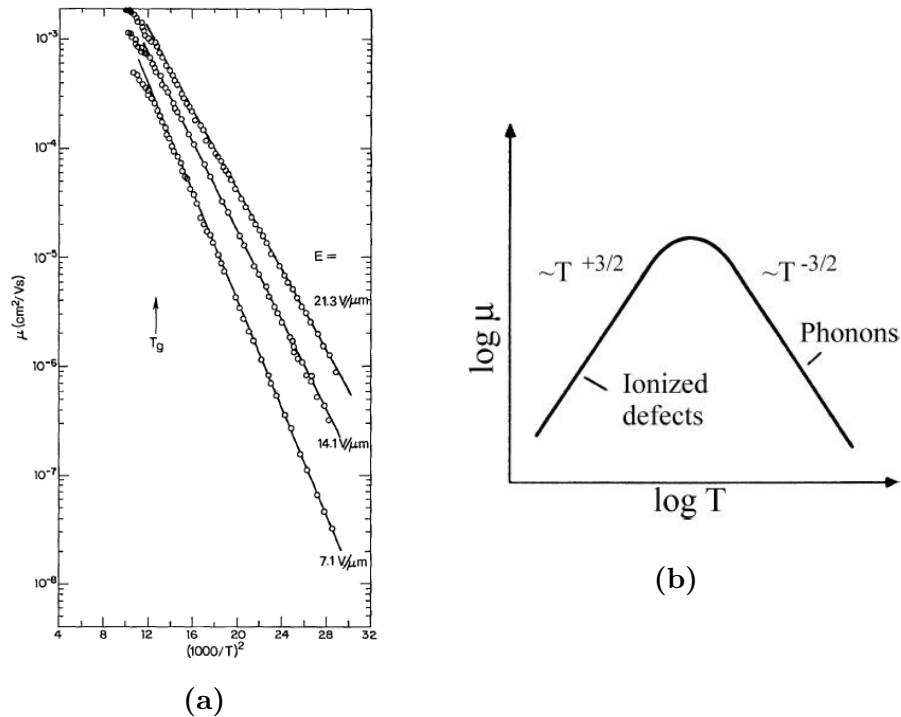


Figure 1.8: Sketch of the temperature dependence of the mobility a) in hopping-like and b) in band-like transport models [41].

interface (in a field-effect transistor). The metal/semiconductor interface can be injection limited, i.e. a potential barrier is formed at the interface through the so called Schottky effect, or not injection limited, i.e. it forms an ohmic contact. In the latter case and under proper conditions, the number of injected charges becomes much larger than the intrinsic ones, i.e. $n_{inj} \gg n_0$, and it is no longer compensated by free charges. Therefore, an additional electric field due to space-charge takes place, thus for large charge injection at high electric field a deviation from linear ohmic behaviour in the current - voltage characteristics can be observed due to Space-charge-limited current (SCLC) more details in section 3.1.1.

1.3.1 Band-like transport in Organic Single Crystals

Since the first studies, in the 1960s, on charge transport in organic materials, a debate was opened on the nature of the charge transport mechanism, if it is band-like (as in inorganic materials) or hopping. In an inorganic material, like silicon, there is a strong interaction between adjacent atoms in the crystalline form, so the overlap of atomic orbitals gives rise to highly delocalized electronic states in the crystal lattice and to the formation of band structure. In a disordered materials no ordered interaction between atoms is possible and the electronic states are spatially localized in the atoms. In this case, charge transport occurs through hopping of the charges between adjacent localized states. The main parameter to discriminate between band transport and hopping transport is to measure the temperature dependence of charge carriers mobility. In fact in a band-like transport the mobility decreases with temperature, with a characteristic potential law $T^{-\frac{3}{2}}$ due to an increasing of electron-phonon scattering, and only at very low T the mobility μ increases with temperature, when ionization of shallow traps takes place (figure 1.8b). On the other hand for typical hopping transport, the charge transport process should be thermally assisted, therefore the mobility increases with temperature as T^n . A temperature activated hopping-like model is typical of the majority of organic materials, and several examples can be found in literature for thin films both by TOF and OFET measurements [42, 43]. The first reliable model to describe hopping in organic materials and to model experimental data was developed in 1991 by Bassler [44]; in his description the mobility increases exponentially with the temperature:

$$\mu = \mu_0 \cdot e^{-\frac{T_0}{T}} \quad (1.5)$$

Nowadays more theoretical studies are ongoing to understand deviations from this model [45].

Regarding ordered structure, e.g. organic single crystals, the picture is even more complex. Many organic molecular crystals, in particular naphthalene, anthracene, tetracene, pentacene and perylene have been grown with ex-

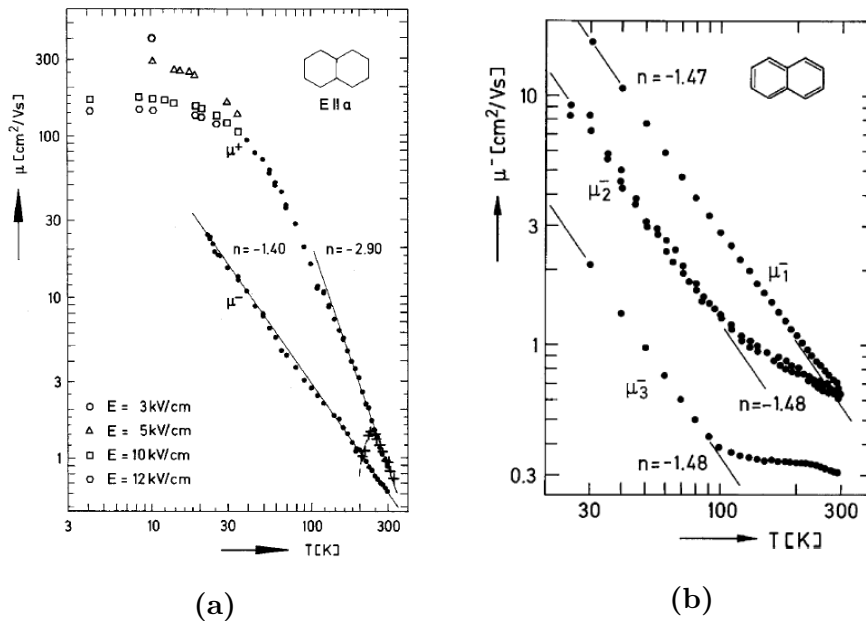


Figure 1.9: a) Proof of band-like transport in naphthalene ultrapure single crystal at low temperature [46]. b) Mobility vs Temperature dependence along all crystallographic axis, showing a deviation from band-like model at $T > 100$ K [35].

tremely high quality through improvement of purification and crystal-growth procedures. In these ultrapure crystals the concentration of impurities and structural defects is exceedingly low; so providing tools to investigate intrinsic mobility. Indeed, experimental evidences are in line with band-like transport, as assessed by TOF mobility measurements in ultrapure naphthalene single crystal in figure 1.9. In figure 1.9a many intrinsic effects typical of ultrapure organic crystals can be observed: i) organic single crystals have the highest mobility among organic framework, approximately of $1 \text{ cm}^2/\text{Vs}$ at room temperature, but they reach even much higher mobilities, up to $400 \text{ cm}^2/\text{Vs}$, at low temperature of 10 K and 3 kV/cm of electric field. ii) the inverse power law $\mu \propto T^{-n}$ is typical of band-like transport, in particular for electron mobility μ^- , $n = 1.4$, it is extraordinarily comparable to that typical of inorganic band model. iii) at high mobility values and temperatures below 40K the mobility becomes dependent on the electric field strength in

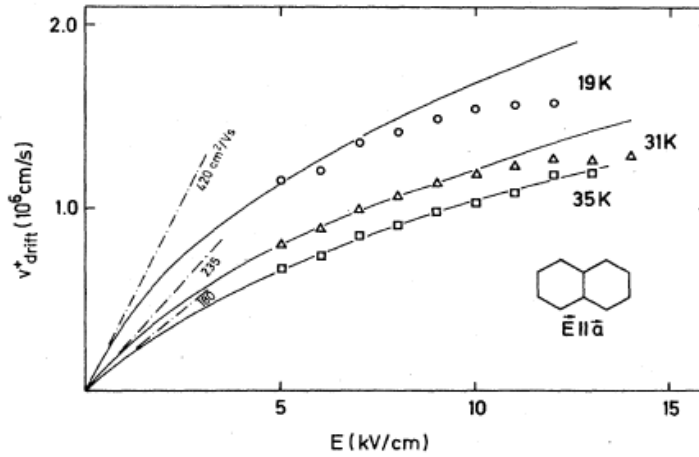


Figure 1.10: Drift velocity vs electric field behaviour in ultrapure naphthalene single crystal. The velocity saturation at high electric field well fit with Schottky model, typical of band transport [47].

a characteristic manner: it decreases with increasing field. The saturation of drift velocity (related to the mobility by the eq.1.2) with electric field at low T is reported in figure 1.10. The sub-linear velocity-field relation can be interpreted with the aid of the Schottky model of acoustic deformation potential scattering of hot charge carriers, typical of the inorganic materials like silicon or germanium, that fits well with experimental values and by which the following expression had been derived (eq. 1.6):

$$v_D = \mu_0 E \cdot \sqrt{2} \left\{ 1 + \left[1 + \frac{3\pi}{8} \left(\frac{\mu_0 E}{c_l} \right)^2 \right]^{1/2} \right\}^{-1/2} \quad (1.6)$$

where E is electric field, μ_0 is the mobility at low electric field ($\mu_0 = \mu(E \rightarrow 0)$) and c_l the sound velocity. iv) Impurities in single crystals have the effects to dramatically decrease mobility and break the band-like transport (e.g. look at + symbol plot in figure 1.9a). These results are explained in more details and are in [46] where similar measurements on perylene ultrapure crystals are reported.

There is no doubt left that charge carrier transport in pure and perfect

low molecular weight conjugated organic crystals at low temperatures has to be described by coherent transport in a band of substantial width and with unexpectedly high mobilities. In fact, the μ vs T measurement and the extremely high mobility that results in carriers faster than the sound velocity, are well fitted with band-like model (even some deviations still have to be explained) and are not accountable with any hopping transport models. However, some problems, concerning the interpretation of the transport mechanism, arise when temperature raises. In fact due to physically clear-cut criteria for band conductivity, some conditions must be fulfilled: the mean scattering time τ must be greater than \hbar/W (W is the bandwidth) to have discrete values of the wavevector and to allow a description in terms of an energy-band model:

$$\tau \gg \frac{\hbar}{W} \quad (1.7)$$

Likewise the mean free path λ of the charge carriers must be long if compared to the lattice constant a_0 :

$$\lambda \gg a_0 \quad (1.8)$$

A typical bandwidth in organic crystal is of the order of 0.1 - 0.5 eV (from optical measurements), thus $\tau \gg 10^{15}$ s, and a typical lattice constant is $a_0 \approx 0.5$ nm, thus $\lambda \gg 0.5$ nm. Whether or not this condition are fulfilled is not easy to discriminate, nevertheless an estimation of these values has been done with the experimentally determined values of mobilities [41, 48]. The results showed that for $T < 150$ K, the condition for the existence of band conductivity are well fulfilled in high-purity naphthalene crystal within the a-b plane. The same holds for other ultrapure molecular crystals at low temperature. On the other hand at room temperature the above physical conditions are no longer satisfied: the charge carriers get more frequently scattered and mobility is reduced, moreover the coherent delocalization decreases and the more localized charge carriers get more coupled to the polarizable crystal lattice, whereby their effective mass m^* (their inertia against acceleration) is increased. In general resulting also in a smaller bandwidth, mean free path reduce to on lattice constant and the extended Bloch waves are break

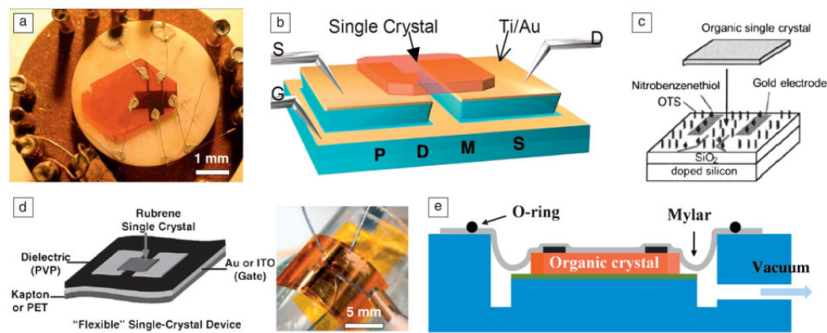


Figure 1.11: Some fabrication method of single crystal FET: a) parylene coating b) PDMS stamp c) lamination d) polymer gate flexible dielectric e) removable membrane gate [1].

down. Through of this mechanism it is possible to explain the mobility deviation from band-like behaviour reported in figure 1.9b for the weak coupling crystallographic c -direction (μ_3) in naphthalene, where the mobility is almost constant up to 300 K. In this case a superposition between two competitive processes, band-like transport and a thermally activated one, is shown. Further studies through computational models show that transport depends on the intermolecular transfer integral (i.e. the strength of $\pi-\pi$ interaction) and the electron-phonon coupling, via both Holstein and Peierls models [49, 33]. Recently, it has been shown that thermal fluctuations at $T > 100$ K induces modulations in the transfer integrals that can be as large as the average transfer intergral itself [50]. Therefore we can conclude that, even in well ordered ultrapure molecular crystals, a polaron-hopping electronic transport mechanism exists.

1.4 Single Crystal Field-Effect Transistors

The development of OFETs is driven by industrial application in plastic electronics and large efforts have been made in pushing transistor performances and in the optimization of materials and fabrication processes, especially in Organic Thin Film Transistors (OTFTs). Thanks to such ef-

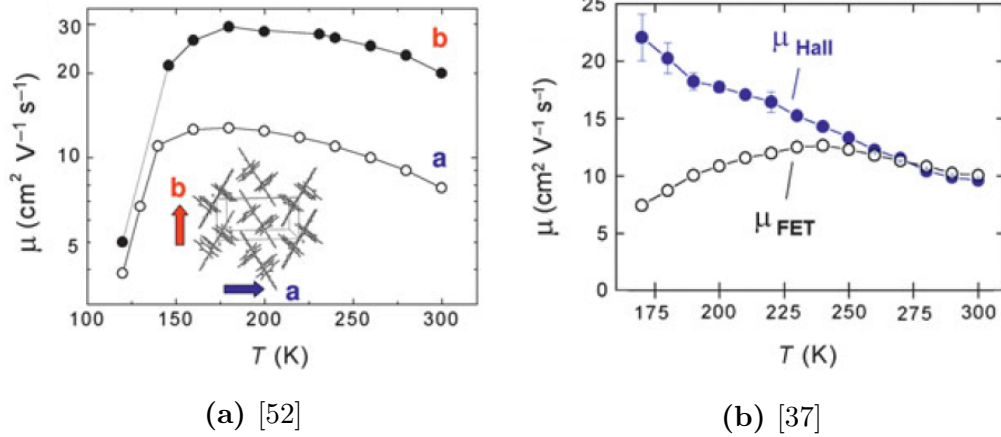


Figure 1.12: Intrinsic coherent charge transport in rubrene molecular crystals. A band-like behavior is measured both for **a** and **b** longitudinal axis (a) and also in hall mobility measurements (b)

OTFTs have reached recently single crystalline performances [27, 51]. Nonetheless the investigation of Single Crystals FET (SCFETs) is arising with the aim of studying the intrinsic transport properties of organic semiconductors and their interfaces. In fact, SCFETs have now set the benchmarks for the FETs performances and have led the knowledge of new phenomena in molecular materials. A variety of techniques have been developed to realize SCFETs, mostly divided in two big categories. The first refers to crystal growth directly on substrates, e.g. by vapour phase on controlled location, or by drop-casting a solution on the channel region and let the material crystallize. However, the most common techniques involve separately the crystal growth and the transistor assembly. The latter case helps the employment of extremely high purity crystals. In figure 1.11 some SCFET fabrication methods are shown [1]. Among others, in particular the methods reported in figure 1.11b is interesting: a single crystal is electrostatically bonded on a pre-fabricated transistor stamp of PDMS (polydimethylsiloxane), a soft rubber-like insulating polymer that well adapt to organic crystal surface. A thin gap is left between source-drain level and gate level, in this way a thin layer of air plays the role of dielectric between gate electrode and or-

organic crystal, such kind of structure is therefore called air-gap OFET. The organic/dielectric surface, that usually play a critical role in the device and strongly influence the transistor performance [53, 54], is in this case completely free of defects. As a consequence, employing the trap-free surface of air-gap OFET band-like transport also for SCFET have been observed. In figure 1.12 it is shown for rubrene, but similar results have been obtained also for tetracene and pentacene SCFET.

Beyond intrinsic transport investigation, the highest mobility in organic materials has been recorded for rubrene single crystal FETs, $\mu = 40 \text{ cm}^2/\text{Vs}$ [52, 55]. For many years it keeps the limit to reach for OTFTs based on amorphous organic materials, that remain more suitable for practical applications, but with a smaller mobility of more than one order of magnitude [56]. A big effort has been made in the last ten years to push such limit, improving the growth techniques, that now allow to fabricate thin films with aligned crystalline domains, thus reaching mobility values comparable to single crystal FETs. this result has been reached employing the well know soluble molecule of 6,13-bis(triisopropylsilylethynyl) pentacene (TIPS-pentacene, see par. 3.4.3) [27], and even better exploiting new promising materials such as a meta stable blend of 2,7-dioctyl[1]benzothieno[3,2-b][1]benzothiophene (C8-BTBT) and polystyrene [51]. Rubrene is not soluble and hence its use for thin film electronic is discouraged, however it still remains the best performing organic material in FET electronics. Following this way several works are being carried on in trying to control the growth of very thin layer of crystalline rubrene [57, 58, 59], leading to the possibility of combining the intrinsic studies on bulk crystals properties to the good technological features of thin films.

Chapter 2

Overview on Organic X-ray Detectors

2.1 General concept of X-ray detectors

X- and gamma-ray radiation constitutes the part of electromagnetic spectrum with wavelength in the range $0.1 \div 100 \text{ \AA}$, or $0.12 \div 120 \text{ keV}$ in energies. X-rays have typical energies of the inner shell of the atomic orbitals since they are generated by the electron decay, processes involving the inner shells, and differ from gamma-rays radiation that have higher energies, in the order of MeV, and are generated by nuclear reaction decays. The employment of X-rays spans from material science (e.g. material properties investigation techniques) to medicine (e.g. diagnostic imaging techniques) and to the control procedures of industrial processes [60, 61, 62]. The X-rays wavelengths are of the same order of magnitude of the crystal lattice constant; this kind of radiation is therefore widely used in diffraction techniques in order to analyze details of material structures, and in absorption techniques to reveal the presence of specific elements in a sample.

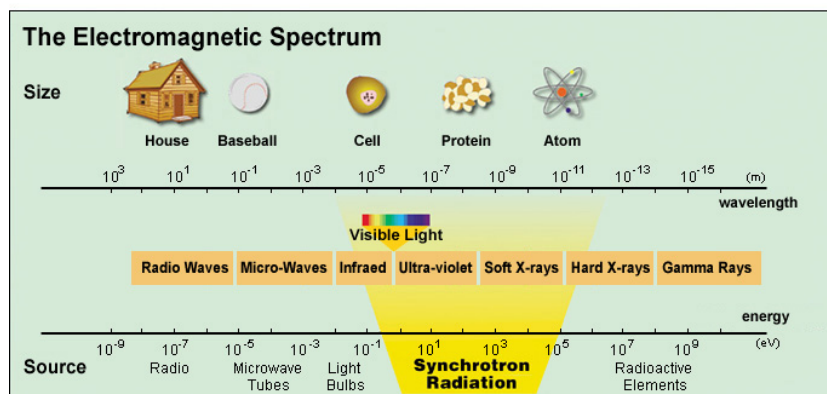


Figure 2.1: Electromagnetic spectrum with X-ray, gamma ray and synchrotron light range pointed out.

2.1.1 Sources of Electromagnetic Radiation

As already mentioned, the actual difference between gamma and X radiation lays on their own generation processes [63]. Gamma rays can be produced following a beta decay, following a nuclear reaction or by electron-positron annihilation. They are emitted by excited nuclei in their transition to lower nuclear levels: when a former beta decay leads the daughter nucleus to an excited state, the subsequent relaxation to the equilibrium state takes place through the emission of a photon with nucleus characteristic energies, thus are used for the precise energy calibration of radiation detectors. Nuclear relaxation is a very fast process (typically in the order of picoseconds), compared to beta decay that is a relatively slow process. Therefore gamma rays have an half-life typical of beta decay, but energies that reflect the nuclear structure. This kind of photons are typically limited to 2.8 MeV. Gamma radiation is also generated by annihilation of a positron-electron couple after a β^+ decay, producing two gamma rays of 0.511 MeV traveling in opposite directions. The third generation process occurs when a nuclear reaction leave and the produced nuclei in an excited state. Although these gamma photons have high energy, they have very short lifetime and aren't useful for practice application unless the exciting nuclear process is kept running.

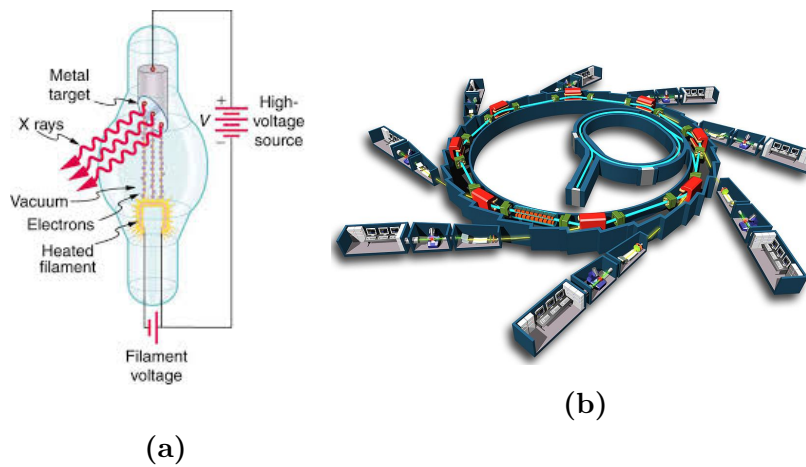


Figure 2.2: Illustration of two X-ray sources: an x-ray tube (a) and synchrotron light (b).

X-ray photons, on the other hand, can be generated by three processes: bremsstrahlung, atomic characteristic transitions and synchrotron radiation. Bremsstrahlung is the electromagnetic radiation emitted when fast electrons interact with matter. The fraction of electron energy converted into bremsstrahlung increases with the electron energy and is largest for absorbing materials with an high atomic number. The energy spectrum is continuous with a predominance of low photon energies that extent as high as the electron energy itself. The process is important in the production of X-rays from conventional X-ray tubes. A characteristic X-ray of an element is produced when an electron from an outer shell fills a vacancy in an inner shell of the atom, such relaxation causes the emission of a photon with energy equal to the difference between the initial and the final state. The discrete energies emitted in the transition correspond to K, L and M shells of atomic orbitals and therefore identify the particular element from which are produced. Bremsstrahlung and characteristic radiation are the two processes involved in the generation of x-rays in typical x-ray tubes. In a X-ray tube an electron beam, produced by thermoionic emission from a hot filament (cathode) heated through an high-current flow, is accelerated at very high potential (tenth of kV) to an anode, made of a target material (usually W, Mo or Cu).

The interaction between the electron beam and the target creates a vacancy in the inner shell of the target exciting the inner-shell electrons to outer shells; X-rays are the produce following the relaxation process described above. The typical emitted spectra of an x-ray tube consists therefore in a convolution of a continuous bremsstrahlung part and the target characteristics energies (figure 2.2a). Compared to that produced by typical gamma-ray sources, the radiation produced by a X-ray tube is more intense, but has a large broad spectrum. The shape of the energy spectrum can be altered by an appropriate insertion of filters, made of absorber materials, between the target and the detector. A proper adjustment of the absorber, i.e. changing the materials and the thickness, allows to shift from a broad to a peaked spectrum, even if still far from monoenergetic one. The third highly exploitable kind of X-ray radiation is synchrotron radiation [64, 65]. From classical electrodynamics an accelerated charged particle emits electromagnetic radiation, synchrotron radiation occurs when a charge moving at relativistic speeds follows a curved trajectory, and part of the energy is irradiated in a tangent direction to the orbit. For relativistic Doppler effects the angular dispersion is $\Delta\Phi \simeq 1/\gamma$, as electron beam in a typical synchrotron facility has $\gamma = 10^3 - 10^4$, the emitted electromagnetic radiation is highly collimated. An illustrative synchrotron facility, a particle accelerator several hundred of meters long, is shown in figure 2.2b: an electron gun emits particle in a booster ring and than the beam is injected in the principal accelerator, the storage ring, where small independent experimental setups, the beamlines, are built for every insertion device that bent the beam and emits synchrotron radiation. Insertion devices define the spectral distribution, the photon flux and coherence of the radiation. Three different system are developed, all used depending on the specific beamline application: bending magnet, wiggler or undulator. Synchrotron facilities are spread in the world because they offer unique characteristics for many applications [66]: high collimation, e.g. the possibility to focus the beam down to few millimeters , high flux, e.g. up to 10^{15} photons/s-mrad (0.1% bandpass), wide spectrum, e.g. from visible to hard X-rays; moreover

photons can be polarized, temporal structured and monochromatic.

2.1.2 Radiation Interaction with Matter

Among the large number of interaction mechanisms (between electromagnetic radiation and matter) known, the three major types take in account to be important in radiation measurements are: photoelectric absorption, Compton scattering and pair production. The importance of the three processes is illustrated in figure 2.3, where it is plotted in function of the photon energy and the atomic number of the absorber material. The photoelectric absorption process involves a photon absorbed by an atom: after the absorption the photon completely disappears and an electron is emitted from the inner shells of the atom. The kinetic energy of the electron is given by $E_{e^-} = h\nu - E_b$, where E_b is the binding energy of the shell and ν the frequency of the photon. The emitted electron leaves a vacancy site in the inner shells of the atom that is quickly filled through a capture of an electron from outer shells. Similarly to what explained in the previous paragraph, this transition generates the emission of characteristics x-ray photons of K, L or M shells. In some cases the relaxation takes place through the emission of an Auger electron that may substitutes the characteristic radiation. Furthermore, the emitted photoelectrons, the characteristic radiation and the Auger electrons may be reabsorbed, thus a complex cascade sequence of electron transitions and x-ray emissions. As the photoelectric effect, also the Compton (or Incoherent) scattering takes place between a photon and an electron in the absorbing materials. In this process the photon is deflected and transfers a portion of its energy. The Compton scattering probability increase with the number of electrons of the target material, and is typically dominant at photon energies of MeV. The pair production process arises at higher energy, when the photon energy exceeds twice the rest-mass on an electron (1.02 MeV). In this process, the photon interacts with coulomb field of a nucleus, having enough energy to create an electron-positron pair. In the medium the pair is slowed down and the positron then annihilates with

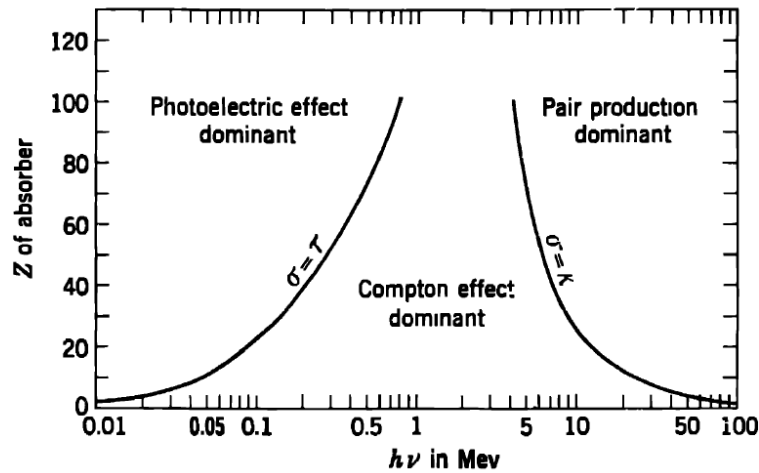


Figure 2.3: The relative importance of the three major types of gamma-rays interaction[67]. The line represent the limits in which the adjacent effects having equal probability.

the emission of two photons as secondary products of the interaction. Even if the process is energetically possible at 1.02 MeV, its probability is still very low and rises only at very high energies. In figure 2.4 the mass absorption coefficient (refers to paragraph 2.1.3) of Selenium ($Z = 34$), the most used material in photoconductor detectors (see paragraph 2.2.2) is shown; the relative contribution of the above described processes with the addition of Rayleigh (or Coherent) scattering, a process in which the photon interacts with the atom and medium and his trajectory is deflected without net transfer of energy, so usually is ignored in radiation absorption processes. The photoelectric absorption is the dominant process at low radiation energies, and plays the main role in the absorption mechanism that occur in x-ray detectors for medical, diagnostic or imaging applications.

2.1.3 Radiation Quantities Glossary

Mass Absorption Coefficient. The mass absorption coefficient (μ/ρ) is a quantity that described the ability of a medium in stopping an electromagnetic radiation. It is defined as the weighting factor in the exponential

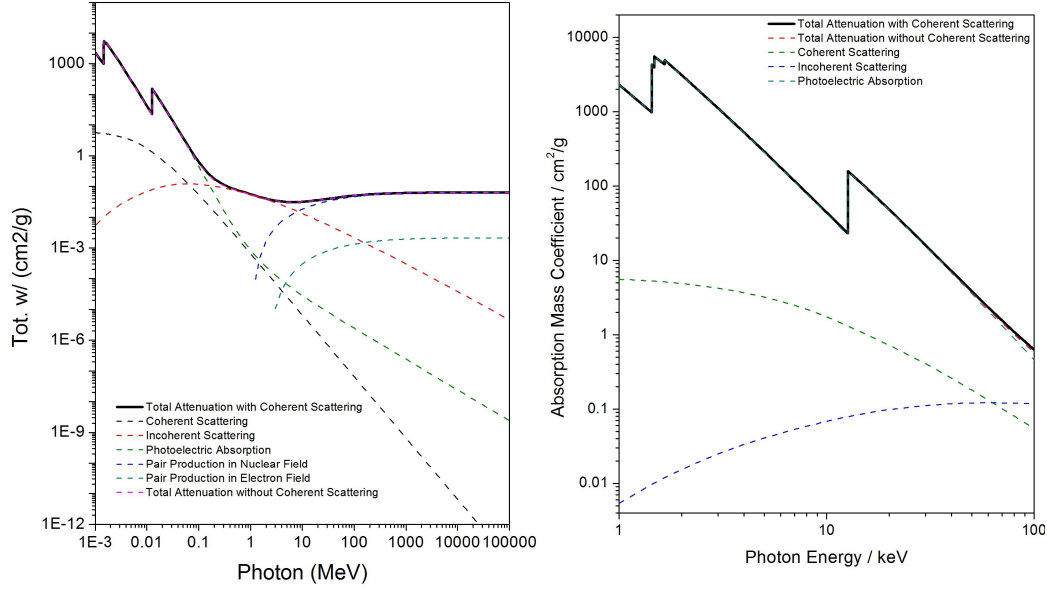


Figure 2.4: a) Total attenuation mass coefficient of Selenium with all the relative contribution of interaction mechanisms, computed by XCOM database [68]. b) highlight on the energy range typical of medical applications; photoelectric absorption is the main process involved at this energies.

decay of the radiation intensity through the medium (eq. 2.1).

$$\frac{I}{I_0} = e^{-\frac{\mu}{\rho} \cdot x} \quad (2.1)$$

where I is the transmitted intensity, I_0 the incident intensity and x the medium thickness ($x = \rho \cdot t$). The theoretical value is correlated to the atomic mass unit ($u = 1.6605402 \times 10^{-24}$ g), atomic mass A , and to the total cross-section σ_{tot} . It can be written as the sum over contribution from the principal photon interactions: atomic photoelectric effect, coherent and incoherent scattering, pair production and photonuclear effects.

$$\mu/\rho = \frac{\sigma_{tot}}{u \cdot A} \quad (2.2)$$

In a compound or a mixture the mass attenuation coefficient is simply the mass weighted sum of the μ/ρ factors of the single elements. In order to describe photon interaction and absorption, two other quantities can be defined: the mass energy-transfer coefficient (μ_{tr}/ρ , eq. 2.3) and the mass

energy-absorption coefficient (μ_{ab}/ρ , eq. 2.4)

$$\mu_{tr}/\rho = (f_{PE}\sigma_{PE} + f_{incoh}\sigma_{incoh} + f_{pair}\sigma_{pair} + f_{trip}\sigma_{trip})/u \cdot A \quad (2.3)$$

$$\mu_{ab}/\rho = (1 - g) \cdot \mu_{tr}/\rho \quad (2.4)$$

where f_i are the factors representing the average energy transferred in the i interaction, and g is the kinetic energy lost in bremsstrahlung. Tabulated value of known elements and for more informations refer to [68]. It is noteworthy that another quantity is used in spite of mass absorption coefficient: the attenuation length δ . It is defined as the depth into the material measured along the surface normal where the intensity of x-rays falls to $1/e$ of its value at the surface.

Activity The Activity of a radiation source is defined as the number of decays per second.

Fluence Radiation from a radioactive source consists of a beam of photons, if the beam is monoenergetic the Fluence can be defined as the number of photons per unit of area (eq 2.5):

$$\Phi = \frac{dN}{dA} \quad [cm^{-2}] \quad (2.5)$$

Energy Fluence The Energy Fluence is another way to describe a radiation beam. In terms of the energy transported, it is defined as the number of photons crossing a specific area per energy carried by each photon.

$$\Psi = \frac{dN \cdot h\nu}{dA} \quad \left[\frac{eV}{cm^2} \right] \quad (2.6)$$

Exposure The exposure (X) exists in each point of the space surrounding a radiation source at fixed intensity and it is defined as the charge dQ due to ionization in air volume-element with mass dm (eq. 2.7). In the SI units it is thus defined as coulomb per kilogram (C/Kg), but the historical unit is the *röntgen* (R): $1 \text{ R} = 2.58 \times 10^{-4} \text{ C/Kg}$.

$$X = \frac{dQ}{dm} \quad (2.7)$$

KERMA Kinetic Energy Released per unit MAass in a medium.

Photons interact with matter through two stages: (a) energy is transferred to charged particles and (b) charged particles transfer energy directly through excitations and ionizations. The first interaction can be described with KERMA, and is defined in eq. 2.8, where E_{tr} stands for the kinetic energy transferred to the medium. Kerma can be related to the photon Fluence through the linear attenuation coefficient (eq. 2.9). The radiation intensity in a specific point can be specified by the photon flux or the exposure, but it is often given in terms of AIR KERMA, which is the energy released in that point in a mass dm of air. This is a useful quantity because it can be easily converted in the kerma in any medium simply multiplying to the ratio between the linear attenuation coefficients of air and of the medium.

$$\kappa = \frac{dE_{tr}}{dm} \quad (2.8)$$

$$\kappa = \Phi \left(\frac{\mu_{tr}}{\rho} \right) E_{tr} \quad (2.9)$$

Absorbed Dose The second stage of energy transfer in a medium is described with the absorbed dose, which is the energy absorbed from any type of radiation per unit mass of the absorber. The unit in SI is joule per kilogram (J/kg) and it is named as *Gray*(Gy). Sometimes it may be reported as the old CGS definition of ergs/gram named *rad*. Thus $1 \text{ Gy} = 1 \text{ J/kg} = 100 \text{ rad}$. An exposure of 1 R corresponds to an absorbed dose in air of 8.7×10^{-3} Gy.

The energy transfer to the charge particles (Kerma) does not take place at the same location of the energy absorption, because a charge particle moves into the medium before being absorbed. However in a thick medium, if the condition of electronic equilibrium has been reached, $E_{tr} = E_{ab}$, thus the KERMA can be considered equal to Absorbed dose. Electronic equilibrium is reached when, in each moment, in every volume of the medium an equal number of particles are stopped and set in motion. Refers to [69] for details about kerma, absorbed energy and Bragg-Grey cavity theory. The mathe-

Radiation type		Weighting factors, w_R
Photons		1
Electrons and muons		1
Protons and pions		2
alpha particles and heavy ions		20
Neutrons ^a	< 10keV	5
	10keV to 100keV	10
	100keV to 2MeV	20
	2MeV to 20MeV	10
	> 20MeV	5

Table 2.1: Radiation weighting factors in accordance with ICRP Publication 103 [70]

^aNeutrons weighting factor is a continuous function with a peak about 1MeV. Here only some approximated slot are reported.

mathematical expression for the absorbed dose is reported in eq.2.10

$$D = \frac{dE_{ab}}{dm} \quad \left[1 \frac{J}{kg} = 1Gy = 100rad \right] \quad (2.10)$$

Equivalent Dose The effects of radiation on tissues and biological systems strongly depend on the nature of the absorbed radiation. The equivalent dose (H_T) in a specific tissue T is a quantity defined as the product between the absorbed dose of the radiation R , in the tissue T , and a weighting factor depending of the radiation type R . The weighting factors w_R are given in table 2.1 and refers to the recommendations of International Commission on Radiological Protection [70].

$$H_T = D_{T,R} \cdot w_R \quad (2.11)$$

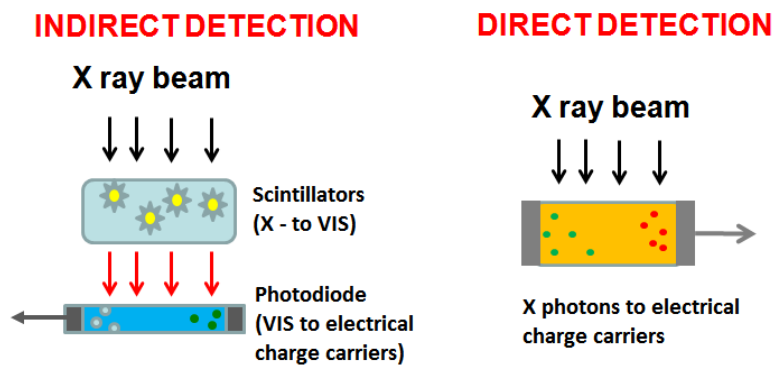


Figure 2.5: Schematic representation of indirect detection (left) and direct detection (right).

2.2 X-ray Detectors

The detection of ionization radiation (e.g. X-rays, electrons and alpha particles) is a constantly growing area of research thanks to its vast and numerous application fields, which span from astrophysics to nuclear power plants, to industrial and civil security and to medical imaging and diagnostics. The first radiation detectors were developed in the 50s and were based on gas devices, like ionization chambers or Geiger counters; they are very effective still today for some specific and rough applications, but present very slow charge collection and long dead time between two subsequent detectable signals. The improvement in radiation detector technology of high energy photons (X- and gamma-rays) arose from the development of two different categories of functional materials: scintillators and semiconductors. In both cases, the interaction with a high energy photon first induces primary excitations and ionization processes (ions and electrons) which, at a second stage, interact within the volume of the detection material and produce a majority of secondary excitations (electronhole pairs), within a picosecond timeframe. The by-products of both the primary and secondary excitations are electronhole pairs (excitons) that can be transduced into an output signal following different pathways in semiconductor detectors and in scintillators, described in more detail in the following. The material requirements for the

two different detection mechanisms share some similarities: high stopping power to maximize the absorption efficiency of the incident radiation, high purity to minimize exciton trapping, and good uniformity to reduce scattering and good transparency, possibly coupled to the ability to grow the material into a large size to increase the interaction volume [71].

2.2.1 Scintillators

Scintillators are materials that exhibit luminescence upon irradiation by charged particles, neutrons, gamma rays, and X-rays. There have been a wide variety of materials studied and used for scintillation since the employment of ZnS for α -particle detection early last century [72]. Scintillators had specific features with different distinctions: sufficient detection efficiency, capability for spectroscopy, excellent radiation hardness, ease of fabrication and short response time. However, there is no ideal material that combines all of these desirable features. The selection of a practical scintillator is always a compromise which depends on application specifications. The performance of a scintillator depends on several factors, including stopping power (absorption efficiency of the incident radiation), photoelectric generation, proportionality, internal quantum efficiency, transparency, decay time, light yield, emission wavelength, stability and physical form [73]. The process of photon generation involved three stages. First, an incident ionizing particle collides and deposits its energy in the material, through excitons generations. Here high stopping power is required to absorb incident energy as much as possible. In the second step, the excitons transfer their energy to luminescent centers which are often intentionally introduced. These centers release the energy radiatively. Here high quantum efficiency ensures that more photons are generated. The resulting photons, typically in the visible wavelength range, escape the scintillator and are collected by a coupled photo-multiplier tube (PMT) or a photodiode to obtain an electrical signal associated to the incident radiation beam (figure 2.5). Scintillators must have an efficient cascade energy transition series to achieve a high light emission yield, in general,

indicative of high sensitivity and also of high energy resolution. Sodium iodide doped with thallium, NaI(Tl) is the most significant scintillator. The photoelectric peak can be readily observed in the NaI(Tl) spectrum, which is considered to be a landmark in gamma ray spectroscopy [74]. A number of new inorganic scintillators have been developed and optimized, including bismuth germanate (BGO), gadolinium orthosilicate (GSO), caesium iodide (CsI), yttrium aluminum perovskite (YAP), and lutetium aluminum perovskite (LuAP). They have been proposed for different applications, though none of these has reshaped the landscape of the field of gamma ray detection dominated by NaI(Tl).

2.2.2 Semiconductor Detectors

In indirect detectors (scintillator-photodiode coupled) the radiation detection passes through several stages of conversion, with a subsequent loss of signal and enhancement of noise. In a semiconductor detector (e.g. CdTe, SiC), an electric field is applied to dissociate the electronhole pairs and to sweep the electrons and holes to the positive and negative electrodes, respectively. The resulting photocurrent is directly recorded as the output electrical signal associated to the high energy radiation particles (figure 2.5). The direct conversion of ionizing radiation into an electrical signal within the same material, and thus within one single device, is a more effective process than indirect conversion, since it improves the signal-to-noise ratio and it reduces the device response time. For semiconductors, high carrier mobility and low intrinsic carrier density are essential to obtain high sensitivity and a low background current. To fulfill this material properties, a combination of different properties are requested. Among others, high- Z materials to maximize X-ray absorption, large bandgap to reduce dark current, but small enough to have small pairs creation energy, and extremely pure crystal with low defects concentration. Nowadays the detectors with the best performances at room temperature are made with CZT ($Cd_{1-x}Zn_xTe$, $x \approx 0.1 - 0.2$) crystals, with direct bandgap of about 1.5 - 2.2 eV, depending on Zn concentration x . It

is possible to produce extremely high purity crystals several centimeters in size and up to 1 cm thick, almost free of defects. The resistivity is in the order of $10^8 - 10^{11} \Omega\text{cm}$, and the electron and hole mobilities, $1000 \text{ cm}^2/\text{Vs}$ and $50 \text{ cm}^2/\text{Vs}$ respectively [75]. Unfortunately, such direct detectors are very expensive devices and cannot cover large areas. To overcome this issue, flat panel X-ray imagers based on amorphous or polycrystalline X-ray photoconductors, such as amorphous selenium (see next section 2.2.2) have been developed in the last fifteen years.

Photoconductor Material Properties

The characteristics required in order to achieve a photoconductor material are several:

- **Quantum Efficiency Q.E.** Also called Attenuated fraction, reported in eq. 2.12, where δ is the attenuation depth and must be substantially less than the photoconductor layer thickness L . $\delta = \delta(E_{ph}, Z, \rho)$ is a function of photon energy, atomic number and density, and can be correlated to the mass attenuation coefficient. High-Z element are suitable photoconductors, especially for high energies application.

$$Q.E. = 1 - e^{-L/\delta} \quad (2.12)$$

- **Electron-hole pair Creation Energy W_{\pm} .** The amount of energy required to create a free electron-hole pair should be as low as possible, because the generated charges can be calculated as $\Delta Q = e\Delta E/W_{\pm}$, where e elementary charge and ΔE is the absorbed energy. For most of the crystalline inorganic semiconductor, the empirical Klein's rule states:

$$W_{\pm} \simeq 2.8E_g + E_{phonon} \quad (2.13)$$

- **Dark Current.** The dark current of the photoconductor under a bias voltage should be small. Two factors affect the dark current flowing

in a material: the injection of carriers from the contact and the thermal generation of carriers. This implies that small dark current needs blocking contacts and a wide semiconductor bandgap to reduce thermal carrier generation. A generally accepted dark current should be below 1 nA/cm². A quantitative formulation of the dark current limit estimation is in [76].

- **Charge Collection Efficiency CCE.** The photogenerated charges could be lost due to recombination or trapping during the charge transport from the collection at the electrodes. The mean distance that a carrier can go through without occurring in recombination or trapping is called *schubweg* or *drift length* and it is defined as $\mu\tau F$, where F is the electric field, μ is the carrier mobility and τ is the mean lifetime of carriers. In order to reduce loss and maximize CCE, the condition $\mu\tau F \gg L$ should be satisfied for both electrons and holes (L is the layer thickness). The charge collection efficiency of a single pixel sandwich structure, in the simplest geometry configuration, in uniform electric field condition can be theoretically calculated by means of the following expression (eq.2.14) as reported in [77, 78]

$$\begin{aligned} \eta_{CC} &= \eta_{HCC} + \eta_{ECC} & (2.14) \\ &= x_h \left(1 - \frac{1 - \exp(-1/\Delta - x_h)}{[1 + (\Delta/x_h)][1 - \exp(-1/\Delta)]} \right) \\ &\quad + x_e \left(1 - \frac{\exp(-1/x_e) - \exp(-1/\Delta)}{[1 - (\Delta/x_e)][1 - \exp(-1/\Delta)]} \right) \end{aligned}$$

where $\Delta = \delta/L$, $x_{h,e} = \mu_{h,e}\tau_{h,e}F/L$. Obviously the CCE decreases as the thickness L increases while keeping the same electric field.

- **Radiation Hardness.** A detector is exposed to high x-ray doses over time, so the damage and structural changes due to irradiation have to be taken into account. The primary effect is the generation of trapping sites that modify $\mu\tau$ of the carriers and polarize the sample affecting the charge collection efficiency.

- **Speed.** Mammography works with interframe time equal to 33 ms for 30 fps. The collection time in the photodetectors must be much lower than this value.
- **X-ray Sensitivity** The detection process involves three stages: x-ray absorption ($Q.E.$), charge carriers generation (W_{\pm}) and collection (η_{CC}). The x-ray sensitivity of a photoconductor can be defined as the charge collected per unit of incident radiation per unit area (eq.2.15, and a more detailed expression is reported in the equation 2.16 in units of $C \cdot m^{-2} \cdot R^{-1}$, or in terms of kerma in $C \cdot cm^{-2} \cdot Gy^{-1}$).

$$S = \frac{\text{charge collected}}{\text{incident radiation} \times \text{area}} \quad (2.15)$$

$$S = \left(\frac{5.45 \times 10^{13} e}{(\alpha_{en}/\rho)_{air}} \right) \times Q.E. \times \left(\frac{(\alpha_{en}/\alpha) E_{ph}}{W_{\pm}} \right) \times \eta_{CC} \quad (2.16)$$

The 2.16 summarizes well the entire detection process: the first term is the photon fluence per unit of roentgen, the second is the absorbed fraction in terms of quantum efficiency, the third is the number of electron-hole pairs generated and the last is the charge collection efficiency. The sensitivity has a strong dependence on the photodetector thickness L , since the x-ray absorption enhances as L increases, but η_{CC} decreases with L at the same electric field: therefore there is an optimum thickness value beyond which the sensitivity decreases [78]. Therefore, from experimental point of view, plotting the signal current, i.e. the charge collected, in function of the incident radiation dose rate is possible to estimate the X-ray detector sensitivity as the slope of the linear of the plot (2.15).

Large Area Direct X-ray detectors

The requirement of large area detectors for applications in medical, security and industrial imaging, highlighted the limits of Silicon photodiodes or CCD sensors: typical CCD camera is no larger than 2×2 cm, thus to obtain a detection area with a sufficient size for many clinical studies, several CCDs

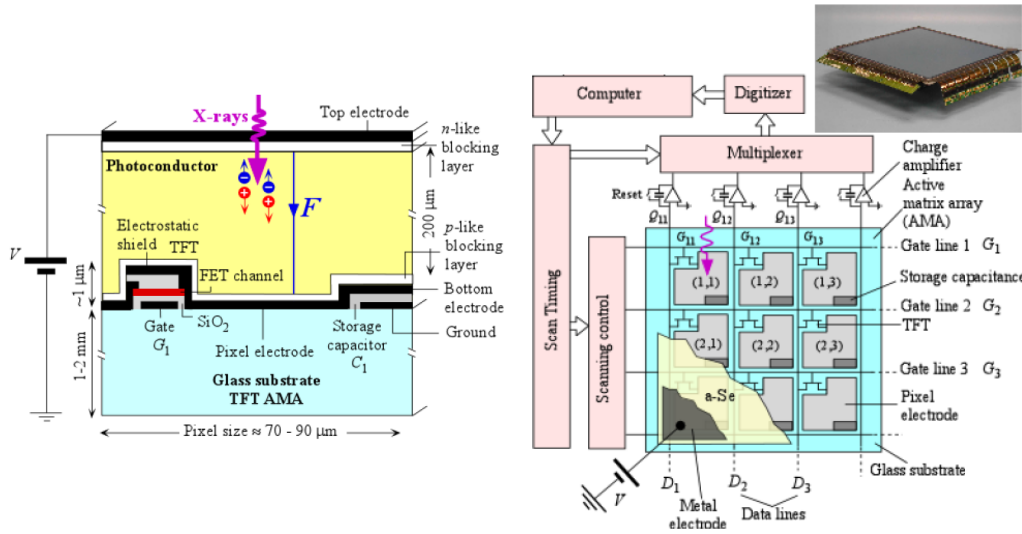


Figure 2.6: A simplified schematic diagram of a single pixel with a TFT and a full FPXI matrix.

must be used together. Flat panel x-ray imagers (FPXI) consist of a large array of pixels as part of an active matrix array (AMA), a two dimensional array of pixels in which each pixels has a thin film transistor (TFT) that can be electrically addressed [79, 80]. The active matrix is coated with a suitable layer of x-ray photoconductor and a top electrode to provide bias voltage. In figure 2.6 the principle of operation of a single pixel is shown: when a x-ray is absorbed in the semiconductor a charged couple is generated and collected by the applied electric field. Refers to [76], a good recent review on FPXIs detectors and amorphous selenium properties, for more details. FPXI detectors can easily reach an active panel area of 24×30 cm using an appropriate photoconductor that can be deposited over large areas with very few defects, reproducible characteristics and employing low cost deposition techniques. There are several semiconductor candidates that can be employed as suitable photoconductors, such as: amorphous silicon (a-Si), amorphous selenium (a-Se), polycrystalline TlBr, PbI_2 , HgI_2 , CdZnTe and PbO , but the most used and promising material until now is a-Se.

Regarding the photoconductor properties discussed above in 2.2.2, Selenium

is possess several interesting features, among them it can be grown over large area in its amorphous phase. Moreover, in terms of electron-hole pair creation energy W_{\pm} , a-Se represents an exception to the rule as W_{\pm} decreases with the applied electric field as following the eq. 2.17:

$$W_{\pm} = W_{\pm}^0 + \frac{B}{F} \quad (2.17)$$

The "infinite field" intrinsic electron-hole pair creation (EHP) is given by $W_{\pm}^0 \approx 6$ eV and constant is $B \approx 4.4 \times 10^2 eV \cdot V\mu m^{-1}$. Working at high electric field in order to reduce W_{\pm} implies that dark current become too large, and two blocking layers are necessary to reduce it to acceptable values. As already mentioned before, in a-Se the strong electric field applied could give rise to high dark current; such problem has been overcome with the addition of a hole blocking layer on one electrode and an electron blocking layer on the other one, that inhibit the charge injection from electrodes but still enable the extraction of the photogenerated carriers with opposite sign. The electron transit time of 1000 μm a-Se is typically 0.5 ms under an applied field of 10 V/ μm . In table 2.2 a summary of the main features of a-Se detector material is reported.

Therefore, commercial FPXIs commonly use a-Se as photoconductor layer with the aim to achieve a good compromise between all the characteristics requested above, although it presents some drawbacks: the need of blocking layers to reduce dark current, the necessity of being stabilized with arsenic (otherwise it exhibits variation in performances upon prolonged irradiation), the working point at several kV to obtain high electric fields (to reduce the electron-hole pair creation energy W_{\pm}). A typical a-Se layer of 200 μm thick at 10 V/ μm corresponds to an applied bias of 2000 V. New solutions are under research to overcome these limitations, like the use of a lateral structure electrode geometry, which allows to reduce the bias voltage and to lower the dark current without the assistance of blocking layers [81]. The most important requirement for a large area photoconductor in a FPXI is that it must be capable of easily cover a large area Active Matrix Array (AMA), at least 24 \times 30 cm necessary for a mammography. This requirement

is the most restrictive limit for the most sensitive silicon photodiode or CCD camera. a-Se can be easily deposited in form of thick films (100 - 500 μ m) onto suitable substrates by conventional vacuum deposition techniques, keeping the substrate temperature below 60-70 °C and maintaining uniform characteristics in very fine scale over large areas.

A great and potentially breakthrough innovation is brought in the field by organic materials. Organic photoconductors can be easily deposited on very large areas with low cost techniques, replacing a-Se, as deeply discussed in the next section 4.1.1. For this reason they are currently dominating the xerographic industry. Despite the low Z elements composition of organic materials strongly limits their use for high-energy radiation detection, they are currently used as blocking layers in a-Se FPXI [82]. However in the last years, interesting effects concerning the electrical response of such materials under irradiation has been seen, opening the way to their application as active layer materials in x-ray detectors (paragraph 2.4).

2.3 Organic Indirect Radiation Detectors

As already seen in 2.2, radiation detector are divided in two main categories, indirect and direct detectors (figure 2.5). In this section we focus on the organic materials used for indirect detection: the primary interaction occurs in a scintillator (2.3.1) which absorb the incoming radiation and emits photons in the visible range, and the secondary interaction is the detection of visible photons by means of a photodiode (2.3.2).

2.3.1 Organic Scintillators

Organic scintillators commonly contain a large amount of aromatic compounds whose electronic states are excited by radiation, and scintillation occurs via relaxation from these excited state to the ground state, through

a-Se	
E _g	2.2 eV
δ	49 μm at 20 keV 998 μm at 60 keV
W _±	45 eV at 10V/μm 20 eV at 30V/μm
Electron μ _e τ _e	3 × 10 ⁻⁷ ÷ 10 ⁻⁵ cm ² /V
Hole μ _h τ _h	10 ⁻⁶ ÷ 6 × 10 ⁻⁵ cm ² /V
Dark Current	0.1 pA/mm ² at 10V/μm
Electric Field	10 ÷ 30V/μm
Thickness	200 ÷ 1000 μm
Electron transit time	0.1 ÷ 0.5 ms at 10V/μm

Table 2.2: Typical important parameters for a-Se. Other materials can be found in [76]

a mechanism explained by Birk in the 1964 [83]. Organic scintillators can be divided into 3 groups: crystals, liquids and plastics. The most widely used are the plastic scintillators initially developed in 1960s. So far, they are mostly based on polyvinyl-toluene (PVT), due to its ruggedness, extremely low cost, and ease of fabrication. Based on the PVT system, various solute combinations have been carefully examined and employed to obtain scintillation emission at a desired wavelength, to reduce self-absorption, and to relieve attenuation of light output as well. They serve as efficient luminescence centers for energy decay and photon generation. Plastic scintillators are by far the only viable choice for large area detection (several m²) with spatial resolution. However, they have relatively poorly light yield (typically 10000 photons /MeV) and non-linear ionization energies in conjunction with strongly ionizing radiation. Furthermore, due to the polymers' low density ($\sim 1 \text{ g/cm}^3$) and low effective atomic number ($Z \sim 6$), plastic scintillators have low stopping powers and low photoelectric peak ratio for gamma ray

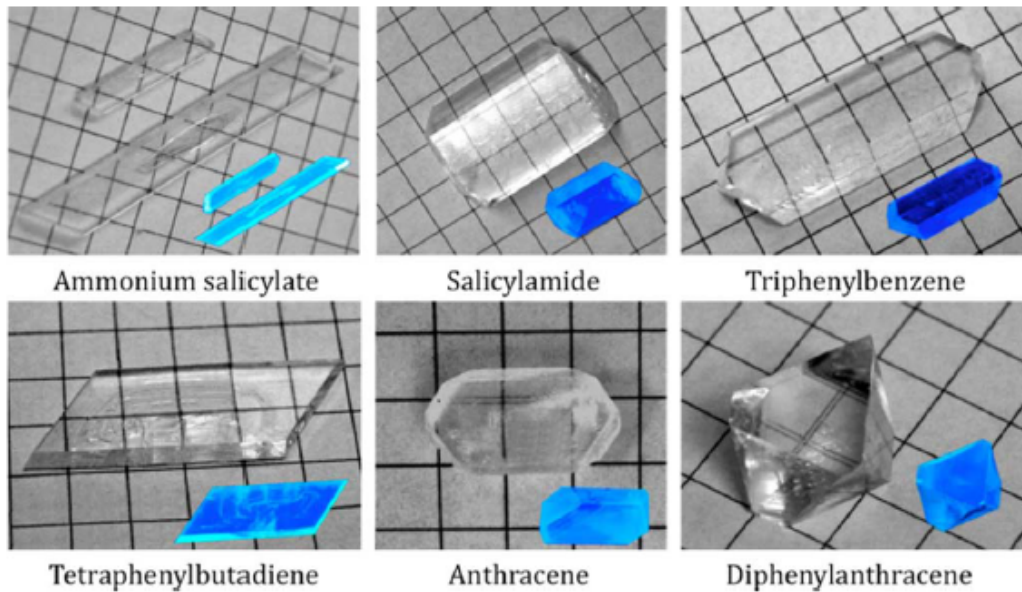


Figure 2.7: Solution-grown single crystals of organic scintillators. Pictures were taken under white- and UV-light (blue colour) illumination. The size of the background square is 6.5 cm [2].

radiation, which limits their use in high-energy spectroscopy [71]. It is worth noting that the compatibility of polymers with other scintillator materials could be exploited to fabricate composite materials with improved high energy resolution. Moreover, organic scintillators are employed to detect fast neutrons partly thanks to their high content of hydrogen that allows neutron detection via proton recoil [63]. At present, liquid organic scintillators are the most used for neutron detection due to their high Pulse Shape Discrimination (PSD) property. It is noteworthy that, among solid compounds, single-crystals have been found to be the most effective material for PSD, even though they present the limit of high production costs. However, scintillation features of low cost solution-grown organic single crystals have been assessed (figure 2.7) [2].

In conclusion, organic scintillators have been studied, so far, coupled with inorganic photodetectors, taking advantage of flexibility and ease of deposition on any shapes. The following step to be carried out in order to

develop full-organic X-ray detectors, is to replace inorganic photodetectors with organic ones, possibly directly covering the whole scintillator surface, reaching a large increase of light collection and device performances [84].

2.3.2 Organic Photodiode

A photodetector is a device that converts an optical signal (UV - VIS - IR) into an electrical one. Organic semiconductors are very appealing for light detection thanks to their large absorption coefficient and an optimum spectral sensitivity in the region spanning from UV to the near infrared and they have rapidly moved from being emerging materials to reach commercial exploitation. Several innovative applications of organic materials can be gathered thanks to capability to cover large area, flexible and transparent substrates by means of low-temperature processes. Therefore in several laboratories researcher are working for the realization of fully organic or fully printed devices. According to the different working mechanisms organic photodetectors can be divided in organic photodiodes, organic photoconductors and organic phototransistor. The operating principles and the structure of these devices is well reviewed in [85] and here we will briefly review only photodiodes since they are the most diffused structure. To assess the performances of an organic photodiode some parameters are defined: i) spectral photoresponse, i.e. the response to a specific wavelength; ii) external quantum efficiency (EQE), i.e. the ratio of the number of photogenerated charge carriers to the number of incident photons, interestingly in an organic photoconductor can exceed 1; iii) responsivity, i.e. the ratio of output current to the power of the input optical signal.

In an organic semiconductor upon light irradiation and photon absorption, a neutral excited state, called exciton, is formed as an electron-hole pair with few hundreds of meV of binding energy, which does not spontaneously dissociate as a result of low dielectric constant in organic materials. Charge pair generation is assisted by an external applied electric field. To further enhance photogeneration it is typically adopted a Donor(D)-Acceptor(A) ar-

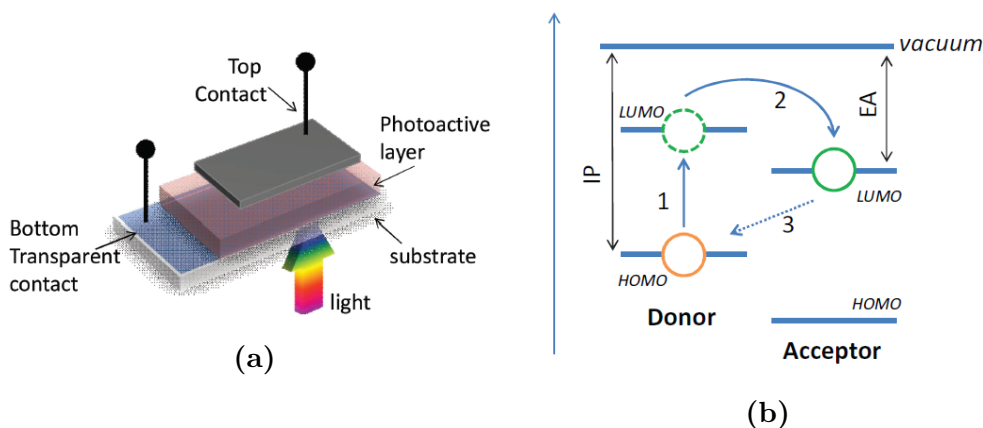


Figure 2.8: a) Typical device configuration of photodiode. b) A simplified schematic diagram of D/A interface. 1) exciton creation. 2) charge separation at the interface. 3) Possible, but ineffective, electron-hole recombination. Reported from [85].

range, an interface between a low ionization potential (D) and a high electron affinity (A) materials. An exciton that reaches a D-A interface decays into a charge transfer state (CT), a less bound state that promotes dissociation (figure 2.8).

Several materials are investigated to perform the best donor-acceptor heterojunction, among them the most representative structure is the well studied solution processed poly(3-hexylthiophene) (P3HT) - phenyl-C61-butryc acid methyl ester (PC₆₁BM) that provides an EQE above 70% in a good coverage in the range 400-600 nm [86].

Only since 2006 the organic community began to concern about radiation effects on organic semiconductors, to explore the potentiality of organic materials in space related applications. The effects of prolonged exposure under x-rays of a pentacene organic thin film transistor (OTFT) have been studied [87]. A threshold voltage shift has been observed but only a 14% decrease of mobility has been recorded, suggesting that organic devices are intrinsically radiation hard. Similar results have been observed in OTFTs based on other polymers like polytriarylamine (PTAA) and polyfluorene (F8T2) [88] and

more recently even with heavy radiation [89].

In 2008 the radiation hardness of three polymeric photodiodes for imaging applications has been assessed [90], proving the stability of EQE of the devices exposed to a dose of 500 Gy only for two polymers - Poly(9,9-di-n-octylfluorene-cobenzothiadiazole):perylene diimide (F8BT:PDI) and poly[2,7 - (9,9-di-n-octylfluorene) - co - (1,4 - phenylene - [(4-secbutylphenyl)imino] - 1,2 - phenylene)]:perylene diimide (TFB:PDI) -, while for the P3HT:PCBM based devices, slightly decrease of EQE is recorded. Coupling the photodiodes with a $\text{Gd}_2\text{O}_2\text{S:Pr}$ phosphor scintillator layer, an x-ray photocurrent in the device has been measured, opening the way to the development of organic indirect detectors [91, 92, 93].

2.4 Organic Direct Detectors

Direct detectors are devices that absorb X-rays and directly convert it to a current signal. The X-ray photon creates charge carriers inside the device that are directly collected and converted into an electrical signal, with the advantage of reduce charge loss between different stages of the detector, reduce dead time and reduce the collection time, producing in practice a real-time radiation detection. The ideal direct detector should have the following characteristics:

- large active volume to maximize x-ray attenuation;
- high charge carrier mobility to reduce loss of energy in recombination and to enhance the charge collection efficiency;
- low dark current, at least less than 1 nA, in order to have higher signal-to-noise ratio;
- chemical (small reactivity to atmosphere gas or environment) and electrical (small bias stress) stability;
- radiation hardness up to the typical dose required from the applications.

Conventional silicon-based detectors have been the first choice for x-ray radiation detection applications so far. However, regardless the excellent performances, silicon suffers from several weaknesses. The size of device is limited by silicon wafers, usually of 6 - 8 inches (15 - 20 cm) and cannot be bent. Moreover large area and high-quality silicon is really expensive and difficult to fabricate. Large area inorganic detectors based on amorphous selenium have been studied, nonetheless they still suffer of some disadvantages (par. 2.2.2). On the other hand, organic materials offers several advantages to overcome these problems: the possibility of producing large area devices with low-cost techniques, their easy growth on flexible and bendable substrates (see par. 1.2.1); moreover, since they are low-Z, human tissue equivalent, organic materials can be considered the ideal candidates for medical diagnostic application, as personal dosimeter or imagers. Despite the advantages and the fast growing interest in organic electronics, in the past decade researchers working with organic materials for radiation detection focused the attention on their employment in indirect detection approach, developing organic devices as photodiodes (par. 2.3.2), which take advantages of the high conversion efficiency of visible light or as scintillators (2.3.1), exploiting the possibility of large area deposition and their flexibility. Very preliminary studies were carried on in the 1950's, by Fowler [94], on x-ray induced conductivity in insulating materials. Among them poly(methyl methacrylate) (PMMA) and polyethylene(PE) were employed and it was observed a x-ray induced current characterized by very slow (several tenths of minutes) and temperature dependent hyperbolic discharging transient, due to distribution of trapping sites in the materials. Fowler concluded that the combination of very low mobilities and short charge carrier lifetimes severely limited the insulating polymer x-ray sensitivity.

Few research groups in the last years began to study conjugated polymer films as direct x-ray organic detectors [3, 4]. Polymer films have the typical mechanical flexibility of organic materials, and are easy to process with liquid-phase techniques i.e. dip coating, spin coating and inkjet printing. The

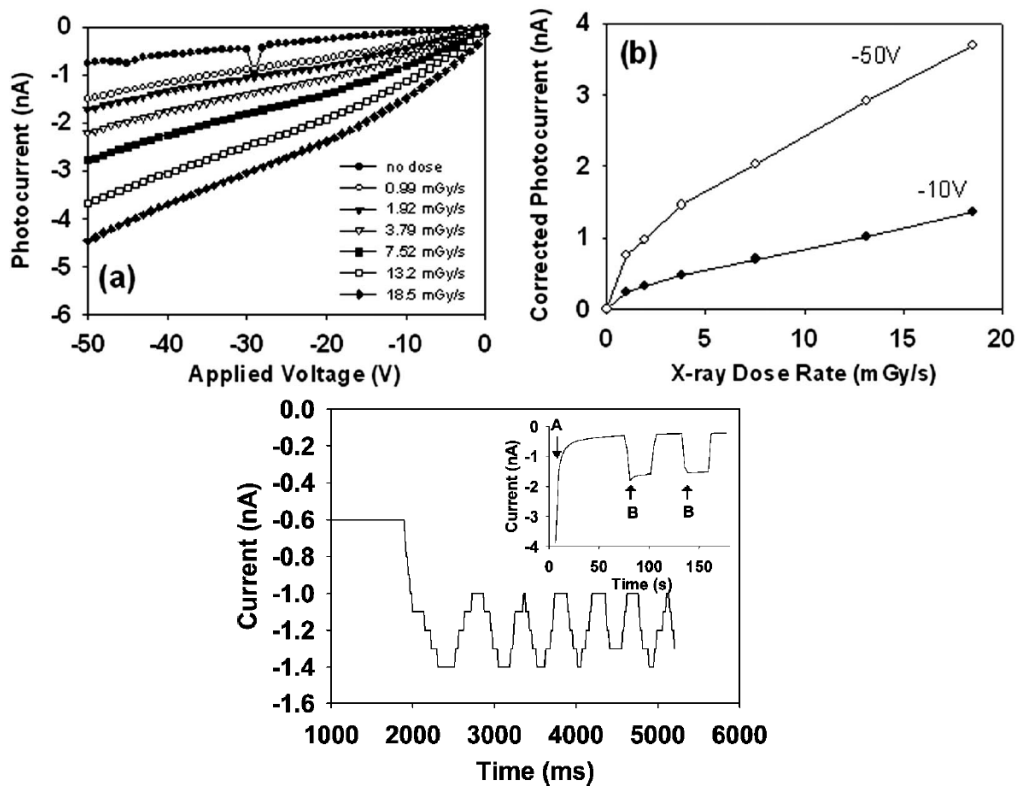


Figure 2.9: a) Current-Voltage characteristics for variable x-ray dose rate in a PFO device, b) and its corresponding deduced photocurrent. c) Dynamical x-ray response of the detector [3].

first devices were composed by thick films of $5 \div 30 \mu\text{m}$ of poly[1-methoxy-4-(2-ethylhexyloxy)-phenylenevinylene] (MEH-PPV), poly(9,9-dicylfluorene) (PFO) and poly(triarylamine) (PTAA), spin coated on a glass substrate covered with ITO and PEDOT:PSS layer as bottom contact, an Aluminum layer, thermally evaporated, as rectifying top electrode. The thick film is required in order to maximize the x-ray photon attenuation and the interaction volume of the detectors, even if a $100 \mu\text{m}$ thick polymer layer has a quantum efficiency (Q.E.) of only 1% (par. 2.1). The device consists in a Schottky diode to limit the dark current to $10 \text{ nA}/\text{cm}^2$ at -50V of applied bias. In figure 2.9 the first X-ray direct detection signal in a polymer film is reported. The film was exposed to the radiation coming from a X-ray tube with Molyb-

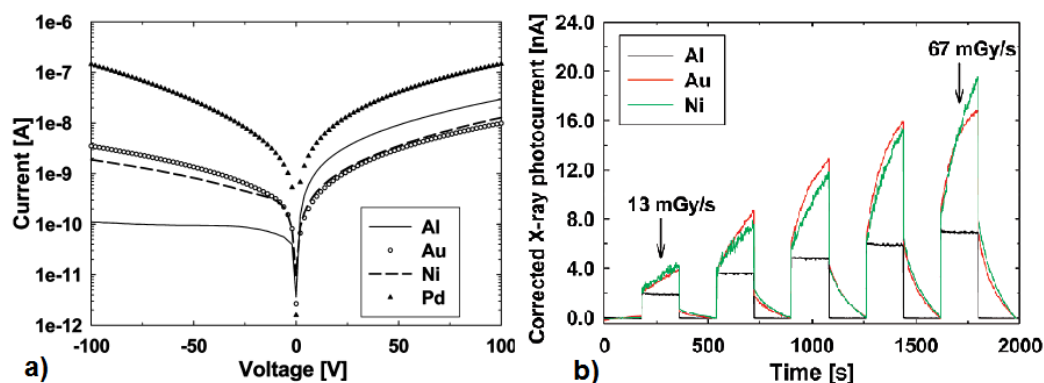


Figure 2.10: a) Current voltage characteristics for ITO/PTAA/metal diodes, with $20\mu\text{m}$ thick PTAA layer, showing the different rectification effects of Aluminum, Gold, Nickel and Palladium (from rectifying electrodes to the ohmic one). b) Time-dependent x-ray response for the three rectifying metals (Al, Au, Ni) [96].

denum target (50kV of accelerating voltage and 1 mA of filament current at its maximum intensity equal to dose rate of 18 mGy/s). The photocurrent signal is in the order of nanoampere, an estimate of the response time of the detector is higher than 150 ms. The signal increases proportionally to the dose rate, from the linear region it is possible to evaluate the device Sensitivity as the slope of the linear fit of the corrected photocurrent vs dose rate plot (par. 2.1). In table 2.3 a review of the sensitivity of the three polymers is reported: noteworthy the sensitivity is comparable with that of amorphous silicon, equal to 500 nC/mGy/cm^3 [95]. Regarding the stability, the photocurrent shows a standard deviation of less than 0.1 nA after 6 months and an accumulate dose of about 600 Gy, if the sample is stored in dark and under controlled nitrogen atmosphere to prevent oxidation. To overcome this problem the device can be encapsulated by wax dip coating. The relative good transport properties of PTAA makes it a good candidate for a deeper study of stability, repeatability and quality of the signal. In particular the top electrode material has a great influence on the performance and on the dynamic of the devices. In figure 2.10a the current-voltage characteristics of four different metal electrodes - aluminum (Al), gold (Au), nickel (Ni) and

palladium (Pd) - are shown. Because of the different work functions and their relative value with PTAA HOMO level, generate different Schottky barriers with the organic material. Palladium, which has the highest work function (5.4 eV), makes an ohmic contact, thus it is not suitable for detection because dark current in such system is too high; in the other three metals, the lower is the work function, the higher is the barrier height and the bigger is the rectification value (I_{rev}/I_{fw}). Low rectification leads to two drawbacks: first, higher dark current values, and second a very low x-ray transient response (figure 2.10b). For the ITO/PTAA/Au device at an operating voltage of 200V and x-ray dose rate of 67 mGy/s, a characteristic time constant of 71 s is obtained, and a even higher time constant is measured for ITO/PTAA/Ni device. A similar effect has been reported in organic photodiodes [97]: the authors describe the observed slow time constant in terms of a modified space-charge distribution at the Schottky barrier: the injection of photocarriers generated by x-ray causes the build-up of space-charge limited current. A large effective barrier minimizes the x-ray space-charge, compared to low barrier diode that are more sensible to changes at the interface. In fact, from the experimental point of view, the signal is fast for low voltages and low biases, but the slow transient time appears for high voltage (more space-charge effects) and for high dose rate (more injected photocurrent). The stability and the quality of the signal in terms of signal-to-noise ratio, are reported in figure 2.11a,b respectively. Most of the times, organic polymer film devices are covered by a protective layer of dip coated wax, to prevent oxidation from environmental agent that quickly degrade the device. The flexibility of polymeric active film has been demonstrated in 2009 with a F8T2 polymer spin coated on a plastic (polyimide) flexible substrate [98], and encapsulated in a protective layer of dip coated wax, since F8T2 polymer shows marked bias stress in air.

Despite the appealing properties of organic direct detectors based on polymers, two drawbacks that limit the radiation detector performances can be identified:

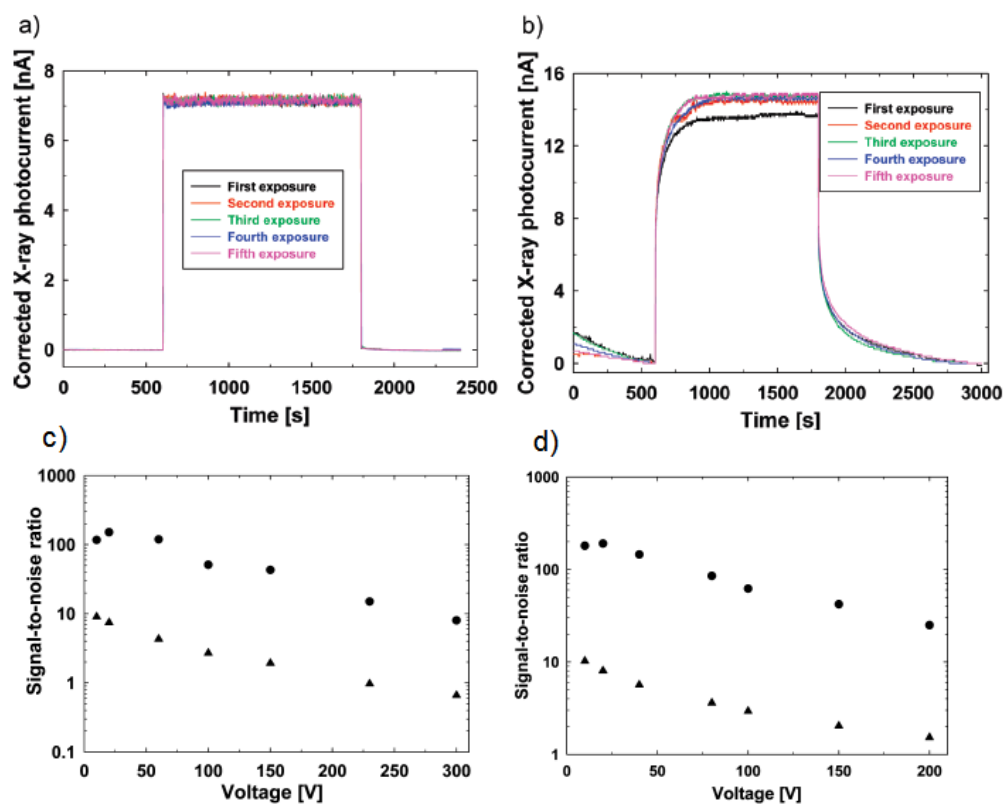


Figure 2.11: Corrected x-ray photocurrent response for (a) ITO/PTAA/Al and (b) ITO/PTAA/Au devices, irradiated at 67 mGy/s dose rate and biasing 300 V. c,d) Corresponding signal-to-noise ratio expressed as $SNR = \frac{\Delta I}{I_{dark}}$ [96].

1. the first concerns the low atomic number of the molecular elements, which strongly limits the stopping power of high energy electromagnetic radiation (in a PTAA polymer no more than 1% of the incident x-ray at 17 keV is absorbed in the active film and generates charge couple carriers);
2. the second is related to the low mobility of charge carriers in polymers, in the order of $10^{-5} \text{cm}^2/\text{Vs}$ for PTAA films, that limits the charge collection at the electrodes and results in loss for recombination of the photogenerated carriers.

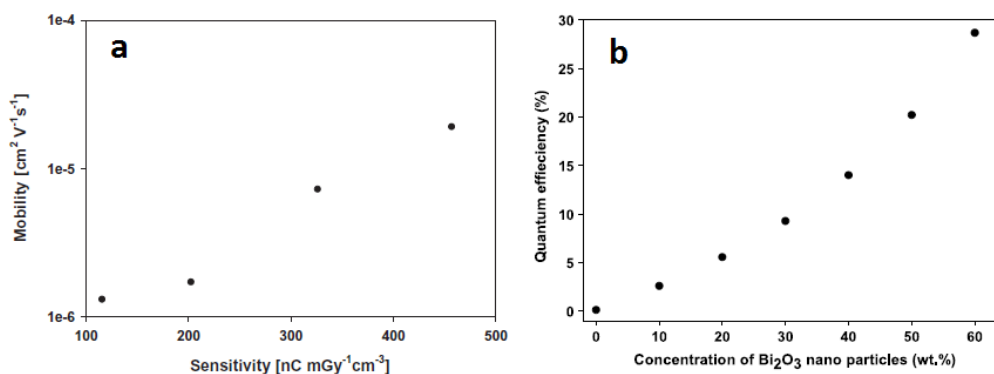


Figure 2.12: a) Correlation between x-ray sensitivity of the device and charge carrier mobility of the PTAA:TIPS-pentacene blend[99]. b) Theoretical quantum efficiency of 20 μm thick film of PTAA blended with Bi₂O₃ nanoparticles[5].

To overcome the latter issues a blend of PTAA and TIPS-pentacene has been processed and employed[99]. TIPS-pentacene is a derivative molecule of pentacene, well known for its solubility and a very high hole mobility (>1 cm²/Vs). The polymer blend mobility rises as the TIPS-pentacene concentration increases, from TOF (Time of flight) experiments a field-averaged mobility of 2.2 × 10⁻⁵ cm²/Vs in the 1:25 molar ratios sample, which is about 17 times higher compared to the value of 1.3 × 10⁻⁶ cm²/Vs in the pure PTAA sample. In figure 2.12a trend of x-ray sensitivity increase as function of the device mobility is plotted, for a device detector with an Al Schottky barrier as described above. The highest performance reached in terms of sensitivity for the 1:17 device is 457 nC/mGy/cm³, which is four times 116 nC/mGy/cm³, obtained for pure PTAA devices, that is the highest value recorded for an organic direct detectors till now. As TIPS-pentacene has a high charge carrier mobility, the rise in the blend sensitivity can be ascribed to the better collection of generated charge carriers. However, higher concentration of TIPS-pentacene in the blend enhance the conductivity, reduces the rectifying diode effects but at the same time increases the dark current too much to enable its use in detectors, marking an upper limit to the increase in sensitivity through the addition of TIPS-pentacene. The other possibil-

ity to enhance sensitivity of organic semiconductor detectors is to improve the stopping power of the active film, adding heavy (high atomic number) elements in the polymer blend[5, 100]. In figure 2.12b the strong quantum efficiency increment in a PTAA film when adding nanoparticles of bismuth oxide (Bi_2O_3 , $Z = 83$) of less than 100nm diameter is shown. The quantum efficiency increases from less than 1% in pure PTAA to 30% in the film with 60wt% of np- Bi_2O_3 , and results in an increase in device sensitivity from 78 nC/mGy/cm³ (pure PTAA) to 200 nC/mGy/cm³ in 60wt% Bi_2O_3 sample (see par. 2.3). Despite the increase in device sensitivity, a twofold values is not enough to justify a stronger rise of $Q.E.$. This behavior could be explained by the reduction of electrical transport performance with the addition of nanoparticles, since there is more x-ray absorption, but less charge collection efficiency. A strong evidence of the latter mechanism has been obtained adding metallic nanoparticles of Tantalum (Ta)[100]; the comparison between pure F8T2 polymer film, a F8T2 blend with 30%wt of np- Bi_2O_3 and one with 30%wt of np-Ta is reported in table 2.3. The np- Bi_2O_3 device has better sensitivity than the pure one, as expected, but the np-Ta sample has the highest sensitivity, even if its $Q.E.$ is lower than that of Bi_2O_3 because of the better charge transport of the metallic nanoparticles if compared to the insulating ones.

Polymer	Bias V	Sensitivity nC/Gy	Volume Sensitivity nC/mGy/cm ³
MEH-PPV	10	100	200
PFO	50	240	480
PTAA	300	300	—
PTAA	100	—	116
PTAA	200	—	78
PTAA:TIPS	100	—	457
PTAA:np-Bi ₂ O ₃	200	—	200
F8T2 (flex)	50	35	158
F8T2	50	—	141
F8T2:np-Bi ₂ O ₃	50	—	288
F8T2:np-Ta	50	—	434

Table 2.3: Overview on the performance of the reported organic polymer direct detectors.

Chapter 3

Materials and Methods

In this chapter several details about materials and experimental methods will be presented. In the first part, two methods are described: the electrical characterization techniques used to measure the electrical performances of organic crystals, and the experimental setups for the characterization of the detector's X-ray response. In the second part the investigated materials will be shown, in particular the organic molecules, their crystal structures and their main characteristic.

3.1 Electrical Characterization

Electrical characterizations are performed in air and at room temperature in a customized probe station equipped with micro-probe tips and with a thick metal box to shield the low current (< 1 nA) output signal from environmental electrical noise. BNC cables connect probes to a *Keithley 6517A electrometer* or *Keithley 2400 source-meter*. GPIB-USB connection with the computer, and a custom Labview software drives the instruments, composed the acquisition system.

Temperature and atmosphere controlled measurements were performed in a vacuum chamber. Vacuum is kept by means of a rotative pump at the value of about 100 mTorr. A series of valves enable to purge the chamber

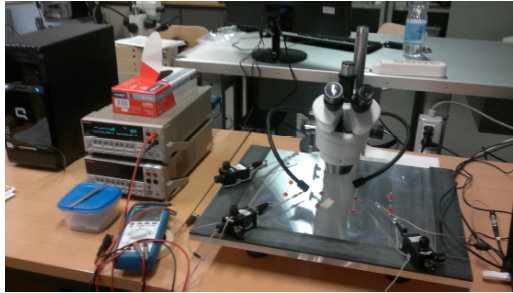


Figure 3.1: Probe station.

with air, or insert a flow of gas like nitrogen or argon. The sample holder of the chamber is a copper block of $5 \times 5 \times 2 \text{ cm}^2$ provided with two independent closed circuits: one for pumping liquid nitrogen and cooling the sample down to 77 K, and the other one is a resistive circuit for heating through joule effect. The describe measurement setup system has been employed to perform:

- Current-Voltage measurements (I-V), analysed by means of Space-Charge Limited Current theory (SCLC, see par. 3.1.1);
- Organic Thin Film Transistors characterization (OTFT, see par. 3.1.2).

3.1.1 Space Charge Limited Current

Space-Charge Limited Current (SCLC) is a transport regime typical of high resistivity materials, like insulators or organic crystals, which is activated at high electric fields and high charge carriers injection. Thanks to its simplicity it is used to analyse organic crystal properties. Several charge-transport parameters like mobility, density of free charge carriers, density of states and energy distribution of traps, can be extracted starting from I-V characteristics. The earliest theory for SCLC was developed by Mott and Gurney in 1940 [101] for insulating materials, and adapted for organic crystals by Mark and Helfrich [31]. The theory was first developed for two ohmic sandwich-type electrodes (figure 3.2a) on a bulk material. Within years the model was refined first taking into account different distributions of traps (e.g. single levels, exponential distribution, gaussian

	Experimental	Input parameters	Output parameters
SCLC	$j(V)$	$h(E)$	N_T and μ_0
DM-SCLC	$j(V)$	N_t and μ_0	$h(E)$
TM-SCLC	$j(V)$ and $j(T)$	-	$h(E)$

Table 3.1: Summary of SCLC methods. Classical Mott-Gurney theory, Differential Method (DM-SCLC) and Temperature Modulated method (TM-SCLC).

distribution)[31, 102, 103], then introducing a formulation also for gap-type electrodes (figure 3.2b) in thin films (Geurst,1966) [104]. In the last decades a differential methods exploited by Nespurek and Sworakosvki [105] allowed to extract from I-V curve the density and the energy distribution of trap states without any a priori assumption on their distribution, namely the Differential Method Space-Charge Limited Current (DM-SCLC). The theory was refined with the Temperature Modulated Space Charge Limited Current (TM-SCLC) model, that overcomes the main source of errors in the previous methods, however it requires more complicated measurements in controlled temperature and atmosphere, as well as more computational analysis. In the present thesis we use classical, DM-SCLC with the gap-type formulation, and all the methods will be briefly discussed in this section, in the following. Table 3.1 gives the input and output parameters for the three different methods. $J(V)$ stands for the measured current-voltage characteristics, N_t is the total trap density, μ_0 the mobility of the delocalized states and $h(E)$ stands for the density of states distribution (DOS) in the energy gap.

SCLC basic theory

The fundamental concept to understand SCL transport is the *dielectric relaxation*. It is well known from basic electromagnetic theory that a conductive material cannot support any free charge that is not compensated by an equal and opposite charge. Therefore, any injected free charge must be

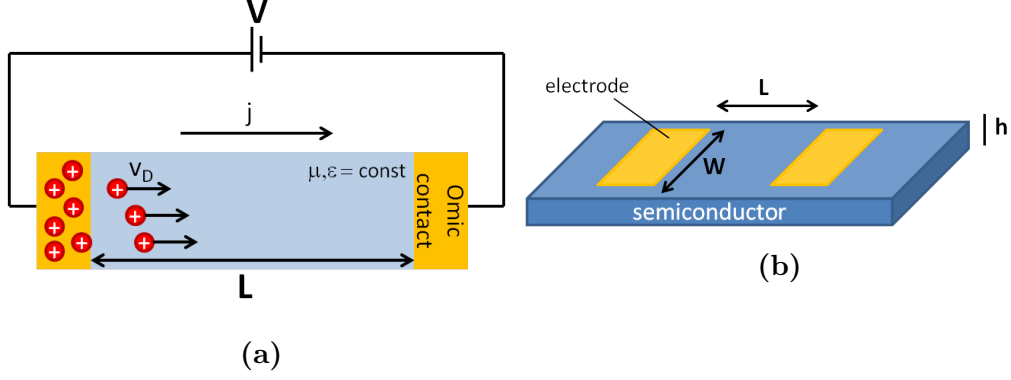


Figure 3.2: Schematic views of a) sandwich-type geometry and b) gap-type geometry structure.

neutralized and this relaxation occurs in a finite amount of time, which results from Maxwell equations, the relaxation time $\tau_r = \epsilon/\sigma$. It is negligible for a conductor, but it can be very large for an high resistivity material. In particular, if we define the transit time of a mobile charge in the materials as $\tau_t = L/v_D$ (L is channel length and v_D is the drift velocity), when the transit time becomes shorter than the relaxation time, the injected carriers cannot be relaxed by thermal carriers before they exit the material, and the SCLC regime occurs. In figure 3.2a a schematic of the problem is shown and it may be mathematically treated by solving simultaneously the current equation and the Poisson equation, respectively:

$$j = e\mu_0 \left[n_f(x)E(x) - \frac{kT}{e} \frac{dn_f(x)}{dx} \right] \quad (3.1)$$

$$\frac{dE}{dx} = -\frac{e}{\epsilon} [n_s(x) - n_{s0}] \quad (3.2)$$

where $n_s(x) = n_t(x) + n_f(x)$ is the total density of charge carriers in the sample after the voltage is applied (n_f and n_t are the free and trapped carriers, respectively), and n_{s0} , n_{f0} and n_{t0} are the corresponding values at thermodynamic equilibrium. The basic SCLC theory makes some assumptions: i) electric contacts are ohmic, i.e. they are an infinity reservoirs of charges: $n_f(x=0) \rightarrow \infty$; ii) only one type of charge carriers is taken into account,

i.e. unipolar transport is considered; iii) electric field $E(x=0) = 0$ at the contacts, iv) mobility μ and permittivity ϵ are constant in the sample; v) the diffusion current is negligible, i.e. only the drift current is taken into account. Furthermore, considering a sufficient high injection $n_s \gg n_{s0}$ and an ideal case of a trap free material ($n_s = n_f$) the first formula of Mott-Gurney theory is obtained (mathematical details in [101, 102]):

$$j = \frac{9}{8} \mu_0 \epsilon \frac{V^2}{L^3} \quad (3.3)$$

This is named the *trap free case* and it is also often called Child's law.

In a real case, the materials, e.g. organic crystals, are not perfect and trap local states play a role in the concentration of free carriers: trapped charges are no longer available for conduction, while they still contribute to space charge in the sample. Let us introduce the free-to-total charge concentration ratio:

$$\theta = \frac{n_f(x)}{n_s(x)} = \frac{n_f(x)}{n_f(x) + n_t(x)} \quad (3.4)$$

Upon solving eqs. 3.1 and 3.2 with θ , one obtains:

$$j = \frac{9}{8} \theta \mu_0 \epsilon \frac{V^2}{L^3} \quad (3.5)$$

The shape of the SCL current-voltage characteristic strongly depends on the quasi-Fermi level and its position respect to the energy distribution of states. The factor θ depends on traps distribution, and only for few simple cases it has been analytically calculated: a discrete local level [102], an exponential distribution [31], and a Gaussian distribution [103]. Traps levels may be roughly classified in shallow levels ($E_F > E_t$) or deep levels ($E_F < E_t$). In the first case traps are all ionized and almost empty, thus the states can act as traps of injected carriers and the current-voltage characteristic follows the eq. 3.5; in the second case trap levels are full and cannot act as traps. It should be stressed that injected charges shift the quasi-Fermi level toward the band edge, thus for sufficient high voltages all the traps are filled and the sample behaves like the trap-free case (eq. 3.3). This happens over the

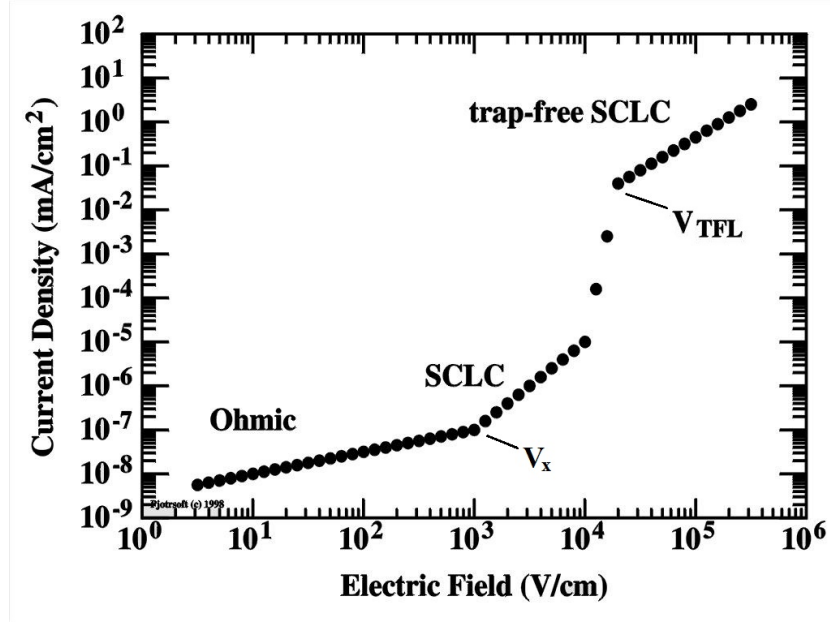


Figure 3.3: Ideal plot of SCLC characteristics for a discrete level of traps. Adapted from [106].

so called *trap-filled-limit voltage* which can be shown to amount to:

$$V_{TFL} = \frac{eN_t L^2}{2\epsilon} \quad (3.6)$$

In figure 3.3, the behaviour of SCLC plot in the ideal case of a discrete level energy state is reported. Four main regime can be identified: a) *ohmic regime* at low voltages: thermally generated n_{s0} are still dominant; b) *SCLC trap-dominated regime*: trapped charge carriers in shallow traps limit the current; c) *trap fill limit*: quasi-Fermi level reaches the trap energy E_t , traps are filled and a step increase of current takes place; d) *trap-free regime*: all traps are fulfilled and the child's law occurs. From the experimental point of view, from a typical SCLC current-voltage characteristic three important parameters of a material can be extracted: the mobility μ from trap-fill regime, N_t from trap-fill voltage, and n_{s0} from the ratio between V_x and V_{TFL} .

SCLC in a gap-type structure

The Child's law (eq. 3.3) illustrated in the previous paragraph stands for a 3D sandwich-type geometry. Two basic architectures can be used for a SCLC analysis: sandwich-type geometry (3D), in which both electrodes are on the opposite face of the sample (figure 3.2a) and the gap-type structure (2D) where both contacts are deposited in the same side of the sample (figure 3.2b). The gap structure presents two limit cases as pointed out in [107]: small thickness h of the film ($h \rightarrow 0$), or thickness h higher than the distance between electrodes L . The first case corresponds to the current flowing in a thin semiconductor layer as developed by Geurst [104] using a model in which the thickness of the layer and the electrodes are considered negligible if compared with the separation of the electrodes. He founds, theoretically and experimentally [108], a quadratic inverse proportionality of the current density to the value of channel length ($j \propto V^2/L^2$). In the second case the current is function of h and the equation that describes the I-V characteristic is similar to Mott-Gurney equation developed for 3D structure, in which the current is inversely proportional to the cubic value of the channel length. The current for each case is expressed by:

$$I \cdot \frac{L^2}{W} = \frac{2}{\pi} \epsilon \mu V^2(\text{film}) \quad (3.7)$$

$$I \cdot \frac{L^2}{W} = \frac{9}{8} \epsilon \mu \frac{h}{L} V^2(\text{bulk}) \quad (3.8)$$

where L is the distances between two electrodes, W the width of channel and h the sample thickness. Organic crystals ($h \gg 0$), with both the electrodes on the same face, are in an intermediate situation in which the transition between 2D and 3D cases depends on the ratio h/L [109]. It will be expected that 2D Geurst law dominates for $h/L \ll 1$, while 3D Child's law for $h/L \gg 1$; more precisely the bulk description is used as long as:

$$\frac{9}{8} \frac{h}{L} \gg \frac{2}{\pi} \quad (3.9)$$

The above equation can be assumed as an expression to approximately discriminate between the two limiting cases, however the common practice is

to plot the current at a given voltage as function of electrode distance L in order to recognize the Mott-Gurney bulk conduction ($j \propto L^{-3}$) or the Geurst thin film conduction ($j \propto L^{-2}$).

Differential Method of SCLC

The method developed by Nespurek and Sworakowki [110] gives a simple mathematical tool to calculate the bulk localized states $h(E)$, from a single experimental current-voltage characteristics. It is based on the concept that on changing the position of the quasi-Fermi level E_F , one can determine the distribution of traps for which the occupancy is changed. The quasi-Fermi level is shifted by increasing the voltage applied to the sample. Thus, the shape of I-V characteristics contains informations about the density-of-states (DOS) function.

$$h(E) = \frac{dN_t}{dE} \quad (3.10)$$

Referring to [110], this differential method is valid under the following assumptions:

- a sample of a uniform dielectric in sandwich-type parallel plates electrodes is considered. The density of traps and the mobility are assumed constants over sample. Two contacts are placed at $x=0$ and $x=D$.
- The energy scale is referred to the band edge with positive direction pointing towards the gap (valid for both electrons and holes).
- The diffusion current is neglected.
- To describe the free carriers density we use the Boltzmann statistics, while we adopt the Fermi-Dirac statistics for trapped carriers.

If the contribution of the diffusion current is negligible, then the position of the quasi-Fermi level at the collector electrode can be calculated by combining the current equation 3.1 and the free carrier density being given by

Boltzmann statistics:

$$E_F(D) = kT \ln \frac{D}{\kappa_1 N_0 e \mu} + kT \ln \frac{j}{V} \quad (3.11)$$

Upon the differentiation of the free-to-total carrier concentration θ with respect to E_F and after several manipulations, one obtains:

$$h(E_F) = \frac{\epsilon \kappa_1 \kappa_2}{2eD^2 kT} \frac{V}{m-1} \quad (3.12)$$

where m is the slope I-V characteristics in double logarithmic scale:

$$m = \frac{d \ln j}{d \ln V} \quad (3.13)$$

and the correction parameters κ_1 and κ_2 describe the spatial distribution of the electric field through the sample, they can be rewritten as:

$$\kappa_1 = \frac{2m-1}{m} \quad (3.14)$$

$$\kappa_2 = \frac{m-1}{m} (1+B) \quad (3.15)$$

which have values of $1 \leq \kappa_1 \leq 2$ and $\frac{1}{2} \leq \kappa_2 \leq 1$, and B is a correction of the second order that introduce an error of 10% if not considered. Although DM-SCLC is a simple and powerful tool to extract energetic information from a single experiment, it is strongly affected by noise and spikes in the I-V curve, due to its derivative nature. Moreover, the correct calibration of the energy scale is still an open issue and the results expressed by eq. 3.11 is not in agreement with that calculated by Arkhipov [111], who obtained a different relation for Fermi level. Only experimentally obtained values of the energy scale are reliable, and could overcome such discrepancy in the theory.

3.1.2 Organic Thin Film Transistors

The electrical characterization on OTFTs were carried out in air, at room temperature. The measurements were analysed and the parameters were extracted following the well know OFET theory [39]. In order to power an OTFT, two voltages have to be applied to the device: the drain voltage

V_{ds} and the gate voltage V_{gs} (both referred to the usually grounded source electrode). The complete electrical characterization of the transistor includes the acquisition of two different curves:

1. the I_{ds} vs V_{ds} curve, named output characteristic, where the gate voltage is kept constant while the drain voltage is swept in a proper range. Usually I_{ds} vs V_{ds} characteristics for different values of V_{gs} are recorded.
2. the I_{ds} vs V_{gs} curve, named transfer characteristic, where the drain voltage is kept constant while the gate voltage is swept in a proper range. During such a measure also the current flowing between the gate and the source electrodes (I_{gs}) is collected in order to monitor possible leakage phenomena.

3.2 Photocurrent Spectroscopy

The experimental technique named Photocurrent Spectroscopy (PC) is based on photoconductivity, an optoelectronic phenomenon which is the increase of electrical conductivity when a material is exposed to electromagnetic radiation (i.e. visible light, ultraviolet light, infrared light, or X-ray radiation). Essentially the physical phenomenon of photoconduction in a semiconductor is based on the absorption of a photon by an electron (*internal photoelectric effect*). If the photon energy is higher than the energy gap, the absorption causes the creation of an electron-hole pairs, i.e. an electron is excited from the valence band to the conduction band in inorganic semiconductors, and from HOMO to LUMO in organic ones. Thus, the number of free electrons and holes changes, and the conductivity is raised. The photocurrent is the increase of dark current observed when this optically injected free charges are collected by an electric field. It is also possible to observe photoconductivity when the energy of the incident photon is smaller than that of the band gap, actually also transitions from impurity levels eventually present in the bandgap can occur.

As regards photoconductivity in organic semiconductors, we have to consider that charge carrier creation is not so easy as for inorganic materials, owing to the different nature of *excitons*. An exciton is a bound state of an electron and a hole, which in inorganic semiconductors has a weak binding force (1 meV to 20 meV), and so it can easily dissociate forming an electron-hole pair, while in organic semiconductors the excitonic bond is stronger (between 100 eV and 300 eV). However, the nature of the excitons as well as the charge separation remains unclear and various optical spectroscopic studies have been dedicated to shine light on this issue, typical of organic photovoltaic and organic photodiode (2.4) [85]. It should be noted that, since in an organic molecule several anti-bonding orbitals are present (LUMO representing the lowest one), the absorption of radiation with energy higher than the bandgap corresponds to transitions between higher energy levels for an organic semiconductor. Also, once generated, the electron-hole pair has an average life time τ , at the end of which the charge carriers are not more available for conduction, due to recombination processes or trapping. Traps states, usually associated with crystal imperfections, dislocations, grain boundaries, and the surface of the material, can hold charge carriers for a certain time, thus possibly causing the enhancement of the recombination probability and a decrease of photocurrent [112].

The conductivity of a semiconductor in darkness condition can be expressed as function of electron and holes concentration, indicated with n and p respectively, as follows:

$$\sigma = e(n\mu_n + p\mu_p) \quad (3.16)$$

where e is the electronic charge and $\mu_{n/p}$ is the electrons/holes mobility. As explained above, when the material is exposed to an electromagnetic radiation with an appropriate energy, the absorption of a photon results in the generation of an electron-hole pair and thus in an increase of the conductivity:

$$\sigma + \Delta\sigma = e[(n + \Delta n)\mu_n + (p + \Delta p)\mu_p] \quad (3.17)$$

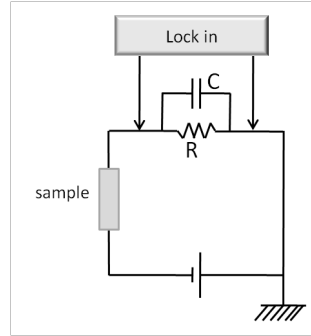


Figure 3.4: Electrical circuit employed in PC measurements.

Consequently, the current density $J = \sigma E$, where E is the electrical field applied, increases to the value:

$$J = (\sigma + \Delta\sigma)E = J_{bulk} + J_{ph} \quad (3.18)$$

Through the measurement of the variation of J in the sample is therefore possible to detect the light absorption by the material.

From the experimental point of view, the photocurrent is detected measuring the voltage across a load resistor R_L in series with the sample and a stabilized voltage generator or a battery (figure 3.4). The change of conductivity $\Delta\sigma$, and the corresponding photocurrent causes an increase of the voltage drop across R_L . In Figure 3.5 the block diagram of the experimental set-up used for PC measurements is reported. As radiation source a QTH (Quartz Tungsten Halogen) lamp (22 V, 150 W) is employed. The white light produced by the lamp is collected by a Cornerstone 260 monochromator (spectral resolution $\Delta\lambda=1$ nm), which selects the output wavelength radiation by means of a rotating diffraction grid and projects it on the sample through a system of optical mirrors. Two slits are located at the entry and at the exit of the monochromator in order to collimate the light beam, whose width is varied between $200 \mu\text{m}$ and 2 mm to search a good sensitivity and a strong signal. Between the lamp and the monochromator a chopper (a dark disk with periodic holes rating in order to chop the incident light beam) is placed. A photodiode mounted on the chopper thus gives a reference square wave signal, corresponding to the dark/light alternative periods

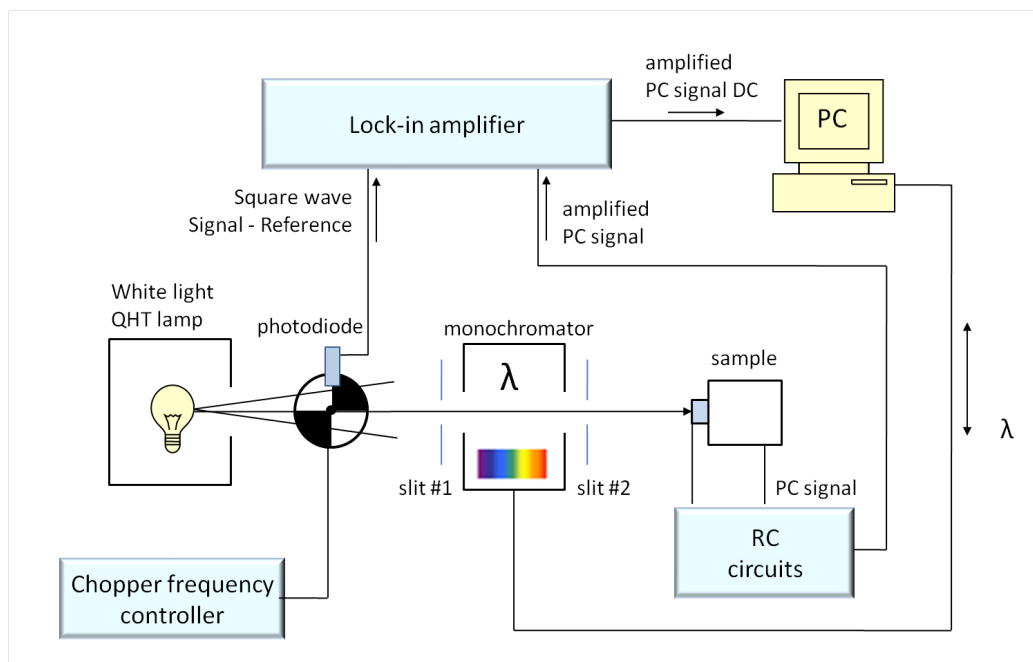


Figure 3.5: Block diagram of photocurrent experimental set-up.

(frequency=19 Hz), to a Stanford Research 530 lock-in amplifier, which basically makes the sampling of the alternate signal from the photodiode, in order to separate the signal from the noise generated by the measuring system. The circuit employed is reported in Figure 3.4: it is biased with two chemical batteries, that can be of 3 V 18 V in order to maximize photocurrent signal. Organic semiconductors are characterized by very high resistivity (about $R_{dark} \div 10G\Omega$ in organic crystals) so the choice is a compromise between a clean signal (low R_L), as expressed in the chapter and a strong signal (high R_L). The R_L of 100 k Ω is put in parallel with a capacitor of 4 nF, to constitutes a low pass filter in order to cut high frequencies and don't let them enter the lock-in amplifier. The collected photocurrent spectra have to be normalized to the intensity of light incident on the sample, since the lamp spectra vary with wavelength. The photon flux of the employed QTH lamp is in figure 3.6. For the photon flux measurement we used a thermopile, a thermal detector which consists in a series of connection of a certain number of thermocouple junction. It has the characteristics of having a flat respon-

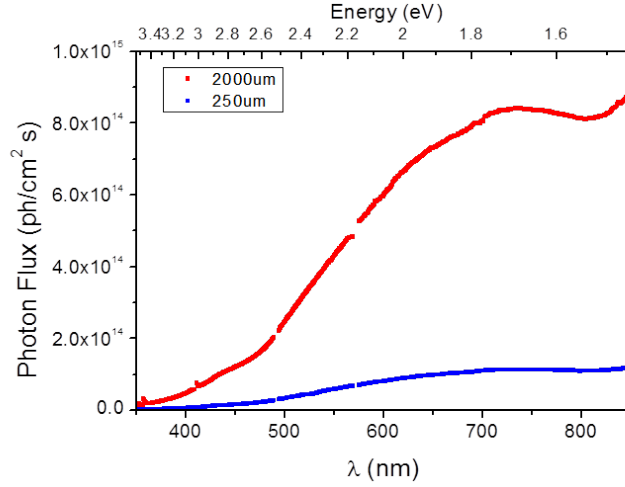


Figure 3.6: Photon flux of QTH lamp, with 2000 μm and 200 μm slits aperture.

sivity that is independent of wavelength. The photon flux is calculated from eq. 3.19:

$$\Phi = \frac{\text{signal}}{r A_{th} h\nu} \quad (3.19)$$

where $r = 7.8 \mu\text{V}/\mu\text{W}$ is the thermopile responsivity, $A_{th} = 0.0078 \text{ cm}^2$ is the thermopile area and $h\nu$ is the photon energy.

3.3 Detectors Characterization

3.3.1 X-ray Mo Tube

The X-ray irradiation measurements have been performed with a commercial PANalytical PW2285/20 X-ray tube with a Molybdenum target at 35 keV of accelerating voltage and for various filament currents, in order to acquire data at different dose rates for detector sensitivity measurements. A shutter is placed in front of the tube to allow an instantaneous (at least for our purpose) opening/closing the beam. The samples is placed 21 cm far from the source, in a metal box with a window of 4 cm^2 , in such way the X-rays impinge on the sample without further filtration. At this position the X-ray incident beam has a circular spot with a 7 mm diameter. The calibra-

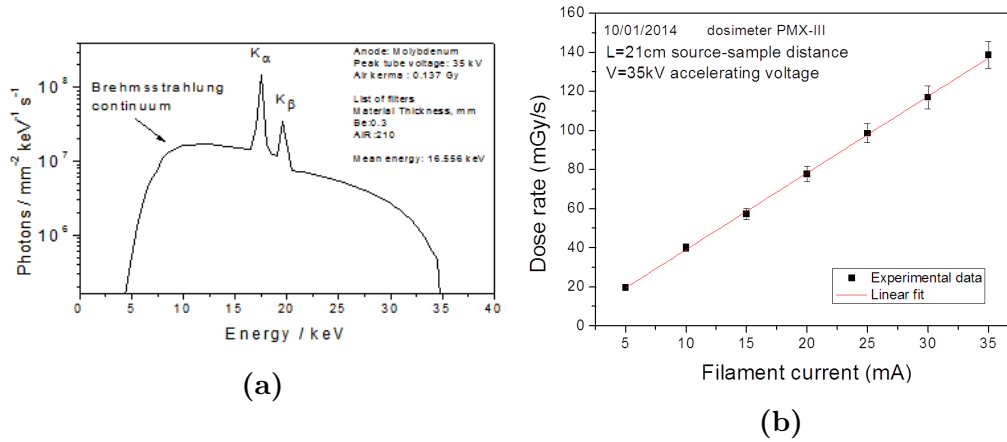


Figure 3.7: Simulated spectra of 35 keV 35 mA Mo tube (left) corresponding to a dose rate of 137 mGy/s (right).

tion has been carried out replacing the sample with a PMX-III detector. The calibration plot of the filament current vs dose rate and the simulated X-ray spectrum of the Mo tube at maximum irradiation of 35 mA (137 mGy/s) are reported in figure 3.7. The characteristic peak $K_{\alpha} \simeq 17.4$ keV and $K_{\beta} \simeq 19.6$ keV, and bremsstrahlung radiation are highlighted (see par. 2.1.1) The entire X-ray irradiation system is located into a lead-glass cap for protection of the operators by radiation, and the electrical connections and characterizations have been carried out as described in 3.1.

3.3.2 SYRMEP Beamline - ELETTRA

SYRMEP is a beamline at ELETTRA Synchrotron Trieste, which was designed for the study of synchrotron radiation in medical diagnostic radiology applications [64]. Thus, the beamline is particularly suitable for exploiting organic crystal detectors for dose rates and energy range typical of mammography and medical applications. The light source is a bending magnet coupled with a double-crystal Si (111) monochromator which works in an energy range between 8 keV and 35 keV. The maximum dose rate is on the order of few mGy/s and depends on the selected energy value. A series of Al

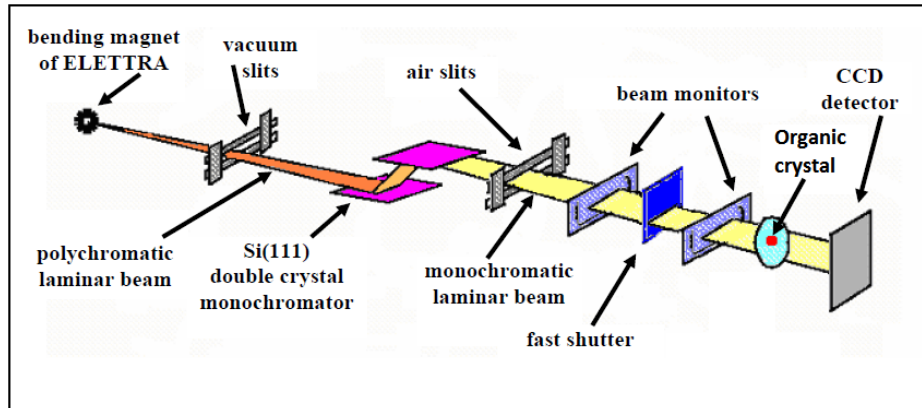


Figure 3.8: Scheme of the SYRMEP@ELETTRA beamline experimental setup.

filters allows to reduce dose rate down to $50 \mu\text{Gy/s}$. The beamline provides, at a distance of about 20 m from the source, a monochromatic laminar-section X-ray beam with a maximum area of $120 \times 4 \text{ mm}^2$, but which two series of motorized slits can focus with a precision of about $100 \mu\text{m}$. A calibrated ionization chamber is placed in front of the sample, giving a real-time monitoring of the incoming dose, while a CCD camera behind the sample permits an accurate alignment of the beam-slit-sample system (figure 3.8). A fast shutter, i.e. a lead chopper, at a frequency of 9 Hz, has been used to carry out fast time-resolved X-ray transient measurements. The electrical connections and characterizations have been carried out as described in 3.1, with the *Keithley 6517A electrometer* for common I-V and I-t measurements, and with *AH501 digital oscilloscopes* for fast I-t measurements.

3.3.3 Gamma Sources

The high energy gamma radiation used in this thesis consisted in a Cs^{137} radiation source sealed in dumpbell leaded shield. The source emits a primary electromagnetic radiation at 661 keV and the activity is 3.83 MBq (at the 12/07/2014). The measurements were performed in air and at room temperature, and the source laid on an adjustable spacer. Three source-sample distances have been investigated: $L1 = 7.1 \text{ mm}$ (corresponding dose rate 5.8

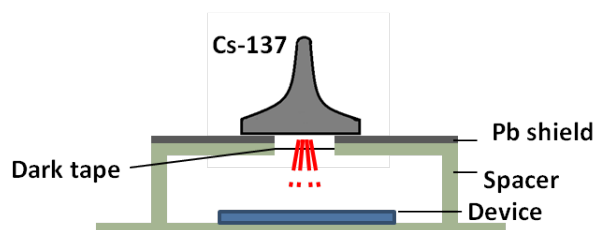


Figure 3.9: Scheme of the setup for high energy gamma irradiation of Cs^{137} .

mSv/h), $L2 = 9.2$ mm (corresponding dose rate 3.5 mSv/h) and $L1 = 13.1$ mm (corresponding dose rate 1.7 mSv/h). As we tested also TIPS-pentacene, which photoconductivity under visible light are well known, a dark tape strip has been placed between the source and the organic sample blocking visible light without affecting such high energy radiation.

3.4 Materials

In this section the organic molecules composing the crystals investigated in this thesis will be presented. We will report about 4-hydroxycyanobenzene (4HCB), a solution-grown single crystal that presents a 3D tunable structure, particularly suitable for radiation detection (3.4.1). Two well known high performance small-molecules will be presented: 5,6,11,12-Tetraphenyltetracene (rubrene, see par. 3.4.2), the benchmark for organic electronic based on single crystals, and 6,13-bis(triisopropylsilylethynyl)pentacene (TIPS-pentacene, see par. 3.4.3) widely used in organic thin film electronics for its particularity of growing in polycrystalline form when dropcasted. In addition, other solution-grown molecule, e.g. 1,5-dinitronaphthalene (DNN) (3.4.4) and 1,8-naphthaleneimide (NTI) (3.4.5), differing in polarizability, packing, molecular structure and geometry was studied, to investigate how the above parameters affect organic single crystal sensing properties.

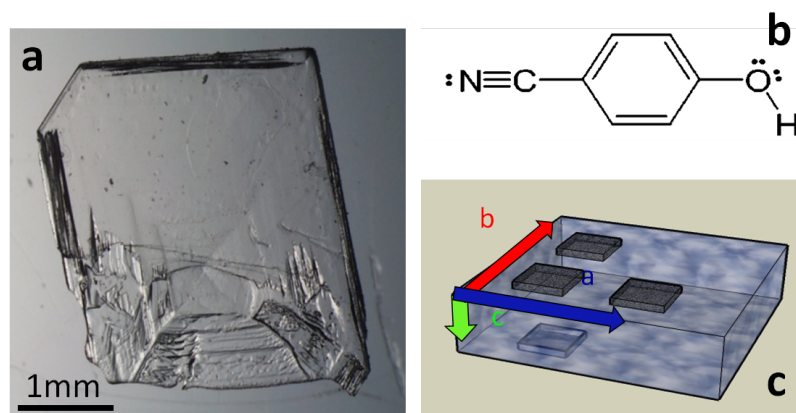


Figure 3.10: a) Optical microscopy image of 4HCB single crystal. b) 4HCB molecule c) L-shaped contacts with epoxy silver paint to electrically investigate the three crystallographic axes.

3.4.1 4-hydroxycyanobenzene (4HCB)

4-hydroxycyanobenzene (4HCB, C_7H_5NO) is a well characterized known solution-grown semiconducting single crystal, the basic molecule and the optical image of a large 4HCB crystal are shown in figure 3.10. 4HCB molecule was purchased by FLUKA (99+%) and used as follows. A first crystallization was obtained dissolving an amount of material in pure ethylic ether (technical grade), and letting the solvent evaporate under a hood in standard laboratory conditions. The resulting crystals were washed thoroughly with warm petroleum ether (technical grade). After this step, the remaining crystals were completely dissolved in ethylic ether (concentrations ranging from 10 to 50 mg mL⁻¹; at higher concentrations, larger crystals, both in size and thickness, were obtained). The mixture was filtered through a 0.45 mm Teflon filter, poured in a beaker, and covered with a Petri dish. The system was then left undisturbed to allow the complete and slow evaporation of the solvent. After that, the transparent crystals left in the beaker were gently removed using a spatula, and used for the preparation of the devices with no further treatments [113]. The crystals have 3D tunable dimensions, up to few millimeters in lateral dimension and up to 1 mm in thickness (figure

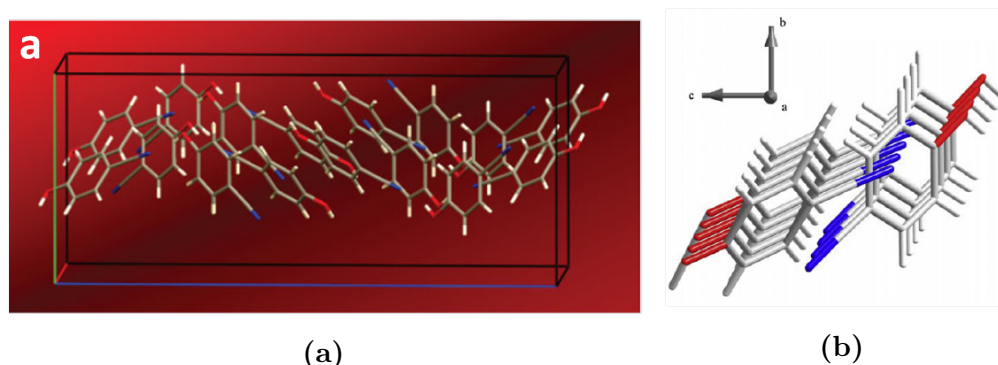


Figure 3.11: Structure of a-axis of 4HCB single crystal. a) Lateral 3D view, shows short distance between molecules. b) In line view, highlight the $\pi-\pi$ stacking and the particular position of N atoms [116, 113].

3.10a), by properly modifying the solution growth conditions. The large size of the crystal translates into a radiation interaction volume for detector applications, which is much larger than those typically accessible with polymer films (which are a few micrometers thick at most). The as obtained single crystals are very robust to physical manipulation (they can be easily moved and positioned on substrates, electrodes arrays, sample holders, etc.) and to environmental conditions (air, light, room temperature) [114]. The molecule possesses a strong intrinsic dipolar charge distribution due to the presence of the electron-acceptor cyano-group connected via a conjugated benzenic bridge to an electron-donor group, the hydroxylic one (figure 3.10b). The crystal structure is known for a long time [115], but in figures 3.11, 3.12, 3.13 the structure and molecular packing confirmed by modern X-ray diffraction (XRD) are shown. The axis are labelled as in figure 3.10c.

The packing along the a axis (figure 3.11), a group of four 4HCB molecules at different torsion angles generates a sequence of as many infinite columns, partly overlapping, where the benzenic rings are all eclipsed and separated by a distance of $9.202(2)$ Å. In addition, the nitrogen atoms of the cyano groups belonging to the outer molecules (recognizable in figure 3.11b as blue-colored atoms) are sandwiched between the overlapping rings of the

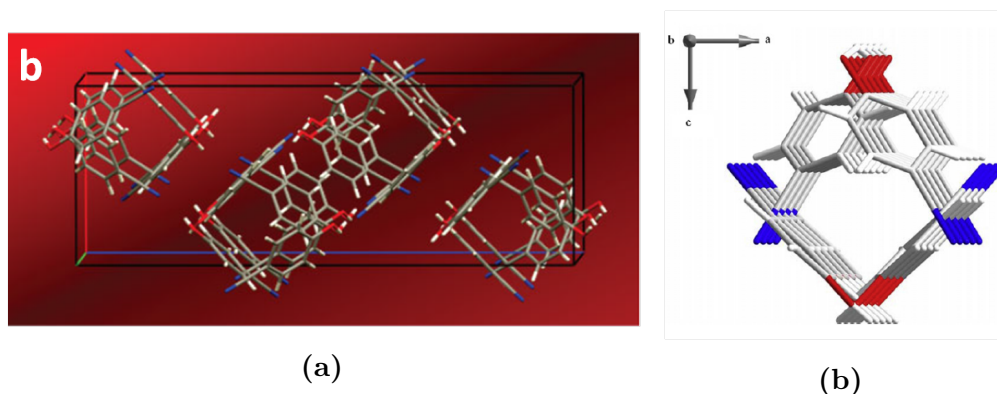


Figure 3.12: Structure of b-axis of 4HCB single crystal. a) Lateral 3D view, shows particular packing shape. b) In line view, shows that only some rings are overlapped [116, 113].

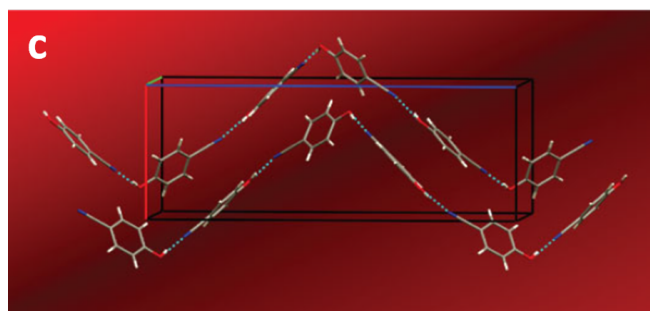


Figure 3.13: Lateral 3D structure of c-axis of 4HCB single crystal. The long distance between aromatic rings is highlighted [113].

two central ones, and may contribute to increase the net electron density of the system. Concerning the b axis, it develops in two entangled ABAB sequences of benzenic rings, arranged to form a sort of square-based columns parallel to the crystallographic axis (figure 3.12a). The first sequence of the AA and BB rings are side by side and connected with weak intermolecular hydrogen interaction. Only in the second sequence the AA and BB rings are partially overlapping, where the rings are separated by distance of $10.738(2)$ Å, about 1.5 Å larger than in the case of axis a. Finally, the structure along the c axis grows in a complex pattern of parallel spirals (figure 3.13), and no appreciable overlapping of benzenic rings can be identified. Therefore no ap-

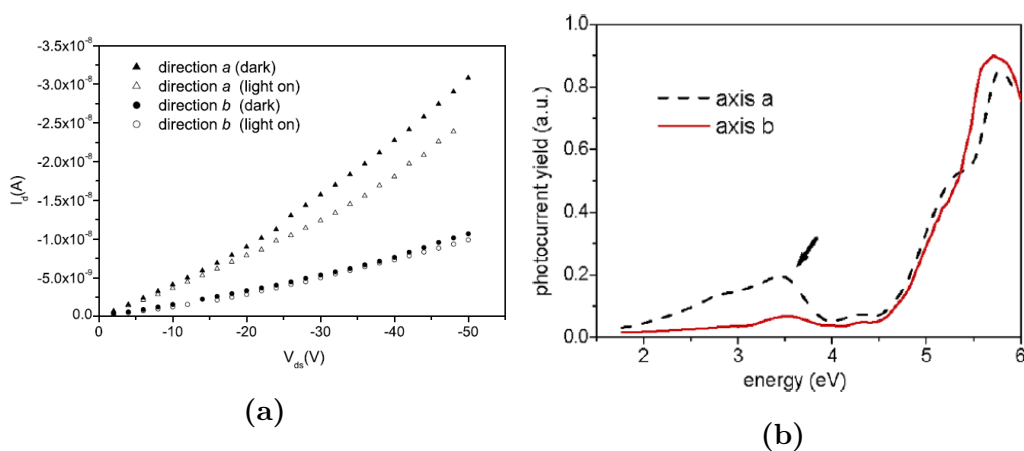


Figure 3.14: Electrical characterization of 4HCB single crystals. a) Current-Voltage characteristics along two coplanar axes, a and b, in the dark (solid marks) and under white light illumination (open marks) [116]. b) Photocurrent yield along the two planar direction of the crystals. The arrow highlights the peak associated to the band states located in the band-gap [117].

preciable intrinsic charge transport is expected to occur along this direction. In conclusion, a and b are the two axes that presents $\pi - \pi$ overlapping and, in agreement with organic single crystal structural properties (see 1.2.2), they are the planar and strongest growth axes [113].

Transport Properties

Current-voltage characteristic of a 4HCB crystal in the dark along the two planar axes, in figure 3.14a, shows a better transport along a axis, than along b, in agreement with the better $\pi - \pi$ stacking and shorter intermolecular distance in a. Under white light irradiation the current along a decreases of about 20%, while the b current it is only slightly affected. The I-V characteristic recovers to pristine values after few hours of relaxation in the dark. In addition, the anisotropy transport properties have been assessed also with a Field-Effect Transistor (FET) configuration, where the FET mobility of the two planar axes differs of one order of magnitude (table 3.2), even though the two mobilities have the same value under light exposure [116]. Moreover,

due to the negative biasing of the gate electrode to induce field-effect, the p-type transport have been assessed. The two above effects may both ascribed to the presence of N atoms that imply a local electrostatic distortion that may induce the formation of trapping sites able to interact with photons. It has been hypothesized that the traps are neutral in their ground state and that the interaction with photons may induce the emission of an electron from trapping state, leaving a positive electrically active charged state. The excess electrons may readily recombine with injected holes and reduce the collected current.

The photoconductivity spectrum is reported in figure 3.14b, showing the HOMO-LUMO transport edge located at 4.5 eV, for both planar axes [117]. A large band of deeper states is clearly visible at lower energies in the spectrum, starting at 3.9 eV, i.e. 0.45 eV from the HOMO-LUMO gap. It is also evident that the number of electrons excited per incident photon is larger along axis a than along axis b, confirming the presence of photo-activated defective states, more effective along axis a than along b.

Typical SCLC measurement plot is reported in figure 3.15a, and the calculated mobilities from trap-free regime is reported along all three crystallographic axes. The inset shows the L^{-3} dependence of the current, typical of bulk transport. The mobility and density of states values for 4HCB single crystals have been summarized in table 3.2. SCLC mobilities values are in agreement with FET ones, they confirm the anisotropy between a and b planar axis, and highlight the very low mobility along c ($\mu_c^{SCLC} \approx 10^{-5}$). A DM-SCLC analysis confirms the presence of electrically active states in planar axes, around 0.46 eV, more pronounced for a axis. Density of trap states N_T calculated from V_{TFL} are underestimated compared to N_T^* , which are extracted from DOS function. I-V characteristics, FET mobility, photocurrent spectroscopy and DM-SCLC analysis are all in agreement with the presence of electrically active states for the two planar axes, that are more effective along axis a than along b.

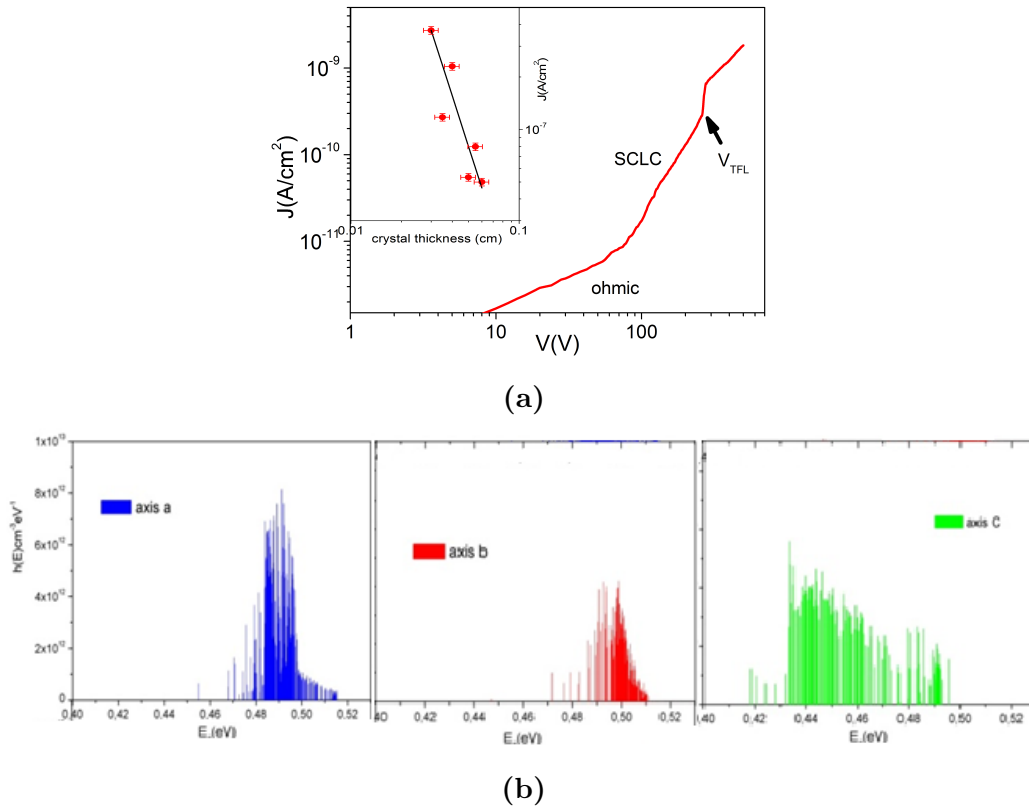


Figure 3.15: a) Typical SCLC characteristic, the ohmic, SCLC and trap-fill limit voltage area highlighted. The inset shows the L^{-3} dependence of the measured current as function of crystal thickness. b) DOS function as extracted from DM-SCLC analysis [117].

3.4.2 5,6,11,12-Tetraphenyltetracene (Rubrene)

5,6,11,12-Tetraphenyltetracene (rubrene, $C_{42}H_{28}$) is one of the best performing organic semiconducting single crystal for electronic device application. At the same time it's still presenting some open problems which limit its performances, as its chemical instability in presence of oxygen and the difficulty to obtain a good crystalline quality samples. Rubrene belongs to the group of polycyclic aromatic hydrocarbons and consists of a tetracene backbone (it's built with four benzene rings placed side by side each other), with a phenyl ring bonded on each side of the two central benzene rings, as shown

Crystal axis	μ_{FET}	(cm^2/Vs)	μ_{SCLC}	(cm^2/Vs)	N_T (cm^{-3})	N_T^* (cm^{-3})
	Max	Ave.	Max	Ave		
a	8×10^{-2}	3×10^{-2}	1×10^{-1}	5×10^{-2}	3×10^{11}	9×10^{12}
b	9×10^{-3}	5×10^{-3}	2×10^{-2}	6×10^{-3}	1×10^{11}	4×10^{12}
c	-	-	2×10^{-5}	5×10^{-6}	5×10^{12}	2×10^{13}

Table 3.2: Summary of electrical parameters of 4HCB single crystal along all three crystallographic axes [117].

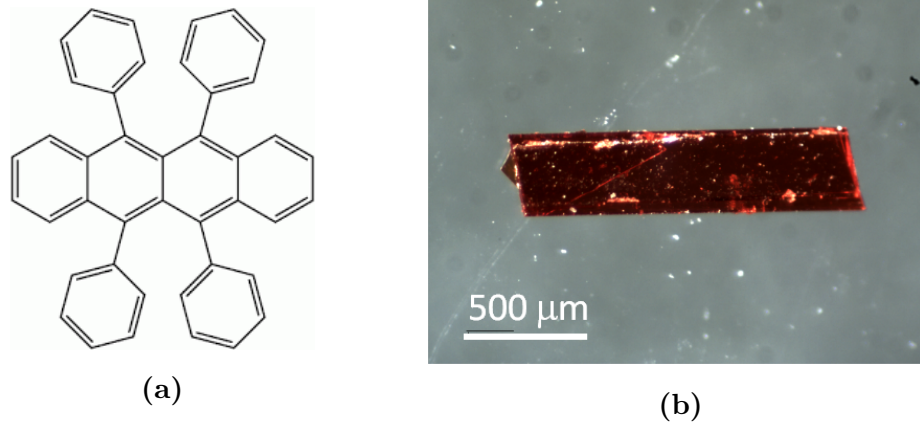


Figure 3.16: a) Chemical structure of Rubrene. b) Optical microscopy image of a rubrene single crystal.

in figure 3.16a. Rubrene molecules, in liquid or amorphous phase, tend to oxidize when exposed to air; light strongly enhances this process [118, 119]. An oxidized rubrene molecule becomes a rubrene peroxide and experiments show that the most common form of peroxide formed after oxidation is the endoperoxide [120], in which molecular oxygen is lined to one of the two central rings of the tetracene backbone. The bonding with oxygen generates a deformation of the molecular organization, this causes a break of the π molecular orbital. This contamination affects optical properties of the crystal, at a first look rubrene solution and amorphous film became transparent from their original reddish colour. One of the most important achievement

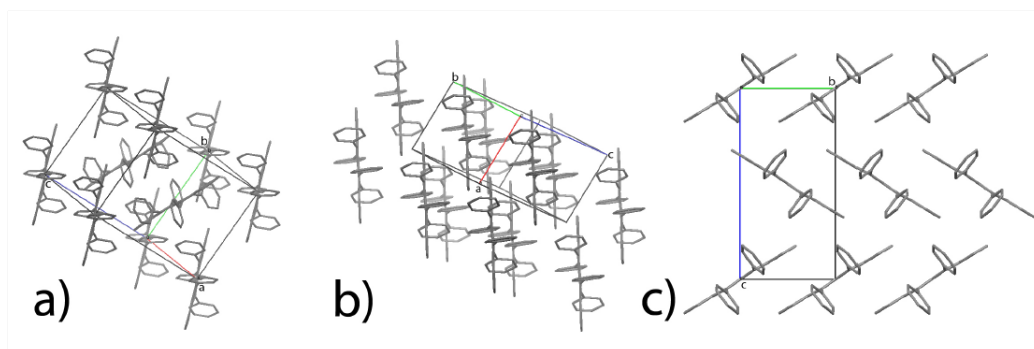


Figure 3.17: Arrangement of molecules in the three known rubrene polymorphs: monoclinic (a), triclinic (b), orthorhombic (c).

reached with rubrene is its highly crystalline structure which improves enormously its potential application in electronic devices, thanks to its electrical parameters and efficiency. The molecular arrangements in the three main known rubrene polymorphs are monoclinic, triclinic and orthorhombic. In figure 3.17 the three kinds of lattice in which it's possible an arrangement of rubrene molecules are shown. Looking at the three structures from a direction normal with respect to the long axis of molecule, it's possible to identify the amount of $\pi - \pi$ stacking between the conjugate backbones of adjacent molecules. In the monoclinic and triclinic polymorphs only a partial $\pi - \pi$ stacking is present, instead in orthorhombic polymorph the molecules are arranged in the herringbone packing, with an almost complete $\pi - \pi$ stacking in the b lattice direction. The reported distance of the unit cell in orthorhombic configuration are: $a = 26.86(1) \text{ \AA}$, $b = 7.193(3) \text{ \AA}$, $c = 14.433(5) \text{ \AA}$ [121]. To obtain that form it's necessary to follow a particular growth processing, since the way used to create crystals influences their final structure. Operatively, monoclinic and triclinic lattice structures can be obtained by solution crystallization methods, while the third unit cell, orthorhombic, needs physical vapour deposition (PVT) to be formed [122]. As mentioned above, Rubrene is strongly affected by oxidation. Indeed, rubrene peroxide has been shown to be the dominant impurity in commercial rubrene powder and the presence of small amounts of oxygen in the inert gas flow used for crystal growth

has been shown to increase the amount of such impurities in the crystals [123, 124]. In order to improve material quality a deal may be a purification of the pristine material through several sublimation cycles and a carefully controlled growth environment. Kafer et al. [120] performed a very interesting analysis on the concentration of peroxide molecules in rubrene in function of depth, when exposed to air for several days: it has been experimentally proven that a crystalline form dramatically reduces the oxidation effects and it is present only in the first layers of the material.

The interest on rubrene is mainly motivated by its outstanding electrical transport properties, since the first measurements on rubrene single crystals have presented high charge carriers mobility values. Charge carriers mobility in rubrene orthorhombic single crystals can reach values as high as $40 \text{ cm}^2/\text{Vs}$, a value comparable to that found for amorphous silicon [52]. As for most organic crystals, electrical transport in crystalline rubrene is strongly anisotropic, with the highest mobility values measured along the b lattice direction [52, 125], which corresponds to the direction of the maximum $\pi - \pi$ stacking (figure 3.17). Rubrene, like most organic semiconductors is a unipolar p-type material, while electron mobility is several orders of magnitude smaller [126]. The outstanding transport properties of rubrene single crystals, and the inverse dependence of the mobility on temperature up to temperatures as high as 300 K suggest that the conduction mechanism may be band-like (see section 1.4).

In addition to extremely high charge carrier mobility, rubrene single-crystals have a huge photoconductivity, with a photocurrent generation efficiency close to unity. Najafov et al. have shown, by studying the photocurrent dynamics, that photoconductivity in rubrene single crystals is mainly due to free charge carriers that are released from a long-lived intermediate state $\approx 100 \mu\text{s}$ after the excitation pulse [127]. In subsequent works they showed that this process is mainly limited to the surface region, suggesting a role of the crystal surface in the photoconductivity of rubrene [128]. From photoconductivity measurements the longest exciton diffusion length

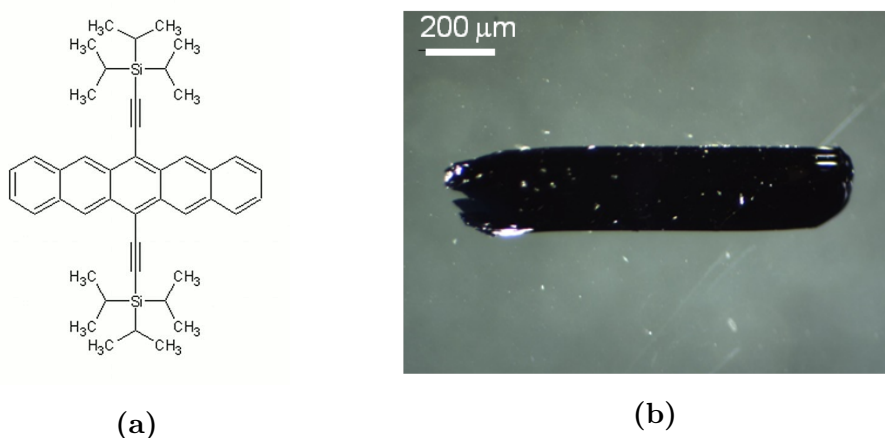


Figure 3.18: a) Chemical structure of TIPS-pentacene. b) Optical microscopy image of solution-grown TIPS-pentacene single crystal.

in organic materials, in the range of 8-10 μm has been measured [8]. In this thesis rubrene has been employed mainly for two purposes: the electrical performances and potentiality of an highly oriented crystalline rubrene thin film have been assessed (see par. 8); PVT rubrene single crystals have been tested under X-rays to compare the behaviour of solution grown crystal-based devices with a high performing benchmark material (see section 4.3).

3.4.3 TIPS-pentacene

6,13-bis(triisopropylsilylethynyl)pentacene (TIPS-pentacene, $\text{C}_{44}\text{H}_{54}\text{Si}_2$) is a derivative of the organic molecule *pentacene*, which share with rubrene the highest performances in terms of measured mobilities (up to 30 cm^2/Vs for single crystals) [129, 130]. Pentacene unprocessability in liquid phase represents a huge limitation in terms of low cost deposition techniques. TIPS-pentacene is composed by the five fused benzene rings typical of pentacene, functionalized by means of the carbon atoms of the triisopropylsilylethynyl chains, chemical bonded with the carbon atoms in position 6 and 13 of the pentacene molecule. It is soluble in most of the common organic solvents (e.g. toluene, chlorobenzene, tetrahydrofuran and chloroform [131]) and, in

addition, the bulky functionalized groups in TIPS-pentacene efficiently maximize π -orbital overlap, and the triple bond between the carbon atoms (figure 3.18) promotes the face-to-face packing motif between adjacent molecule [132]. This inter-molecular interaction improves π -orbital coupling and potentially increases the carrier mobility, making TIPS-pentacene one of the most popular and appropriate materials used for thin-film transistors [133]. Thanks to its solubility, TIPS-pentacene is commonly spin coated [25], drop cast [131] and inkjet printed [134] in order to constitute the active layer in OTFTs. The electrical performances of TIPS-pentacene devices were found to be strongly dependent on processing conditions, i.e. the solvent used, the post processing treatment and the deposition method, since they determine the morphology of the films. Usually the drop casting method and the use of high boiling point solvent permit a slower evaporation rate leading to the formation of films with polycrystalline structure. Recently, employing shear-aided crystallization technique, highly ordered films with oriented crystals showing remarkable OTFTs mobility up to $11 \text{ cm}^2/\text{Vs}$ have been realized [27]. In this thesis the exploitation of TIPS-pentacene as active materials in ionizing radiation detection systems, in polycrystalline structure both in resistor-like and in OTFT configuration, has been investigated (see par. 5). In addition, X-rays photorensponse of solution-grown TIPS-pentacene single crystals have been compared to other organic molecules (see par. 4.3).

3.4.4 DNN

1,5-dinitronaphthalene (DNN, $\text{C}_{10}\text{H}_6\text{N}_2\text{O}_4$) is a small molecule composed by, as suggested by extended name, a naphthalene core with two nitro functional groups in opposite position. Thus it doesn't have a net dipole moment due to its symmetric structure, however the charge distribution is strongly localized to the functional groups (figure 3.19a). DNN grows in crystalline form by solution-grown methods from a widely available solvent/non-solvent solution of chloroform, benzonitrile, or acetone. Their size can be controlled by varying parameter such as the solvent/non-solvent volume ratio or the or-

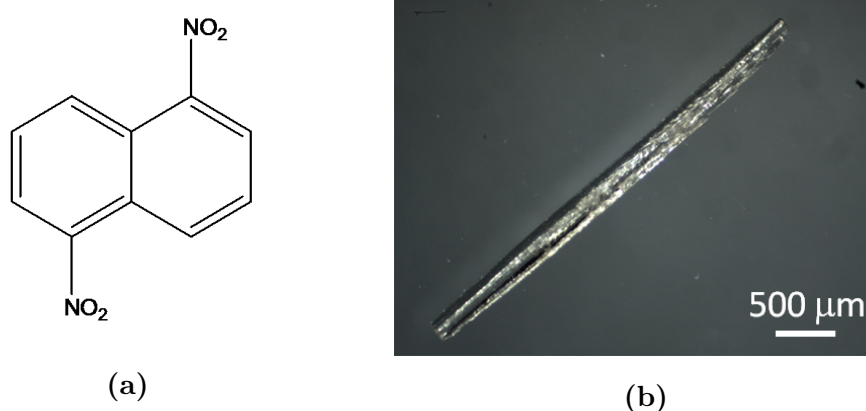


Figure 3.19: a) Chemical structure of DNN. b) Optical microscopy image of DNN single crystal.

organic molecule concentration in the solution. The solution is left to slowly dry at room temperature in controlled atmosphere. Long needle-shaped single crystal with an opaque yellow colour are formed by means of this procedure and the common geometrical sizes are about 3-4 mm in the long growth direction and 200-500 μm in lateral sizes. In figure 3.19b an optical image of a DNN single crystal. The crystalline structure measured with XRD is reported in figure 3.20a: is a monoclinic structure with the following cell parameters $a = 7.7(6) \text{ \AA}$, $b = 16.3(2) \text{ \AA}$, $c = 3.7(0) \text{ \AA}$ and $\beta = 101^\circ$ [135]. The density of the crystal, fundamental for the calculation of X-ray quantum efficiency, results $d_{DNN} = 1,579 \text{ g cm}^{-3}$. The crystal arrangement follow herringbone shape. In this thesis the electrical characterization and the X-ray response under X-ray have been performed along the crystal axis of major growth (see par. 4.3).

3.4.5 NTI

1,8-naphthalimide (NTI, $\text{C}_{12}\text{H}_7\text{NO}_2$) is a derivative molecule of naphthalene. In similarity with DNN it is a solution-grown single crystal that grows in needle-like shape at room temperature. The solvent is a tetrahydrofuran (THF). The single crystals in figure 3.21b have a bright yellow colour. From

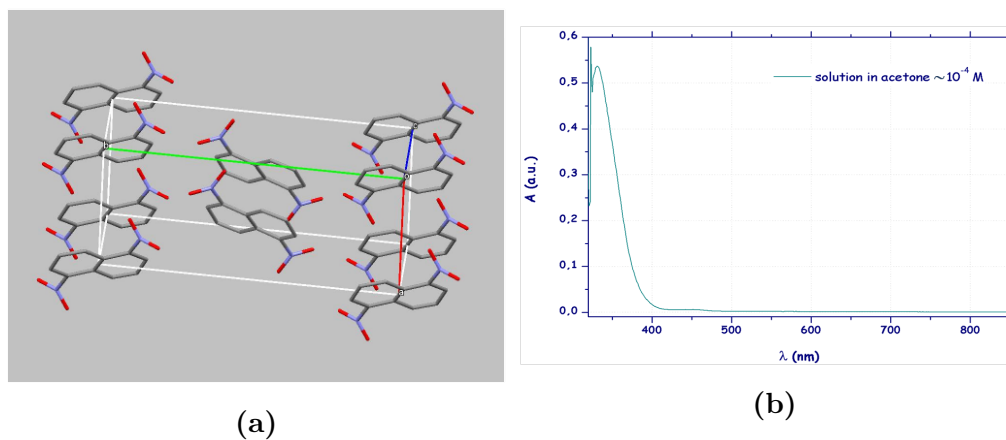
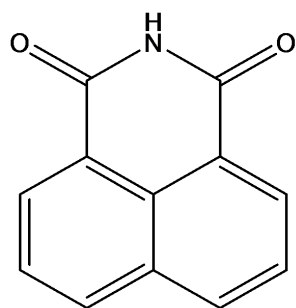


Figure 3.20: a) Crystallographic structure [135] and b) absorption spectrum of DNN.

the XRD structure reported in figure 3.22a the dimensions of the unit cells have been calculated: $a = 11.009(2)$ Å; $b = 5.4134(8)$ Å; $c = 15.675(3)$ Å, $\alpha = 90^\circ$, $\beta = 108.917(15)^\circ$, $\gamma = 90^\circ$ [136]; and it grows in herringbone packing arrangement [137]. The density of the crystal is $d_{NTI} = 1,482$ g cm $^{-3}$.

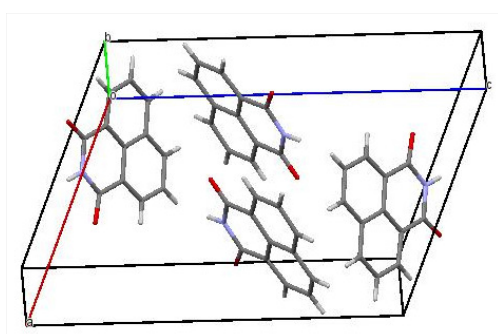


(a)

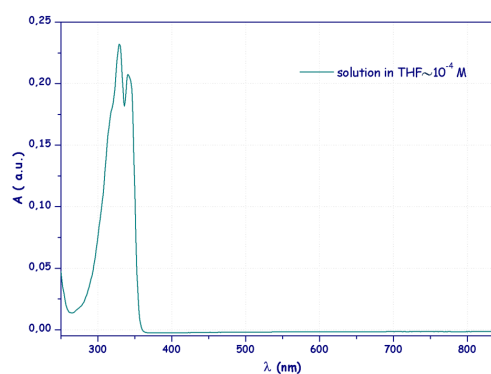


(b)

Figure 3.21: a) Chemical structure of NTI. b) Optical microscopy image of NTI single crystal.



(a)



(b)

Figure 3.22: a) Crystallographic structure and b) absorption spectrum of NTI.

	Molecular weight starting molecule (g/mol)	Crystal density (g/cm ³)	Melting point (°C)	Optical bandgap (eV)	Molecular polarizability (Å ³)	Molecular surface area (Å ²)
4HCB	119.12	1.20	112-113	4.2	12.76	164.31
DNN	218.17	1.586	213-215	3.3	21.58	271.69
NTI	197.19	1.482	299-300	3.5	21.63	244.69
Rub		1.176	315	2.2	78.13	745.46
TIPS-pen	639.07	1.104	239-240	2.0	85.9	1053.84

Figure 3.23: Some physical and chemical parameters of the molecular crystals under study.

Chapter 4

OSSCs as X-ray Detectors

The fourth chapter is dedicated to the study of OSSCs under X-ray irradiation. Organic materials have been so far mainly proposed as detectors for ionizing radiation in the indirect conversion approach, i.e. as scintillators, which convert ionizing radiation into visible photons (2.3.1), or as active layer in photodiodes (2.3.2), which detect visible photons coming from a scintillator and convert them into an electrical signal. Recent examples of organic devices used as direct photon detectors have been presented for operation in the UV-NIR range [85], with very interesting values for figures of merit such as photo-conversion efficiency, speed and minimum detectable signal level, and even though the simultaneous attainment of all these relevant parameters is demonstrated only in a limited number of papers, real applications are within reach for this technology, where the best reported photo-responsivity outperform amorphous silicon-based devices. Furthermore, organic semiconductors are very promising candidates also for the detection of higher energy photons (X- and gamma rays) [3, 138], nevertheless nowadays a small number of informations on the processes involved in organic/X-ray interaction are known.

We report in this chapter on the characterization of OSSCs as X-ray direct detectors, exploiting the variation of electrical properties induced by X-ray beam in organic single crystals and to investigate on the X-ray re-

sponse of a large number of samples, differing by molecular structure, crystal morphology, electrode configuration and materials. This study offers the possibility to deeper understand the nature of the interaction between X-rays and organic materials. In addition, the X-ray energies and dose rates are comparable to those employed in medical diagnostic applications (typically mammography), assessing thus the behaviour of the crystal-based detectors in medically relevant conditions. In fact, the low atomic number of all organic compounds is similar to the average human tissue-equivalent Z , and makes them ideal candidates for radiotherapy and medical applications. The first section is focused on 4HCB single crystal, providing a full characterization of the X-ray response along the three crystal axis and different electrodes configuration, showing, among others, the linearity of the intrinsic X-ray response, the sensitivity and the radiation hardness. In the second section the results will be compared with other molecular crystals, that differs in molecular composition, shape and crystal structure. In the last section, a preliminary assessment of detection of high energy X-ray (661 keV of Cs^{137}) will be discussed.

4.1 4HCB Single crystal direct detectors

This paragraph describes the research carried out on 4-hydroxycyanobenzene (4HCB) single crystals (see par. 3.4.1) which have been grown from solution. The large size of the crystals translates into a radiation interaction volume which is much larger than those typically accessible with polymer films (which are a few tens of micrometers thick at most)(2.4). The as obtained single crystals are very robust to physical manipulation (they can be easily moved and positioned on substrates, electrodes arrays, sample holders, etc.) and to environmental conditions (air, light, room temperature).

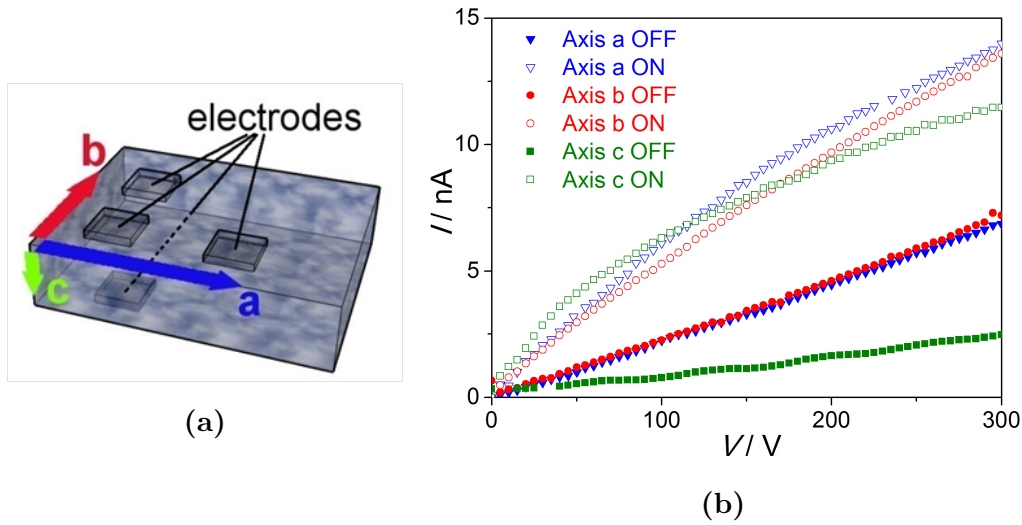


Figure 4.1: a) Sketch of the L-shaped contacts on a 4HCB platelet single crystal and the single bottom contact. The three crystallographic axes are in evidence. b) Current-voltage curves probed along the three axes with a 35 keV and 170 mGy/s X-ray beam switched on (empty symbols) and off (filled symbols).

4.1.1 X-ray Direct Detectors

We investigated the photoelectric response of 4HCB crystals under an X-ray beam in air at room temperature and under ambient light. The 4HCB crystal is a solution grown crystal, with tunable dimensions up to few millimeters in the a and b axis, and up to 1 millimeters along c axis, taking the shape of a platelet that permits to easily investigate all crystallographic axis as shown in figure 4.1a. The crystal structure and the electrical characteristics of 4HCB single crystal are well known and were previously reported (see par. 3.4.1). The electrodes consist of small drops of an epoxy conductive silver paint (EPO-TEK E415G) with low solvent concentration. The measurements were made with a Mo X-ray tube, accelerating at 35 keV and with dose rates ranging between 2 and 170 mGy/s (see par. 3.3.1).

In these conditions the bulk dark currents I_{OFF} , that is, those measured in the absence of the X-ray beam, along the two planar axes a and b are comparable (Figure 4.1b), while the one along the vertical axis c differs (in

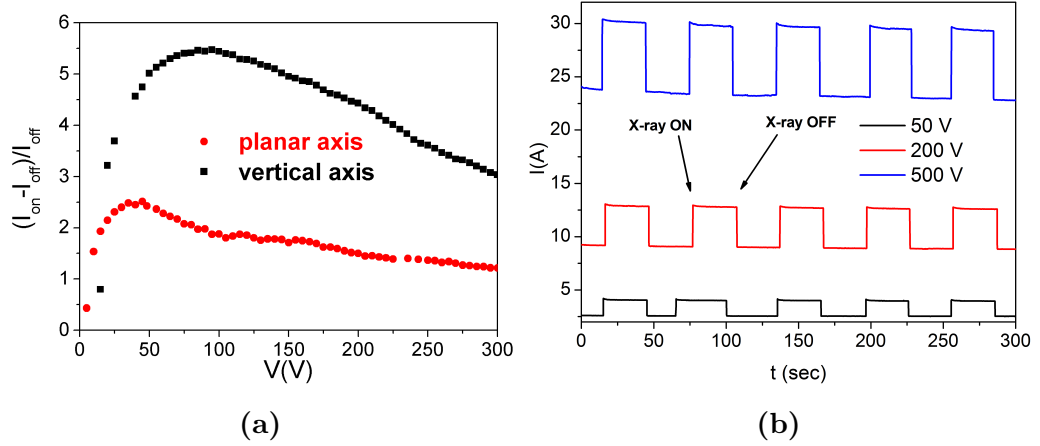


Figure 4.2: a) Comparison between the normalized X-ray induced photocurrents $(I_{ON} - I_{OFF})/I_{OFF}$ along the planar and vertical axes of a 4HCB crystal. b) Repeated on/off switching of the X-ray-beam along a planar direction (a-axis) of a 4HCB crystal, shown for different applied bias voltages.

line with previously reported data [116]). Therefore, we will refer in the following only to the behaviour along vertical and planar axes, without distinguishing between the two planar axes a and b. As shown in Figure 4.1b, the irradiation of 4HCB crystals with a 35 kV X-ray beam induces a significant increase in the photocurrent along both the planar and vertical axes, indicating the creation of photogenerated charge carriers. Interestingly, the normalized photocurrent $(I_{ON} - I_{OFF})/I_{OFF}$ vs V curve presents a maximum at rather low voltages for both axes, suggesting that practical devices may be operated at voltages as low as 50 V, hence with low power requirements (Figure 4.2a). No hysteresis, and no appreciable current drift, are observed upon repeated X-ray beam on/off cycles (Figure 4.2b) for different bias voltages. The response time, shorter than 70 ms, is remarkably fast for organic electronic devices[3]. Over thirty samples have been fabricated and tested both electrically and under X-ray exposure, pointing out a remarkable fluctuation between crystals, due to the extreme variability of organic materials: the data reported show the typical behaviour of 4HCB devices. The photocurrent values $\Delta I = I_{ON} - I_{OFF}$ obtained for the vertical and planar

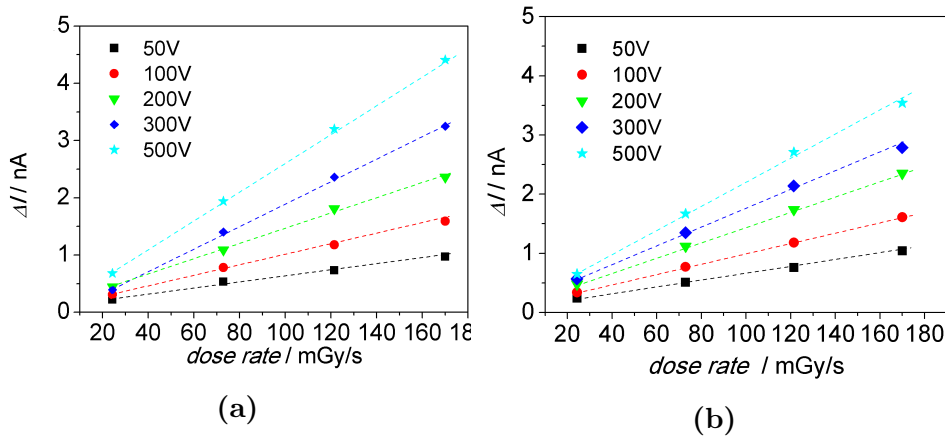


Figure 4.3: The X-ray induced current variation $\Delta I = I_{ON} - I_{OFF}$ is reported for increasing dose rates and different biases for the vertical (a) and planar (b) axes of a 4HCB crystal on a glass substrate with Ag electrodes shielded from the X-ray beam.

directions (reported in figures 4.3a and 4.3b) demonstrate that the response for an increasing X-ray dose rate is linear for each tested bias voltage for both axes, confirming that it is possible to effectively drive a device even at a few volts. The sensitivity defined as $S = \Delta I/D$, where D is the dose rate, was evaluated to be up to 50 nC/Gy at 400V for the reported devices.

4.1.2 Substrate and Electrodes contribution to X-ray induced signal

The electrical response of radiation detectors based on organic semiconductors may be influenced by the emission of secondary electrons from high-Z electrodes or substrates. Therefore, an assessment of these possible contributions to the detector response was carried out by testing several devices fabricated using various combinations of substrates and electrode materials, and different methods of device exposure to X-rays. Three different electrode materials have been tested placed on glass or copper substrates: a bicomponent epoxy silver paste (EPO-TEK E415G), colloidal graphite (AGAR SCI-

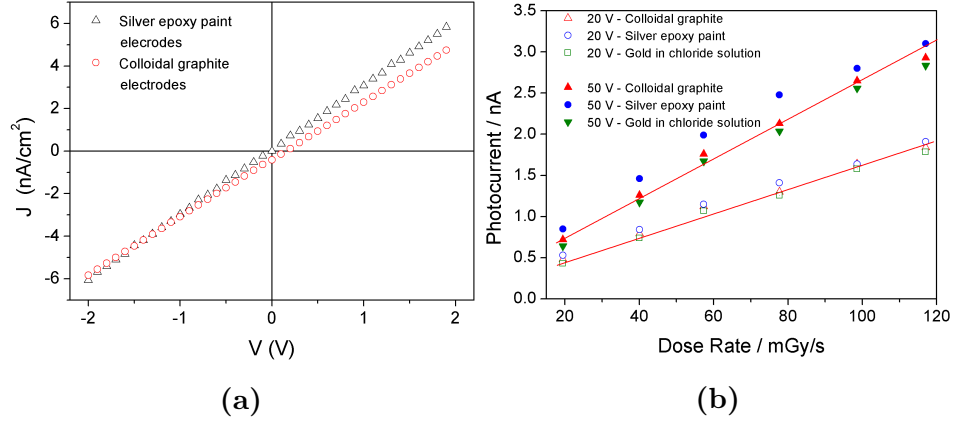


Figure 4.4: a) Current-Voltage characteristics of 4HCB crystal, showing ohmic behavior for the reported electrode materials. b) Photocurrent vs Dose Rate plot for three different electrode materials. It shows linear response for all tested electrodes materials, colloidal graphite (red upper triangles), silver epoxy paint (blue circles) and gold deposited from chloride solution (green lower triangles), and for two typical bias 20V (open symbols) and 50V (filled symbols). Linearity and sensitivity aren't affected by contact materials.

ENTIFIC AQUADAG AGG303), and gold from chloride solution (SIGMA ALDRICH 334049 AuCl_3). All materials used have been chosen taking into account the p-type conductivity of 4HCB crystals (3.4.1) and the possibility of realizing different electrode geometries and sizes, from a small area ($\approx 0.15 \text{ cm}^2$) to a large area (2 mm^2) electrodes. The first test was to verify that they make a good ohmic contacts to 4HCB OSSCs (Figure 4.4a). Then they have been tested under X-ray and comparable electrical performances has been proved. It is noteworthy that identical results have been obtained and no major differences have been observed in the measured photocurrent variation, that remain within the statistical samples variation error (about 15%) over about five tested crystals for each configuration type and with different electrode materials (Figure 4.4b). Moreover, in some devices fabricated on a glass substrate, the Ag electrodes have been shielded from the incoming X-ray beam with Pb layers, as sketched in figure 4.5a. Figure 4.5b reports the response along the vertical axis of a device, as already shown in

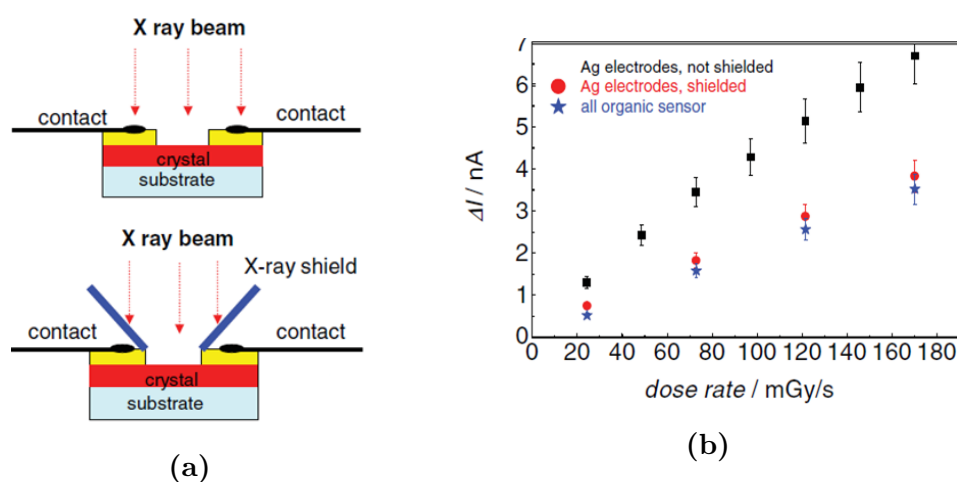


Figure 4.5: a) Sketches of the two different measurement configurations used to probe the detectors, that is, with unshielded (upper panel) and shielded (lower panel) metallic electrodes. b) Comparison of the ΔI response vs the dose rate at an applied bias $V = 500$ V for a device with shielded (solid red circles) and unshielded (solid black squares) Ag electrodes, compared with an all-organic identical geometry device (solid blue stars). When organic electrodes were used, the measurement configuration was the unshielded one.

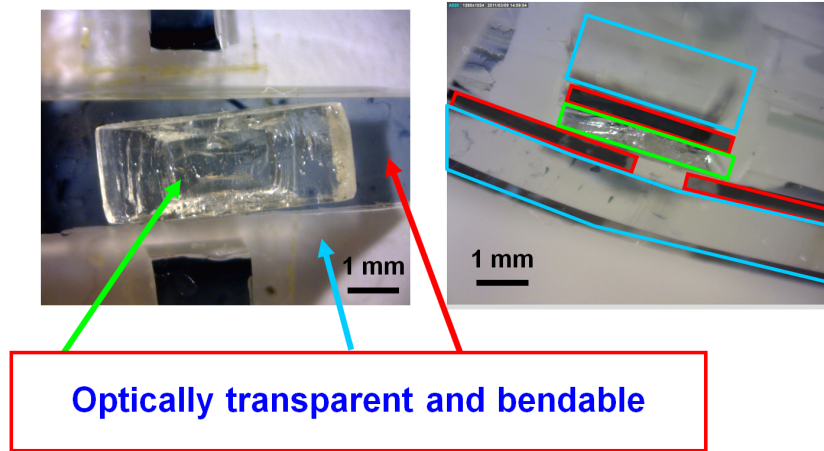


Figure 4.6: Optical microscopy images of top (left) and side (right) view of an optically transparent and bendable all-organic device. The PDMS substrate, the 4HCB crystal and the PEDOT:PSS electrodes have been highlighted with colour frames.

the previous section, with the metal electrodes directly exposed to the X-ray beam (solid squares) and shielded from it (solid circles). It is evident that the collected electrical signal is larger when the electrodes are exposed to radiation, possibly due to an extra contribution of secondary electrons released by the interaction of the X-rays with the metal electrodes (an effect already observed by other researchers in thin-film-based organic photodetectors [90, 88]). We observed the same behavior for various combinations of substrates (glass, SiO_2 , Cu), metal electrodes (Ag, Au, Cu), and geometries, thus assessing that high-Z substrates and/or electrodes give a non-negligible contribution to the collected electrical signal. In order to eliminate the contribution, it has been estimated as ≈ 3 nA at 500 V (figure 4.5b) and ≈ 100 pA at 10 V for dose rate of 180 mGy/s, thus it was subtracted to the measurements.

4.1.3 All Organic Detectors

We fabricated all-organic devices to remove the possible contribution from higher-atomic-number device components, using a low-Z organic elastomer as a substrate (PDMS, poly(dimethylsiloxane)) and a low-Z conducting polymer for the electrodes (PEDOT:PSS, poly(ethylenedioxythiophene)-poly(styrenesulfonate)) [139]. Such devices are biocompatible and were found to be optically transparent and reasonably conformable (figure 4.6), hence possibly also useful for bioelectronic applications. A typical response along the vertical axis of such a device is reported in Figure 4.5b (solid stars). The signal is comparable to that obtained from devices with shielded metallic electrodes, confirming that organic single crystals exposed to X-rays can directly convert the incoming radiation into an electrical signal with no need for additional high-Z components in the device. The X-ray induced photogenerated current in the all-organic device and in devices with shielded electrodes are compared to the data reported in figure 4.9c and 4.9d in the previous section. The predominant mechanism of radiation conversion and detection is thus intrinsically due to the crystals, that therefore can be exploited thanks to their considerable interaction volume with the incoming radiation (thicknesses up to millimeters), much larger than for organic semiconducting thin films (2.4) (which are typically only a few hundred nanometers thick). Moreover, the highly ordered and tight molecular packing of OSSCs offers the possibility of directly exposing the crystal surface to the radiation, with no need for passivation layers to limit the interaction of the organic material with the atmosphere.

4.1.4 Detector Characterization and Performances

So far we have shown the fundamental direct response of OSSC-based device under X-rays, here we would deeply characterize the single crystal detection features, assessing the detector performances and exploiting the differences between planar and vertical axes.

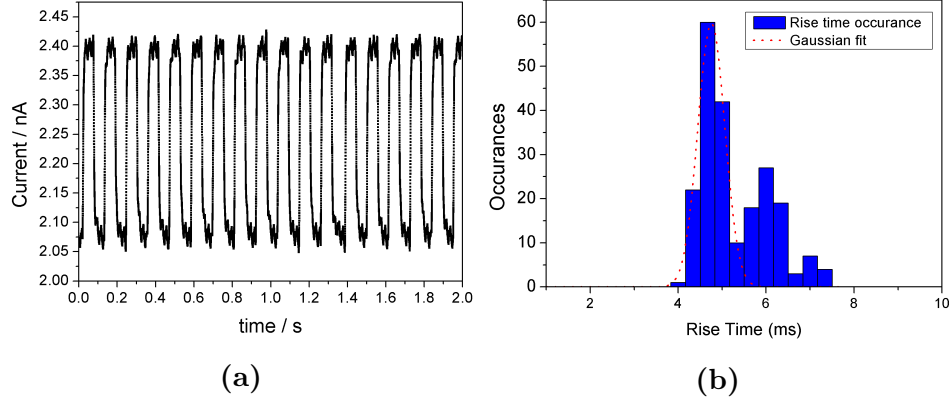


Figure 4.7: a) Photo-response of a 4HCB detector under an on/off switching X-ray beam (Synchrotron monochromatic beam with energy 10 keV, dose rate 40 mGy/s and 20 V applied bias) showing the fast rise time, < 5 ms, as better reported in (b), and good repeatability and stability of response.

From the measured photocurrent $\Delta I = (I_{ON} - I_{OFF})$ the fraction of $e^- - h^+$ pairs collected at the electrodes following X-ray irradiation was evaluated. We estimated that the quantum efficiency (see par. 2.1.3) within a typical crystal thickness of $400 \mu\text{m}$ is about 5%, i.e. the fraction of the impinging photons that are absorbed, by calculating the absorption coefficients to the Mo K lines (17.9 and 19.5 keV) with the XCOM code [140]. The photon absorption rate is then given by $\Phi = \epsilon D m_s / E_{ph} \approx 4 \times 10^8 \text{ photons s}^{-1}$, where D is the dose rate, m_s the sample mass, ϵ the fraction of absorbed photons, and E_{ph} the photon energy. Assuming that the maximum number of photogenerated carriers per photon could be $\beta = E_{ph} / \Delta$, where $\Delta \approx 10 \text{ eV}$ is the energy of pair creation (2.5 times the bandgap of 4 eV), for a current variation $\Delta I \approx 5 \text{ nA}$ the effective efficiency for the production of charge carriers can be evaluated as $f = \Delta I / [\Phi \beta (2e)]$. Therefore, we have an estimated $f \approx 2\%$, which takes into account both the pair production efficiency and the collection efficiency of the electrodes.

The Synchrotron X-ray source at ELETTRA (SYRMEP Beamline, see par. 3.3.2) allowed to deliver onto a 4HCB-based device focused monochromatic X-ray beams with energies in the range 10-21 keV and highly controlled

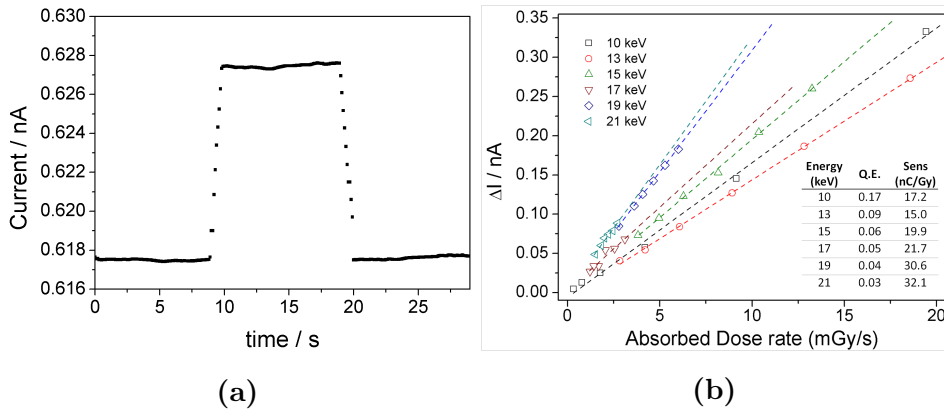


Figure 4.8: a) On/off switching for a monochromatic 10 keV Synchrotron X-ray beam, for low dose rate of $50 \mu\text{Gy/s}$. b) Electrical photo-response, i.e. ΔI , reported as a function of increasing dose rate, for a 4HCB single crystal detector under synchrotron X-ray monochromatic beams of different energies (from 10 keV to 21 keV), with an applied bias of 50V. The calculated quantum efficiency (Q.E.) and sensitivity are reported in inset.

dose rates. The speed and stability of the response provided by OSSCs-based radiation sensors, and the minimum dose that they are able to detect, have been probed. In fact, the monochromatic synchrotron radiation allows to avoid all spurious effects due to used broad molybdenum x-ray emission spectrum, and, moreover, the SYRMEP beamline setup is set to obtain very low and controlled dose rate values ($\approx 50 \mu\text{Gy/s}$). Exploiting these peculiarities, a lead-based chopper with a frequency of 9 Hz was placed in front of the X-rays beam in order to explore the time response of the device. In figure 4.7 it is possible to appreciate that the signal rise time and the decay time are below 5 ms, and that the overall response presents a very good stability and repeatability, with a baseline shift below 5% after up to 50 on/off cycles. Figure 4.8a shows the photoresponse of a crystal when exposed to doses of $50 \mu\text{Gy/s}$, using a 10 keV synchrotron X-ray radiation. The signal-to-noise ratio is very good even at these extremely low dose rates. Remarkably, this value is in line with the typical ones for medical imaging and clinical analysis (presently dose rates around $25 \mu\text{Gy/s}$ are required for such applications

[141]).

Taking further advantage of the X-ray monochromatic beam @SYRMEP, the focused monochromatic X-ray beams have been scanned with energies in the range of 10-21 keV. Figure 4.8b shows the slope of the output electrical signal vs. absorbed dose rate at some representative monochromatic photon energies over this energy range. The absorbed dose rate for a 400 μm thick 4HCB crystal has been determined by the calculation of quantum efficiency reported in table in inset in figure 4.8b. The observed change in the gradient of the data reported as a function of photon energy indicates a increase in X-ray sensitivity as the photon energy increase, from 17.2 nC/mGy at 10 keV to 32.1 nC/mGy at 21 keV (inset). In the inset is also shown the corresponding increase in quantum efficiency as the photon energy decreases.

In order to assess their radiation hardness under X-rays, different 4HCB crystal-based devices were continuously exposed for 3 h to a 170 mGy/s dose rate (total dose of 2.1 kGy) and then tested under an X-ray beam that was switched on and off (figures 4.9a and 4.9b); their electrical response along both the vertical and planar axes was recorded. After this rather high dose irradiation the devices response to X-rays did not vary significantly; moreover, the same devices still provided a reliable response even after aging for 1 month. It is noteworthy that, in all the tested conditions, ΔI increases almost linearly with the bias voltage applied to the crystal along the vertical axis (figure 4.9c), while it tends to saturate along the planar ones (figure 4.9d). This behaviour can be ascribed to the anisotropy of both the molecular packing and the electrical characteristics of the crystals, as is better evidenced by the current-voltage curves measured on the two axes of the same crystal with and without exposure to an X-ray beam (figure 4.10a and 4.10b, vertical and planar axes, respectively). In fact, the curves measured along any direction when the crystal is in the dark follow the space charge limited current (SCLC) behavior, typical of high resistivity semiconductors (see par. 3.1.1). As is evident from figure 4.10a, the electrical response of our crystals under X-ray exposure remains purely ohmic along the vertical

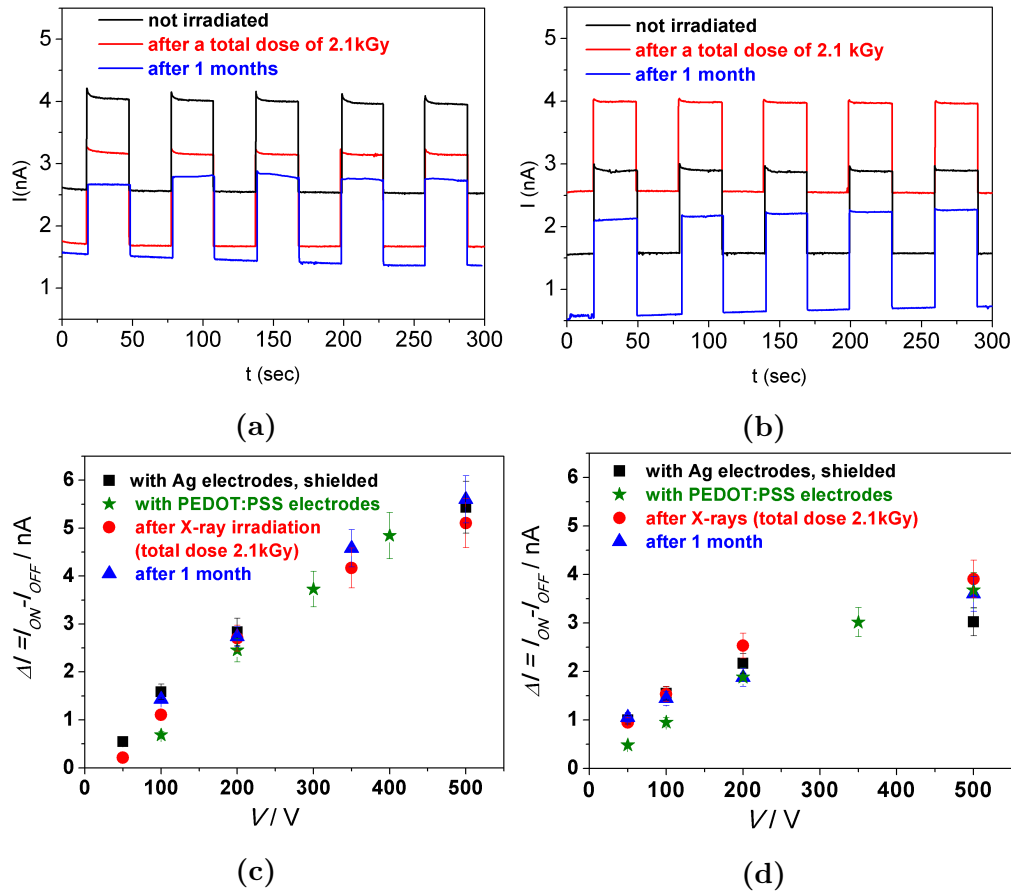


Figure 4.9: Electrical response of a 4HCB device to a on-off switching X-ray beam at a bias voltage $V=100\text{V}$. The response is reported for an as-prepared device (black line) after it has been exposed for 3 hours to a 170mGy/s dose rate (total dose of 2.1kGy) (red line) and after 1 month of storage in the ambient atmosphere (blue line). X-ray induced current variation ΔI reported for different bias voltages applied to crystals contacted with Ag electrodes, before (black squares) and after irradiation (red circles). The responses of crystals after ageing (blue triangles) and of crystals contacted with PEDOT:PSS electrodes (green stars) are also reported. The response along the vertical (a,c) and planar (b,d) axes.

direction, while it still follows the SCLC behavior at higher voltages along the planar axis. This suggests that the electrically active traps that control the SCLC transport in the dark play no major role along the vertical axis

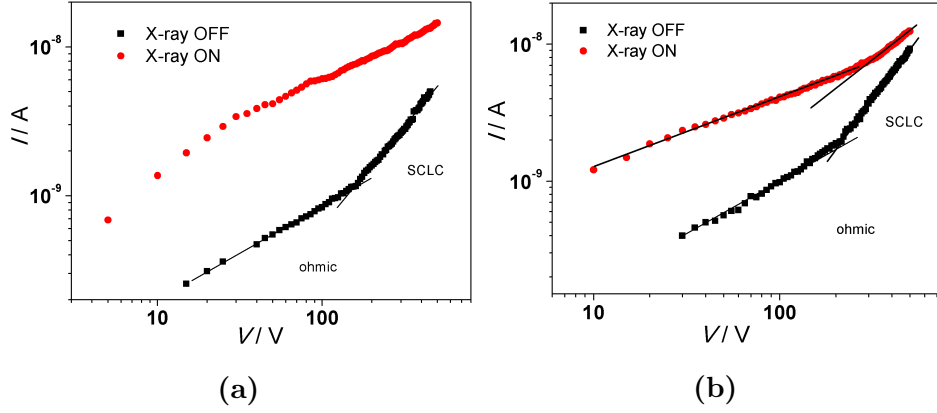


Figure 4.10: Current-Voltage curves for 4HCB-based devices in the dark (black squares) and under X-ray irradiation at 170 mGy/s (red circles), for the vertical (a) and planar (b) axes. Under X-ray irradiation no ohmic-SCLC transition is detected along the vertical axis.

when the crystal is probed under X-rays.

Taking advantage from 4HCB platelet shape and 3D dimensions, we were able to investigate different detector configurations, i.e. vertical and planar ones, on the really same sample, permitting a deeper study on the anisotropy effects, which are not negligible as already discussed above. In fact, as can be inferred from the measured mobility values, the tighter π -stacking axes are the two planar axes which possess good mobility ($\mu_a = 10^{-1} \text{ cm}^2/\text{Vs}$, $\mu_b = 10^{-2} \text{ cm}^2/\text{Vs}$), while the vertical axis is characterized by a poorer π -stacking degree and by a much smaller mobility value ($\mu_c = 10^{-5} \text{ cm}^2/\text{Vs}$). Starting from the above considerations an insight in the geometrical effects has been carried on, preparing two devices with identical experimental conditions (i.e. the same distance of 200 μm between the electrodes and the same X-ray irradiation conditions). Quite surprisingly, a direct comparison between the X-ray-induced photocurrent of a 4HCB crystal in the vertical collection geometry (small electrode on the top and on the bottom of the crystal) and in the planar collection geometry (two small electrodes on the top crystal surface), shows that the X-ray sensitivity is smaller along the planar axes (7 vs. 24 nC/Gy at 10 V) despite the fact that the charge car-

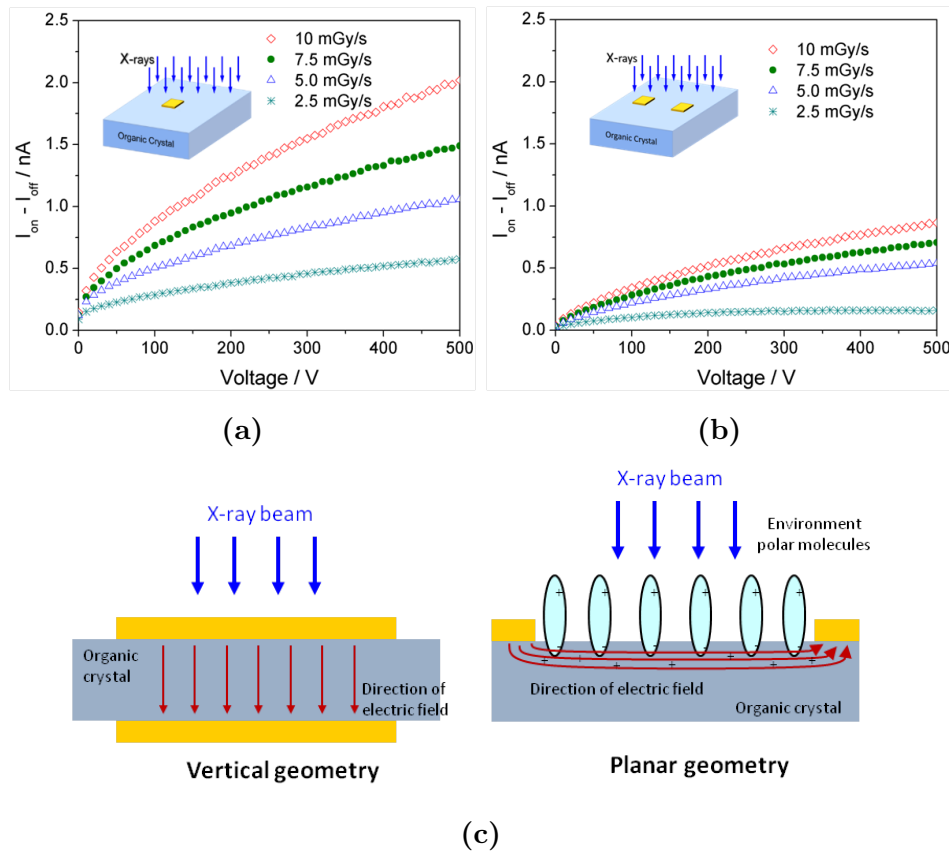


Figure 4.11: X-ray-induced current variation of a 4HCB crystal in the vertical geometry (a) and planar geometry (b) for different X-ray doses. c) Sketch of the electric field distribution in the vertical and planar geometries. The hypothetical effect of polar environmental molecules at the crystal surface in the planar geometry is also shown.

rier mobility is about 3 order of magnitude higher than along the vertical axis (figure 4.11). These results (i.e. the crystal axes characterized by the strongest π -stacking, that generally coincide with the best current transport axes, show a poorer X-ray photo-response) suggest that the planar electrode configuration is less performing. Three main causes can be hypothesised for this behaviour.

- i. The better electrical transport properties along crystal axes with strong π -stacking may be a limiting factor with respect to the crystals sensitivity to X-rays, due to the higher off currents.
- ii. The electric field distribution in the vertical geometry is much more effective in collecting the photogenerated carriers than that in the planar geometry (see fig. 4.11c). In the vertical geometry the whole electrode area can actively collect the induced charge carriers, while only a thin region around the electrode edge is effective in the planar geometry, even if the exciton diffusion length in OSSCs has been recently assessed to be about $8 \mu\text{m}$ [8].
- iii. The high polarizability of the π -electrons at the crystal surface, possibly further enhanced by the direct exposure to X-rays that are known to cause the ionization of organic molecules, may results in interactions with polar environment molecules (water etc.), that when adsorbed at the surface can affect the carrier density distribution or trapping states in the first monolayer below the surface, as sketched in fig. 4.11c (an effect which is analogous to the operating principle of organic field effect transistors).

Even if the device electrode geometry appears to play a major role in the performance of the radiation detector, it is noteworthy that all axes can be used for the effective detection of ionizing radiation, paving the way to unprecedented radiation detector architectures. Interestingly, in 4HCB crystals, the largest sensitivity is obtained in the vertical geometry, even if in this configuration the electrodes do not connect the crystal axis with the

Sample configuration	Electrode area mm ²	Crystal thickness μm	Sensitivity Mo Tube @35keV		
			50V nC/Gy	100V nC/Gy	500V nC/Gy
S0	0.25	150 ^a	18	28	77
S1	0.15	400	53	69	170
S2	2.0	400	87	117	175
S3	2.0	40	87	114	150

Table 4.1: Summary of the sensitivity of the reported 4HCB x-ray direct detectors, under a Mo tube at 35kV. S0 is the sample in planar configuration. S1,S2,S3 are in vertical configuration with different geometrical dimensions.

^a Electrodes distance in planar configuration is 400 μm .

best molecular π -stacking and carrier mobility. Further work is ongoing to better understand this point and the photo-physical processes generating the X-ray-induced charge carriers, together with their transport and collection mechanisms within the organic semiconducting single crystals (see section 4.1.5).

4.1.5 Electrodes Geometric effects

In order to identify the role of: i) the electrode area, and ii) the crystal thickness with respect to the X-rays detection response, we performed Current-Voltage and Current-Time analyses on 4HCB crystals, in the configurations reported in Table 4.1.

Table 4.1 summarize the four kind of electrode geometric configuration tested: configuration S0 is the planar configuration (inset in figure 4.11b) with two small area top silver epoxy electrodes; S1 is the small area electrodes, thick

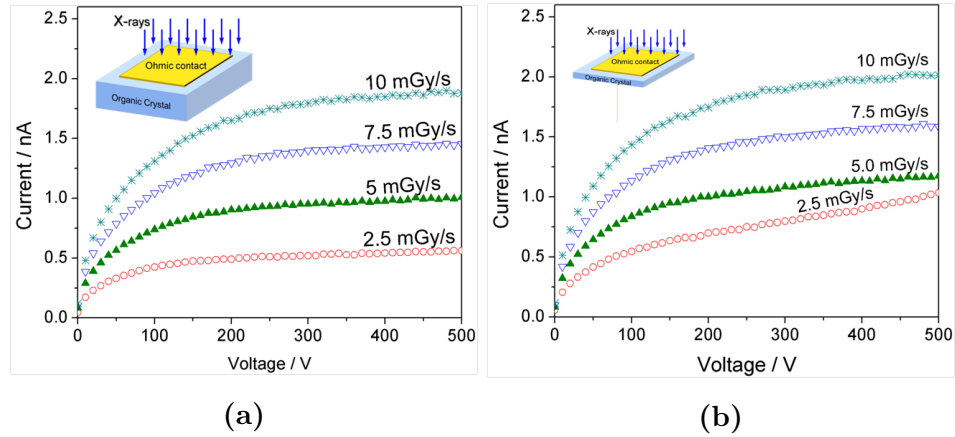


Figure 4.12: Current-Voltage characteristics of 4HCB organic crystals under X-ray exposure (measured along the vertical axis). The photo-response of the two large electrode area (2 mm^2) samples: a $400 \text{ }\mu\text{m}$ thick crystal (a) and a $40 \text{ }\mu\text{m}$ thin crystal are reported.

crystal in vertical configuration (inset in figure 4.11a) with epoxy silver electrodes; S2 and S3 are the large area, thick and thin crystals in vertical configuration with colloidal graphite top electrode (inset in figure 4.12a and 4.12b), respectively. Different electrode materials do not affect induced X-ray current, as already discussed in 4.1.2. Figure 4.11a, reported in section 4.1.1, shows the electrical photo-response induced by the X-ray beam from a Mo tube and impinging on a $400 \text{ }\mu\text{m}$ thick crystal with a small top electrode (configuration S1). As is visible, the photo-current does not reach saturation at any bias nor at any dose, indicating an incomplete collection of the photo-generated charge carriers. Figure 4.12a, on the other hand, shows identical measurements carried out on a crystal with the same thickness but with a much larger (one order of magnitude, see Table 4.1) top electrode area (configuration S2): the collected current signal reaches a saturation regime at low bias voltages ($< 200 \text{ V}$). Figure 4.12b reports the X-ray photo-response obtained from a much thinner crystal ($40 \text{ }\mu\text{m}$) with an electrode of the same area of the previous case (configuration S3), showing that the collected current tends to saturate at low bias values as well. It is noteworthy that the

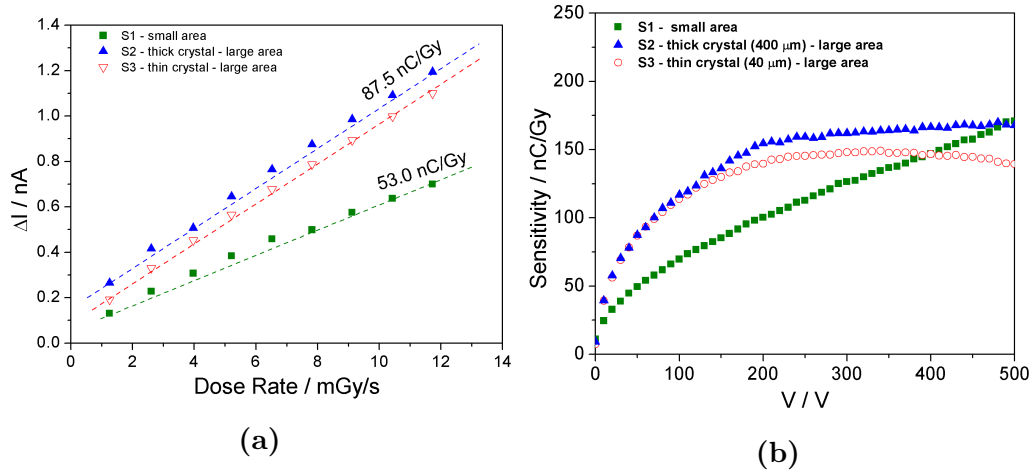


Figure 4.13: a) Linear photo-response trend, i.e. ΔI , reported as a function of increasing dose rate at 50 V applied bias for a small area and 400 μm thick sample (green squares), for a large area and 400 μm thick sample (blue solid triangles), and for a large area and 40 μm thin sample (red open triangles). b) Sensitivity progression with applied voltage for the same three samples. The maximum obtained sensitivity for large electrode area samples is 175 nC/Gy.

current saturation value reached with the large electrode configuration is comparable with the maximum value measured at the highest tested bias voltage in the small area electrode sensors, providing a strong evidence of a better charge collection process in devices with a large area electrode and clearly assessing how the crystal thickness can be reduced down to few tens of microns without affecting the charge collection properties of the sensor. This observation could be associated and ascribed to the recently reported values of several microns for exciton diffusion length in organic single crystals, as directly measured by optoelectronic analyses [8], suggesting that only the charge carriers photo-generated within a few microns from the electrode can be effectively collected and generate an electrical output signal. Furthermore, we have assessed that in all three tested configurations, S1, S2 and S3, organic semiconducting single crystals provide a perfectly linear response to an X-ray beam with dose rates varying in the range 0.05-120 mGy/s and at different bias voltages in the range 10-500 V. Figure 4.13a reports the linear

response in the 1-15 mGy/s dose rate range at 50V applied bias. Crystals with large area contacts (blue and red triangles in figure 4.13a), hence with optimized charge collection, present the same sensitivity of 87.5 nC/Gy at 50V, despite the difference in thickness, while identical samples with small electrode area have a significantly smaller sensitivity. Figure 4.13b shows a direct comparison between the sensitivity of the same samples reported in Figure 4.13a but as a function of increasing bias voltage. It clearly confirms that thin (40 μm) and thick (400 μm) crystals with large area electrodes have comparable sensitivity values at relatively low biases, while with increasing ones some differences are noticed. In particular, thin crystals (S3) evidence a slight decrease in sensitivity at higher voltages, likely due to the onset of space charge effects in the dark current at lower bias voltages. It is remarkable that crystals with large area electrodes (S2, S3) reach saturation/change the curve slope at voltages about <150 V, while samples with small contact area (configuration S1) reach the same sensitivity of those with large electrode area only at biases as high as 500 V. Overall, the here reported devices show a maximum sensitivity of 175 nC/Gy at 500 V, a value that is four-times higher than the sensitivity values reported in the first experiment with OSSC X-ray direct detectors (section 4.1.1) and than that reported for thin film polymers with metal nanoparticles (see section 2.4). Most importantly, this value is comparable to those reported for inorganic semiconductor Silicon-based dosimeters (e.g. 150 nC/Gy) [95, 142, 143, 144]. In addition, state-of-the-art detectors based on a-Se, that can be considered a benchmark photoconductor material for dosimetry applications, have sensitivity about $0.2 \mu\text{Ccm}^{-2}\text{R}^{-1}$ [145], is not so far from the performance of the here reported 4HCB detectors (about $0.1 \mu\text{Ccm}^{-2}\text{R}^{-1}$, if converted in the same unit of measure). The effective efficiency for the production of charge carriers calculated in par. 4.1.4 results increased in the optimized detector geometry (large area thin crystals of figure 4.12b) from 2% to 20 %. These findings clearly indicate that the electrodes extension area and their separation are crucial parameters to control the collection process of the photo-generated

charge, and that the organic crystal thickness does not have an effect on the device performance and sensitivity down to thicknesses of few tens of micrometers, thus suggesting that the charge carriers drift length is less than 40 μm . Indeed, the charge carrier (exciton) diffusion length is quite short in thin film organic semiconductors ($< 50 \text{ nm}$ [146, 147]), but recent direct measurements in organic single crystals report top values of up to 8 μm [8]. Crystals only a few tens of microns thick thus grant a full photo-generated charge collection (either in the vertical or planar electrode geometry) and this opens the possibility to integrate radiation detectors based on organic crystals into flexible electronic devices, exploiting the enhanced bendability of thin crystals and the recently reported possibility to cover large areas with inkjet printed single crystalline thin films [26, 27]. Moreover, by properly designing the electrode geometry, by proper channel distance and an improved collecting area, the sensor photo-response can be significantly enhanced at lower operating voltages.

4.2 Flexible devices

Recently reported results indicate how thin organic crystals can be reliably used in flexible electronic devices thanks to their bending properties [148, 149, 150] and the above described findings (section 4.1.5) suggest also that 4HCB thin crystals can be excellently used to fabricate flexible X-rays detecting devices. We combined two of the described results (i.e. thin crystals are suitable for detection and large collection area improves their performance) by realizing a flexible X-ray detector by bonding a thin 4HCB crystal on an Au interdigitated electrode pattern (electrode separation $25\mu\text{m}$), onto a flexible and transparent PET substrate, as shown in Figure 4.14a and 4.14b. Hence, the crystal/electrodes interface is maximized, as well as the collecting area of the detector.

The X-ray induced photoresponse (under a monochromatic Synchrotron 17keV beam) of this device is shown in Figure 4.14c, together with the

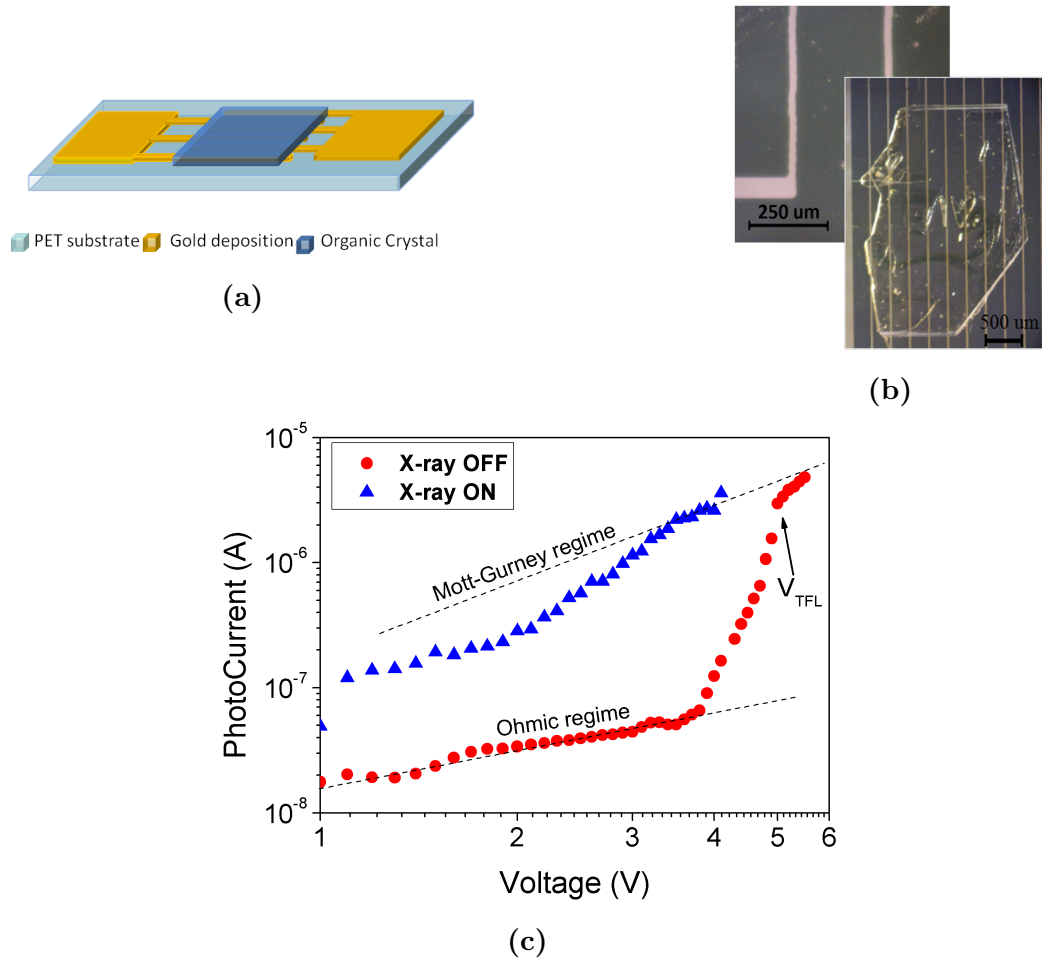


Figure 4.14: a) Schematic layout of the flexible X-ray detector fabricated with interdigitated Au electrodes patterned onto a thin and flexible PET substrate. The electrodes distance is 25 μm (b). The electrical photoresponse of a 4HCB crystal in the dark (red circles) and under a monochromatic X-ray beam (energy 17keV and dose rate 50mGy/s) (blue triangles) is reported in (c) as a function of the remarkably low applied bias voltage.

current-voltage curve measured in the dark. The curve in the dark follows the Space-Charge Limited Current trend typically observed in high resistivity semiconductors and in organic single crystals [109, 151], with the ohmic region, the SCLC regime and the trap-filled limit voltage (V_{TFL}) easily identified, and the notable characteristic of containing all these regimes within 5 V of bias, which is exceptionally low, and to the best of our knowledge yet unreported. The current-voltage curve recorded under X-ray irradiation shows much higher current values (almost one order of magnitude, as usual for this type of devices), that reach the Mott-Gurney quadratic behaviour at bias voltages above V_{TFL} , which again remarkably is below 4 V. A further point of interest is that the photo-current value is of the order of μA , already at 3 V.

4.2.1 Space Charge Transport analyses

Figure 4.14c shows the typical SCLC behaviour for 4HCB single crystals (see par. 3.4.1). However, in this case the short channel length $L = 25 \mu\text{m}$ (one order of magnitude less than the previously reported values [113, 117]) and the charge collection area offered by the interdigitated electrode pattern, enable the activation of the trap-free regime (V_{TFL}) for applied bias voltages as low as 5 V, while it is usually observed at hundreds of volts. As the trap-fill limit is reached both for X-ray beam off and on (figure 4.14c), it is possible to perform SCLC analyses as explained in par. 3.1.1, in order to better understand charge carrier transport processes in organic single crystals. In particular, the effect of X-ray irradiation is to shift V_{TFL} toward lower values, from 5.1 V in the dark (red plot) to 3.2 V under X-rays (blue plot). The mobility results equal in both cases with $\mu = (1.1 \pm 0.1) \times 10^{-2} \text{ cm}^2/\text{Vs}$ and so does the density of states $N_T = 1 \times 10^{13} \text{ cm}^{-3}$, in agreement with previously reported value for planar axis [113, 117], and they are remarkably unaffected by exposure to X-rays.

Moreover, single crystals excel for an intrinsically low trap concentration, and are thus well suited to study traps in a controlled way. Thus, further

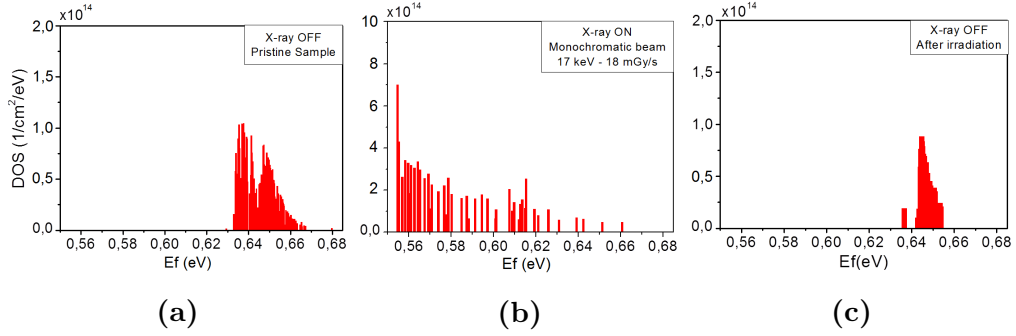


Figure 4.15: Traps Density of States (DOS) of 4HCB single crystal reported in figure 4.14. a) Pristine crystal in the dark. b) Under 17 keV monochromatic X-ray beam. c) After X-ray irradiation, in the dark.

investigation has been carried out through the application to SCLC curves of Nespurek-Sworakowski differential methods in order to estimate the Density Of States (DOS) distribution of the traps states that control the transport process. Figure 4.15a shows the energy distribution calculated from the measurement in the dark (figure 4.15b), for the subsequent measurement under monochromatic 17 keV X-ray beam, and in figure 4.15c another measure in dark, after X-ray irradiation. One has to keep in mind that, by assuming a unipolar majority carrier type conduction, the method of DM-SCLC allows to reveal only the deep states that interact with the majority carrier band. This means that the peak energies in the DOS functions shown in figure 4.15 correspond to the dominant deep states. In the first plot (a) the DOS in pristine crystal presents a monoenergetic deep trap centered at an energy of (0.64 ± 0.01) eV; in the second plot (b) under X-ray irradiation there is a broad exponential trap distribution with an activation energy of (0.06 ± 0.01) eV; in the last plot (c) the peak reappears as in pristine crystal at (0.65 ± 0.01) eV. From the integration of the DOS distribution a more accurate density of traps can be calculated. In fact, the density of traps N_T extracted by means of the V_{TFL} method is often underestimated, due to inhomogeneities in the traps distribution. In table 4.2 the integrated N_T^* values are reported, with a summary of the SCLC analysis calculated parameters.

Sample	V_{TFL} V	μ cm^2/Vs	N_T cm^{-3}	N_T^* cm^{-3}	DOS shape
pristine	5.1 ± 0.1	1.0 ± 0.1	1.6×10^{13}	1.6×10^{13}	peak
irradiated	3.2 ± 0.1	1.1 ± 0.1	1.0×10^{13}	1.4×10^{13}	exponential

Table 4.2: Summary of parameters extracted from SCLC analysis.

The very interesting result is that the crystal mobility μ_{SCLC} and the total density of states N_T are not affected by X-rays irradiation, that indeed has the effect to produce a reversible change of the trapping sites, from a energetically localized peak to a broad exponential distribution, which is recovered to pristine shape once the X-rays are turned off. Further and deeper investigations are needed, but the above results give a first insight into the understanding of X-ray detection mechanism in organic single crystals.

4.2.2 Bendability Properties

The bendability of these detectors has been assessed by repetitively bending the device while monitoring the current, assessing how a bending radius up to 1cm and up to 100 bending cycles do not affect the device electrical response (Figure 4.16). This particular series of tests have been carried out at the Department of Electrical and Electronic Engineering, University of Cagliari. These noteworthy results suggest that flexible detectors can be built and operated at extremely low voltages, possibly even fed with very common button batteries, opening the way to envisaging novel portable and low-power consumption X-ray detectors that can reliably provide output signals with a very good signal-to-noise-ratio, easily fed to an external readout electronic circuit. Regarding flexible OSSCs detectors, it should be pointed out that even the all-organic detector discussed in 4.1.3 is on a PDMS flexible substrate, suggesting the possibility of realize an all-organic interdigitated, flexible, low voltage detector. These features, together with the other reported results (i.e. the proved effectiveness with crystal thicknesses con-

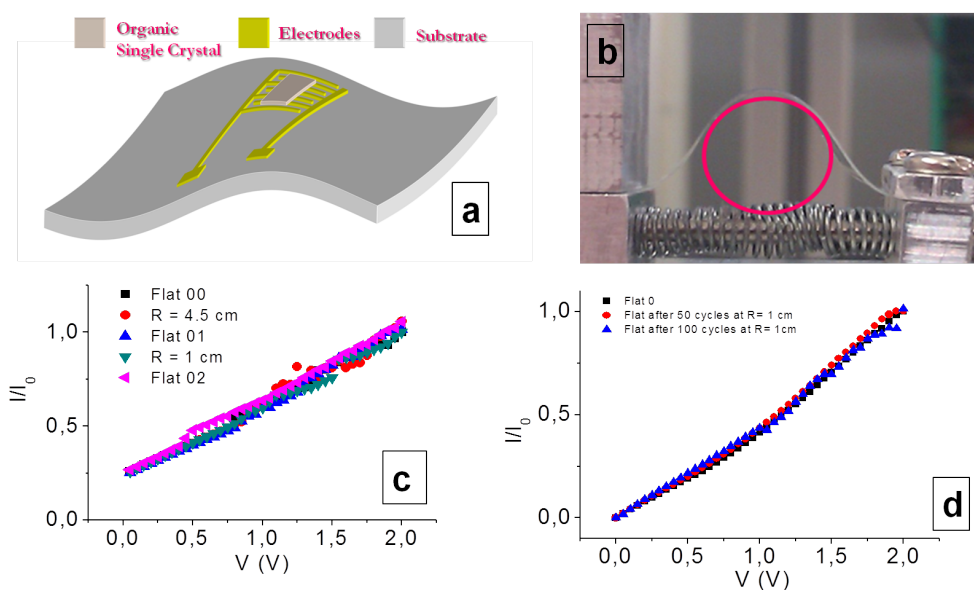


Figure 4.16: a) Sketch of the interdigitated device on flexible PET substrate. b) Optical image of bend radius measurement setup, showing the bendability of the device. c) Normalized Current-Voltage characteristic of flat and bent device and d) after 100 bending cycles.

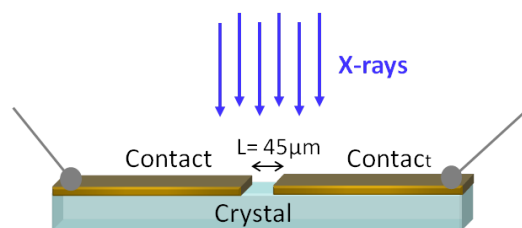


Figure 4.17: Sketch of planar geometry for needle-like crystals.

sistent with flexible devices, the stable and repeatable room temperature response, and the spectroscopic grade operation) suggest that OSSCs allow to envisage breakthrough and disruptive applications, such as a large area, flexible matrices with direct X-ray detecting properties operating at room temperature and with low power requirements, to be used in a vast variety of fields spanning from for medical diagnostic, to civil security and industrial applications.

4.3 Other molecules

Starting from the above reported results and considering the 4HCB device as benchmark single crystal based detector, we carried out a comparative analysis on a novel class of low-cost solution-grown OSSCs, differing by electrical transport properties, optical band-gap, geometry, molecular packing and polarizability, developed for ionizing radiation detection applications [152]. The aim of this section it to investigate how the physical and chemical properties of the crystals affect the X-ray sensing behaviour in order to reach a deeper understanding on the intrinsic photon-charge conversion mechanism, and to give an insight into the identification of the key parameters that control the photoconversion process. Two needle-like shaped polar molecular crystals were studied, 1,5-dinitronaphthalene (DNN, see par. 3.4.4), 1,8-naphthaleneimide (NTI, see par. 3.4.5), where the electronic transport axis, i.e. the highest π -orbitals overlap, is clearly identifiable and easily electrically accessible. In order to investigate how the polarizability of the molecule

affects the response of the detector, we characterized Rubrene (RUB, see par. 3.4.2) and 6,13-Bis(triisopropylsilylethynyl)pentacene (TIPS-pen, see par. 3.4.3) OSSCs-based devices, since they are characterized by high polarizability constants and molecular surface areas. Furthermore, it is noteworthy that the assessment of the performances as detectors of TIPS-pen based device are of great interest in order to evaluate if and how much the Si-atoms contained in their molecular structure influence the photon/charge conversion process.

Even if we have shown in section 4.1.4 that the crystal axes characterized by the strongest π -stacking, that generally coincide with the best current transport axes, show a poorer X-ray photo-response than the vertical one, regardless of the crystal shape (either needle-like or platelet) [153], the planar configuration is in the case of needle-like shaped crystal the easiest electrical accessible. Therefore, in order to obtain comparable data for all the sample tested, the electrical contacts have been realized in a planar configuration (see figure 4.17), depositing the metal on the top face of the sample and with a channel length of 45 μm between the electrodes.

DNN

Figure 4.18 reports the typical current-voltage and current-time curves measured for a DNN crystal exposed to an X-ray beam from a Mo tube. The dark current (figure 4.18a) always lies below 500 pA, a very good value for radiation detection applications. We determined the intrinsic charge carrier mobility of the material by means of Space Charge Limited Current (SCLC) analysis, and the recorded mobility was about $1 \times 10^{-3} \text{ cm}^2/\text{Vs}$ for the DNN crystals [153]. The strong modification induced in the current, measured as a function of the applied voltage when the DNN crystal is exposed to the X-ray beam, due to the photo-induced generation of charge carriers, is visible in figure 4.18b. The I-V measurements were taken at different dose rates, which an “off” current taken after each irradiation run. An evident dark current drift arises after each measurement under X-rays; if the drift is due to bias

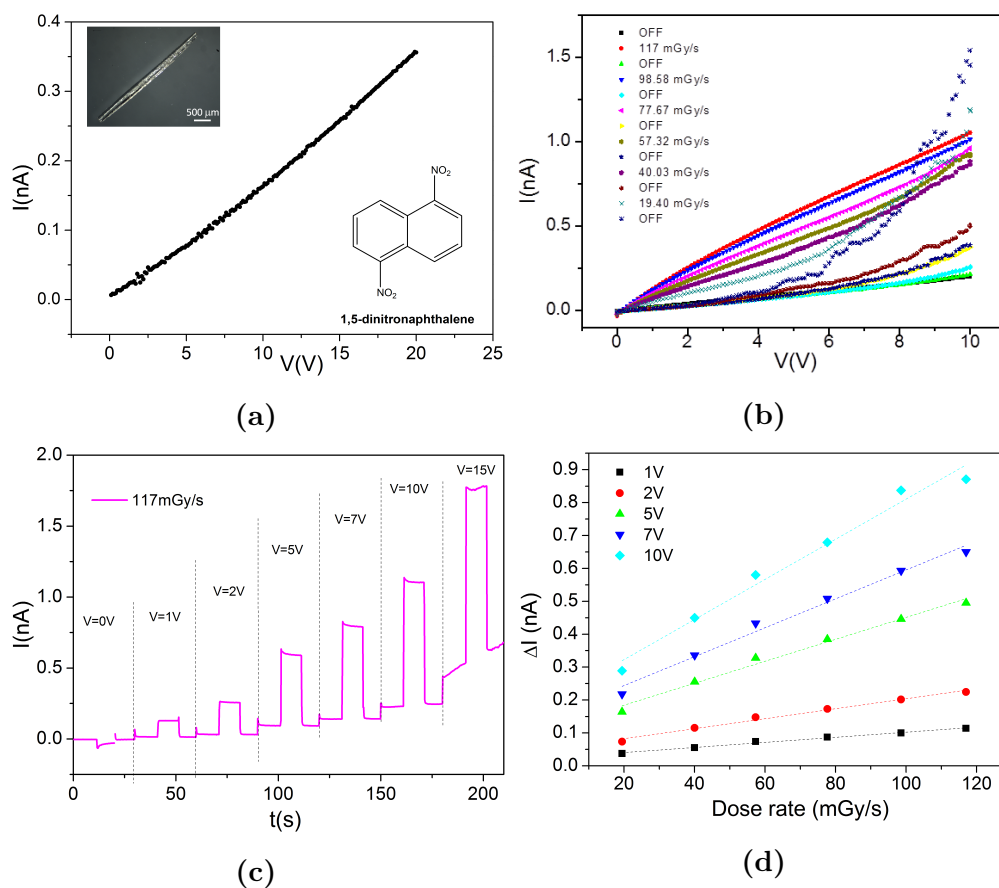


Figure 4.18: Characterization of DNN solution-grown single crystal. Current-voltage measurements performed (a) in the dark and (b) under different X-ray dose rates (labels in chronological order) between 0 and 10 V. c) Current-time curve at voltages of 0, 1, 2, 5, 7, 10, 15 V at dose rate of 117 mGy/s. X-rays are switched on/off every 30 s for each voltage. d) Linearity of ΔI vs. dose rate plot.

stress is still to be assessed but it is surely enhanced by X-ray exposure. Thus the I-V characterization has been limited to 10 V as maximum bias voltage. Figure 4.18c reports the I-t curve as function of the applied voltage when on-off X-ray switching is performed. It is noteworthy that sharp response was obtained even with applied voltages as low as 2 V, very small values for radiation detectors. A further advantageous feature of this device is that the current vs. time curve recorded under an on-off switching X-ray beam (figure 4.18c) clearly shows a fast dynamic response and how repetitive exposures to X-rays do not alter the sensor photo-response in terms of ΔI and of the baseline current shift if the applied bias is lower than 10 V. The induced photocurrent values are reported in figure 4.18d and demonstrate that the crystal response for an increasing X-ray dose rate is linear for each tested bias voltage, assessing that it is possible to effectively drive an OSSC detector even at a few bias volts. The detector sensitivity was evaluated to be about 6.1 nC/Gy at 10 V.

NTI

The same current-voltage and current-time measurements were performed also for NTI single crystals (figure 4.19). It shows as well low dark current (≈ 1 nA even at 100 V), but the space-charge current didn't reach V_{TFL} at even voltages as high as 1000 V, thus only the upper limit of the mobility value can be estimated as $< 10^{-5}$ cm²/Vs. Figures 4.19b and 4.19c exhibit how NTI single crystals are stable both under X-ray irradiation, i.e. dark current in pristine crystal only slightly changes after all X-ray exposures (black and dark yellow in figure 4.19b, respectively), and under bias stress (no dark current drift is shown up to 200 V, figure 4.19c). The X-ray response is fast and repeatable (figure 4.22b). The induced photocurrent increase linearly with the dose rate (figure 4.19d) and sensitivity was evaluated about 5.6 nC/Gy at 10 V and a maximum value of 27 nC/Gy at 100 V.

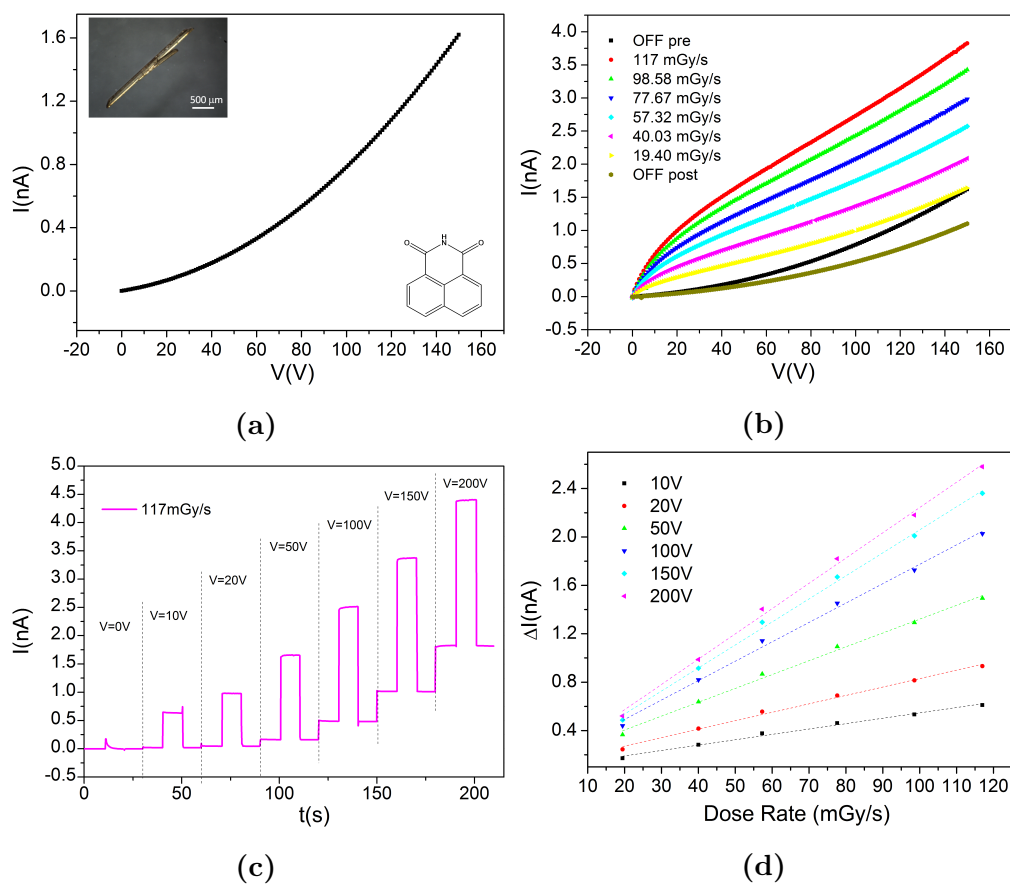


Figure 4.19: Characterization of NTI solution-grown single crystal. Current-voltage measurements performed (a) in the dark and (b) under different X-ray dose rates (labels in chronological order) between 0 and 150 V. c) Current-time curve at voltages of 0, 10, 20, 50, 100, 150, 200 V at dose rate of 117 mGy/s. X-rays are switched on/off every 30 s for each voltage. d) Linearity of ΔI vs. dose rate plot.

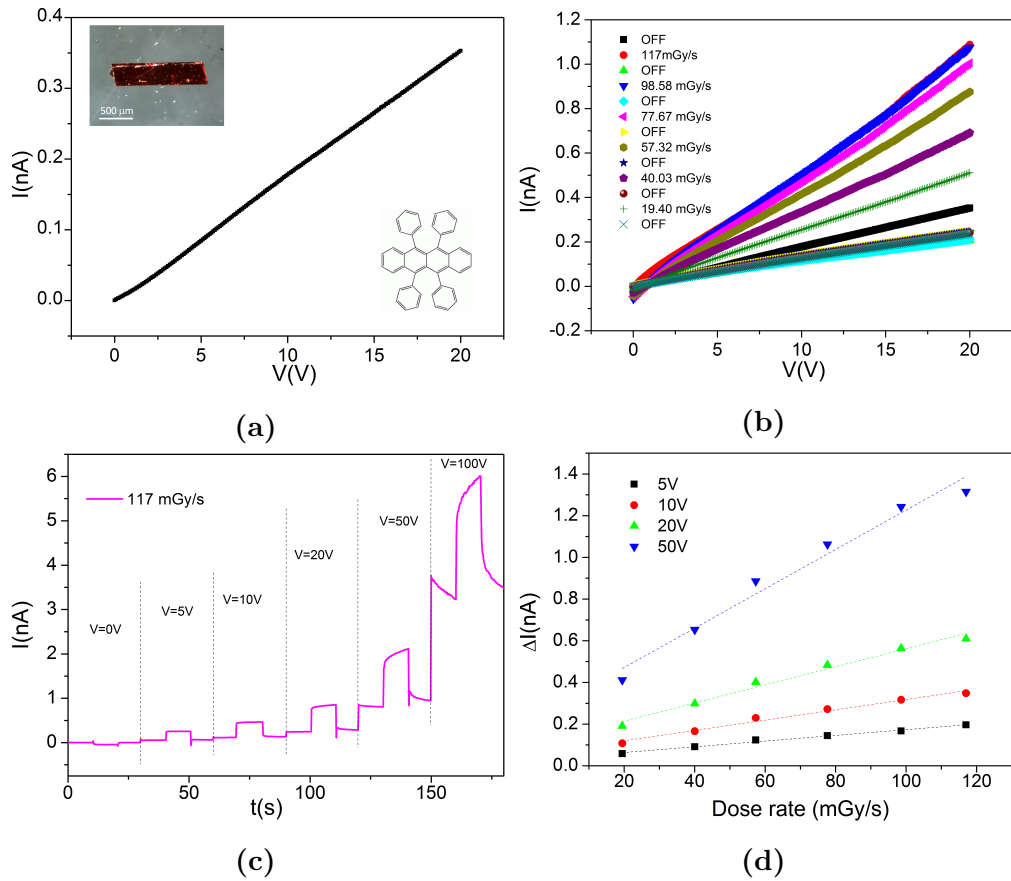


Figure 4.20: Characterization of conventional RUB single crystal. Current-voltage measurements performed (a) in the dark and (b) under different X-ray dose rates (labels in chronological order) between 0 and 20 V. c) Current-time curve at voltages of 0, 5, 10, 20, 50, 100 V at dose rate of 117 mGy/s. X-rays are switched on/off every 30 s for each voltage. d) Linearity of ΔI vs. dose rate plot.

RUB

Rubrene, indeed, has been chosen in order to test the performances as X-ray detector of a high-mobility material, since it is considered the benchmark for high performances OSSCs application. It should be noted that, even if the mobility measured for the rubrene crystals tested in this work ($\mu_{RUB} \approx 1 \text{ cm}^2/\text{Vs}$) is one order of magnitude below the top-performing rubrene crystal reported in literature (up to $20 \text{ cm}^2/\text{Vs}$ for Rubrene single crystal OFETs [52]), it remains several order of magnitude higher than the average mobility recorded for the other crystal under study and then still adapt for our purposes. It is noteworthy that higher performing RUB single crystals present a dark current too high to observe a good X-ray photo-induced signal. Remarkably the dark current is stable under several X-ray irradiation (figure 4.20b), but it suffers of bias stress at high voltages (figure 4.20c). However, the X-ray dynamic response is very slow, especially at high voltages, i.e. the transient do not reach saturation in the time window chosen of 30 s (figures 4.20c and 4.7a). From the linear photocurrent vs. dose rate plot we estimate a maximum sensitivity of 10 nC/Gy and of about 2.5 nC/Gy at 10 V.

TIPS-pen

TIPS-pentacene has been chosen because its molecular composition has silicon atoms inside, heavier element compared to light weight atoms of most of the organic materials. Furthermore, like rubrene, it is known to be a high mobility material in its polycrystalline shape. Solution-grown TIPS-pentacene single crystals has been synthesized in order to be comparable with the other studied single crystals. Preliminary, but very interesting, results are shown in figure 4.21. Current-time measurements have been performed at a constant voltage of 10 V at different dose rates in order to evaluate the X-ray photocurrent linearity. The calculated sensitivity is 3.63 nC/Gy . Noteworthy, TIPS-pen X-ray response dynamic is really slow, current takes tenths of seconds to saturates when irradiated, and the discharge dynamic, i.e. the time taken to recover pristine dark current once the X-rays are

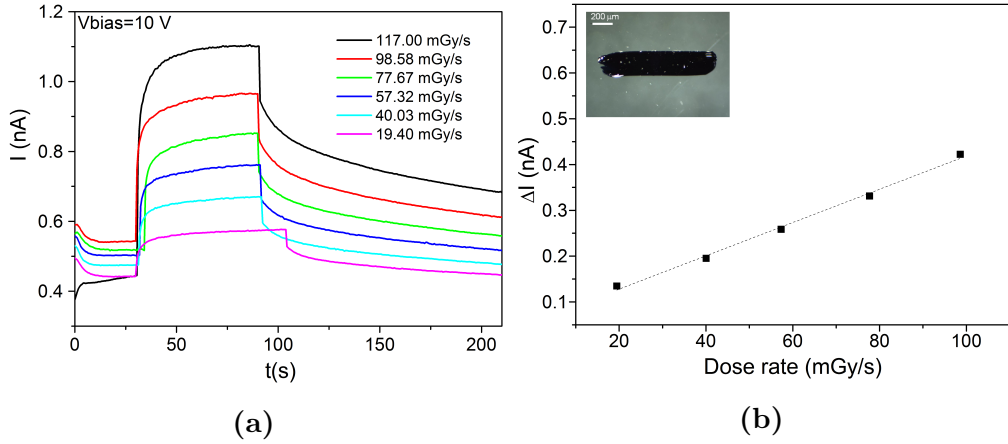


Figure 4.21: Characterization of TIPS-pen solution-grown single crystal. a) Current-time measurement performed at 10 V for different dose rates. X-rays are switched on for 60 s and then switched off. d) Corresponding linear ΔI vs. dose rate plot.

switched off, is even slower as the discharge is not completed after 100 s showed in the plots of figure 4.21a.

Comparison

Among the screened crystals the mobility values measured span of several orders of magnitude, from about less than 10^{-5} cm^2/Vs of NTI up to 1 cm^2/Vs of Rubrene. Some common properties could be observed, for example, for almost all the samples screened and the dose rates and bias voltages employed, we observed a linear gradient of the photocurrent signal $\Delta I = I_{ON} - I_{OFF}$ with the dose rate. The X-ray response ΔI , the signal to noise ratio ($\text{SNR} = \Delta I / I_{OFF}$) and the sensitivity recorded at a bias voltage of 10V for all the devices tested are reported in table 4.23 together with their typical charge carrier mobility values. Very interestingly, the sensitivity and, in general, the detector performances of the devices, seem not to be correlated to the charge carrier mobility of the material. Referring to table 4.23, for example, we recorded a mobility for the DNN device of about 1×10^{-3} cm^2/Vs , with sensitivity (about 6 nC/Gy at 10 V bias) comparable to that

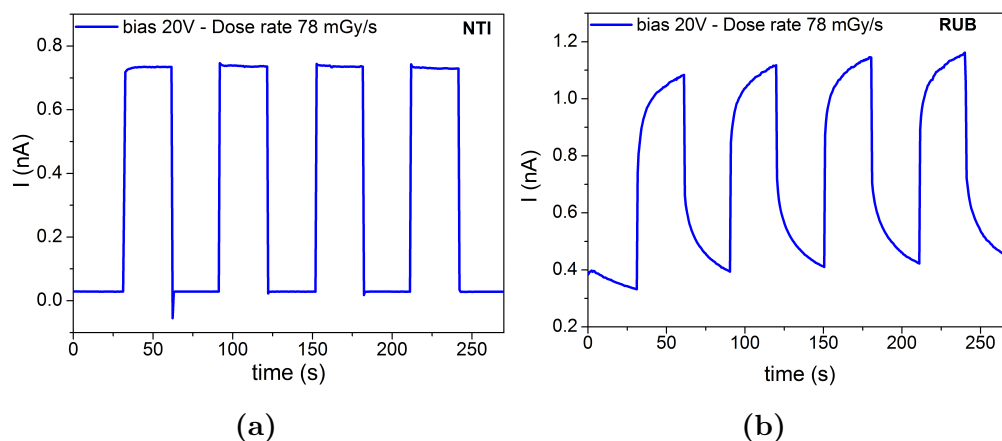


Figure 4.22: Comparison between current-time measurements of NTI (fast response time) and RUB (slow response time) over 4 repeated X-ray switched on/off every 30 s. Reported for an applied bias of 20 V and dose rate of 78 nC/Gy.

	Molecular polarizability (\AA^3)	μ (cm^2/Vs)	I_{off} (A) @ 10V	S (nC/Gy) @ 10V	SNR @ 10V	ΔI (A) @ 10V (dose rate 120 mGy/s)
4HCB	12.76	0.02 (a/b axis)	6.0×10^{-11}	7 (a/b axis)	15 (a/b axis)	1.10×10^{-9} (a/b axis)
NTI	21.63	$< 10^{-5}$	2.0×10^{-11}	4.4	34	6.9×10^{-10}
DNN	21.58	1×10^{-3}	2.0×10^{-10}	6.1	4	8.7×10^{-10}
Rub	78.13	1	1.5×10^{-10}	2.5	3	3.0×10^{-10}
TIPS-pen	85.9	TBD	3.0×10^{-10}	3.5	1.5	6.6×10^{-10}
Reference						1.4×10^{-10}

Figure 4.23: Comparison of the main X-ray detection features of investigated single crystals. Reference is the output of system (substrate + electrodes) without organic crystals.

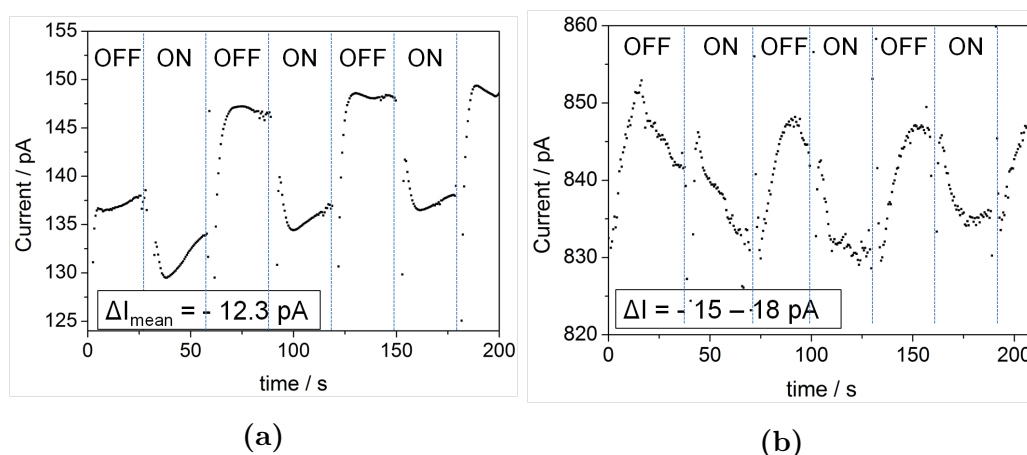


Figure 4.24: On/off switching electrical output of 4HCB single crystal at 50 V applied voltage, under Cs^{137} radiation source. a) vertical and b) planar axes, respectively.

of 4HCB, while RUB-based detectors showed poor performances, with sensitivity of 2.5 at 10 V, but much higher mobility values (up to $1 \text{ cm}^2/\text{Vs}$). On the other hand, we can also say that the low mobility doesn't assure good detectors performances. Neither the presence of silicon atoms in the molecule have a dramatic effect on X-ray response, since TIPS-pen has a sensitivity value higher than RUB but still lower than 4HCB and DNN single crystals. Furthermore, RUB and TIPS-pen are both high polarizable molecules, and both present slow X-ray response, thus suggesting a correlation between this feature and the dynamic of X-ray sensing mechanism. The investigation of X-ray sensing over organic molecule is still ongoing, nevertheless the study of customized molecules with different properties in form of single crystals (to reduce growth fluctuation) seems to be the right way.

4.4 High Energy Detection

So far OSSCs direct X-ray detectors were characterized under 35 kV Mo tube and monochromatic synchrotron radiation, in a photon energy limited between 10 keV and 35 keV, a range suitable for medical purposes, like

mammography. In order to expand the assessment for practical applications, in particular in the interesting field of security control, as airport luggage security, the sensing of higher energy photon should be verified. We use a γ source of Cs^{137} which has the primary emission at 661 keV 3.3.3. The challenge arises from the high penetration depth of such high energy photons (up to several cm in lead), thus reducing their absorption by the organic crystals. However, we have assessed, how for low X-ray energies discussed until now, that even a small fraction of absorbed photon can be collected and generates a good electrical output signal in organic crystals devices. Figure 4.24 shows the current signal output in function of time for 4HCB single crystal with epoxy silver paint electrodes biased at 50 V, under the γ radiation source placed at a distance of 7 mm from the sample, corresponding to a dose rate of 5.8 mSv/h. The gamma source is added and removed from top of the spacer every 30 s. Regarding the vertical axis (figure 4.24a) the radiation source has the effect to induce a decrease of the current equal to 12 pA, and then, after few seconds, a slow increase just before recover to the initial current when the source is removed. Analogue observations can be made about planar axis (figure 4.24b), the induced current is about - 15 ÷ - 18 pA, even if in this case the effects are even slower. In addition, here the dark current is too high and the signal is affected by the superposition of noise and current drift. Reference measurements have been carried out, in order to exclude spurious effects due to charges extracted from substrate or from the electrodes. First the top electrode has been physically disconnected and exactly the same measurement has been performed. Then the same procedure has been repeated with only the substrate in place of the sample. In both cases no marked effects have been observed, only noisy fluctuation < 1 pA in amplitude and big spikes corresponding to the induction of the source when it is move in and out.

To summarize, we carried out very preliminary results on the detection of high energy photons from Cs^{137} by 4HCB single crystals. The interaction process is still unknown, considering that the induced current has a slow dy-

namic and negative values, thus it exhibits the opposite behaviour to what we have discussed until now for low energy X-rays, but the results are promising for the use of organic crystals as γ radiation detectors.

Chapter 5

OTFTs as X-ray Sensors

The fifth chapter is dedicated to the investigation of direct X-rays detection of organic semiconductor thin film structures widely used in flexible organic electronics. TIPS-pentacene is a soluble derivative of pentacene (see par. 3.4.3) and is one of the most common small molecule used as active semiconducting layer in high-performance solution-processed Organic Thin Film Transistors (OTFTs), thanks to its ability to form crystalline domains upon the solvent evaporation [27, 154]. Recently, TIPS-pentacene has been introduced in a blend with a polymer in sandwich-type organic direct detectors based on spin-coated PTAA thick films in order to improve the transport properties of the polymer and to enhance the X-ray sensitivity through a better charge collection (see par. 2.4, [99]). Moreover, in the previous chapter, the direct detection of pure TIPS-pentacene has been proved in its single crystal shape (see par. 4.3).

In this chapter the characterization of TIPS-pentacene thin films as direct photoconductor X-ray sensor will be reported. TIPS-pentacene solution in toluene was drop-casted onto flexible and transparent polyethylene terephthalate (PET) substrate, patterned with interdigitated electrodes. The so-obtained structure was characterized both under the irradiation of a Mo tube (see par. 5.1.1) and under high energy radiation source (see par. 5.1.2), assessing how TIPS-pentacene thin films are able to detect X-ray radiation

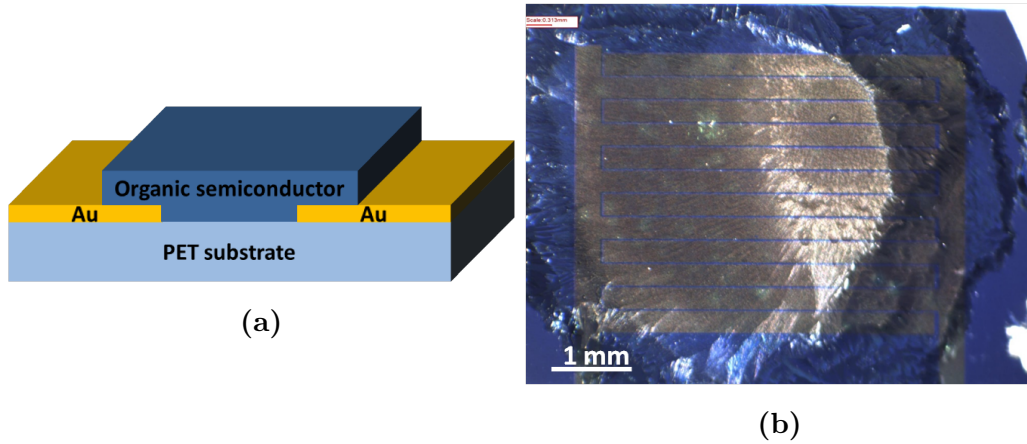


Figure 5.1: a) Sketch and b) optical microscope image of the photoresistor thin film planar structure.

at extremely low working voltages and with outstanding sensitivities. Moreover, the X-ray response of high performing Organic TFTs based on TIPS-pentacene, deposited as described above, operating at extremely low voltages (< 1 V) [155], was observed in function of the working regime of the transistor (see par. 5.2). This study has been carried out in collaboration with the group of Prof. A. Bonfiglio at the University of Cagliari, Italy.

5.1 Thin film planar structure

Ultrapure TIPS-pentacene in toluene solution was deposited, by drop-cast method, on interdigitated gold electrodes deposited by thermal vacuum evaporation, and then patterned by means of photolithography, onto a flexible and transparent PET substrate. A high concentrated solution (5%wt.) of TIPS-pentacene, that produces thick films once deposited, and a lower concentrated solution (0.5%wt.) that originates thinner samples, have been prepared. The interdigitated active area is 20 mm^2 , with electrodes $25 \mu\text{m}$ spaced. The thin film configuration, about 100 nm thick, could strongly limit the X-ray absorption, due to the small interaction volume compared to that of single crystals, several tenths of micrometers thick. However in

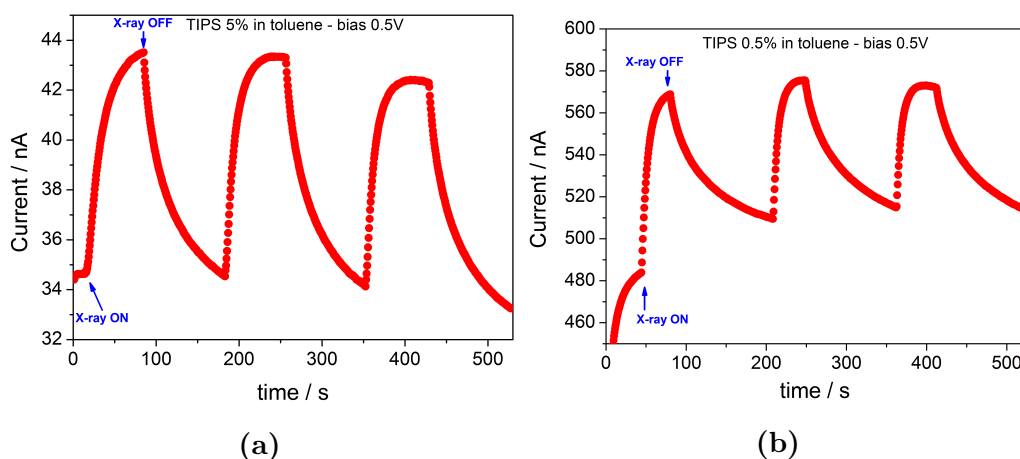


Figure 5.2: X-ray induced photocurrent of TIPS-pentacene thin films biased at 0.5V when the beam is switched ON and switched OFF. a) 5%wt. and b) 0.5%wt. The dose rate is fixed at 117 mGy/s.

the previous chapter it has been showed that even crystals as thin as $40 \mu\text{m}$ can effectively detect X-rays and that the interdigitated structure strongly enhances the charge collection efficiency. A schematic view of the thin film planar device and an image under optical microscope of the full device are shown in figure 5.1.

5.1.1 X-ray Direct Detectors

The devices sketched of figure 5.1 have been tested as direct X-ray detectors under a Mo X-ray tube, operating at 35 kV of acceleration voltage and up to 35 mA of filament current (see par. 3.3.1 for the description of apparatus). The measurements have been carried out at room temperature and in the dark, in order to exclude the high photosensitivity of TIPS-pentacene to visible light, that induces strong current drift. Figures 5.2a and 5.2b show the current-time measurements, probed under switching ON and OFF X-ray beam, of 5%wt. and 0.5%wt. TIPS-pentacene films, respectively. The dose rate is fixed at 117 mGy/s. The applied bias, equal to 0.5 V, is extraordinary low for this kind of detectors that usually require tenths or hundreds of volts;

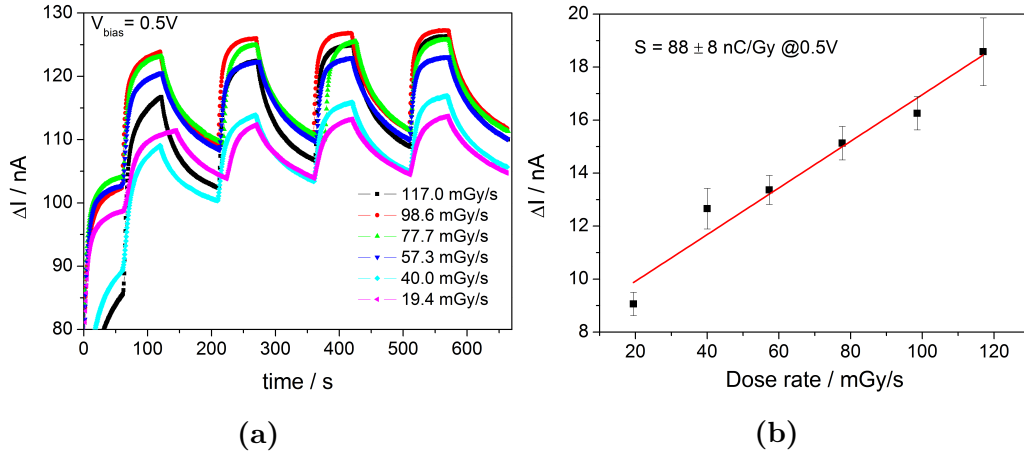


Figure 5.3: a) Current vs. time measurement of 0.5%wt. TIPS-pentacene biased at 0.5 V under different dose rates. b) ΔI vs. dose rate plot and the calculated sensitivity from the linear fit (red line).

it is in our knowledge the first X-ray organic detector working at such low voltages (see par.2.4, table 2.3). The signal is slow, it takes more than 40 s to reach saturation when X-ray beam is switched ON, and the relaxation transient, i.e. when X-rays are switched OFF, is even slower. Thus the absolute photocurrent value $\Delta I = I_{ON} - I_{OFF}$ has been extracted from the values I_{ON} and I_{OFF} after 40 s from the switching ON or OFF, respectively, and averaged upon three repetitions. It is very high, $\approx 9 \text{ nA}$ for 5%wt. sample and $\approx 70 \text{ nA}$ for 0.5%wt. sample, comparable or higher than the best reported organic film direct detectors, but with one order of magnitude less of biasing voltage. The current induced variation has been investigated at different dose rates, from 117 mGy/s down to 20 mGy/s, and the corresponding plots are reported in figure 5.3a for the 0.5%wt sample at 0.5 V. The induced current ΔI scales roughly linearly with the dose rate, as shown in figure 5.3b. The experimental data points are scattered respect to the ideal linearity, probably due to the errors in the extraction of ΔI values, strongly dependent on the chosen time window and on the dynamic of the response. The sensitivity results of $88 \pm 8 \text{ nC/Gy}$. If we consider the full active area (of 20 mm^2) and a film thickness of 100 nm, the sensitivity per unit volume results of 44

$\mu\text{C}/\text{mGy cm}^3$, two orders of magnitude larger than the reported values of organic film direct detectors in sandwich-type geometry (see table 2.3).

The extraordinary high sensitivity and the high current signal at such low voltages make the TIPS-pentacene thin films on interdigitated pattern extremely interesting for ionizing radiation detection; however, several drawbacks have to be taken into account in order to realize an high performing detector. The response time is really long, more than 40 s are necessary to reach saturation of the signal when the X-rays are switched ON and the detector does not fully discharge when the X-rays are turned OFF. The response could be faster working at higher bias, but in this case the dark current would also increase. In fact, the dark current is already very high (in the order tenths of nA), with the consequence of an evident current drift, clearly visible in the baseline shift of figure 5.2, and of the instability of the dark current shown in figure 5.3a (i.e the I_{dark} at 0.5 V is different at each run). In addition, it strongly limits the signal-to-noise ratio despite the high absolute photocurrent signal.

It is noteworthy that the 0.5%wt. film (the thinnest one) has a better electrical transport (e.g. higher dark current) than the one at 5%wt. concentration (as already observed in TIPS-pentacene dropcast [16]), but it has also the highest X-ray ΔI response. Therefore a better charge collection (strongly dependent on a good charge transport) has a bigger contribution than the interaction volume in the X-rays detection performance.

In conclusion, this preliminary assessment on the X-ray detection performances of TIPS-pentacene thin films stated that they are very promising for the realization of a flexible, transparent and low cost organic direct detector. Furthermore, the solution processability of TIPS-pentacene thin films can be technologically exploited for the realization of ink-jet printed organic detectors over large area and on any kind of substrate.

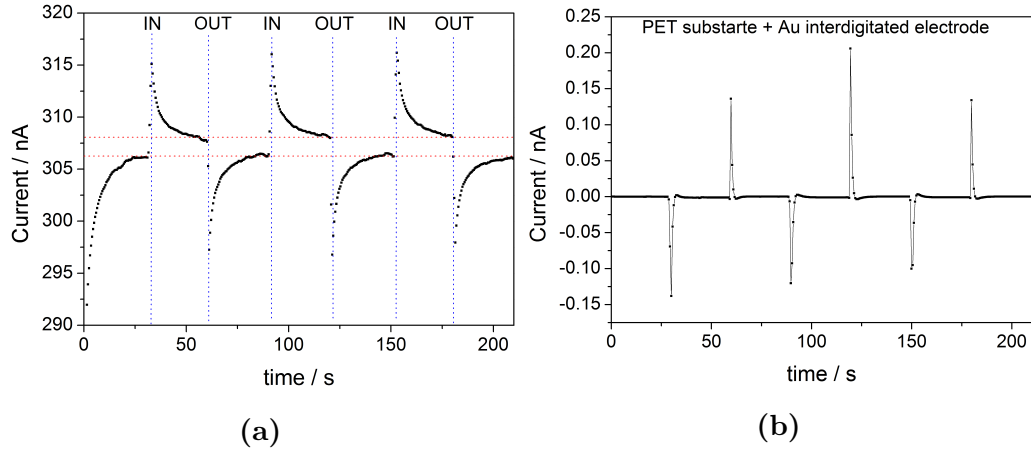


Figure 5.4: a) Current vs. time plot of 0.5%wt TIPS-pentacene biased at 0.5 V. A Cs^{137} source has been placed and removed on top of the sample every 30 s. b) Same measurements performed on a bare PET substrate and interdigitated gold electrodes, as reference.

5.1.2 High Energy Detection

TIPS-pentacene films have been investigated also under a γ source of Cs^{137} which has the primary emission at 661 keV, as have been already reported for 4HCB single crystals (see par.4.4). The experimental setup is described in par. 3.3.3. Figure 5.4a shows the current signal output in function of time for the 0.5%wt. film biased at 0.5 V, under the γ radiation source placed at a distance of 7 mm from the sample, corresponding to a dose rate of 5.8 mSv/h. The gamma source is added and removed from top of the spacer every 30 s (IN and OUT in the picture, respectively). First, upon the positioning of the source, a large spike is induced in the device, then the sample slowly relax, until another spike in the opposite direction appears when the source is removed. Furthermore, after the device relaxation, a gap can be seen between the two transient baselines (dotted red lines in figure 5.4a). Thus the gamma Cs^{137} source has two macroscopic effects: i) causes large spikes (greater than 10 nA), and ii) induces a persistent photocurrent equal to 1.8 ± 0.4 nA, in average. Moreover, similar measurements on bare PET

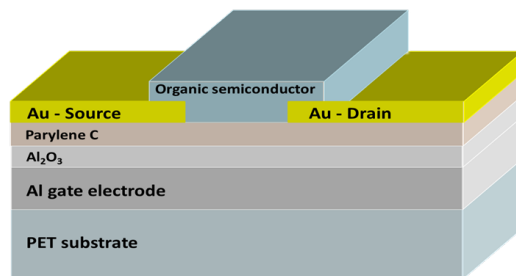


Figure 5.5: Sketch of the OTFT structure as described in [155].

substrate with interdigitated gold electrodes, without any organic materials have been carried out, in order to evaluate the substrate and electrodes contributions (figure 5.4b). Small spikes can be seen when the source is moved IN or OUT, due to the electronic noise of the source movement, but the absolute value is really small (≈ 100 pA) and no other persistent effect has been observed.

5.2 OTFT structure

In the previous section the photoconductive effects of TIPS-pentacene under X-ray irradiation have been shown. Despite the good sensing properties, the devices are affected by a high dark current and baseline drift. In order to figure out the role of dark current and to control the charge carrier flowing into the semiconductor, an OTFT bottom-gate/bottom-contacts structure has been employed. The OTFTs have been fabricated on flexible PET films. The aluminium gate was deposited by thermal evaporation and patterned using a shadow mask. The dielectric is a combination of 6 nm of Al₂O₃ (by means of UV-ozone oxidation of bottom aluminium layer) and a layer of 35 nm of parylene C (by chemical vapour deposition). Thermally evaporated gold source and drain contacts were realized on top of parylene layer with a photolithographic process using an interdigitated mask, as in the previous section. We performed the characterization of TIPS-pentacene deposited by drop-casting of the 0.5%wt. concentrated solution in toluene. Figure 5.5

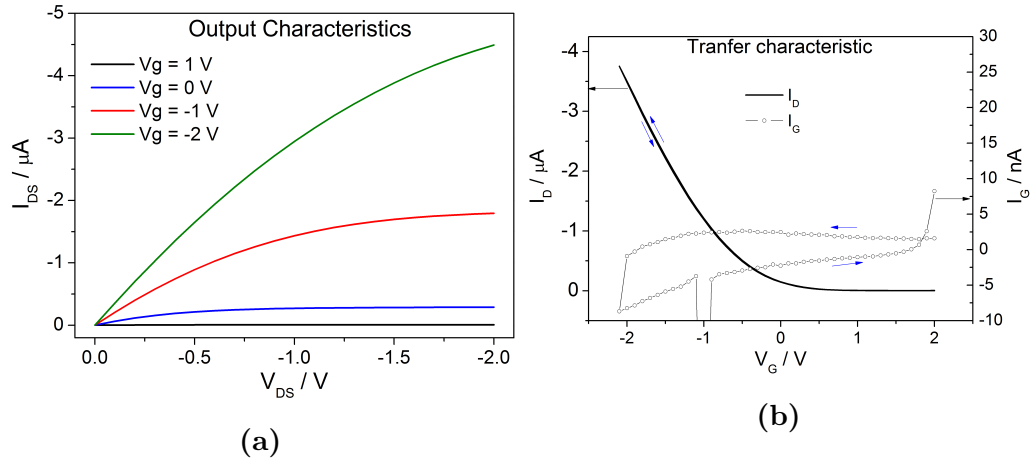


Figure 5.6: a) Output characteristics of low-voltage dropcasted TIPS-pentacene organic TFT. b) Corresponding transfer characteristic at $V_D = -2$ V. The low leakage current I_G is also plotted on the right scale.

shows a sketch of the full device. The OTFTs fabricated, provided by group of A. Bonfiglio at University of Cagliari, are ultra-low voltage devices (can be operated at < 1 V), free of hysteresis effects and showing a very low leakage current density ($\approx 2 \times 10^9$) with TIPS-pentacene as active semiconducting material [155]. In figure 5.6 the fundamental transistor characterization, performed before the experiments under X-rays, is reported. The output and the transfer characteristics (figures 5.6a and 5.6b, respectively) are in line with the average performances for these devices. The low dark current (< 5 nA) is also shown in figure 5.6b (right axis).

A characterization, similar to that performed for resistor structure, has been carried out under irradiation of X-ray Mo tube. The dynamic photocurrent plot at different dose rates is shown in figure 5.7a for $V_G = -1$ V and $V_D = -0.5$ V (linear regime for the p-type transistor). The measurements were performed from the lowest dose rate (19 mGy/s, magenta line) to the highest one (117 mGy/s, black line). The X-ray response in the OTFT linear regime is similar to what have been observed for the planar resistor structure described in the previous section (see par. 5.1.1 and figure 5.3a). In particular, the response is in the order of tenths of seconds and the ΔI is huge (≈ 40 nA)

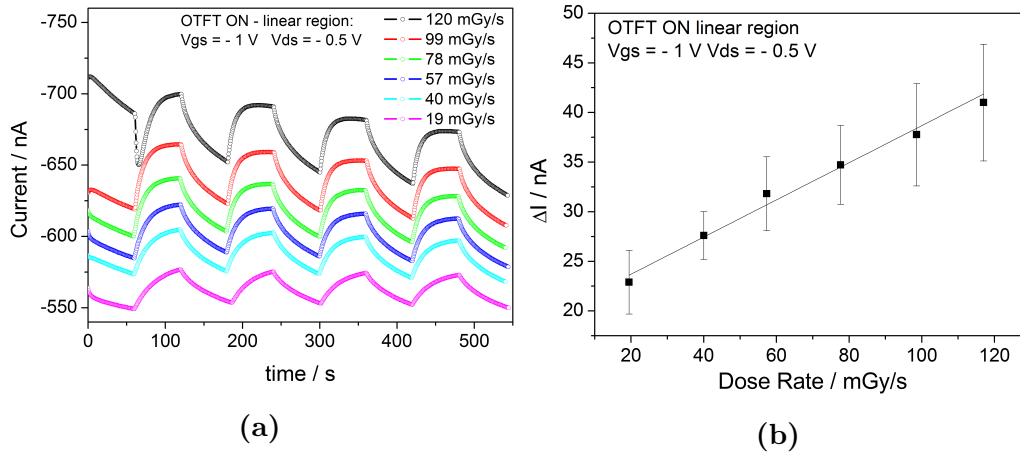


Figure 5.7: a) Dynamic current vs. time measurement of the TFT biased at $V_G = -1$ V and $V_D = -0.5$ V (linear regime). b) Corresponding ΔI vs. dose rate plot. The data are the average value over four switching ON and OFF.

at maximum dose. However, the signal is affected by large dark current ($\approx 600 - 700$ nA) that causes low signal-to-noise ratio and an evident baseline instability, i.e. the drift toward higher current of the baseline after each run. Nonetheless, the signal repeatability is really good, over subsequent switching ON and OFF of the X-rays (figure 5.7a). The calculated sensitivity is 187 nC/Gy (linear fit in figure 5.7b).

Taking further advantage of the TFT configuration, the X-ray response under different operating regimes of the transistor have been investigated (figure 5.8). Figure 5.8a shows the saturation regime (i.e. working in the zone where the output curve saturated) and the linear regime (i.e. working in the zone where the output plot is linear with V_D). Both transport regime exhibited strong X-ray photocurrent responses and they are pretty similar, even if the saturation dark current is higher and presents higher baseline drift. Thus, it is convenient working in the linear regime, at lower bias and lower dark current without affecting too much the generated photocurrent. Remarkably, when the transistor is OFF (i.e. the accumulation of charge in the active channel is interdicted through a positive gate voltage) no X-ray signal has been recorded (figure 5.8b). The small current variation observed

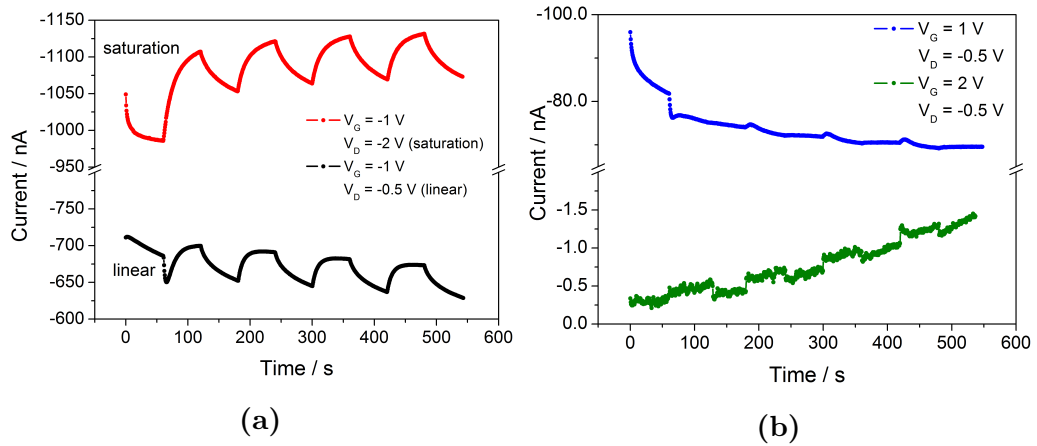


Figure 5.8: Dynamic current vs. time measurement of the TFT at dose rate of 117 mGy/s in different regimes. a) Transistor turned ON: saturation ($V_G = -1$ V, $V_D = -2$ V, red line) and linear ($V_G = -1$ V, $V_D = -0.5$ V, red line) regime. b) Transistor turned OFF with charge carriers transport interdicted.

concerns only the electrodes contribution. In this case the dark current is very low due to the low charge carrier density in the channel, but a source-drain bias of $V_D = -0.5$ V is still present between the two electrode to collect the X-ray photogenerated carriers. The lack of an X-ray signal in this latter case suggests two hypothesis: i) the X-ray generated charges are not collected by the electrodes; ii) the photocurrent signal in the saturation and linear regimes, as well as in the resistor configuration, has a different nature. In both cases the processes involved in the X-ray detection in TIPS-pentacene photoconductors and thin film transistors are still unknown, but the OTFT structure offers great advantages for a deeper investigation of this behaviour.

Chapter 6

OSSCs as Alpha particle Sensors

Alpha particles consist of 2 protons and 2 neutrons bonded by the nuclear strong force, chemically a (fully ionized) helium atom (He^{++}). They are massive monoenergetic particles (range $4 \div 6$ MeV) and they are usually emitted by alpha decay of heavy nuclei. Alpha particles have strong interaction with matter and therefore a high ionizing power and low penetration depth, up to few centimeters in air (figure 6.1) and few micrometers in matter. Charged particle detectors have wide application in any field that involve nuclear radioactive materials, from nuclear physics and medical monitoring to national security purposes. Semiconductors are widely used for charged particle detectors. So far all such devices have been made of inorganic materials, primarily using silicon but also with wide bandgap materials such as diamond or CZT. Since the great results obtained employing organic materials in X-ray sensing application, their further exploitation in charge particles detection application is extremely interesting. In this chapter I will discuss the state of art of organic alpha detection (6.1) and the first experimental evidence for charge particle detection employing 4HCB OSSCs, obtained by means of pulse-height analysis and of the transient response of pulses generated from alpha particles at room temperature (6.3). This work has been

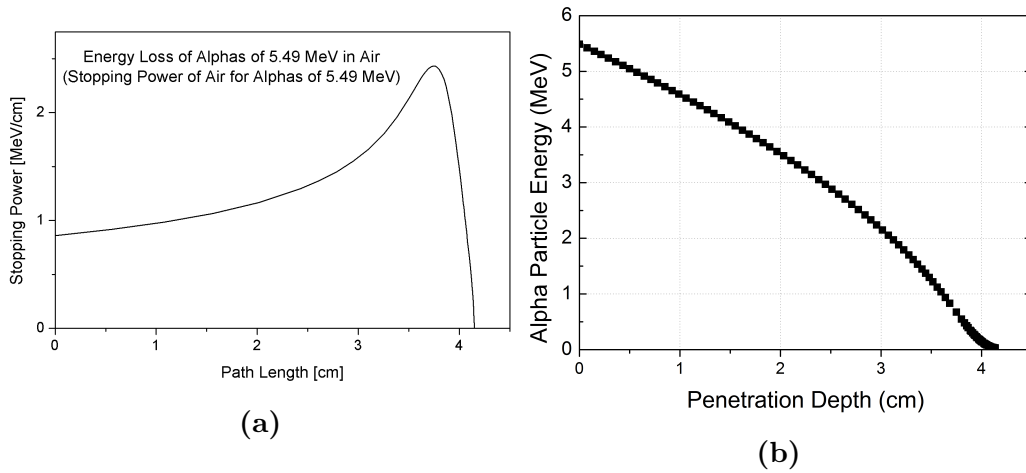


Figure 6.1: Energy loss (a) and residual energy (b) in air of an alpha particle with initial energy of 5.49 MeV (from SRIM calculation) [156].

carried out during my stay at the University of Surrey (UK), in the group of Prof. P. Sellin.

6.1 Overview on Organic alpha particle detectors

The possibility to detect charge particles with organic materials (polymers) has been demonstrated by Beckerle and Strobele [157]. They used a standard polyacetylene synthesized in foils of thicknesses of 10, 50 and 100 μm , mounted on a rigid frame. The charges, created by the α -particles of 5.4 MeV from ^{242}Am source, were separated and transported to the electrodes by the electric field which resulted from the very high voltage (1 - 5 kV) applied to two coplanar gold contacts. The foil dimensions were 1 cm x 1 cm; the particle beam was collimated down to 3 mm and its position was known to a precision of better than 1 mm. The experiment demonstrated that charge transport was effective over the full distance between the electrodes (about 1 cm) at a drift velocity of about 40 cm/s, but that only those charges which were set free in the 6-7 μm nearest the contact surface of the

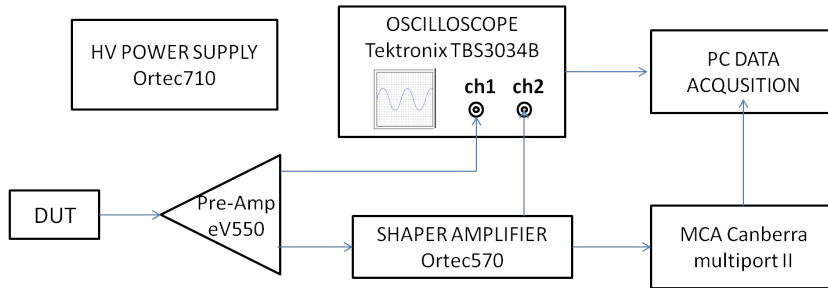


Figure 6.2: Schematic diagram of the analog pulse height analysis arrangement.

foil were collected. All other charges were probably trapped when trying to move perpendicular to the surface of the foils. This trapping process has the implication of strongly limiting the charge collection efficiency. By stretching the foil, the drift velocity in the direction of the stretching is shown to increase, indicating a strong anisotropy of the charge transport. During all experiments the device was kept under dry argon atmosphere because polyacetylene was destroyed with time when exposed to traces of oxygen and water.

6.2 Experimental Setup

The alpha particle detector used in this work was fabricated by a 150 μm thick 4HCB single crystals. Electrical contacts were fabricated both in a planar structure, with pads 400 μm away from each other, and in a sandwich configuration with 100 nm thick gold electrodes on both the top surface and the substrate surface of the crystal, forming a metal-semiconductor-metal (MSM) device structure. The pulse height spectrum of alpha particles produced by the 4HCB devices was acquired using the setup schematically illustrated in figure 6.2. Alpha particle irradiation was performed in air at room temperature using a ^{241}Am source, with the alpha particles impinging on the top surface. In sandwich configuration the bias voltage was supplied to the electrode on the top surface, with the electrode on the substrate surface connected to ground. Measurements were made with both positive and

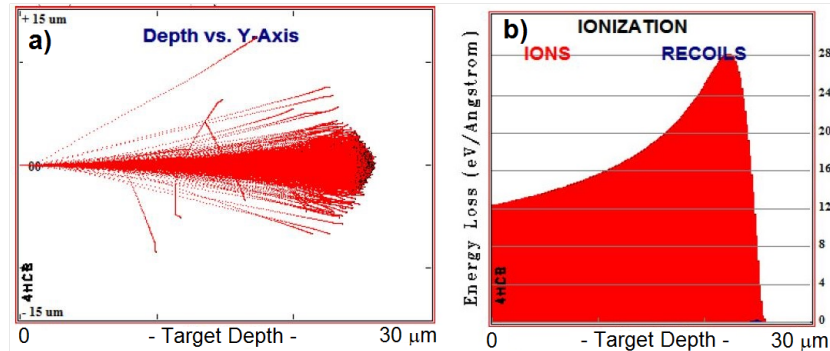


Figure 6.3: TRIM simulation of 4.48 MeV (residual energy after 1 mm of air) alpha particles into the 4HCB crystal: a) trajectories struggling and b) energy loss through the material.

negative bias, in the range 100-800 V, if this doesn't make any differences in planar configuration, it corresponds to irradiation of the anode and cathode, respectively, in sandwich-type samples. The uncollimated 5.49 MeV ^{241}Am source, with an activity of 185 kBq, was positioned inside a chamber at a distance between approximately 5 mm and 17 mm from the device, so that the mean energy loss of the alpha particles in air was evaluated from the calculation-derived plot reported in figure 6.1b. In figure 6.3 the simulation of 4.48 MeV (energy after 1 mm of air) alpha particle trajectories and energy loss in 4HCB crystal are shown. The mean particle range is approximately 25 μm . The contact on the top surface of the device was connected to a charge sensitive preamplifier (eV model 550), with a rise time of approximately 160 ns, through which the bias voltage was applied. The preamplifier output was connected to an analog multi-channel analyzer (MCA CANBERRA model multiport II) via a spectroscopy shaper amplifier (ORTEC model 570, max shaping time of 10 μs) which simultaneously acquired pulse height spectra. The preamplifier and shaper amplifier outputs were connected to a four channel digital oscilloscope (Tektronix TBS3034B, 300 MHz bandwidth), triggered on each pulse, to monitoring the signal and the noise. The acquisition time was set to 1000 sec live (i.e. excluding the MCA dead time that in this measurements can be as high as 20%). After a

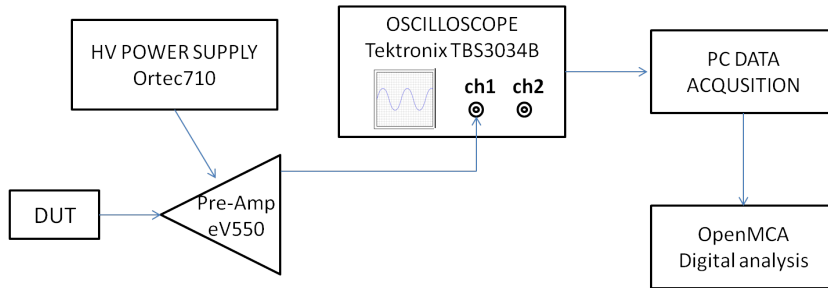


Figure 6.4: Schematic diagram of the digital pulse height analysis arrangement.

proper calibration, MCA channels were associated to energy values. In another configuration the preamp output was directly connected to the digital oscilloscope and the pulses were captured on an event-by-event basis and the waveforms were digital stored in a file (figure 6.4). The acquired data file was analysed offline on a pulse-by-pulse basic using Labview software. The analysis used a digital CR-RC shaper (time constant of $50 \mu\text{s}$) to histogram the pulse amplitude and also the preamplifier 20-80% pulse rise time. An example of the same digital shaping already used in detectors pulse height analysis can be found in [158].

6.3 Results and Discussion

Figure 6.5 shows ^{241}Am alpha pulse height analog spectra for 4HCB OSCs devices, in planar and sandwich configuration respectively, acquired for 1000 s, with an analog MCA and shaping time of $10 \mu\text{s}$, for various applied positive voltages after the background subtraction. The first 150 channels of the spectra are cut in order to exclude large background counts that cause the instrument saturation; nevertheless the MCA acquisition dead time is still about as high as 10%. The figures don't show any characteristic alpha peak but only large broad distributions in which the counts increase as the voltage increases. Figure 6.6a reports the comparison between the spectrum at $V = 300 \text{ V}$ in figure 6.5a and one obtained in the same conditions but with a paper foil interposed between the alpha source and the detector. The

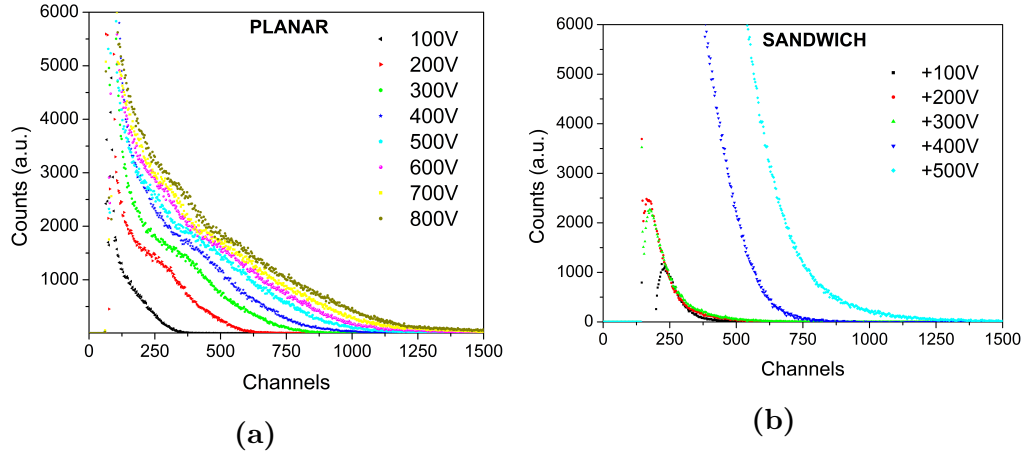


Figure 6.5: Pulse height spectra collected with analog MCA acquisition for a) planar configuration ($L = 400 \mu\text{m}$) and source-sample distance $D_{s-\alpha} = 6 \text{ mm}$. b) vertical sandwich configuration ($L = 150 \mu\text{m}$) and $D_{s-\alpha} = 10 \text{ mm}$.

paper is thick enough ($\approx 100 \mu\text{m}$) to stop all the alpha particles. The plot obtained from the shielded sample is completely flat, hence the broad distribution in the black plot (obtained from the unshielded measurement) is effectively due to alpha particles. Figure 6.6b shows the dependency of the spectrum on shaping time. This, together with large dead time and broad spectrum, suggests an incorrect shaping of the signal that causes high charge loss. Indeed, in this configuration the measurements are affected by the very slow transients typical of organic materials. The typical pulse in 4HCB single crystal is reported in figure 6.7a, as acquired from preamp output; it shows that the transient time is in the order of $100 \mu\text{s}$, much longer than ns , typical of inorganic semiconductor detectors. In such a system the shaping time is limited by the shaper amplifier, thus a different setup based on digital post-processing analysis, that allows arbitrary longer shaping time, has been used. Digital post-process analysis allows to test different shaping settings on the same series of data. After some tests and parameters optimization, we chose an CR-RC shaper with slow time of $50 \mu\text{s}$, fast time of $5 \mu\text{s}$, and a multi-channel digital analyser at 512 channels. An appropriate shaping time reduces the charge loss during the shaping of the signal, and, there-

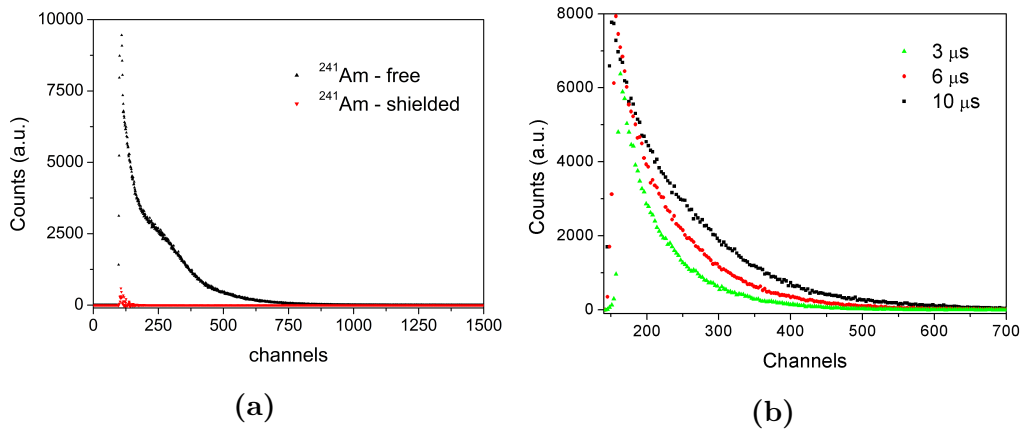


Figure 6.6: a) Spectrum differences between free (black) and shielded (red) alpha radiation source. b) Shaping time dependence of the spectrum. Applied bias $V = + 300 \text{ V}$ in both plots.

fore, by employing digital analysis the detector shows a broad well-resolved full-energy peak (figure 6.7b). Also in the comparison between the spectrum under alpha irradiation and the background spectrum the differences are better resolved. In figures 6.8a and 6.8b the digital pulse height spectra are reported as function of applied bias voltages for planar and sandwich structure respectively. The detectors show full-energy peaks over the full range of bias voltages. The position of the peak centroid increases to higher channels with increasing bias voltage, i.e. due to better charge collection efficiency. Actually, after a proper energy calibration employing the acquisition of pulses of known values, the channel scale has been converted in energy scale. For the calibration an electron-hole pair creation energy estimated as $W = 10 \text{ eV}$ has been used. This procedure allows to perform the calculation of Charge Collection Efficiency (CCE), defined as in eq. 6.1:

$$CCE(\%) = \frac{\text{Collected Charges}}{\text{Total generated charges}} = \frac{\text{Peak Energy}}{\text{Incident Energy}} \quad (6.1)$$

Figures 6.9a and 6.9b show the behaviour of calculated charge collection efficiency. In planar configuration CCE initially increases approximately linearly and then saturates at high voltages ($V > + 600 \text{ V}$; electric field of 15

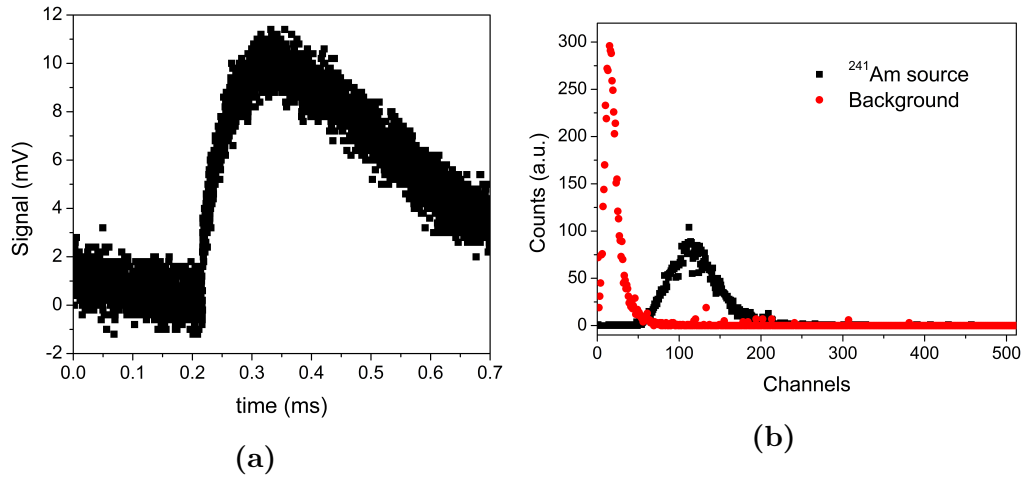


Figure 6.7: a) Typical ^{241}Am pulse in 4HCB single crystal at $V = 500$ V. b) Digital processed pulse height spectrum of ^{241}Am peak (black) compared to the background noise (red) for $V = 300$ V and $50 \mu\text{s}$ of shaping time.

kV/cm). In the sandwich configuration, on the other hand, CCE increases linearly over the full tested voltage range 100 - 500 V (electric field up to 33 kV/cm). Overall, the maximum observed CCEs for organic crystals reach 55 % in planar and 50 % in sandwich configuration, much better than the previous reported value for polymers (< 10 %) [157]. It should be stressed that so far all the spectra have been reported for positive applied biases: this doesn't make any difference in planar geometry because the contacts are ohmic and the alpha particles are stopped close to the crystal surface, thus both electrons and holes are collected at the same time by the two electrode. However, in sandwich configuration the positive bias voltage is referred to the top electrode, i.e. only holes are drifted from top to bottom electrode. Figure 6.10a shows the CCE for the same measurement performed on sandwich configuration for negative voltages (i.e. with cathode irradiation). In this case the signal is due to electrons drifted and collected in the bottom electrode. As in the case of positive bias, CCE is linear over the full range of biases with comparable values (34 % for negative and 38 % for positive at 400 V).

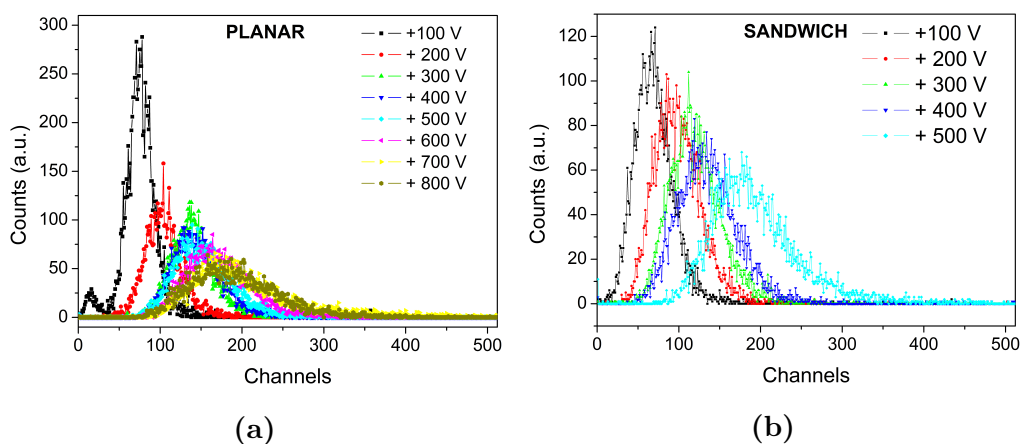


Figure 6.8: Pulse height spectra obtained with digital analysis for a) planar and b) sandwich configurations.

Taking further advantage of the low penetration depth of alpha particle in materials, we can perform time-of-flight analysis. In fact, the charges are all generating in the first 25 μm from the top surface of 4HCB single crystal and therefore under positive bias the holes are drifted and collected toward bottom electrode in a finite amount of time. Histogram of the rise-time of the pulses shows a gaussian distribution peaked around 50 μs [159]. Figure 6.10b reports the corresponding holes drift velocity in function of the electric field. The drift velocity value, up to 280 cm/s, is much higher than what have been reported for polymers with the same techniques (40 cm/s) [157], this underlines the better charge transport in organic single crystals. Remarkably, the holes mobility value, extracted from the linear fit of the velocity vs. electric field plot, is equal to $(5.6 \pm 0.9) \times 10^{-4} \text{ cm}^2/\text{Vs}$, in very good agreement with values reported in literature for best performing 4HCB crystal along c-axis [113].

In this chapter preliminary assessments of the detection capability of alpha particle by means of organic single crystals have been reported, as well as the possibility opened in terms of new tools for organic materials investigation (such as mobility, drift velocity or $\mu\tau$ measurements). However, further investigations are needed in order to perform a direct measurement of the

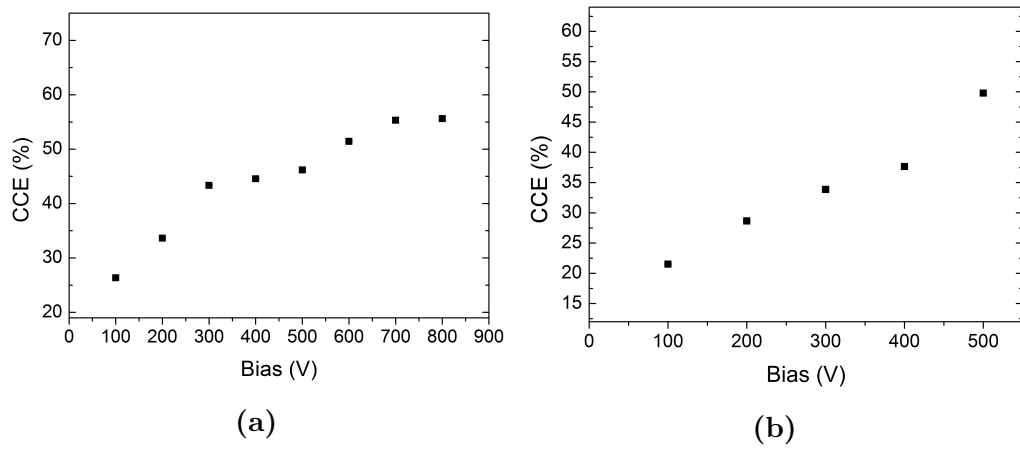


Figure 6.9: Charge Collection Efficiency (CCE) vs. applied voltage plot for a) planar and b) sandwich configurations (anode irradiation).

electron-hole pairs creation energy and a better estimation of CCE. Moreover, to verify the reliability of the exploitation of organic semiconductors for particle detection, the long-term stability and radiation damage of the envisaged material under alpha irradiation should be studied.

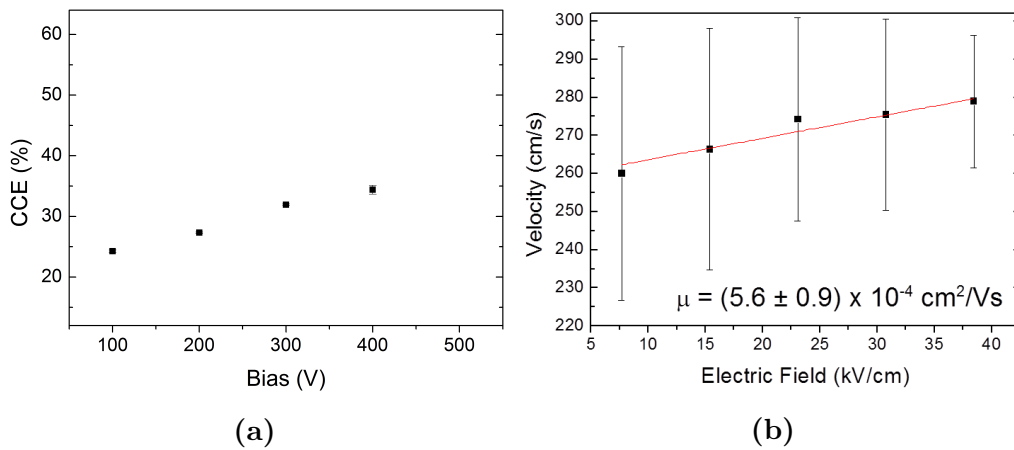


Figure 6.10: a) CCE vs. applied voltage plot for sandwich-type configuration and negative voltage between - 100 V and - 400 V. b) Drift velocity vs. Electric field plot for holes.

Chapter 7

OSSCs as Chemical Sensors

One of the bottlenecks of organic electronics is its extreme reactivity of organic materials to humidity, oxygen and other reagents in the atmosphere, that strongly affect and deteriorate the electrical performances of devices, which often require an encapsulation. However, their reactivity could be exploited for the realization of organic-based chemical sensor. One of the most common transducing mechanisms for organic materials-based sensors is the chemiresistive one, which relies on the variation of the sensing material resistivity when this is exposed to an analyte [160]. Practical advantages of organic-based chemiresistors (OCRs) include operability at room temperature, ease of fabrication (either by wet or vacuum processing), potential for low-cost production and high throughput manufacturing. However, these devices suffer from problems of long response times, pronounced drifts, limited reversibility. Usually in most common OCSs based devices the resistivity increases upon the analyte adsorption, e.g. in OCSs based on composites constituted by carbon black-based phase, dispersed in a host matrix made up by insulating or semiconducting polymers or molecules [160, 161]. This approach allows to reach low detection limits (down to a few ppms of analyte) [162], but the response reproducibility is limited by the difficulty of controlling the film morphology and characteristics. A class of OCRs, based on conjugated polymers are already on the market [163], even if, they suffer

from pronounced sensitivity to humidity, low reproducibility, response drift and short device lifetimes, linked to excessive analyte diffusion into the polymer layer. Moreover, OCRs based on thin films of semiconducting molecules have been made, that thanks to their nanostructured nature reach hence a very good sensitivity, down to a few tens of ppbs [164].

The modulation of the resistivity in Organic Semiconducting Single Crystals (OSSCs) by means of electronic functionalization of the surface with self-assembled monolayers, has been recently assessed [165]. Up to date no report on the use of organic semiconducting single crystals (OSSCs) as sensing materials in OCRs has been published, despite their significant potential interest. In fact, OSSCs possess a well definite bulk structure and controlled and reproducible electronic characteristics, which could be translated into reliable sensing responses. Moreover, the ordered packing of organic single crystals offers a clear potential for an effective limitation of the diffusion of analyte molecules into the compact crystalline lattice, which could result in negligible degradation and/or hysteresis and lower current drifts. From a more fundamental point of view, the study of OSSCs as sensing materials, thanks to their structural order, could add important information on the sensing mechanisms of organic semiconductors.

In this chapter will be presented the study over 4HCB single crystals (see par. 3.4.1) These devices have been tested as chemiresistors under the effect of saturated vapours of ethanol, isopropanol and heptane, in two different experimental setups. In both cases, when exposed to the alcohols, the devices show a marked current increase, of one order of magnitude or more. Notably, the response times are in the range of one second or lower and the overall recovery times found for these devices are very short, lower than 30-40 seconds, with absent (or negligible) drift currents and hysteresis effects, and no need for forced analyte desorption. When exposed to vapours of heptane, which is an apolar molecule, the devices show no appreciable response. On the basis of these evidences, hypotheses over the alcohols detection mechanism are presented.

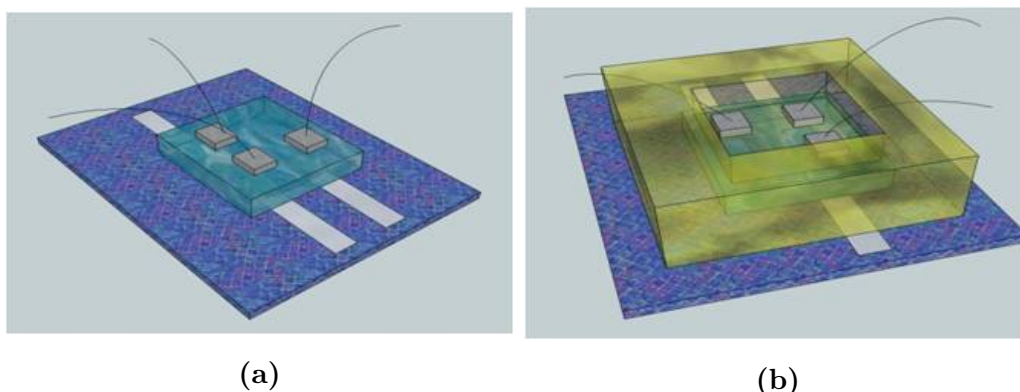


Figure 7.1: Sketch of the two experimental configurations: a) free crystals (setup A), b) sealed crystals (setup B).

7.1 Experimental Setup

4HCB single crystals have been contacted with an electrodes configuration able to probe possible three-dimensional anisotropic response of the crystals to the analytes, and with different measurement setups, aimed to investigate different aspects of the detection phenomenon. In the first used setup A, as depicted in figure 7.1a, electrodes 1, 2 and 3 probed the axes a and b of the planar surface, and the corresponding bottom electrodes probed the axis c (crystal thickness). In the setup B (figure 7.1b), the single crystals contacted as in A, were embedded in epoxy resin on the sides. Saturated vapours of the analyte (ethanol, isopropanol and heptane) were blown towards the contacted crystals using a Pasteur pipette. This method allowed to, simply and reliable, deliver to the crystal surface saturated vapours of the selected analyte, minimizing possible interfering effects from other atmosphere components, like water, nitrogen or CO_2 . A good reproducibility of the response has been assessed over tens of devices (prepared using crystals grown from different batches, with different geometrical parameters, in different experimental sessions and with different applied biases). Besides the positive outcomes, this method had the drawback of not allowing to quantitatively determine the amount of analyte blown onto the device surface. The

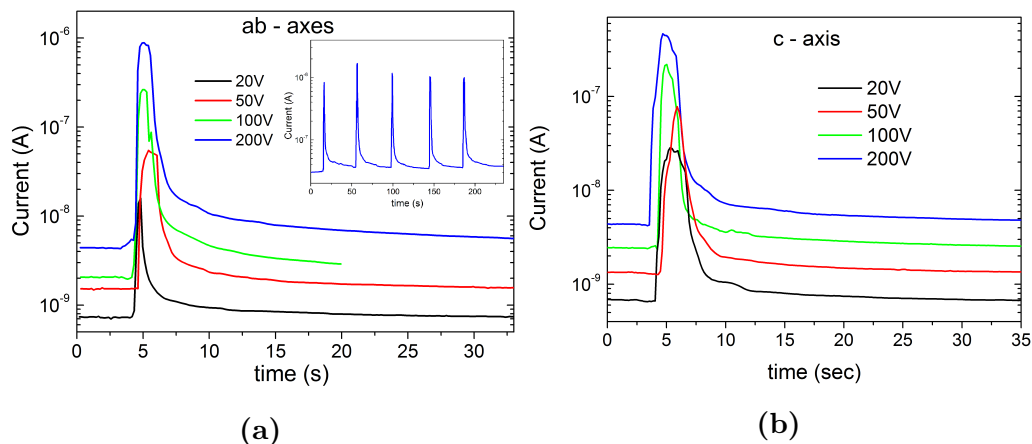


Figure 7.2: Response of 4HCB crystals exposed to ethanol vapours, at different biases, a) along the planar axes and b) along the vertical axis for electrode distance of $500\ \mu\text{m}$. Inset: response of the planar axes to repeated exposures of ethanol.

devices were tested with different bias voltages (between 20 V and 200 V) applied between couples of electrodes selected in order to probe the response of the desired axis of the crystal.

7.2 Chemiresistor effects

Upon exposure to ethanol vapours, 4HCB crystals contacted as in setup A presented a marked current increase (almost two orders of magnitude) along any crystal axis (figure 7.2). This behaviour occurs at all the tested biases, and is opposite to the one observed for most of the currently studied OCRs, where the presence of the analyte causes a decrease of the measured current (i.e. a resistance increase) [160, 161, 162, 163, 164]. Despite the difference in the crystal mobilities along the axes a and b (which are about $10^{-1} - 10^{-2}\ \text{cm}^2/\text{Vs}$) and that along c (which is about $10^{-5}\ \text{cm}^2/\text{Vs}$), we were not able to detect significant and systematic anisotropy in the detected responses. The starting currents were found to be in the range of $10^{-10} - 10^{-8}\ \text{A}$ for each different couple of electrodes probed, and the corresponding current increase upon exposure to the analyte was in the range of one-two orders of

magnitude, independently from the considered crystal axis. Therefore, we will refer from now on, unless differently stated, only to isotropic detection. A typical sample measured in the planar configuration with a 50 V bias, with a contact distance of about 500 μm exhibited a base current of 1×10^{-9} A and a current response of 1×10^{-7} A. Considering the device response to ethanol under an applicative point of view, very interesting features are found:

- the response time (i.e. the time to rise from the baseline up to the maximum peak upon analyte exposure), ranging always below 1 second, are much faster than those of the currently considered OCRs, which are in the best cases in the range of several tens of seconds [160, 161, 162, 163, 164];
- the recovery time (i.e. the decay time back to the baseline value after the exposure) are shorter than 40-50 sec, shorter than those usually found for other non-nanostructured OCRs, that are in the best cases in the range of minutes [160, 161, 162, 163, 164]. This feature is well reproducible over repeated analyte exposures and in several different devices, and the visible changes in the intensities of repeated blows are likely due to non-constant amounts of vapour delivered on the device;
- current drift after recovery is negligible;
- the baseline recovery is achieved without the need for any forced analyte desorption.

All these features suggest a good potential for practical applications of these crystals in alcohol sensing (as for example in portable ethylometers), provided that a more quantitative assessment of the detection performances is conducted. It is also interesting to observe that the above mentioned features are verified at each of the tested biases, clearly pointing to a negligible, if any, penetration of the analyte within the crystal. Only for voltages higher than 100 V a very small current drift was observed, which could be attributed to charge accumulation phenomena, rather common for 4HCB at such high

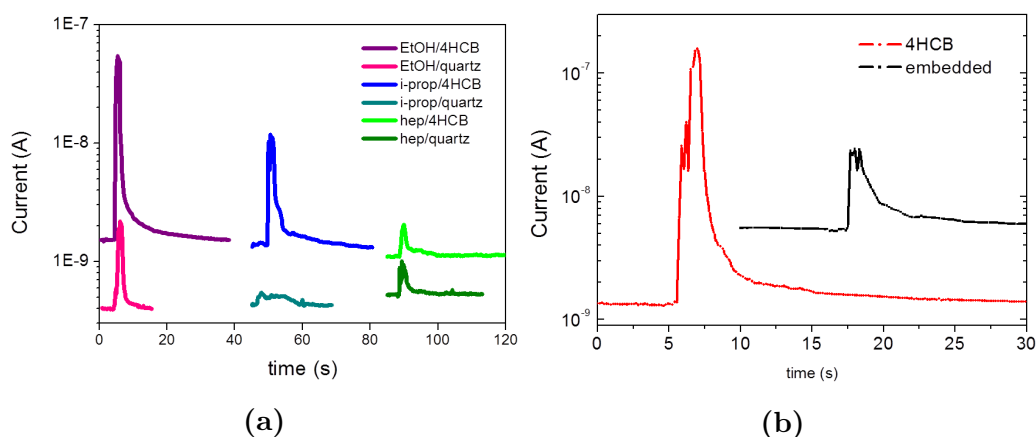


Figure 7.3: a) Response to ethanol (EtOH), isopropanol (i-prop) and heptane of 4HCB and a control glass slide, using the experimental setup A. The measurements are referred to the planar axes of the crystal. b) Comparison of the response to EtOH between setup A (free 4HCB) and setup B (sealed crystal) along *c*-axis. All graphs are reported at 50 V.

fields. The applied voltage does not seem to influence the current response in terms of $\Delta I/I$. As a general observation, the mentioned performances have been obtained in the regime of analyte quasi-saturation. In these conditions the high concentration of the alcohols, which are also solvents for 4HCB, could in principle result in local dissolution of the external crystal layers. However, this possibility was excluded by the enhanced repeatability of the response upon frequent, subsequent measurements on the same sample (figure 7.2a, inset), highlighting an intrinsic robustness of the devices.

7.3 Intrinsic effects

To evaluate the possible influence of a surface thin film layer formed by analyte molecules simply adsorbed on the crystal surface in terms of direct conduction of charges between the electrodes, the response to ethanol of a bare, electrically contacted glass slide, with identical geometries and in the same experimental conditions (setup A) used for the previous tests was

measured. As is visible in figure 7.3a this control device showed a current response almost two orders of magnitude lower than that of the 4HCB crystal (compare the pink curve - glass slide - vs. the violet curve - 4HCB). Using a different alcohol, isopropanol, the overall results in terms of crystal response were of the same magnitude and a similar result was obtained exposing the quartz slide to isopropanol (dark cyan curve - glass - vs. blue curve - 4HCB). In detail, the $\Delta I = I_{ON} - I_{OFF}$ (with ON = current when exposed to the analyte, and OFF = base current) for 4HCB was about 5×10^{-8} A for ethanol and 3×10^{-8} A for i-propanol, while for the glass slide these values were found to be 2×10^{-9} A and 1×10^{-10} A, respectively. Therefore, in each case the current that can be ascribed to the adsorbed analyte layer accounted for no more than 5% of the total signal found when 4HCB was the detecting element, assessing in this way the efficacy of 4HCB crystals as alcohol sensors, and testifying that the conductive layer formed by analyte molecules on the crystal/quartz surface contributed negligibly to the observed current increase upon analyte exposure.

In another test, the apolar n-heptane molecule was blown over 4HCB devices. This resulted in very low currents, similar to that of a glass-based control device exposed to the same vapours (figure 7.3a, olive curve - glass - vs. green curve - 4HCB). This suggests that the polarity of the analyte has an important effect on the detection capabilities of the device. The substantial equivalence of the response of the control quartz slides exposed to vapours of ethanol, i-propanol and heptane indicates that these low-level signals are due to thin layers of analyte adsorbed on the device surface. Although the contribution to conduction of these surface-adsorbed analyte layers is clearly minor with respect to the overall response of the 4HCB-based devices, it was interesting to investigate the role of this conduction pathway with respect to the crystal response along the c axis (crystal thickness).

Therefore, it was realized an experimental design aimed at preventing the analyte to be adsorbed on the lateral crystal facets (i.e. the crystal thickness), by means of embedding the 4HCB crystal in an epoxy resin (gas-impermeable

to alcohols and olefins) (Setup B, figure 7.1b). The measurements carried out along the vertical axis with setup B exhibited a systematic lower response to ethanol with respect to the analogous devices realized with setup A, while at the same time conserving very similar recovery times (see figure 7.3b). This suggests that the molecules that get physically adsorbed on the sides of the crystals when the device is operated in the setup A, contributed partly to the overall response, but not in a substantial way. Most interestingly, the above described results highlight that the presence of a surface-adsorbed analyte conductive pathway on the sides of the crystal is not the primary cause of the current increase upon analyte detection along the crystal thickness. This means that the detection mechanism involves phenomena occurring in the crystal bulk, rather than on its surface, and this represents a truly puzzling finding, especially considering that the average crystal tested had thicknesses ranging from 350 to 700 μm , hence tunnelling effects of any kind are definitely ruled out as possible sources of current increase upon analyte detection. The effect of the alcohol polar molecules on the crystal surface is easily explained considering the documented surface conductivity increase determined by SAMs applied to organic semiconductors [166, 165]. However, these reports refer only to experiments in which the conductivity of the semiconductor surface is enhanced, while in our case the current increase phenomenon is measured through several hundreds of microns of crystal thickness. Therefore, it is necessary to hypothesize that some electronic effect due to the presence of the polar analyte operates throughout the bulk of the crystal, decreasing its bulk resistivity.

7.4 Modeling

The results relative to the poor response caused by the exposure to heptane suggested also a fundamental question: what is the role of polar molecules in inducing the observed current increase? To answer that, we analysed in more depth the detection mechanism. In particular, observing

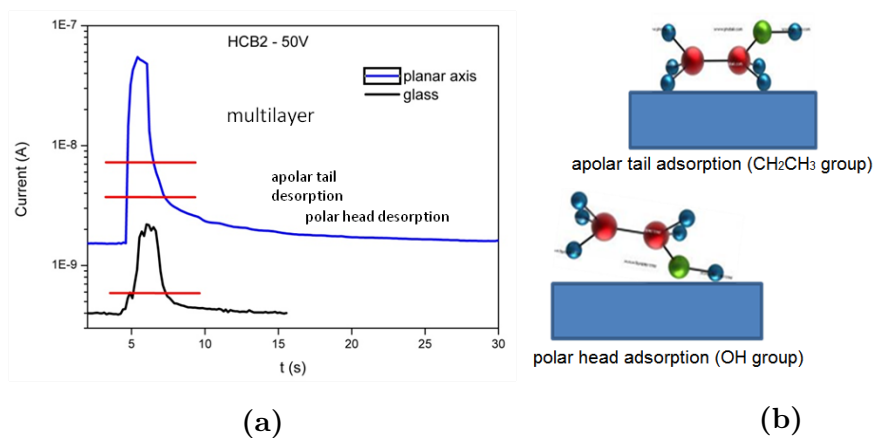


Figure 7.4: a) Transient section indicating different time constants and b) sketch of apolar tails (up) and polar heads (down).

the profile of the response curves, it is possible to notice that the decay part of the curves are not fully exponential, but present more than one contribution to the desorption mechanism. On the basis of this observation, and considering the chemical nature of the analytes and of the 4HCB crystal, it seems reasonable to explain this trend considering the different spatial approach of the analyte molecules to the 4HCB crystal surface. In particular, ethanol can approach the crystal surface via its polar head (the -OH group) or its apolar tail (its -CH₃ group), see figure 7.4b. Previous work carried out by Ghimbeu et al. [167] showed that these two different approaches to the surface of active carbons functionalized with -OH groups (hence a polar surface not dramatically different from that of 4HCB crystals) present two different desorption temperatures, detectable by temperature-programmed desorption coupled to mass spectrometry (TPD-MS). In particular, the alkylic function of ethanol results to be less bound to the polar surface than the alcoholic one, and the higher affinity of the ethanol polar head towards polar surfaces has been assessed also for silica [168]. The decay part of the curves obtained along the planar axes may be divided into three different sections, which are labelled as I, II and III in figure 7.4a. These three parts of the signal have clearly different decay time constants: the fastest one can be ascribed to the

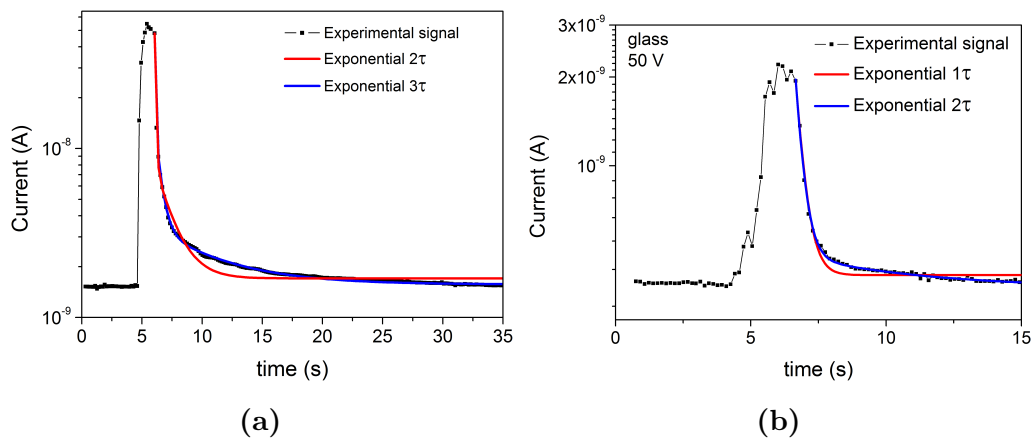


Figure 7.5: Comparison between multi-constant exponential decay. a) between two and three time constant (τ) in 4HCB and b) between one and two time constants in glass.

desorption of ethanol multilayer, the second can be due to the desorption of the apolar tails and the slowest one to the desorption of the stronger bounded polar heads. Upon fitting them with exponential curves, the time constants for the three curve zones are to be determined: the fastest one ≈ 0.06 s, the medium one ≈ 0.5 s and the slowest one ≈ 5 s (see the well fitted curves with three time constant in figure 7.5a). Figure 7.5 highlights that the 4HCB desorption transient is effectively well fitted only through a three time decay constants. Moreover, the different nature of the reference transient on glass, is supported by observing that only two time constants are sufficient to fit the glass transient (see blue line in figure 7.5b), but not for the 4CHB one (see the bad fit of two time constants, blue curve in figure 7.5a).

Chapter 8

High Mobility Crystalline Organic TFTs

So far, rubrene (RUB) has been considered the benchmark among organic semiconductors, since it shows the highest performances observed in its single-crystal phase (see section 3.4.2). Therefore, many efforts have been made to utilize RUB in OFETs and solar cells [169, 170]. If single-crystal thin films could be more easily obtained, they would represent a significant step for the integration of RUB in electronics. Unfortunately, even if single crystals as thin as 150 nm have been grown on flexible and plastic substrates, the poor control of the growing process has limited their integration [148], and only amorphous thin films have been obtained by conventional deposition techniques [171].

Recently, crystalline thin films were deposited by strictly optimizing the growth conditions. RUB films containing large distinct grains were grown by hot-wall deposition [120], while polycrystalline thin films were obtained by evaporating RUB on top of different organic buffer layers [172, 57, 58] or by using post-growth treatments [173, 174]. However, the quality of the resulting organic films was poor in terms of the coherence of the crystalline domains. To overcome these limitations, homoepitaxial and heteroepitaxial RUB thin films have been grown, they exhibited a unique orientation of the crystallites

[175, 176]. These have also been integrated in field-effect transistors [177, 57]. However, in most of these examples, the integration was hindered by the nature of the growth process. Specific crystalline substrates were required for epitaxy, and this prevented the use of epitaxially grown films in FETs that utilize conventional insulators. Recently, crystalline boron nitride as dielectric material has been proposed as a solution to overcome this limitation, allowing the direct integration of high-crystalline RUB thin films with the dielectric in FETs [178]. Unfortunately, despite the good transistor efficiency achieved, this technique gives crystalline RUB domains with lateral sizes limited to a few tens of micrometers. In this chapter, we report about use of Organic Molecular Beam Epitaxy (OMBE see par. 1.2.1) to grow millimeter-sized, crystalline, and fully oriented free-standing thin films of orthorhombic RUB, without any post-growth treatment. The thin film growth, the structural and the morphological characterization were performed by the group of Prof. A. Sassella at University of Milano Bicocca and have been submitted for publication [179], as most of the results presented in this chapter. We carried out the electrical characterization of film as-grown and transferred to different substrates, the photocurrent characterization and in the end we realized a thin-film transistors with the employment of free-standing RUB films, obtaining high-efficiency devices, with performances comparable to transistors made based on RUB single crystals. This part of the work has been carried out during my stay at the Department Mechanical and Process Engineering (D-MAVT) at the Optical Materials Engineering Laboratory (ETH, Zurich) in the group of Prof. D. Norris.

8.1 Rubrene Thin Film Structure and Morphology

RUB thin films were grown by OMBE under ultra-high vacuum (pressure $\leq 5 \times 10^{-9}$ Torr). Film thickness varying between 15 nm and 150 nm have been investigated. Centimeter-sized (010)-oriented single crystals of β -

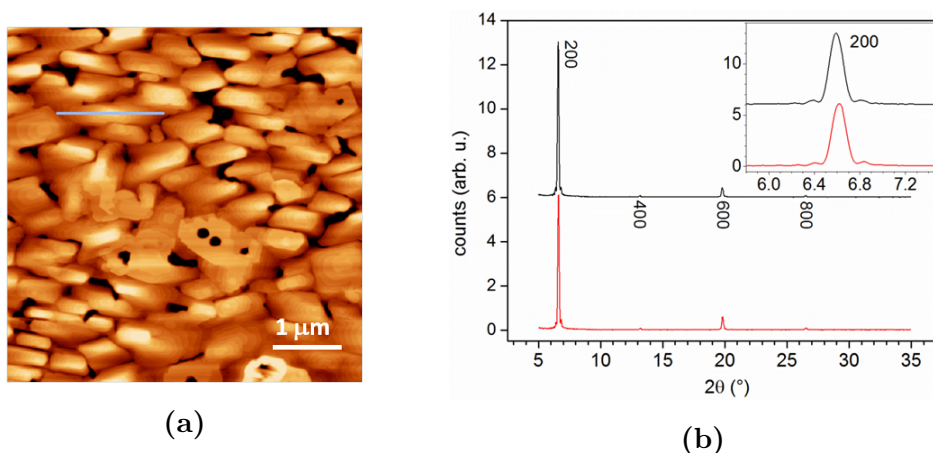


Figure 8.1: a) AFM images of 50 nm-thick RUB films grown on β -ala(010). b) Specular XRD scans of the film wet-transferred onto a Si(100) plate, collected before (black) and after (red) an annealing treatment at 80 °C for 3 h in air. The peaks are indexed in accordance to the orthorhombic polymorph structure. The inset reports a zoomed view of the 200 reflections.

alanine (β -ala) [180] was chosen as substrates, in view of its potential ordering effect on small molecule, thus giving crystalline RUB thin films without any buffer layers or post-growth treatment [181]. The structure and morphology of our RUB thin films were investigated ex-situ by combining atomic force microscopy (AFM), X-ray diffraction (XRD), and electron diffraction. A complete characterization and more detailed discussion about the thin growth are in [179]. RUB thin films grow on β -ala(010) in layered islands, they cover completely the substrate surface after few nanometers of deposition. These layers are arranged in a pyramidal morphology, with polygonal edges having an elongated hexagonal shape. These elongated features run parallel to two directions highlighted by the white arrows in figure 8.1a and are uniformly spaced of around 1.35 nm. The two two symmetrically equivalent RUB domains are rotated by exactly 26.5° ($\pm 13.25^\circ$ to β -ala[001]), as illustrated in figure 8.1a. The high solubility of this substrate in water and the availability of relatively easy techniques for its growth in solution are additional benefits. In particular, the solubility of β -ala enables the trans-

fer of large-area (about 10 to 20 mm²), free-standing crystalline RUB thin films onto any chosen substrate. In figure 8.1b are shown the results of XRD specular scans on films wet-transferred onto Si(100) substrates. The (h00) reflections of the orthorhombic polymorph of RUB [121] are visible, demonstrating the crystallinity of the films and a complete textural order with the RUB(100) plane in contact with β -ala(010).

8.2 Electrical Characterization

To get a further insight into the performances and transport properties of RUB thin films grown on β -ala, an electrical characterization have been carried out. Metallic gold electrodes were deposited on the growth side of the film, by thermal evaporation in high vacuum chamber (10^{-6} Torr), by means of shadow masks so that the conductive channels are aligned to the *c* axis of β -ala (roughly corresponding to the high mobility *b*-axis of rubrene). Two gaps were realised on each crystal, equal to 50 μm and 90 μm . In figure 8.2a an optical microscopy picture, in bright and dark field, of a millimeter sized RUB thin film on β -ala substrate (with *c*-axis highlighted) as well as a sketch of the device for electrical measurements are shown. Three kinds of RUB film with thickness of 15 nm, 50 nm and 75 nm have been tested.

Current-voltage measurements were performed in the dark, in air and at room temperature. Through the Space Charge Limited Current (SCLC, see par. 3.1.1) analysis we studied the electrical transport properties of the thin films determining also the charge carrier mobility as a function of the thin film thickness. Experimental plots that exhibited SCLC behaviour are reported in figure 8.2 for channels length of 90 μm . Two models can be used for SCLC analysis of gap-type structure: the first for thin films that follows the 2D geometry Geurst law (eq. 3.7), and the second for thick samples that follows an equation similar to the Mott-Gurney one for 3D geometry (eq: 3.8). The experimental curves have been analysed employing Geurst law to extract parameters, because in our case the thickness value that discriminate

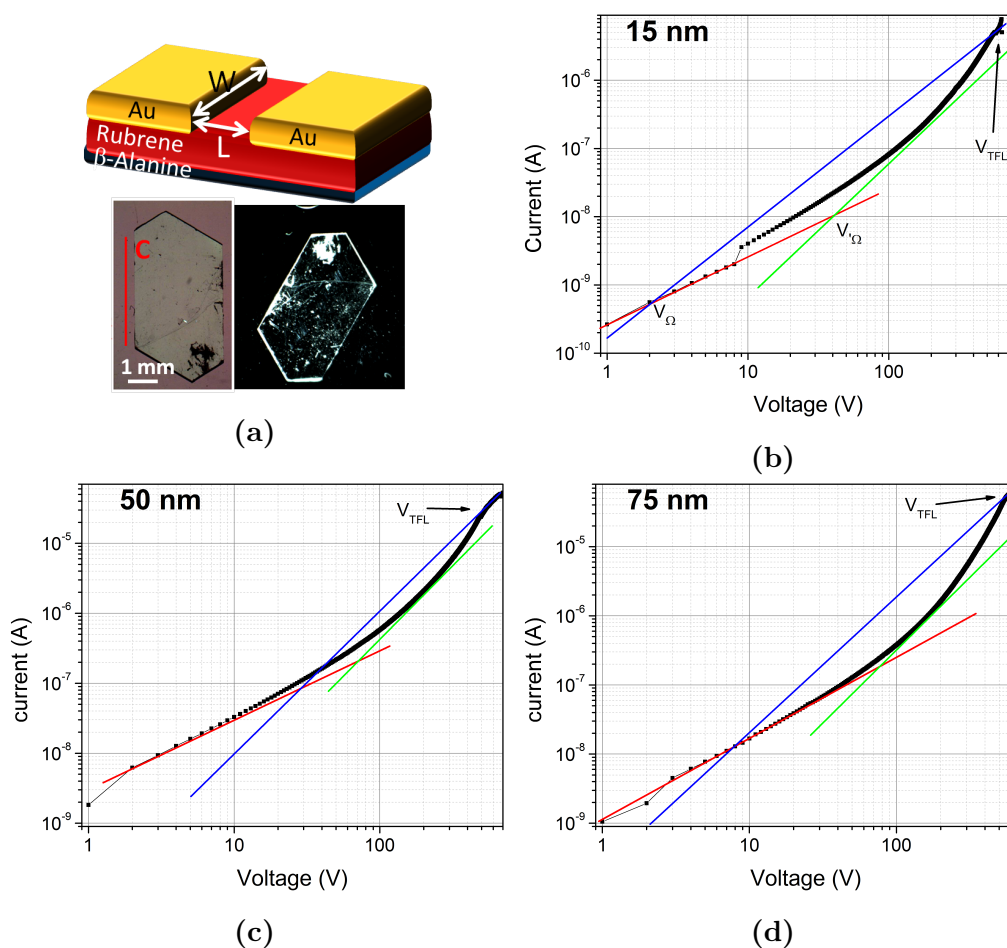


Figure 8.2: a) Scheme of the RUB thin film device for electrical characterization. W is the channel width, L is the channel length ($50 \mu\text{m}$ and $90 \mu\text{m}$). Optical picture in bright and dark field microscopy are also reported. Current-voltage characteristics for RUB thin film on β -ala, b) 15 nm, c) 50 nm and d) 75 nm thick.

Thickness nm	V_{TFL} V	μ cm^2/Vs	θ	N_T $\times 10^{13} \text{ cm}^{-3}$	n_0 $\times 10^{11} \text{ cm}^{-3}$
15	570 ± 5	$(1.3 \pm 0.2) \times 10^{-2}$	0.05	2.3	0.8
50	534 ± 5	0.20 ± 0.02	0.4	0.9	4.5
75	555 ± 5	0.31 ± 0.03	0.1	1.0	1.3

Table 8.1: Electrical parameters for rubrene thin film with three different thicknesses, calculated with the Geurst theory.

between the two models is ≈ 34 nm, according to 3.9. In the plots the red lines indicate the ohmic region at low bias, the green lines the space charge region dominated by traps and the blue lines stand for the trap-free region. Values for V_Ω , $V_{\Omega'}$ and V_{TFL} are written on the graph. From the ratio between V_Ω and $V_{\Omega'}$ it is possible to calculate θ , i.e. the ratio between the density of free carriers achieved under injection and the total density of injected carriers, trapped and free. We note also that the knowledge of V_{TFL} makes it possible to calculate the mobility and to estimate the density of traps N_t of the film. The in-plane rubrene static dielectric constant was assumed to be $\epsilon_r = 2.6$, the mean value extrapolated from the crystal full dielectric tensor at $\omega = 0$ [182]. The extracted values are reported in table 8.1 for $L = 90 \mu\text{m}$; the same measurements performed at channel length of $50 \mu\text{m}$ gave similar results in the experimental errors. The mobility increases with the film thickness. The value of mobility of the thinnest film (15 nm) is very low, suggesting that the electrical transport is not very good with a so thin sample. A completely different situation occurs in thicker samples: the mobility raises more than one order of magnitude already at 50 nm, and only slightly increases for 75 nm film thickness. Also the other parameters get better compared to the thinnest sample ones. The density of traps states N_T decreases, the θ value and the density of thermal carriers n_0 increase. Remarkably, the value of N_T and n_0 for 50 nm and 75 nm films are in good agreement with what have been obtained for rubrene single crystals [109].

Overall, the mobility reaches the average performance value of the rubrene single crystals, however, by employing organic thin film transistor structure and by improving the fabrication technique we reached high mobility values, comparable to those typical of standard rubrene single crystals (see par. 8.4.2).

8.3 Opto-electronic Characterization

Wavelength-resolved photocurrent spectroscopy was performed on both rubrene bulk single crystals and thin films using coplanar contacts oriented along the high-mobility b-axis of rubrene, with the light sent on the sample at normal incidence on the (b,c) plane of the crystal. The spectra have been collected using monochromatic light, emitted by a halogen lamp and selected by a monochromator, with a spectral resolution of 1 nm. Measurements were performed with the aperture of the two slits in input and output of the monochromator equal to 2000 μm and 250 μm . The biases applied to extract the photogenerated charge carriers were 3 V and 13 V. As has been done for electrical characterization, both the two channels of 50 μm and 90 μm were investigated. Preliminary measurements were performed in all of the configurations described above, in order to exclude the presence of effects due to the variation of electric field (applied voltage) or due to the number of photoinjected carriers (slits aperture). Once we assessed that no changes occur in the shape and in the peaks position of photocurrent spectra, 2000 μm slits, 13 V of applied bias and 90 μm of channel length configuration has been chosen. Figure 8.3 reports the photocurrent spectra of rubrene thin films of three different thicknesses: 15 nm, 50 nm and 75 nm, compared with the PC spectrum collected for a rubrene bulk single crystals. All the spectra show the same onset i.e. the energy gap of the three thin film is the same of the single crystal: 2.2 eV. Furthermore, also the peaks above band-gap (i.e. at 2.37 eV, 2.54 eV, 2.73 eV and 2.90 eV) are present in all the spectra collected, indicating a comparable energetic structure of the thin film and single crystal

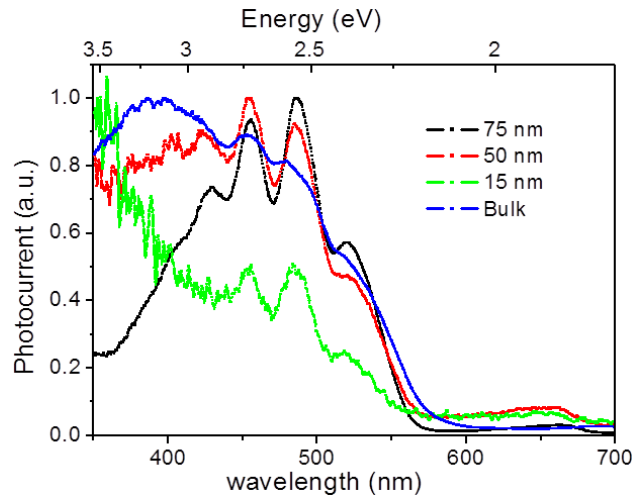


Figure 8.3: Comparison between the photocurrent spectra of a standard Rubrene bulk single crystal (blue line), and thin film samples with three different thicknesses (75, 50 and 15nm).

samples and therefore assessing the single-crystal quality of the thin films of all the investigated thicknesses. The thinnest 15 nm film exhibits a low and noisy signal, denoting a poor charge collection, in accordance with the bad electrical transport properties shown in current-voltage characterization; the energy gap and the peak positions indicate, however, that the structure is ordered even for such a thin film. Further measurements were performed on thin films transferred on different substrates, in order to investigate how the wet-transfer process affects the opto-electronic features of the films. In figure 8.4 the photocurrent spectra of rubrene thin films 150 nm thick transferred on SiO_2 and glass substrates are reported in comparison with an as-grown film on β -ala. All the three spectra present energy gap of 2.2 eV and the same peak positions, typical of rubrene single crystals and already observed for the other thin films. Moreover, the spectra on β -ala and on glass are surprisingly similar, almost completely overlapped; this points out the effective possibility of transferring the film on different substrates without affecting the film structure. On the other hand, the intensity of the spectrum of the sample on SiO_2 is lower and more noisy, probably due to the rough surface of such

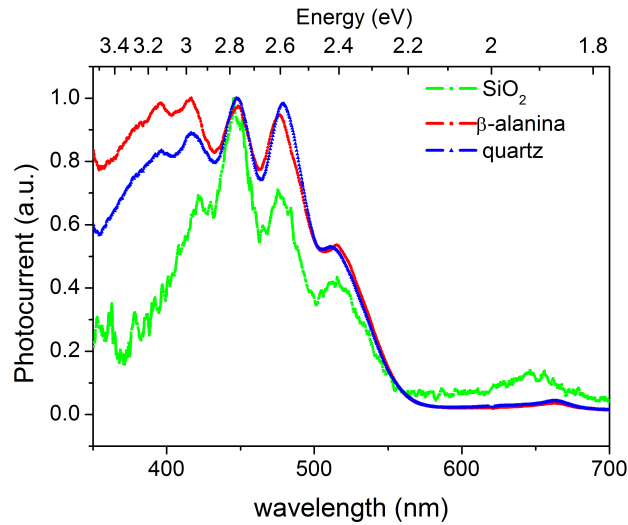


Figure 8.4: Comparison between the photocurrent spectra three rubrene thin film samples: SiO₂ (green), β-ala (red) and glass (blue).

substrate, detrimental for the thin and fragile film more than the transfer process itself. More informations on SiO₂/RUB interface have been obtained by OFET measurements in the next section (see par. 8.4.1). The comparison of the photocurrent with the absorption spectrum of the same film shows an antimodulation of the peaks, i.e. a peak in absorption spectrum corresponds to a valley in the photocurrent spectrum and vice versa (figure 8.5a). In literature the antimodulation observed in bulk rubrene single-crystals has been associated to trap-dominated transport related to oxygen traps, meanwhile only high ultra-pure single crystals exhibit photocurrent spectra correlated to the absorption spectra [128, 8]. Several photocurrent measurements have been carried out on bulk rubrene single crystals. Only few cases present good correlation, thus it may be asserted that the major part of rubrene single crystals show antimodulation behaviour (as reported in figure 8.3). It is noteworthy that photocurrent measurements performed on RUB thin film on cytop in TFT structure (see next section 8.4.2) give spectra correlated with absorption (figure 8.5a) and very similar to high purity pristine RUB single crystal photocurrent spectrum in [128] (figure 8.5b). This is also the con-

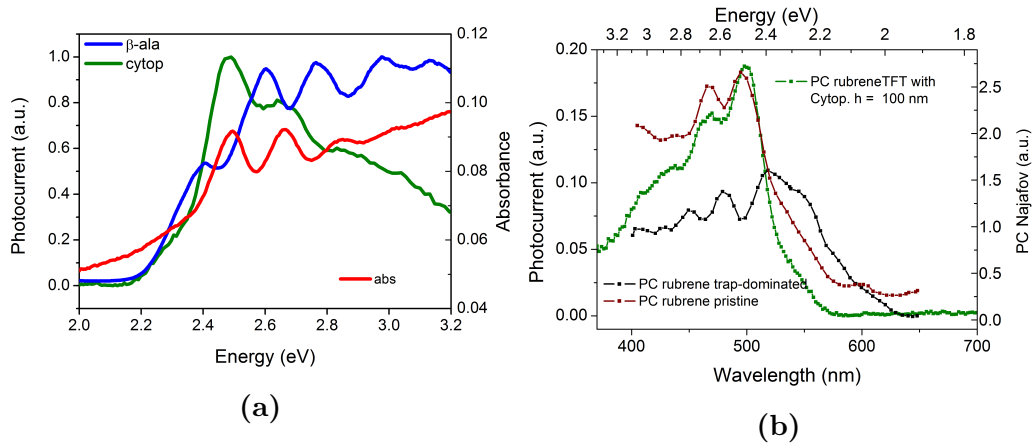


Figure 8.5: a) Comparison between the absorption spectrum (red line) with antimodulated thin film on β -ala (blue line) and the correlated spectrum of thin film on cytop (green line). b) The same spectrum on cytop (green line) compared to pristine (dark red line) and trap-dominated (black line) spectra reported in [128].

figuration with the highest mobility recorded among the investigated RUB thin films.

8.4 Rubrene OTFTs

In order to definitely assess the quality and versatility of our thin films for electronic applications, we fabricated back-gate FETs on two different gate/dielectric systems. The first presents a Si substrate as gate electrode, with few nanometers of thermal SiO₂ as dielectric, employing a wet-transfer method. In the second the RUB thin has been transferred on Cytop[®] as insulating layer. Cytop, a hydroxyl-free fluoropolymer, is the benchmark for the fabrication of high-efficiency organic FETs, showing low-hysteresis and low shift of the threshold voltage under bias-stress [183, 56, 184]. The particular growth of transferable/free-standing RUB thin films overcomes the limits imposed by the high hydrophobicity of Cytop in back-gated thin-film transistors, where the active layer has to be deposited on top of the dielectric

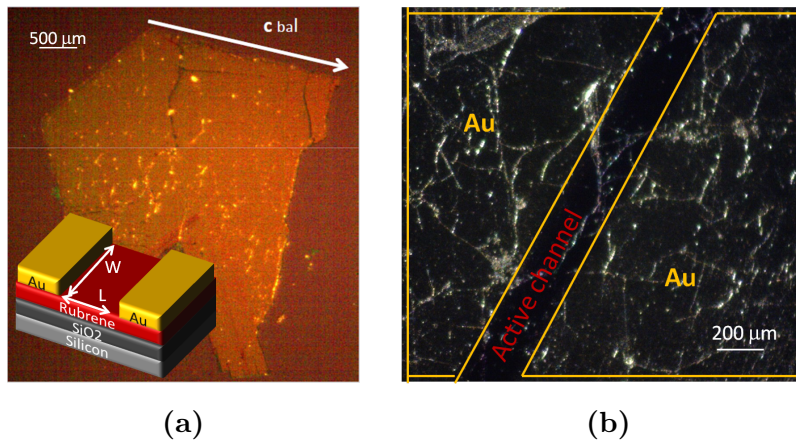


Figure 8.6: Optical microscope picture of RUB thin film 90 nm thick wet-transferred on Si/SiO₂ substrate, a) as transferred, b) details of active channel of $L = 200 \mu\text{m}$ after thermal evaporation of Au 30 nm thick. Sketch of the device in inset.

[185].

8.4.1 OTFTs with SiO₂ dielectric

RUB thin film has been transferred on Si/SiO₂ substrate, by wet-transferred method as described in section 8.1. Then 30 nm of two coplanar source-drain electrode have been thermally evaporated in high vacuum through a shadow mask (channel length of $200 \mu\text{m}$) on top of the semiconducting film. The method enables to transfer large area films on top of the dielectric surface. Figure 8.6a shows a 10 mm^2 films as transferred on SiO₂ and the sketch of the full device in inset. A detailed picture of source-drain and transistor channel is shown in figure 8.6b. The source-drain current (I_D) in function of the drain voltage (V_D) at constant gate voltage (V_G), i.e. the output characteristic, and the I_D in function of V_G at constant V_D , i.e. the transfer characteristic, are reported in figure 8.7 for a 90 nm RUB thin film transistor. From output characteristics the I_D saturation at high V_D in the I-V plot is clearly visible, as well as the good linearity at low biases, suggesting a low source-drain contact resistance. Moreover, from transfer characteristic both conduction

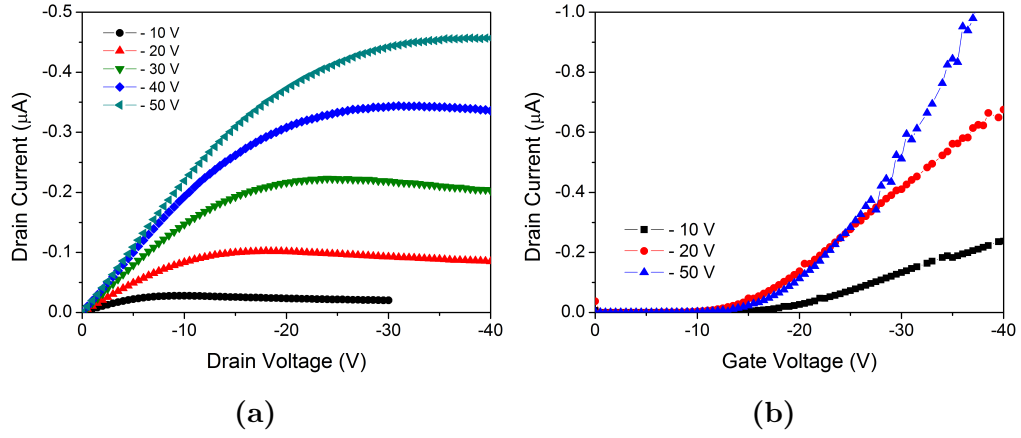


Figure 8.7: Output (a) and transfer (b) characteristic at different V_G and V_D , respectively, for the device reported in figure 8.6.

regimes: linear behaviour at $V_D = 10$ V for linear regime and parabolic behaviour at $V_D = 50$ V for saturation regime, can be clearly recognized. In the plot of $I_D^{1/2}$ vs V_G in figure 8.8a ideal linearity, typical of saturation regime, is better appreciable; no series resistance effects are visible at high voltages. Nonetheless, even if a working OTFT device has been proven, it is far from being satisfactory, in fact it suffers of several drawbacks. The resulting device parameters, extracted from transfer characteristic as shown in figure 8.8a, are $\mu_{SAT} = 2.6 \times 10^{-2}$ cm²/Vs and $V_T = -11.3$ V, for mobility and threshold voltage respectively. The mobility, in particular, is low compared to the value reported for single crystal FETs [52] and even lower than mobility measured by means of SCLC (8.2). It should be noted that the mobility has been extracted from saturation regime, where it is possible to obtain only the mobility mean value because it is not constant along the channel [39]. The mobility value in the linear regime results $\mu_{LIN} = 9.2 \times 10^{-2}$ cm²/Vs, for $V_D = 10$ V (black line in figure 8.7b). Moreover, the source-gate current I_G , i.e. the leakage current is quite high, in the order of 3×10^{-8} A, and induces a slight decrease of the saturation current at high voltages. In addition, the transfer characteristics are affected by huge hysteresis (figure 8.8b), that strongly suggest a really bad dielectric-film interface, probably due the high

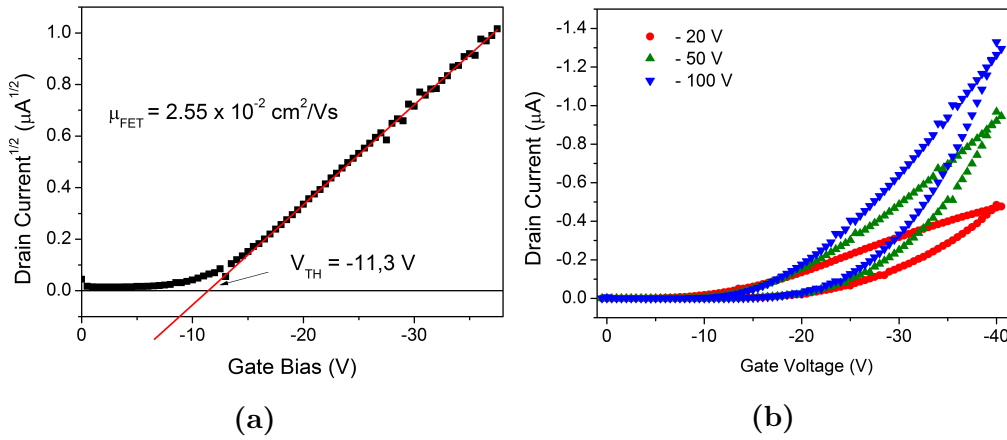


Figure 8.8: a) $I_D^{1/2}$ vs V_G at $V_D = -50\text{ V}$, showing the linearity of the saturation regime. b) Forward and reverse transfer characteristics at different drain voltages showing the hysteresis.

SiO_2 roughness. The limited mobility values may be ascribed to the several inhomogeneities present in the active channel (figure 8.6b), consistently with the above non-ideal effects. In conclusion, we need to improve the transfer process and use a proper dielectric, in order to have an homogeneous film and a better semiconductor/dielectric interfaces. An improved device on Cytop dielectric will be presented in the next section.

8.4.2 OTFTs with Cytop[®] dielectric

Device fabrication

Bottom-gate/top-contact RUB FETs were fabricated in air or under dry N_2 atmosphere, by means of RUB thin film wet-transferred to a glass substrate coated with Indium Tin Oxide (ITO) and Cytop. An ITO-coated glass substrate was rinsed in acetone, isopropanol, deionized water, and ultraviolet/ozone-cleaned for 10 min. The insulating fluoropolymer Cytop was then deposited by spin-coating at 500 rpm from a 3:2 solution on the substrate (270 to 400 nm final thickness), the structure was then subjected to thermal annealing (10 min at room temperature followed by 30 min at $90\text{ }^\circ\text{C}$

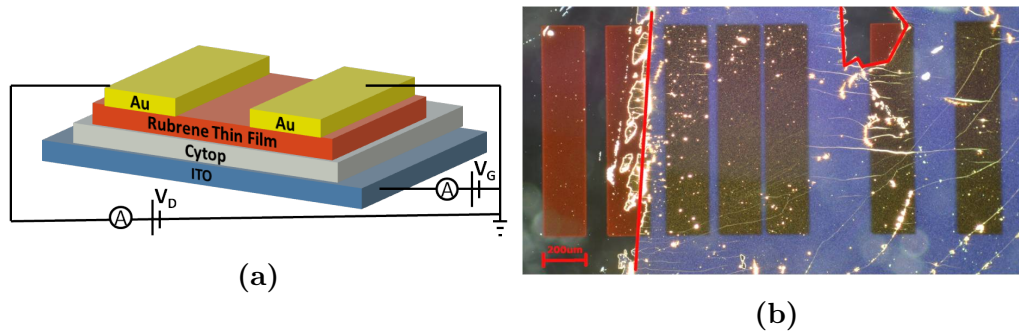


Figure 8.9: a) Schematic of a RUB thin-film transistor. b) Dark-field optical image of a rubrene FET, showing devices with different channel lengths on the same rubrene thin film.

and 30 min at 120 °C, in air). A rubrene thin film (thickness of 50 nm) on a β -ala substrate was transferred upside-down onto the ITO/Cytop gate electrode, after which the substrate was slowly dissolved in deionized water. The transferred thin film on Cytop was thermally annealed in dry N₂ at 45 °C for 1 hour to desorb residual water (that would be detrimental for the transistor performances) and to promote adhesion between the dielectric and the thin film. Gold source and drain electrodes of width $300 \leq W \leq 1000 \mu\text{m}$ and at different spacing (channel length, $25 \leq L \leq 120 \mu\text{m}$) were thermally evaporated in high vacuum ($\sim 10^{-6}$ mbar) through a shadow mask on the RUB thin film. The source-to-drain electric field was preferentially aligned along the original [001] β -ala direction, to be able to exploit the highest mobility in the RUB film (known to be along the [010]RUB in single crystals [186]), thus the shadow mask was aligned to the crystallographic direction of the thin film under an optical microscope equipped with two polarizers. The transistors were characterized before and after annealing of the contacts, performed in air for 3 h on a hot-plate at a temperature of 80 °C. A scheme of the full device is shown in figure 8.9a; the dark field image shows the good quality of the transferred film over an area $> 2 \text{ mm}^2$ and the defect-free active channel of transistors (8.9b).

After the deposition of the contacts, we investigated for imperfections in

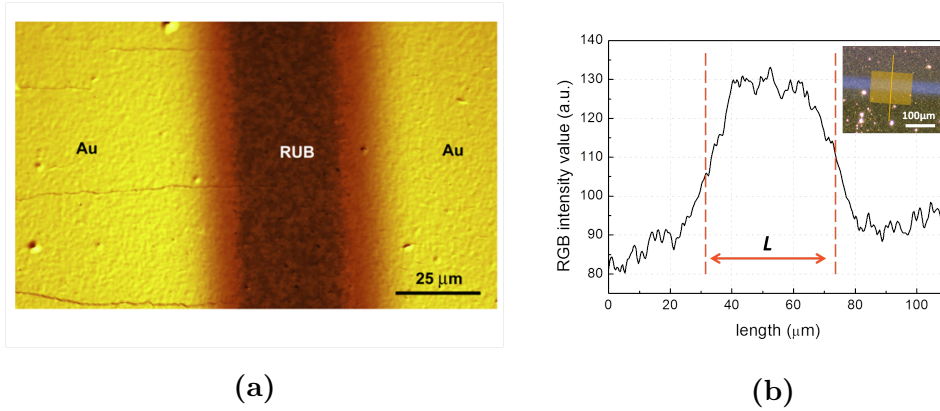


Figure 8.10: a) Optical micrograph of the RUB-based FET acquired with an Olympus B51 microscope in reflection mode with Nomarski differential interference contrast. b) Red-green-blue (RGB) intensity profile of the channel. The channel length L is estimated as the FWHM of the intensity profile, here $L = 42 \mu\text{m}$. Inset: dark field optical image of the device channel.

the as-fabricated device through dark-field optical microscopy. Only devices showing no microscopic imperfections in the active channel area were selected for the electrical measurements. Because of the different morphology of different transferred thin films, the channel width (W) and length (L) of the selected transistors were individually determined under the microscope, as shown in figure 8.10.

Electrical Characterization

Figure 8.11a shows the dependence of the source-to-drain current (I_D) of a RUB-based FET on the drain voltage (V_D), at different gate voltages (V_G). The characteristics show ideal FET behavior: at low V_D the current increases linearly with the applied drain voltage and saturates at $V_D \sim V_G$, as expected for a long-channel FET with negligible contact effects. Moreover, the characteristics are nearly hysteresis-free, indicating a reduced effect of charge trapping at the insulator/semiconductor interface, as for single-crystal OFETs employing Cytop as an insulator [183]. Also, a negligible

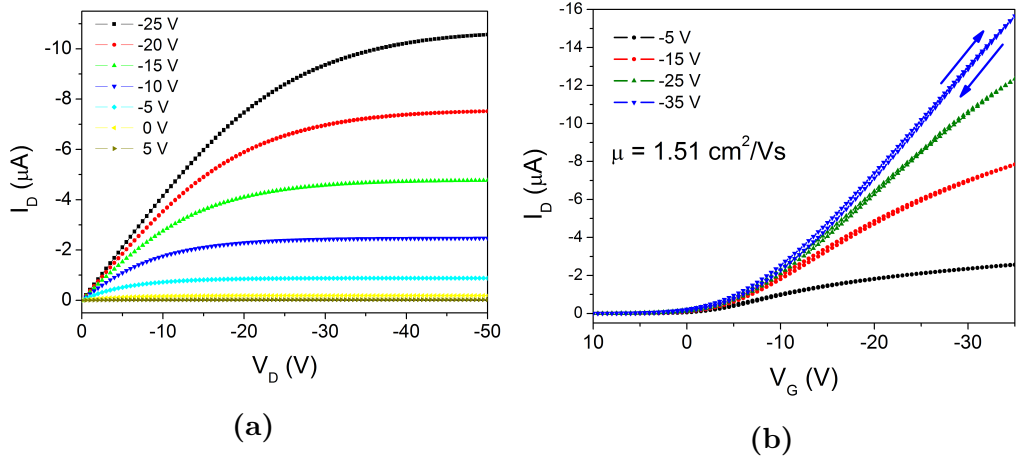


Figure 8.11: a) Output characteristic at different negative gate voltages. It shows remarkable low hysteresis, linear $I_D - V_D$ at low drain voltage, and good saturation of the characteristic when V_D is comparable to V_G , as for a conventional long-channel MOSFET. b) Transfer characteristic at different drain voltages. RUB thin film transfer of $W = 570 \mu\text{m}$ and $L = 120 \mu\text{m}$. The dielectric thickness is $\sim 380 \text{ nm}$.

hysteresis is seen in the transfer characteristics ($I_D - V_G$) of our transistors at different drain voltages (figure 8.11b). However, the trend of the $I_D - V_G$ characteristics deviates from the ideal behaviour observed with RUB single-crystal transistors [187]. In the linear (black curve, $V_D = -5 \text{ V}$) and saturation (blue curve, $V_D = -35 \text{ V}$) regimes, a substantial decrease of the slope is observed at high gate voltages, after the initial increase in the linear and parabolic I_D vs. V_G regimes. This behaviour has been attributed to the contribution of the parasitic resistance of the contacts [188, 189] or to the dependency of the mobility on the gate voltage [190]. Both issues are well known and documented bottlenecks for the development of organic thin-film transistors. To avoid incorrect extraction of the charge mobility (due to incorrect determination of the V_T), the mobility was extracted from the characteristics of devices working in saturation and at the peak of the derivative of the $(I_D)^{1/2} \sim \mu^{1/2}(V_G - V_T)$ characteristics. RUB-based FETs show reasonably high charge carrier mobility (1 to 2 cm^2/Vs values were

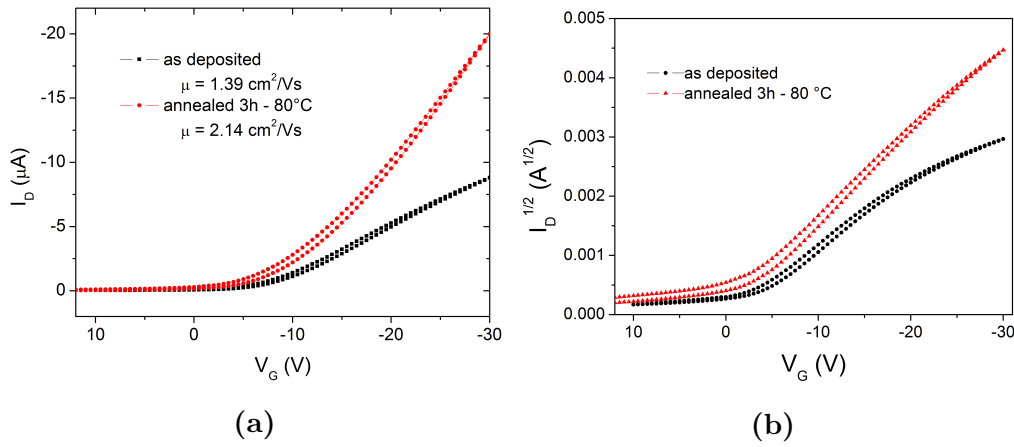


Figure 8.12: Transfer characteristics ((a) I_D and (b) $I_D^{1/2}$ vs. V_G) of a FET before (black) and after (red) annealing at 80°C for 3h, showing a drastic increase of the source-to-drain current at the same V_G and a decrease of slope degradation. Transistor channel dimensions are $W = 290 \mu\text{m}$ and $L = 50 \mu\text{m}$; the thickness of the dielectric is 430 nm . The mobility increase by 1.5 times, from $1.39 \text{ cm}^2/\text{Vs}$ (as evaporated) up to $2.14 \text{ cm}^2/\text{Vs}$ (annealed). Transfer curve after annealing is perfect linear also at high gate voltages. This improvement is due to a lower resistance contact.

obtained for different devices), together with a low threshold voltage ($-2 \text{ V} < V_T < +6 \text{ V}$), an ON/OFF ratio of about 104 at $\pm 15 \text{ V}$ from V_T in the saturation regime, and a normalized subthreshold swing as low as $S = 17 \text{ V nF/dec cm}^2$ [19]. The transistor ON/OFF ratio was determined from figure 8.13 along with additional information regarding the behavior of the thin-film transistors in the subthreshold regime. Clearly, even with a residual current in the OFF-state, the transistors show a reasonably high ON/OFF current ratio ($I_{ON}/I_{OFF} \sim 1 \times 10^4$ at $\pm 15 \text{ V}$ from the V_T in the saturation regime, and slightly lower in the linear regime). Figure 8.14a shows the transfer characteristics of a rubrene thin film FET in the saturation regime ($V_D = -30 \text{ V}$) after a short positive gate-bias stress ($V_G = 20 \text{ V}$ for 30 s). A clear shift of the threshold voltage is observed, together with a current increase, resulting in a small increase of the mobility. This behaviour has

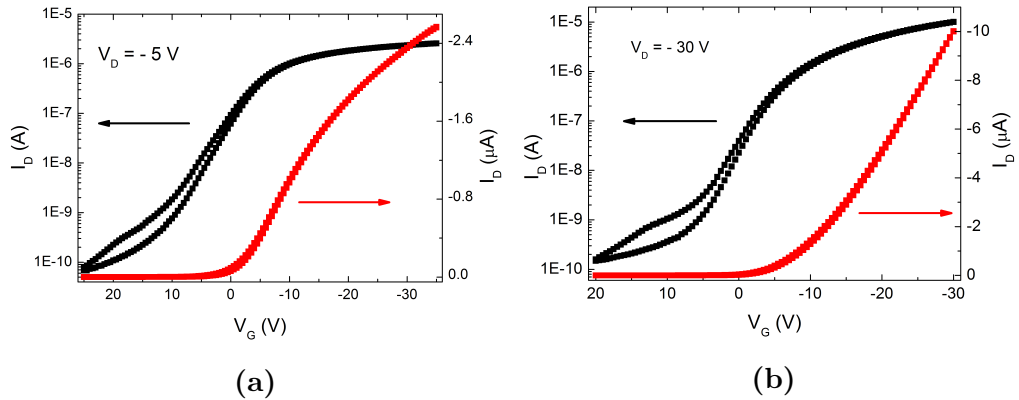


Figure 8.13: Transfer characteristics of a rubrene FET measured at $V_D = -5$ V (a) and -30 V (b), with I_D plotted in logarithmic (black) and linear (red) scale. Transistor-channel dimensions are $W = 570$ μ m and $L = 120$ μ m.

been observed previously for single crystal rubrene transistors [191]. In table 8.2 the parameter extracted from five different devices are summarized.

After a mild thermal annealing of the devices, a considerable increase of the transistor drain current I_D is observed, with the consequent increase of the charge-carrier mobility, possibly due to a reduction of the effect of the contacts. For example, saturation mobility values of 1.39 cm^2/Vs and 2.14 cm^2/Vs were obtained from the characteristics of the same FET before and after annealing, respectively (figure 8.12). Moreover, a significant reduction of the slope degradation is observed in the $(I_D)^{1/2}$ vs. V_G characteristics at high gate voltages, after annealing. It is plausible that the thermal annealing is relaxing the effect of the interface trap states induced during the evaporation of the contacts, with substantial improvement of the charge injection/extraction process. However, also an increased adhesion of the RUB thin film on Cytop is likely to contribute to the observed efficiency increase. Finally, to exclude the possibility of structural changes within the film upon heating, XRD analyses were conducted both before and after annealing (figure 8.1b).

In summary, the group of Prof. A. Sassella at the University of Milano - Bicocca demonstrated that large, crystalline, and fully oriented thin films

	W (μm)	L (μm)	W/L	V_T (V)		μ (cm^2/Vs)		S (V nF / dec cm^2)	
				fw	rev	fw	rev	fw	rev
A	570	120	4.8	2.84	1.97	1.42	1.45	30	24
B	500	98	5.1	2.65	1.84	1.88	1.91	39	36
C	580	80	7.3	5.95	3.74	1.28	1.46	47	32
D	290	50	5.8	-1.16	-2.00	1.32	1.39	30	28
E	1000	42	24	0.87	0.42	1.02	1.05	20	17

Table 8.2: Set of electrical parameters for five different RUB thin-film transistors, as collected in forward (*fw*) and reverse (*rev*) bias. The device-channel width (W) is defined by the lateral dimension of the Au contacts; the channel length (L) was determined by post-processing dark-field optical images of the devices.

of orthorhombic RUB can be obtained by OMBE on suitable, water-soluble crystalline substrates. By working at room temperature and without post-growth treatments, epitaxial RUB film can be grown on (010)-oriented single crystals of β -alanine, thus obtaining removable/free-standing RUB films. We then post-growth transferred these RUB thin-films onto Cytop, which is one of the most exploited high-efficient dielectrics for organic field-effect transistors. The high quality of the dielectric, together with the high quality of the film, makes the mobility of our transistors remarkably high for an organic thin film transistor (table 8.3 for a comparison with similar RUB-based TFT), but still lower than what reported for RUB single crystal devices [52]. Thin-film transistors fabricated with free-standing RUB and Cytop dielectric demonstrate the high quality of the as-grown RUB thin films, and the possible integration of this semiconductor into a wide variety of electronic devices.

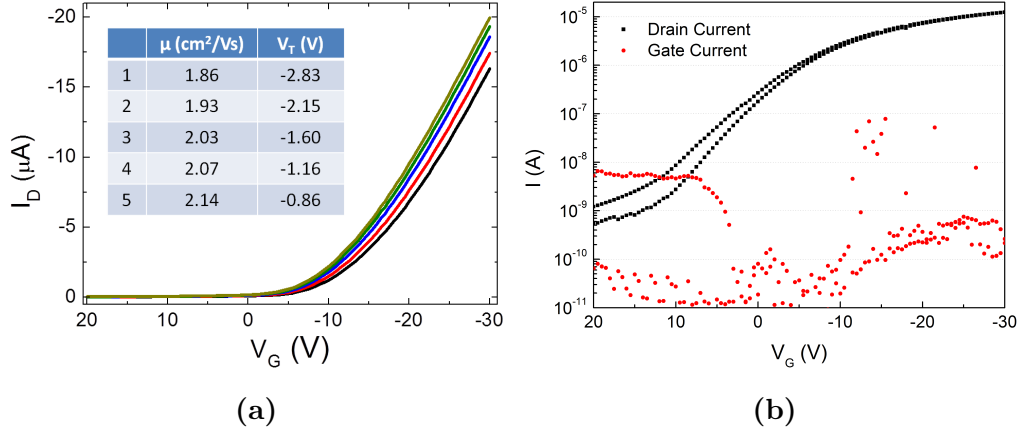


Figure 8.14: a) Transfer characteristics of a FET in the saturation regime ($V_D = -30$ V) after different positive gate-bias stresses at $V_G = 20$ V. The inset lists the mobility and threshold voltage values extracted from the different curves. b) Drain and leakage gate current plotted in logarithmic scale. The transistor-channel dimensions are $W = 290$ μm and $L = 50$ μm .

Device	Dielectric	Electrodes	μ (cm ² /Vs)	V_T (V)	I_{ON}/I_{OFF}
Fig. 8.12	Cytop	Au	2.14	- 0.9	10^4
Ref. [57]	SiO ₂ /DPPC	Au	0.98	- 8	10^7
Ref. [58]	Si ₃ N ₄ /BCBO	Au	3.0	- 7	10^6
Ref. [59]	Si ₃ N ₄ /BCBO	ITO	1.3	- 0.9	10^6

Table 8.3: Comparison between the electrical parameters of one of our RUB thin-film transistors (first row) and those of other RUB-based thin film transistors reported in the literature.

Conclusions

In the present thesis I studied Organic Semiconducting Single Crystals (OSSCs) and crystalline thin films, demonstrating how they can be employed in novel sensing application as solid state detectors ionizing radiation (X-rays, gamma-rays, and alpha particles), and as chemical sensor to polar volatile molecules. In these research fields, organic materials offers a novel and smart alternative to traditional inorganic semiconducting materials thanks to their wide availability, and to the possibility of achieving novel functionalities, such as flexibility and transparency, and of being deposited over large areas by means of low-cost technologies as ink-jet printing. In particular, solution-grown OSSCs have been assessed to be promising materials for radiation detectors thanks to the following particular properties: (a) low dark current due to the wide effective band gap; (b) high degree of packing order; (c) long exciton diffusion length; (d) good carrier mobility; (e) possibility to tune their volume up to mm^3 ; (f) great stability in air.

The organic single crystal-based X-ray detectors fabricated and investigated in this thesis's work allow to direct detect ionizing radiation, that is, the incoming X-ray photons are directly converted into an electrical signal. They provide a linear response to the X-ray dose rate, even for driving voltages as low as 5 V (hundreds of volts are usually required to operate at room temperature for inorganic semiconductors), and they reliably respond to repetitive ON/OFF switching X-ray beam with no hysteresis effects.

Moreover, the studied detectors, based on low-cost solution-grown organic molecular crystals (e.g., 4HCB), can operate at room temperature, in air, and

under ambient conditions with high reproducibility. The response is really fast for an organic device, estimated below 5 ms, and the minimum detectable dose rate has been assessed down to 50 $\mu\text{Gy/s}$. 4HCB-based detectors provide a reliable response even after exposure to significant doses of X-ray irradiation and after being aged for up to one month. Experiments carried out on devices with different electrodes and substrate materials demonstrate that the observed response has to be considered as intrinsically related to the crystal.

A deep investigation of the photo-response of OSSCs along all crystallographic axes, with different crystals thicknesses and for several electrode geometries, has been carried out. Even if the anisotropic packing of the molecules affects the electronic transport properties of the crystal (carrier mobility can vary up to four orders of magnitude along the three crystal axes), it is noteworthy that all axes can be used for the effective detection of ionizing radiation. The organic crystal thickness can be varied between 40 - 500 μm without affecting the device performance, as comparable sensitivity values for thickness down to few tens of micrometers have been recorded. The maximum measured sensitivity of an optimized detectors is over 170 nC/Gy and the effective collection efficiency is up to 20%. Device geometries that maximize the electrode active area (e.g. interdigitated electrodes 25 μm spaced) allow to significantly increase the charge collection efficiency and the X-ray electrical photoresponse of 4HCB single crystals; a strong increase of the output electrical signal and a dramatic reduction of the operating bias voltage (≈ 5 V) have been observed.

Other solution-grown (e.g. DNN, NTI and TIPS-pentacene) and vapour grown (rubrene) organic molecular crystals showed interesting detection features, giving a preliminary insight into the understanding of molecular and crystal properties that rule the X-ray detection in organic materials.

Furthermore, the proof of principle of high energy gamma radiation (661 keV Cs^{137}) and alpha particles detection has been given for 4HCB-based devices.

To further exploits the sensing performances of OSSCs, an investigation on the electrical characteristics of single crystals exposed to vapour of volatile molecules, has been carried out. The obtained results indicate that OSSCs are good candidates for chemical polar molecule sensing applications.

Finally, the characterization of a highly crystalline rubrene thin film (15 - 100 nm thick), grown on water-soluble substrate, has been performed. Once assessed its crystalline structure and morphology, the electrical properties of the film have been investigated by means of Space Charge Limited Current (SCLC) analyses and Wavelength-resolved photocurrent spectroscopy measures. A working thin film FET in bottom-gate/top-contact configuration was fabricated with a Cytop[®] layer acting as gate dielectric. The device showed extremely good characteristics, with FET mobility exceeding 2 cm²/Vs, definitely assessing the quality of RUB films grown by the proposed strategy. The reliability and versatility of the wet-transfer process have been demonstrated, as well as the potential integration of this semiconductor into a wide variety of electronic devices.

In conclusion, solution-grown OSSCs are robust and easy to handle materials that can reliably detect ionizing radiation in the direct approach, operating at room temperature and in air, providing a linear response to increasing X-ray dose rates. The results presented in this thesis indicate how OSSCs based sensors possess a great potential as novel solid-state low cost and tissue equivalent ionizing radiation detectors and dosimeters, paving the way to the development of large-area, thin, flexible and low-power consuming sensors, applicable to biomedical and environmental tasks.

Bibliography

- [1] Vitaly Podzorov. Organic single crystals: Addressing the fundamentals of organic electronics. *MRS Bulletin*, 38(01):15–24, January 2013. ix, 21, 22
- [2] Giulia Hull, N.P. Zaitseva, N.J. Cherepy, J.R. Newby, Wolfgang Stoeffl, and S.A. Payne. New Organic Crystals for Pulse Shape Discrimination. *IEEE Transactions on Nuclear Science*, 56(3):899–903, June 2009. x, 45
- [3] F. A. Boroumand, M. Zhu, A. B. Dalton, J. L. Keddie, P. J. Sellin, and J. J. Gutierrez. Direct x-ray detection with conjugated polymer devices. *Applied Physics Letters*, 91(3):033509, July 2007. x, 49, 50, 89, 92
- [4] Akarin Intaniwet, Christopher A. Mills, Maxim Shkunov, Heiko Thiem, Joseph L. Keddie, and Paul J. Sellin. Characterization of thick film poly(triarylamine) semiconductor diodes for direct x-ray detection. *Journal of Applied Physics*, 106(6):064513, September 2009. x, 49
- [5] A Intaniwet, C A Mills, M Shkunov, P J Sellin, and J L Keddie. Heavy metallic oxide nanoparticles for enhanced sensitivity in semiconducting polymer x-ray detectors. *Nanotechnology*, 23(23):235502, June 2012. x, 54, 55
- [6] V. Podzorov, E. Menard, S. Pereversev, B. Yakshinsky, T. Madey, J. A. Rogers, and M. E. Gershenson. Interaction of organic surfaces with ac-

- tive species in the high-vacuum environment. *Applied Physics Letters*, 87(9):093505, August 2005. 1
- [7] V. Podzorov, E. Menard, A. Borissov, V. Kiryukhin, J. Rogers, and M. Gershenson. Intrinsic Charge Transport on the Surface of Organic Semiconductors. *Physical Review Letters*, 93(8):086602, August 2004. 1
- [8] H. Najafov, B. Lee, Q. Zhou, L. C. Feldman, and V. Podzorov. Observation of long-range exciton diffusion in highly ordered organic semiconductors. *Nature Materials*, 9(11):938–943, November 2010. 1, 7, 83, 104, 107, 109, 167
- [9] Heliatek reaches efficiency record with 40% transparent organic solar cells, December 2014. 4
- [10] Heliatek consolidates its technology leadership by establishing a new world record for organic solar technology with a cell efficiency of 12%, December 2014. 4
- [11] Wikipedia OLED. 4
- [12] Flexible OLED screens. 5
- [13] Henning Sirringhaus. 25th Anniversary Article: Organic Field-Effect Transistors: The Path Beyond Amorphous Silicon. *Advanced Materials*, 26(9):1319–1335, 2014. 5
- [14] Tsuyoshi Sekitani, Ute Zschieschang, Hagen Klauk, and Takao Someya. Flexible organic transistors and circuits with extreme bending stability. *Nature Materials*, 9(12):1015–1022, December 2010. 5
- [15] M. Berggren and A. Richter-Dahlfors. Organic Bioelectronics. *Advanced Materials*, 19(20):3201–3213, 2007. 5

- [16] Laura Basiricò. *Inkjet Printing of Organic Transistor Devices*. PhD Thesis, Dept. of Electrical and Electronic Engineering University of Cagliari, 2012. 5, 131
- [17] M. Berggren, D. Nilsson, and N. D. Robinson. Organic materials for printed electronics. *Nature Materials*, 6(1):3–5, January 2007. 6
- [18] N Karl. Charge carrier transport in organic semiconductors. *Synthetic Metals*, 133–134:649–657, March 2003. 6, 14
- [19] V. Podzorov, S. E. Sysoev, E. Loginova, V. M. Pudalov, and M. E. Gershenson. Single-crystal organic field effect transistors with the hole mobility $\sim 8\text{cm}^2/\text{V s}$. *Applied Physics Letters*, 83(17):3504–3506, October 2003. 7, 175
- [20] Anna S. Molinari, Helena Alves, Zhihua Chen, Antonio Facchetti, and Alberto F. Morpurgo. High Electron Mobility in Vacuum and Ambient for PDIF-CN2 Single-Crystal Transistors. *Journal of the American Chemical Society*, 131(7):2462–2463, February 2009. 7
- [21] Md Minarul Islam, Someshwar Pola, and Yu-Tai Tao. High mobility n-channel single-crystal field-effect transistors based on 5,7,12,14-tetrachloro-6,13-diazapentacene. *Chemical Communications*, 47(22):6356–6358, May 2011. 7
- [22] Hui Jiang and Christian Kloc. Single-crystal growth of organic semiconductors. *MRS Bulletin*, 38(01):28–33, January 2013. 7, 8, 9
- [23] R. W. I. de Boer, M. E. Gershenson, A. F. Morpurgo, and V. Podzorov. Organic single-crystal field-effect transistors. *physica status solidi (a)*, 201(6):1302–1331, May 2004. 8
- [24] Colin Reese and Zhenan Bao. Organic single-crystal field-effect transistors. *Materials Today*, 10(3):20–27, March 2007. 9

- [25] Sung Kyu Park, Thomas N. Jackson, John E. Anthony, and Devin A. Mourey. High mobility solution processed 6,13-bis(triisopropylsilylethynyl) pentacene organic thin film transistors. *Applied Physics Letters*, 91(6):063514, August 2007. 9, 84
- [26] Hiromi Minemawari, Toshikazu Yamada, Hiroyuki Matsui, Jun'ya Tsutsumi, Simon Haas, Ryosuke Chiba, Reiji Kumai, and Tatsuo Hasegawa. Inkjet printing of single-crystal films. *Nature*, 475(7356):364–367, July 2011. 10, 109
- [27] Ying Diao, Benjamin C.-K. Tee, Gaurav Giri, Jie Xu, Do Hwan Kim, Hector A. Becerril, Randall M. Stoltenberg, Tae Hoon Lee, Gi Xue, Stefan C. B. Mannsfeld, and Zhenan Bao. Solution coating of large-area organic semiconductor thin films with aligned single-crystalline domains. *Nature Materials*, 12(7):665–671, July 2013. 10, 22, 23, 84, 109, 127
- [28] Piero Cosseddu, L. Basirico, A. Loi, S. Lai, P. Maiolino, E. Baglini, S. Denei, F. Mastrogiovanni, G. Cannata, and A. Bonfiglio. Inkjet printed Organic Thin Film Transistors based tactile transducers for artificial robotic skin. In *2012 4th IEEE RAS EMBS International Conference on Biomedical Robotics and Biomechatronics (BioRob)*, pages 1907–1912, June 2012. 10
- [29] Jung Ah Lim, Hwa Sung Lee, Wi Hyoung Lee, and Kilwon Cho. Control of the Morphology and Structural Development of Solution-Processed Functionalized Acenes for High-Performance Organic Transistors. *Advanced Functional Materials*, 19(10):1515–1525, 2009. 12
- [30] Z. Li, V. Podzorov, N. Sai, M. Martin, M. Gershenson, M. Di Ventra, and D. Basov. Light Quasiparticles Dominate Electronic Transport in Molecular Crystal Field-Effect Transistors. *Physical Review Letters*, 99(1):016403, July 2007. 12

- [31] Peter Mark and Wolfgang Helfrich. Space-Charge-Limited Currents in Organic Crystals. *Journal of Applied Physics*, 33(1):205–215, January 1962. 13, 58, 59, 61
- [32] N. Riehl, G. Becker, and H. Bässler. Injektionsbestimmte Defektelektronenströme in Anthracenkristallen. *physica status solidi (b)*, 15(1):339–346, 1966. 13
- [33] Veaceslav Coropceanu, Jérôme Cornil, Demetrio A. da Silva Filho, Yoann Olivier, Robert Silbey, and Jean-Luc Brédas. Charge Transport in Organic Semiconductors. *Chemical Reviews*, 107(4):926–952, April 2007. 14, 21
- [34] R. Kepler. Charge Carrier Production and Mobility in Anthracene Crystals. *Physical Review*, 119(4):1226–1229, August 1960. 14
- [35] N. Karl. Charge-Carrier Mobility in Organic Crystals. In Dr Riccardo Farchioni and Professor Giuseppe Grosso, editors, *Organic Electronic Materials*, pages 283–326. Springer Berlin Heidelberg, January 2001. 14, 18
- [36] Martin Pope and Charles E. Swenberg. *Electronic Processes in Organic Crystals and Polymers*. Oxford University Press, New York, 2 edition edition, December 1999. 14
- [37] V. Podzorov, E. Menard, J. Rogers, and M. Gershenson. Hall Effect in the Accumulation Layers on the Surface of Organic Semiconductors. *Physical Review Letters*, 95(22):226601, November 2005. 14, 22
- [38] Gilles Horowitz, Riadh Hajlaoui, Habib Bouchriha, Ramzi Bourguiga, and Mohcen Hajlaoui. The Concept of “Threshold Voltage” in Organic Field-Effect Transistors. *Advanced Materials*, 10(12):923–927, 1998. 14
- [39] Daniele Braga and Gilles Horowitz. High-Performance Organic Field-Effect Transistors. *Advanced Materials*, 21(14-15):1473–1486, 2009. 14, 65, 170

- [40] *Organic Molecular Crystals - Their Electronic States*. December 2014. 14
- [41] Markus Schwoerer and Hans Christoph Wolf. Organic Molecular Solids. In *Organic Molecular Solids*, pages i–xi. Wiley-VCH Verlag GmbH, 2006. 16, 20
- [42] J. Veres, S.d. Ogier, S.w. Leeming, D.c. Cupertino, and S. Mohialdin Khaffaf. Low-k Insulators as the Choice of Dielectrics in Organic Field-Effect Transistors. *Advanced Functional Materials*, 13(3):199–204, March 2003. 17
- [43] Henning Sirringhaus, Matt Bird, and Ni Zhao. Charge Transport Physics of Conjugated Polymer Field-Effect Transistors. *Advanced Materials*, 22(34):3893–3898, 2010. 17
- [44] P. M. Borsenberger, L. Pautmeier, and H. Bässler. Hole transport in bis(4-N,N-diethylamino-2-methylphenyl)-4-methylphenylmethane. *The Journal of Chemical Physics*, 95(2):1258–1265, July 1991. 17
- [45] Rodrigo Noriega and Alberto Salleo. Charge Transport Theories in Organic Semiconductors. In Hagen Klauk, editor, *Organic Electronics II*, pages 67–104. Wiley-VCH Verlag GmbH & Co. KGaA, 2012. 17
- [46] W. Warta, R. Stehle, and N. Karl. Ultrapure, high mobility organic photoconductors. *Applied Physics A*, 36(3):163–170, March 1985. 18, 19
- [47] Wilhelm Warta and Norbert Karl. Hot holes in naphthalene: High, electric-field-dependent mobilities. *Physical Review B*, 32(2):1172–1182, July 1985. 19
- [48] Y. C. Cheng, R. J. Silbey, D. A. da Silva Filho, J. P. Calbert, J. Cornil, and J. L. Brédas. Three-dimensional band structure and bandlike mobility in oligoacene single crystals: A theoretical investigation. *The Journal of Chemical Physics*, 118(8):3764–3774, February 2003. 20

- [49] Jean-Luc Brédas, David Beljonne, Veaceslav Coropceanu, and Jérôme Cornil. Charge-Transfer and Energy-Transfer Processes in π -Conjugated Oligomers and Polymers: A Molecular Picture. *Chemical Reviews*, 104(11):4971–5004, 2004. 21
- [50] David L. Cheung and Alessandro Troisi. Modelling charge transport in organic semiconductors: from quantum dynamics to soft matter. *Physical Chemistry Chemical Physics*, 10(39):5941–5952, September 2008. 21
- [51] Yongbo Yuan, Gaurav Giri, Alexander L. Ayzner, Arjan P. Zoombelt, Stefan C. B. Mannsfeld, Jihua Chen, Dennis Nordlund, Michael F. Toney, Jinsong Huang, and Zhenan Bao. Ultra-high mobility transparent organic thin film transistors grown by an off-centre spin-coating method. *Nature Communications*, 5, January 2014. 22, 23
- [52] V. Podzorov, E. Menard, A. Borissov, V. Kiryukhin, J. Rogers, and M. Gershenson. Intrinsic Charge Transport on the Surface of Organic Semiconductors. *Physical Review Letters*, 93(8):086602, August 2004. 22, 23, 82, 121, 170, 177
- [53] A. F. Stassen, R. W. I. de Boer, N. N. Iosad, and A. F. Morpurgo. Influence of the gate dielectric on the mobility of rubrene single-crystal field-effect transistors. *Applied Physics Letters*, 85(17):3899–3901, October 2004. 23
- [54] I. N. Hulea, S. Fratini, H. Xie, C. L. Mulder, N. N. Iossad, G. Rastelli, S. Ciuchi, and A. F. Morpurgo. Tunable Fröhlich polarons in organic single-crystal transistors. *Nature Materials*, 5(12):982–986, December 2006. 23
- [55] J. Takeya, M. Yamagishi, Y. Tominari, R. Hirahara, Y. Nakazawa, T. Nishikawa, T. Kawase, T. Shimoda, and S. Ogawa. Very high-mobility organic single-crystal transistors with in-crystal conduction channels. *Applied Physics Letters*, 90(10):102120, March 2007. 23

- [56] Tomo Sakanoue and Henning Sirringhaus. Band-like temperature dependence of mobility in a solution-processed organic semiconductor. *Nature Materials*, 9(9):736–740, September 2010. 23, 168
- [57] Chuan Du, Wenchong Wang, Liqiang Li, Harald Fuchs, and Lifeng Chi. Growth of rubrene crystalline thin films using thermal annealing on DPPC LB monolayer. *Organic Electronics*, 14(10):2534–2539, October 2013. 23, 159, 160, 178
- [58] Xianrui Qian, Tong Wang, and Donghang Yan. High mobility organic thin-film transistors based on p-p heterojunction buffer layer. *Applied Physics Letters*, 103(17):173512, October 2013. 23, 159, 178
- [59] Xianrui Qian, Tong Wang, and Donghang Yan. Transparent organic thin-film transistors based on high quality polycrystalline rubrene film as active layers. *Organic Electronics*, 14(4):1052–1056, April 2013. 23, 178
- [60] D. C. Koningsberger and R. Prins. X-ray absorption: principles, applications, techniques of EXAFS, SEXAFS, and XANES. 1988. 25
- [61] Jerrold T. Bushberg and John M. Boone. *The Essential Physics of Medical Imaging*. Lippincott Williams & Wilkins, December 2011. 25
- [62] Electron Beam and X-ray Processing. 25
- [63] G.F. Knoll. *Radiation Detection and Measurement*. Wiley, fourth Edition edition, 2011. 26, 45
- [64] ELETTRA. 28, 71
- [65] ESRF. 28
- [66] Lawrence Berkeley National Laboratory. *X-RAY DATA BOOKLET*. 28

- [67] Robley D. Evans. *The Atomic Nucleus*. Tata McGraw Hill Publishing Company Limited., January 1955. 30
- [68] NIST. X-ray Mass Attenuation Coefficients. 31, 32
- [69] H.E. Johns and J.R. Cunningham. *The Physics of Radiology*. Charles C. Thomas, fourth Edition edition, 1983. 33
- [70] ICRP. The 2007 Recommendations of the International Commission on Radiological Protection. 34
- [71] Qi Chen, Tibor Hajagos, and Qibing Pei. Conjugated polymers for radiation detection. *Annual Reports Section "C" (Physical Chemistry)*, 107(0):298–318, June 2011. 36, 45
- [72] Ernest Rutherford, James Chadwick, and Charles Drummond Ellis. *Radiations from Radioactive Substances*. Cambridge University Press, Cambridge, 2010. 36
- [73] S. E. Derenzo, M. J. Weber, E. Bourret-Courchesne, and M. K. Klintonberg. The quest for the ideal inorganic scintillator. *Nuclear Instruments and Methods in Physics Research Section A: Accelerators, Spectrometers, Detectors and Associated Equipment*, 505(1–2):111–117, June 2003. 36
- [74] Robert Hofstadter and Max H. Stein. Twenty Five Years of Scintillation Counting. *IEEE Transactions on Nuclear Science*, 22(1):13–25, February 1975. 37
- [75] T. E Schlesinger, J. E Toney, H Yoon, E. Y Lee, B. A Brunett, L Franks, and R. B James. Cadmium zinc telluride and its use as a nuclear radiation detector material. *Materials Science and Engineering: R: Reports*, 32(4–5):103–189, April 2001. 38
- [76] Safa Kasap, Joel B. Frey, George Belev, Olivier Tousignant, Habib Mani, Jonathan Greenspan, Luc Laperriere, Oleksandr Bubon, Alla

- Reznik, Giovanni DeCrescenzo, Karim S. Karim, and John A. Rowlands. Amorphous and Polycrystalline Photoconductors for Direct Conversion Flat Panel X-Ray Image. *Sensors*, 11(5):5112–5157, May 2011. 39, 41, 44
- [77] Y. Nemirovsky. Statistical modeling of charge collection in semiconductor gamma-ray spectrometers. *Journal of Applied Physics*, 85(1):8–15, January 1999. 39
- [78] S. O. Kasap. X-ray sensitivity of photoconductors: application to stabilized a-Se. *Journal of Physics D: Applied Physics*, 33(21):2853, November 2000. 39, 40
- [79] T. Peter Brody. The birth and early childhood of active matrix — A personal memoir. *Journal of the Society for Information Display*, 4(3):113–127, October 1996. 41
- [80] Wei Zhao and J. A. Rowlands. X-ray imaging using amorphous selenium: Feasibility of a flat panel self-scanned detector for digital radiology. *Medical Physics*, 22(10):1595–1604, October 1995. 41
- [81] Feng Chen, Kai Wang, Yuan Fang, N. Allec, George Belev, Safa O. Kasap, and K.S. Karim. Direct-Conversion X-Ray Detector Using Lateral Amorphous Selenium Structure. *IEEE Sensors Journal*, 11(2):505–509, February 2011. 42
- [82] Shiva Abbaszadeh, Christopher C. Scott, Oleksandr Bubon, Alla Reznik, and Karim S. Karim. Enhanced Detection Efficiency of Direct Conversion X-ray Detector Using Polyimide as Hole-Blocking Layer. *Scientific Reports*, 3, November 2013. 43
- [83] J. B. BIRKS. CHAPTER 3 - THE SCINTILLATION PROCESS IN ORGANIC MATERIALS—I. In J. B. BIRKS, editor, *The Theory and Practice of Scintillation Counting*, pages 39–67. Pergamon, 1964. 44

- [84] Dario Natali and Marco Sampietro. Detectors based on organic materials: status and perspectives. *Nuclear Instruments and Methods in Physics Research Section A: Accelerators, Spectrometers, Detectors and Associated Equipment*, 512(1–2):419–426, October 2003. 46
- [85] Kang-Jun Baeg, Maddalena Binda, Dario Natali, Mario Caironi, and Yong-Young Noh. Organic Light Detectors: Photodiodes and Phototransistors. *Advanced Materials*, 25(31):4267–4295, August 2013. 46, 47, 67, 89
- [86] Sandro F. Tedde, Johannes Kern, Tobias Sterzl, Jens Fürst, Paolo Lugli, and Oliver Hayden. Fully Spray Coated Organic Photodiodes. *Nano Letters*, 9(3):980–983, March 2009. 47
- [87] R. a. B. Devine, Mang-Mang Ling, Abhijit Basu Mallik, Mark Roberts, and Zhenan Bao. X-ray irradiation effects in top contact, pentacene based field effect transistors for space related applications. *Applied Physics Letters*, 88(15):151907, April 2006. 47
- [88] Christopher R. Newman, Henning Sirringhaus, James C. Blakesley, and Robert Speller. Stability of polymeric thin film transistors for x-ray imaging applications. *Applied Physics Letters*, 91(14):142105, October 2007. 47, 96
- [89] B. Fraboni, A. Scidà, A. Cavallini, S. Milita, P. Cosseddu, A. Bonfiglio, Y. Wang, and M. Nastasi. Photocurrent spectroscopy of ion-implanted organic thin film transistors. *Synthetic Metals*, 161(23–24):2585–2588, January 2012. 48
- [90] Panagiotis E. Keivanidis, Neil C. Greenham, Henning Sirringhaus, Richard H. Friend, James C. Blakesley, Robert Speller, Mariano Campoy-Quiles, Tiziano Agostinelli, Donal D. C. Bradley, and Jenny Nelson. X-ray stability and response of polymeric photodiodes for imaging applications. *Applied Physics Letters*, 92(2):023304, January 2008. 48, 96

- [91] E. a. B. Silva, J. F. Borin, P. Nicolucci, C. F. O. Graeff, T. Ghilardi Netto, and R. F. Bianchi. Low dose ionizing radiation detection using conjugated polymers. *Applied Physics Letters*, 86(13):131902, March 2005. 48
- [92] T. Agostinelli, M. Campoy-Quiles, J. C. Blakesley, R. Speller, D. D. C. Bradley, and J. Nelson. A polymer/fullerene based photodetector with extremely low dark current for x-ray medical imaging applications. *Applied Physics Letters*, 93(20):203305, November 2008. 48
- [93] Malinowski, Pawel, Kumar, Abhishek, and Moet. Fully Organic Integrated Arrays on Flexible Substrates for X-Ray Imaging, 2013. 48
- [94] J. F. Fowler. X-Ray Induced Conductivity in Insulating Materials. *Proceedings of the Royal Society of London. Series A. Mathematical and Physical Sciences*, 236(1207):464–480, September 1956. 49
- [95] M. Bruzzi, F. Nava, S. Pini, and S. Russo. High quality SiC applications in radiation dosimetry. *Applied Surface Science*, 184(1–4):425–430, December 2001. 51, 108
- [96] Akarin Intaniwet, Christopher A. Mills, Paul J. Sellin, Maxim Shkunov, and Joseph L. Keddie. Achieving a Stable Time Response in Polymeric Radiation Sensors under Charge Injection by X-rays. *ACS Applied Materials & Interfaces*, 2(6):1692–1699, June 2010. 51, 53
- [97] Kazuhiro Saito and Shunsuke Kobayashi. Bias-Light-Induced Transient Responses of the Modulated Photocurrent in Organic Photovoltaic Cells. *Japanese Journal of Applied Physics*, 42(7A):L781, July 2003. 52
- [98] Christopher A. Mills, Akarin Intaniwet, Maxim Shkunov, Joseph L. Keddie, and Paul J. Sellin. Flexible radiation dosimeters incorporating semiconducting polymer thick films. volume 7449, pages 74491I–74491I–7, 2009. 52

- [99] Akarin Intaniwet, Joseph L. Keddie, Maxim Shkunov, and Paul J. Sellin. High charge-carrier mobilities in blends of poly(triarylamine) and TIPS-pentacene leading to better performing X-ray sensors. *Organic Electronics*, 12(11):1903–1908, November 2011. 54, 127
- [100] Christopher A. Mills, Hulayel Al-Otaibi, Akarin Intaniwet, Maxim Shkunov, Silvia Pani, Joseph L. Keddie, and Paul J. Sellin. Enhanced x-ray detection sensitivity in semiconducting polymer diodes containing metallic nanoparticles. *Journal of Physics D: Applied Physics*, 46(27):275102, July 2013. 55
- [101] N. F. Mott and Ronald W. Gurney. *Electronic processes in ionic crystals*. Clarendon Press, Oxford, 1940. 58, 61
- [102] Murray A Lampert and Peter 1931 Mark, (joint author.). *Current injection in solids*. New York : Academic Press, 1970. Bibliography: p. 332-338. 59, 61
- [103] S. Nešpurek and E. A. Silinsh. Space-charge-limited current theory for molecular crystals with gaussian distribution of local trapping states. *physica status solidi (a)*, 34(2):747–759, 1976. 59, 61
- [104] J. A. Geurst. Theory of Space-Charge-Limited Currents in Thin Semiconductor Layers. *physica status solidi (b)*, 15(1):107–118, 1966. 59, 63
- [105] S. Nešpurek and J. Sworakowski. A differential method of analysis of steady-state space-charge-limited current-voltage characteristics. *physica status solidi (a)*, 41(2):619–627, 1977. 59
- [106] Peter Stallinga. Two-Terminal Devices: DC Current. In *Electrical Characterization of Organic Electronic Materials and Devices*, pages 45–64. John Wiley & Sons, Ltd, 2009. 62

- [107] Anatoly A. Grinberg, S. Luryi, M.R. Pinto, and N.L. Schryer. Space-charge-limited current in a film. *IEEE Transactions on Electron Devices*, 36(6):1162–1170, June 1989. 63
- [108] R. Zuleeg and Peter Knoll. SPACE-CHARGE-LIMITED CURRENTS IN HETEROEPITAXIAL FILMS OF SILICON GROWN ON SAPPHIRE. *Applied Physics Letters*, 11(6):183–185, September 1967. 63
- [109] D. Braga, N. Battaglini, A. Yassar, G. Horowitz, M. Campione, A. Sassella, and A. Borghesi. Bulk electrical properties of rubrene single crystals: Measurements and analysis. *Physical Review B*, 77(11):115205, March 2008. 63, 111, 164
- [110] S. Nespurek and J. Sworakowski. Use of space-charge-limited current measurements to determine the properties of energetic distributions of bulk traps. *Journal of Applied Physics*, 51(4):2098–2102, April 1980. 64
- [111] J. Reynaert, V. I. Arkhipov, G. Borghs, and P. Heremans. Current–voltage characteristics of a tetracene crystal:Space charge or injection limited conductivity? *Applied Physics Letters*, 85(4):603–605, July 2004. 65
- [112] Richard H. Bube. *Photoconductivity of solids*. Wiley, 1960. 67
- [113] Beatrice Fraboni, Cristina Femoni, Ivan Mencarelli, Leonardo Setti, Riccardo Di Pietro, Anna Cavallini, and Alessandro Fraleoni-Morgera. Solution-Grown, Macroscopic Organic Single Crystals Exhibiting Three-Dimensional Anisotropic Charge-Transport Properties. *Advanced Materials*, 21(18):1835–1839, 2009. 74, 75, 76, 77, 111, 145
- [114] A. Fraleoni-Morgera, L. Benevoli, and B. Fraboni. Solution growth of single crystals of 4-hydroxycyanobenzene (4HCB) suitable for electronic applications. *Journal of Crystal Growth*, 312(23):3466–3472, November 2010. 75

- [115] T. Higashi and K. Osaki. p-Cyanophenol. *Acta Crystallographica Section B*, 33(2):607–609, 1977. 75
- [116] B. Fraboni, R. DiPietro, A. Castaldini, A. Cavallini, A. Fraleoni-Morgera, L. Setti, I. Mencarelli, and C. Femoni. Anisotropic charge transport in organic single crystals based on dipolar molecules. *Organic Electronics*, 9(6):974–978, December 2008. 75, 76, 77, 92
- [117] B. Fraboni, A. Fraleoni-Morgera, and A. Cavallini. Three-dimensional anisotropic density of states distribution and intrinsic-like mobility in organic single crystals. *Organic Electronics*, 11(1):10–15, January 2010. 77, 78, 79, 80, 111
- [118] Takashi Takahashi, Yoshiya Harada, Naoki Sato, Kazuhiko Seki, Hiroo Inokuchi, and Shoji Fujisawa. Gas and Solid Phase Photoelectron Spectra of 5,6,11,12-Tetra-phenylnaphthacene (Rubrene). *Bulletin of the Chemical Society of Japan*, 52(2):380–382, 1979. 80
- [119] M. Kytka, A. Gerlach, F. Schreiber, and J. Kováč. Real-time observation of oxidation and photo-oxidation of rubrene thin films by spectroscopic ellipsometry. *Applied Physics Letters*, 90(13):131911, March 2007. 80
- [120] D. Käfer and G. Witte. Growth of crystalline rubrene films with enhanced stability. *Physical Chemistry Chemical Physics*, 7(15):2850–2853, July 2005. 80, 82, 159
- [121] Oana D. Jurchescu, Auke Meetsma, and Thomas T. M. Palstra. Low-temperature structure of rubrene single crystals grown by vapor transport. *Acta Crystallographica Section B Structural Science*, 62(2):330–334, April 2006. 81, 162
- [122] Liwei Huang, Qing Liao, Qiang Shi, Hongbing Fu, Jinshi Ma, and Jiannian Yao. Rubrene micro-crystals from solution routes: their crys-

- tallography, morphology and optical properties. *Journal of Materials Chemistry*, 20(1):159–166, December 2009. 81
- [123] C. Kloc, K. J. Tan, M. L. Toh, K. K. Zhang, and Y. P. Xu. Purity of rubrene single crystals. *Applied Physics A*, 95(1):219–224, April 2009. 82
- [124] Oleg Mitrofanov, Christian Kloc, Theo Siegrist, David V. Lang, Woo-Young So, and Arthur P. Ramirez. Role of synthesis for oxygen defect incorporation in crystalline rubrene. *Applied Physics Letters*, 91(21):212106, November 2007. 82
- [125] C. Reese and Z. Bao. High-Resolution Measurement of the Anisotropy of Charge Transport in Single Crystals. *Advanced Materials*, 19(24):4535–4538, December 2007. 82
- [126] Satria Zulkarnaen Bisri, Taishi Takenobu, Tetsuo Takahashi, and Yoshihiro Iwasa. Electron transport in rubrene single-crystal transistors. *Applied Physics Letters*, 96(18):183304, May 2010. 82
- [127] Hikmat Najafov, Ivan Biaggio, Vitaly Podzorov, Matthew F. Calhoun, and Michael E. Gershenson. Primary Photoexcitations and the Origin of the Photocurrent in Rubrene Single Crystals. *Physical Review Letters*, 96(5):056604, February 2006. 82
- [128] Hikmet Najafov, Daniel Mastrogiovanni, Eric Garfunkel, Leonard C. Feldman, and Vitaly Podzorov. Photon-Assisted Oxygen Diffusion and Oxygen-Related Traps in Organic Semiconductors. *Advanced Materials*, 23(8):981–985, February 2011. 82, 167, 168
- [129] R. G Endres, C. Y Fong, L. H Yang, G Witte, and Ch Wöll. Structural and electronic properties of pentacene molecule and molecular pentacene solid. *Computational Materials Science*, 29(3):362–370, March 2004. 83

- [130] J. Takeya, T. Nishikawa, T. Takenobu, S. Kobayashi, Y. Iwasa, T. Mitani, C. Goldmann, C. Krellner, and B. Batlogg. Effects of polarized organosilane self-assembled monolayers on organic single-crystal field-effect transistors. *Applied Physics Letters*, 85(21):5078–5080, November 2004. 83
- [131] Chang Su Kim, Stephanie Lee, Enrique D. Gomez, John E. Anthony, and Yueh-Lin Loo. Solvent-dependent electrical characteristics and stability of organic thin-film transistors with drop cast bis(triisopropylsilylethynyl) pentacene. *Applied Physics Letters*, 93(10):103302, September 2008. 83, 84
- [132] John E. Anthony, David L. Eaton, and Sean R. Parkin. A Road Map to Stable, Soluble, Easily Crystallized Pentacene Derivatives. *Organic Letters*, 4(1):15–18, 2001. 84
- [133] Olga Lobanova Griffith, John E. Anthony, Adolphus G. Jones, and Dennis L. Lichtenberger. Electronic Properties of Pentacene versus Triisopropylsilylethynyl-Substituted Pentacene: Environment-Dependent Effects of the Silyl Substituent. *Journal of the American Chemical Society*, 132(2):580–586, 2009. 84
- [134] J. A. Lim, W. H. Lee, H. S. Lee, J. H. Lee, Y. D. Park, and K. Cho. Self-Organization of Ink-jet-Printed Triisopropylsilylethynyl Pentacene via Evaporation-Induced Flows in a Drying Droplet. *Advanced Functional Materials*, 18(2):229–234, 2008. 84
- [135] J. Trotter. The crystal structure of 1,5-dinitronaphthalene. *Acta Crystallographica*, 13(2):95–99, February 1960. 85, 86
- [136] Tomoyuki Kakinuma, Hirotaka Kojima, Minoru Ashizawa, Hidetoshi Matsumoto, and Takehiko Mori. Correlation of mobility and molecular packing in organic transistors based on cycloalkyl naphthalene diimides. *Journal of Materials Chemistry C*, 1(34):5395–5401, August 2013. 86

- [137] A. Yu Kovalevsky, I. I. Ponomarev, M. Yu Antipin, I. G. Ermolenko, and O. V. Shishkin. Influence of steric and electronic effects of substituents on the molecular structures and conformational flexibility of 1,8-naphthalenedicarboximides. *Russian Chemical Bulletin*, 49(1):70–76, January 2000. 86
- [138] Beatrice Fraboni, Andrea Ciavatti, Francesco Merlo, Luca Pasquini, Anna Cavallini, Alberto Quaranta, Annalisa Bonfiglio, and Alessandro Fraleoni-Morgera. Organic Semiconducting Single Crystals as Next Generation of Low-Cost, Room-Temperature Electrical X-ray Detectors. *Advanced Materials*, 24(17):2289–2293, 2012. 89
- [139] P. Cosseddu and A. Bonfiglio. Soft lithography fabrication of all-organic bottom-contact and top-contact field effect transistors. *Applied Physics Letters*, 88(2):023506, January 2006. 97
- [140] NIST US Department of Commerce. NIST XCOM: Photon Cross Sections Database. NIST XCOM: Photon Cross Sections Database. 98
- [141] I. Clairand, J. M. Bordy, E. Carinou, J. Daures, J. Debroas, M. Denozière, L. Donadille, M. Ginjaume, C. Itié, C. Koukorava, S. Krim, A. L. Lebacq, P. Martin, L. Struelens, M. Sans-Merce, and F. Vanhavere. Use of active personal dosimeters in interventional radiology and cardiology: Tests in laboratory conditions and recommendations - ORAMED project. *Radiation Measurements*, 46(11):1252–1257, November 2011. 100
- [142] F. Nava M. Bruzzi. Characterisation of silicon carbide detectors response to electron and photon irradiation. *Diamond and Related Materials*, pages 657–661, 2001. 108
- [143] Mohamed A. E. Abdel-Rahman, Annika Lohstroh, Imalka Jayawardena, and Simon J. Henley. The X-ray detection performance of polycrystalline CVD diamond with pulsed laser deposited carbon electrodes. *Diamond and Related Materials*, 22:70–76, February 2012. 108

- [144] S. Spadaro, G. Conte, M. Pimpinella, and A. S. Guerra. Electrical and dosimetric characterization of a CVD diamond detector with high sensitivity. *Radiation Measurements*, 48:1–6, January 2013. 108
- [145] M. Kabir, Safa Kasap, and John Rowlands. Photoconductors for X-Ray Image Detectors. In Safa Kasap Prof and Peter Capper Dr, editors, *Springer Handbook of Electronic and Photonic Materials*, pages 1121–1137. Springer US, January 2007. 108
- [146] Thomas Stübinger and Wolfgang Brütting. Exciton diffusion and optical interference in organic donor–acceptor photovoltaic cells. *Journal of Applied Physics*, 90(7):3632–3641, October 2001. 109
- [147] S. Matthew Menke, Wade A. Luhman, and Russell J. Holmes. Tailored exciton diffusion in organic photovoltaic cells for enhanced power conversion efficiency. *Nature Materials*, 12(2):152–157, February 2013. 109
- [148] A. L. Briseno, R. J. Tseng, M.-M. Ling, E. H. L. Falcao, Y. Yang, F. Wudl, and Z. Bao. High-Performance Organic Single-Crystal Transistors on Flexible Substrates. *Advanced Materials*, 18(17):2320–2324, 2006. 109, 159
- [149] Hee Taek Yi, Marcia M. Payne, John E. Anthony, and Vitaly Podzorov. Ultra-flexible solution-processed organic field-effect transistors. *Nature Communications*, 3:1259, December 2012. 109
- [150] Lei Zhang, Hanlin Wang, Yan Zhao, Yunlong Guo, Wenping Hu, Gui Yu, and Yunqi Liu. Substrate-Free Ultra-Flexible Organic Field-Effect Transistors and Five-Stage Ring Oscillators. *Advanced Materials*, 25(38):5455–5460, October 2013. 109
- [151] R. W. I. de Boer, M. Jochemsen, T. M. Klapwijk, A. F. Morpurgo, J. Niemax, A. K. Tripathi, and J. Pflaum. Space charge limited transport and time of flight measurements in tetracene single crystals:

- A comparative study. *Journal of Applied Physics*, 95(3):1196–1202, February 2004. 111
- [152] Laura Basiricò, Andrea Ciavatti, and Beatrice Fraboni. Comparative study of Organic Semiconducting Single-Crystals as Direct X-ray Detectors. 2015. 115
- [153] Beatrice Fraboni, Andrea Ciavatti, Laura Basiricò, and Alessandro Fraleoni-Morgera. FD 174: Organic semiconducting single crystals as solid-state sensors for ionizing radiation. *Faraday Discussions*, June 2014. 116
- [154] Gaurav Giri, Steve Park, Michael Vosgueritchian, Max Marcel Shulaker, and Zhenan Bao. High-Mobility, Aligned Crystalline Domains of TIPS-Pentacene with Metastable Polymorphs Through Lateral Confinement of Crystal Growth. *Advanced Materials*, 26(3):487–493, 2014. 127
- [155] P. Cosseddu, S. Lai, M. Barbaro, and A. Bonfiglio. Ultra-low voltage, organic thin film transistors fabricated on plastic substrates by a highly reproducible process. *Applied Physics Letters*, 100(9):093305, February 2012. 128, 133, 134
- [156] James Ziegler. SRIM. 138
- [157] P Beckerle and H Ströbele. Charged particle detection in organic semiconductors. *Nuclear Instruments and Methods in Physics Research Section A: Accelerators, Spectrometers, Detectors and Associated Equipment*, 449(1–2):302–310, July 2000. 138, 144, 145
- [158] S. K. Chaudhuri, A. Lohstroh, M. Nakhostin, and P. J. Sellin. Digital pulse height correction in HgI₂ γ -ray detectors. *Journal of Instrumentation*, 7(04):T04002, April 2012. 141

- [159] Sigen Wang, Paul Sellin, and Annika Lohstroh. Alpha particle transient response of a polycrystalline diamond detector. *Carbon*, 43(15):3167–3171, December 2005. 145
- [160] J. Ho, A. Rose, T. Swager, and V. Bulović. Solid-State Chemosensitive Organic Devices for Vapor-Phase Detection. In Dr Daniel A. Bernards, Professor George G. Malliaras, and Dr Róisín M. Owens, editors, *Organic Semiconductors in Sensor Applications*, number 107 in Materials Science, pages 141–184. Springer Berlin Heidelberg, January 2008. 149, 152, 153
- [161] Brian C. Sisk and Nathan S. Lewis. Vapor Sensing Using Polymer/Carbon Black Composites in the Percolative Conduction Regime. *Langmuir*, 22(18):7928–7935, 2006. 149, 152, 153
- [162] Stephen Maldonado, Edgardo García-Berríos, Marc D. Woodka, Bruce S. Brunshwig, and Nathan S. Lewis. Detection of organic vapors and NH₃(g) using thin-film carbon black–metallophthalocyanine composite chemiresistors. *Sensors and Actuators B: Chemical*, 134(2):521–531, September 2008. 149, 152, 153
- [163] Keith J. Albert, Nathan S. Lewis, Caroline L. Schauer, Gregory A. Sotzing, Shannon E. Stitzel, Thomas P. Vaid, and David R. Walt. Cross-Reactive Chemical Sensor Arrays. *Chemical Reviews*, 100(7):2595–2626, 2000. 149, 152, 153
- [164] J. Brunet, V. Parra Garcia, A. Pauly, C. Varenne, and B. Lauron. An optimised gas sensor microsystem for accurate and real-time measurement of nitrogen dioxide at ppb level. *Sensors and Actuators B: Chemical*, 134(2):632–639, September 2008. 150, 152, 153
- [165] M. F. Calhoun, J. Sanchez, D. Olaya, M. E. Gershenson, and V. Podzorov. Electronic functionalization of the surface of organic semiconductors with self-assembled monolayers. *Nature Materials*, 7(1):84–89, January 2008. 150, 156

- [166] David J. Ellison, Bumsu Lee, V. Podzorov, and C. Daniel Frisbie. Surface Potential Mapping of SAM-Functionalized Organic Semiconductors by Kelvin Probe Force Microscopy. *Advanced Materials*, 23(4):502–507, 2011. 156
- [167] Camelia Matei Ghimbeu, Roger Gadiou, Joseph Dentzer, Dominique Schwartz, and Cathie Vix-Guterl. Influence of Surface Chemistry on the Adsorption of Oxygenated Hydrocarbons on Activated Carbons. *Langmuir*, 26(24):18824–18833, 2010. 157
- [168] Masashi Mizukami, Yasuhiro Nakagawa, and Kazue Kurihara. Surface Induced Hydrogen-Bonded Macrocluster Formation of Methanol on Silica Surfaces. *Langmuir*, 21(21):9402–9405, 2005. 157
- [169] E. Menard, V. Podzorov, S.-H. Hur, A. Gaur, M. E. Gershenson, and J. A. Rogers. High-Performance n- and p-Type Single-Crystal Organic Transistors with Free-Space Gate Dielectrics. *Advanced Materials*, 16(23-24):2097–2101, 2004. 159
- [170] Bregt Verreet, Paul Heremans, Andre Stesmans, and Barry P. Rand. Microcrystalline Organic Thin-Film Solar Cells. *Advanced Materials*, 25(38):5504–5507, 2013. 159
- [171] D. Käfer, L. Ruppel, G. Witte, and Ch. Wöll. Role of Molecular Conformations in Rubrene Thin Film Growth. *Physical Review Letters*, 95(16):166602, October 2005. 159
- [172] J. H. Seo, D. S. Park, S. W. Cho, C. Y. Kim, W. C. Jang, C. N. Whang, K.-H. Yoo, G. S. Chang, T. Pedersen, A. Moewes, K. H. Chae, and S. J. Cho. Buffer layer effect on the structural and electrical properties of rubrene-based organic thin-film transistors. *Applied Physics Letters*, 89(16):163505, October 2006. 159
- [173] Se-W. Park, S. H. Jeong, Jeong-M. Choi, Jung Min Hwang, Jae Hoon Kim, and Seongil Im. Rubrene polycrystalline transistor channel

- achieved through in situ vacuum annealing. *Applied Physics Letters*, 91(3):033506, July 2007. 159
- [174] Hyeok Moo Lee, Hanul Moon, Hyo-Sik Kim, Yong Nam Kim, Sung-Min Choi, Seunghyup Yoo, and Sung Oh Cho. Abrupt heating-induced high-quality crystalline rubrene thin films for organic thin-film transistors. *Organic Electronics*, 12(8):1446–1453, August 2011. 159
- [175] Marcello Campione. Rubrene Heteroepitaxial Nanostructures With Unique Orientation. *The Journal of Physical Chemistry C*, 112(42):16178–16181, 2008. 160
- [176] Adele Sassella, Luisa Raimondo, Marcello Campione, and Alessandro Borghesi. Patterned Growth of Crystalline Organic Heterostructures. *Advanced Materials*, 25(20):2804–2808, 2013. 160
- [177] Zhefeng Li, Jun Du, Qin Tang, Feng Wang, Jian-Bin Xu, Jimmy C. Yu, and Qian Miao. Induced Crystallization of Rubrene in Thin-Film Transistors. *Advanced Materials*, 22(30):3242–3246, 2010. 160
- [178] Chul-Ho Lee, Theanne Schiros, Elton J. G. Santos, Bumjung Kim, Kevin G. Yager, Seok Ju Kang, Sunwoo Lee, Jaeun Yu, Kenji Watanabe, Takashi Taniguchi, James Hone, Efthimios Kaxiras, Colin Nuckolls, and Philip Kim. Epitaxial Growth of Molecular Crystals on van der Waals Substrates for High-Performance Organic Electronics. *Advanced Materials*, 26(18):2812–2817, 2014. 160
- [179] Raimondo, Trabattoni, Campione, Braga, Holmberg, Norris, Moret, Ciavatti, Fraboni, and Sassella. Growth and Device Integration of Large-Area Free-Standing Rubrene Thin Films with Single-Crystal Quality. 2014. 160, 161
- [180] E. Papavinasam, S. Natarajan, and N.c. Shivaprakash. Reinvestigation of the crystal structure of β -alanine. *International Journal of Peptide and Protein Research*, 28(5):525–528, 1986. 161

- [181] Silvia Trabattoni, Massimo Moret, Marcello Campione, Luisa Raimondo, and Adele Sassella. Epitaxial Growth of Organic Semiconductor Polymorphs on Natural Amino Acid Single Crystals. *Crystal Growth & Design*, 13(10):4268–4278, 2013. 161
- [182] S. Tavazzi, A. Borghesi, A. Papagni, P. Spearman, L. Silvestri, A. Yassar, A. Camposeo, M. Polo, and D. Pisignano. Optical response and emission waveguiding in rubrene crystals. *Physical Review B*, 75(24):245416, June 2007. 164
- [183] W. L. Kalb, T. Mathis, S. Haas, A. F. Stassen, and B. Batlogg. Organic small molecule field-effect transistors with Cytop™ gate dielectric: Eliminating gate bias stress effects. *Applied Physics Letters*, 90(9):092104, February 2007. 168, 173
- [184] Nikolas A. Minder, Shimpei Ono, Zhihua Chen, Antonio Facchetti, and Alberto F. Morpurgo. Band-Like Electron Transport in Organic Transistors and Implication of the Molecular Structure for Performance Optimization. *Advanced Materials*, 24(4):503–508, 2012. 168
- [185] K. Willa, R. Häusermann, T. Mathis, A. Facchetti, Z. Chen, and B. Batlogg. From organic single crystals to solution processed thin-films: Charge transport and trapping with varying degree of order. *Journal of Applied Physics*, 113(13):133707, April 2013. 169
- [186] Vikram C. Sundar, Jana Zaumseil, Vitaly Podzorov, Etienne Menard, Robert L. Willett, Takao Someya, Michael E. Gershenson, and John A. Rogers. Elastomeric Transistor Stamps: Reversible Probing of Charge Transport in Organic Crystals. *Science*, 303(5664):1644–1646, March 2004. PMID: 15016993. 172
- [187] M. E. Gershenson, V. Podzorov, and A. F. Morpurgo. Colloquium: Electronic transport in single-crystal organic transistors. *Reviews of Modern Physics*, 78(3):973–989, September 2006. 174

- [188] T. J. Richards and H. Sirringhaus. Analysis of the contact resistance in staggered, top-gate organic field-effect transistors. *Journal of Applied Physics*, 102(9):094510, November 2007. 174
- [189] Daniele Braga and Gilles Horowitz. Subthreshold regime in rubrene single-crystal organic transistors. *Applied Physics A*, 95(1):193–201, April 2009. 174
- [190] Reid J. Chesterfield, John C. McKeen, Christopher R. Newman, Paul C. Ewbank, Demétrio A. da Silva Filho, Jean-Luc Brédas, Larry L. Miller, Kent R. Mann, and C. Daniel Frisbie. Organic Thin Film Transistors Based on N-Alkyl Perylene Diimides: Charge Transport Kinetics as a Function of Gate Voltage and Temperature. *The Journal of Physical Chemistry B*, 108(50):19281–19292, 2004. 174
- [191] C. Goldmann, C. Krellner, K. P. Pernstich, S. Haas, D. J. Gundlach, and B. Batlogg. Determination of the interface trap density of rubrene single-crystal field-effect transistors and comparison to the bulk trap density. *Journal of Applied Physics*, 99(3):034507, February 2006. 176

Acknowledgements

I'd like to thank my supervisor Prof. Beatrice Faboni, this thesis would not have been possible without her help, support, patience and continuous encouragements, not to mention her advice in electrical characterization and organic semiconductor experience.

From the Synchrotron Laboratory ELETTRA, Trieste, Italy I would like to thank Dr. Alessandro Fraleoni-Morgera for the substantial collaboration (preparation of the single crystals, XRD characterization) and for the valuable discussions. I'm very grateful to Dr. Giuliana Tromba and Dr. Diego Dreossi for the given amount of time on beamline SYRMEP and the useful help during the beamtimes at ELETTRA.

I would also like to thank Prof. P.J. Sellin of the Department of Physics, University of Surrey, UK, and Prof. D. Norris of the Optical Material Engineering Laboratory (OMEL), ETH, Zurich for giving me the greatest opportunity to work in their group as visiting student. My sincere gratitude and many thanks go to Dr. Daniele Braga to be fully available for teaching me the fundamental of fabrication and characterization of organic single crystals transistors.

A particular thanks also to our collaborators, Prof. Annalisa Bonfiglio and Dr Piero Cosseddu, from University of Cagliari, Italy for their work with flexible substrates; Prof. Adele Sassella and her group from University of Milano-Bicocca, Italy for their collaboration in the growth, characterization and discussions about rubrene thin films.

I would like to acknowledge the EU Project i-Flexis that provided the

financial support. I would like to acknowledge also the Marco Polo project of the Department of Physics and Astronomy of the University of Bologna, Italy for the financial support of my research period in abroad.

Thanks to Martina, Lucia, Alessandra, Saurabh, Albert, Stefania, Geeta, Shankar, Alberto, Marco M., Isacco, Marco C., Tobias and all my colleagues for their sustain, scientific and not, throughout these years. A special thanks to Dr. Laura Basirico' for the fruitful collaboration and her inestimable support during the last year.